Ioannis Sokratis DRAKATOS

Seismic behaviour of slab-column connections without transverse reinforcement

École
Polytechnique
Fédérale
de Lausanne

2016

EPFL
ÉCOLE POLYTECHNIQUE
FÉDÉRALE DE LAUSANNE

Seismic behaviour of slab-column connections without transverse reinforcement

PAR

Ioannis Sokratis DRAKATOS

EPFL
ÉCOLE POLYTECHNIQUE
FÉDÉRALE DE LAUSANNE

Suisse
2016

Foreword

The gravity load resisting system of mid- to high-rise buildings that are braced by reinforced concrete (RC) walls consists often of slender RC columns and flat RC slabs. This system has a low horizontal stiffness and does not contribute significantly to the horizontal stiffness of the building. However, to avoid premature failure under seismic loading, it is necessary that the gravity load resisting system is able to accommodate the lateral displacements that the horizontal loading evokes. A common premature failure mode of slab-column connection is the brittle punching shear failure. To avoid this failure mode, the designer needs to estimate the deformation capacity of the slab-column connection under seismically induced deformations and compare it to the demand. Current codes predict the deformation capacity of slab-column connections by means of empirical models.

Ioannis Drakatos develops models for predicting the strength and the deformation capacity of slab-column connections under seismic loading. The focus of his work is on the effect of cyclic loading on the deformation capacity. To investigate this effect experimentally, he tested 13 full-scale isolated slab-column connections without shear reinforcement. The test series allowed to compare the response of monotonically and cyclically loaded slabs for different gravity shear ratios and reinforcement ratios. Ioannis Drakatos then extends the model of the Critical Shear Crack Theory for slab-column connections subjected to seismic loading, considering the monotonic load case and the cyclic load case. The model was validated against the own tests as well as tests published in the literature. The comparison shows a very good performance. The thesis concludes with the proposal of an effective beam width method that allows estimating the deformation demand on slab-column connections from elastic finite element analysis.

Lausanne, September 2016

Prof. Dr. Katrin Beyer   Prof. Dr. Aurelio Muttoni

Funding

"αὐτὸν ἄρα νοεῖ (ὁ νοῦς), εἴπερ ἐστὶ τὸ κράτιστον, καὶ ἔστιν ἡ νόησις νοήσεως νόησις."

Ἀριστοτέλης (Μετὰ τὰ Φυσικά, 1074β.15–1075α.10)

Translation

"therefore (mind) thinks itself, if it is the most excellent thing, and its thinking is a thinking of thinking."

Aristotle (Metaphysics, 1074b.15–1075a.10)

Acknowledgements

most special thanks go to Francesco Cavagnis, who has been a "brother" for me during the last four years, both inside and outside EPFL.

I would like to thank friends and colleagues from other research groups (Aida, Albano, Anastasia, Apostolos, Carlos, Eva, Hadi, Kyriaki, Landolf, Maléna, Marc, Mark, Myrsini, Raphaël, Talayeh, Valentina) for the fruitful discussions in the laboratory and during the breaks. Very special thanks to Dimitrios, Manuel, and Vasilios, for all the technical, non-technical, history-related and, most importantly, philosophical conversations. I consider myself very lucky that I have met them.

After my master studies at the University of Patras, Greece, my decision to continue as PhD student at EPFL was largely encouraged by my Professors Michael Fardis, Anastasios Triantafyllou and my master thesis director Stephanos Dritsos. I would therefore like to thank them for supporting my application in the doctoral school of EPFL and for all the useful advices. Moreover, I would like to express my gratitude to the Greek public education system for providing me knowledge and motivation to become a better person day by day.

Thanks to my friends from the University of Patras, mainly Ioannis, Stelios, Charis, and Christos for their support, advices, and fruitful discussions.

My scientific background was deeply influenced by my high-school mathematics teacher Anastasios Rompotis (Αναστάσιος Ρομποτής), to whom I own my big love for mathematics and engineering and several values such as perseverance and rigorousness that guide me through life. Huge thanks to my mother for teaching me French since my early childhood, which contributed significantly to my decision to come in Switzerland and made my stay much more comfortable.

Last but not least, huge thanks to my father Dionysios (Διονύσιος), my mother Chrysoula (Χρυσούλα), and by brother Alexandros (Αλέξανδρος). Special thanks to my father and mother for giving me, through their life, the most important lesson for my career and life: "technological advancements cannot counterbalance any lack of humanistic spirit, conscience, and ethics", a message that is nowadays more contemporary than ever. Thank you from my heart (Ευχαριστώ από καρδιάς!!!).

Ioannis

Abstract

Reinforced concrete (RC) flat slabs supported by slender columns are often used as gravity load resisting system for buildings. In regions of moderate and high seismicity such buildings are typically braced by RC walls, which carry the largest portion of the horizontal loads generated during earthquakes. Therefore, the slab-column system does not contribute significantly to the lateral stiffness and strength of the structure, but each slab-column connection must be able to accommodate the seismically induced drifts of the building while maintaining its capacity to transfer vertical loads from the slab to the columns. Otherwise, brittle punching failure of the slab occurs and the deformation capacity of the entire building is limited by the deformation capacity of the slab-column connection if the building is not designed to resist progressive collapse.

The first part of this work presents an experimental investigation on 13 full-scale internal slab-column connections without transverse reinforcement. The objective of the test campaign is to assess the influence of the loading history (monotonic vs. reversed cyclic) for different gravity loads and reinforcement ratios. The study shows that cyclic loading leads, in particular for slabs subjected to low gravity loads, to significant moment strength and deformation capacity reduction when compared to results obtained from monotonic loading tests. The effect of cyclic loading is more pronounced for slabs with low reinforcement content.

In the second part, a mechanical model is presented for predicting the moment-rotation relationship of interior slab-column connections without transverse reinforcement when subjected to seismically induced drifts. The model accounts explicitly for the three load transfer mechanisms between slab and column contributing to the unbalanced moment resistance, i.e., eccentric shear, flexure and torsion. The moment resistance and deformation capacity are deduced from the intersection of the moment-rotation curve with a failure criterion that is based on the Critical Shear Crack Theory and distinguishes between monotonic and cyclic loading conditions. The model predicts well the moment strength and the deformation capacity of slabs tested within this research and reported in the literature.

The third part of this thesis proposes an extension of the mechanical model for the moment-rotation relationship presented earlier to account for the hysteretic behaviour and cumulative damage effects on slab-column connections subjected to cyclic loading. A hysteretic moment-curvature relationship is proposed for the radial direction, based on local deformation measurements from the cyclic tests. Cyclic damage is considered by adopting a damage index proposed by a previous study. The extended model predicts more accurately the response of cyclic tests than the simplified approach based on the monotonic model.

Finally, based on the theoretical investigation of the two previous parts, two methods are proposed for the numerical analysis of flat slab buildings to simulate the column deformation and the slab deformation until midspan. First, an Effective Beam Width method is presented and compared to test results of flat slab buildings with over-hangs. Then, a simplified method is proposed for the analysis of slab-column connections not part of the lateral force-resisting system. This method allows estimating the contribution of column and slab deformation to the interstorey drift.

Résumé

Les planchers-dalles en béton armé soutenus par des colonnes élancées sont fréquemment utilisés pour la reprise des charges gravitaires de bâtiments. Dans des régions à sismicité modérée et élevée ces bâtiments sont typiquement contreventés par des murs en béton armé qui reprennent une grande portion des charges horizontales générées pendant les tremblements de terre. Le système structural dalle-colonne ne contribue donc que de manière limitée à la rigidité latérale et à la résistance de la structure. Il est nécessaire que chaque connexion doit accommoder les déplacements sismiques du bâtiment et maintenir sa capacité de transférer les charges verticales aux colonnes. Dans le cas contraire, une rupture fragile par poinçonnement se produit et la capacité de déformation du bâtiment dans son ensemble est limitée par celle de la connexion dalle-colonne dans le cas où le bâtiment n'est pas dimensionné pour résister à un effondrement progressif.

La première partie de ce travail présente une étude expérimentale portant sur 13 connexions dalle-colonne intérieures sans armature transversale, testées à pleine échelle. L'objectif de la campagne d'essais est d'évaluer l'influence de l'historique de chargement (monotonique/cyclique) pour différents charges gravitaires et taux d'armature. Les résultats montrent que le chargement cyclique entraîne une réduction significative de la résistance et de la capacité de déformation par rapport à ce qui a été obtenu dans les essais monotoniques, notamment pour les dalles soumises à de faibles charges gravitaires. L'effet cyclique est plus important pour les dalles avec un faible taux d'armature.

Dans la seconde partie, un modèle mécanique est présenté pour calculer la relation moment-rotation des connexions dalle-colonne intérieures sans armature transversale soumises à des déplacements inter-étage dus aux actions sismiques. Le modèle tient explicitement compte des trois mécanismes de transfert de charge de la dalle à la colonne qui contribuent à la résistance, à savoir l'effort tranchant excentré, la flexion et la torsion. La résistance et la capacité de déformation sont obtenus par l'intersection de la courbe moment-rotation avec le critère de rupture qui est basé sur la théorie de fissure critique et distingue les conditions de chargement monotoniques et cycliques. Le modèle prédit de manière satisfaisante la résistance et la capacité de déformation des dalles testées dans le cadre de cette recherche ainsi que celles trouvées dans la littérature.

La troisième partie de cette thèse propose une extension du modèle mécanique pour la relation moment-rotation précédemment présenté avant pour tenir compte du comportement hystérétique et des effets liés à l'endommagement cumulatif sur des connexions dalle-colonne soumises à des charges cycliques. Une loi moment-courbure hystérétique est proposée pour la direction radiale sur la base des mesures de déformation locales obtenues dans les essais cycliques. L'endommagement cyclique est introduit par la considération d'un indice d'endommagement proposé dans une étude précédente. Le modèle cyclique prédit avec plus de précision la réponse d'essais cycliques que le modèle simplifié basé sur le modèle monotonique.

Finalement, sur la base de l'étude théorique des deux parties précédentes, deux méthodes pour l'analyse numérique des bâtiments avec planchers-dalles sont proposées afin de simuler la déformation de la colonne et la déformation de la dalle jusqu'à la mi-travée. Une méthode de poutre équivalente est présentée et comparée aux résultats expérimentaux portant sur des bâtiments avec planchers-dalles. Une méthode simplifiée est ensuite proposée pour l'analyse des connexions dalle-colonne ne partici-

pant pas à la reprise de charges horizontales. Cette méthode permet d'estimer la contribution de la déformation de la colonne et de la dalle au déplacement inter-étage.

Mots-clefs : planchers-dalles en béton armé, connexion dalle-colonne, chargement sismique, théorie de la fissure critique, déplacement inter-étage, moment non balancé, historique de chargement, capacité de déformation, mécanismes résistant aux charges latérales, méthode de poutre équivalente

Zusammenfassung

Flachdeckenplatten aus Stahlbeton auf schlanken Stützen werden oft als statisches System von Gebäuden eingesetzt. In Regionen mit moderater oder hoher Seismizität werden solche Gebäudetypen typischerweise mit Stahlbetonwänden ausgesteift, die den größten Anteil der Horizontallasten während eines Erdbebens abtragen. Auf Grund dessen, tragen die Verbindungen zwischen Stütze und Deckenplatte nicht signifikant zur horizontalen Steifigkeit und Festigkeit des Systems bei. Nichtsdestoweniger müssen diese Verbindungen in der Lage sein, trotz der auftretenden horizontalen Verschiebungen der Struktur während eines Erdbebens, die anstehenden Vertikallasten von den Deckenplatten in die Stützen zu übertragen. Ist dies nicht der Fall, tritt sprödes Durchstanzversagen der Decken-Stützenverbindung auf, was somit die horizontale Verformungskapazität des gesamten Gebäudes auf die Kapazität der Verbindung limitiert, wenn dies nicht in der Planung des Gebäudes berücksichtigt wurde.

Der erste Teil dieser Arbeit präsentiert eine Versuchsreihe von 13 maßstäblichen internen Decken-Stützenverbindungen ohne Querbewährung. Das Ziel der Versuche ist, einen besseren Einblick in den Einfluss der Lastgeschichte (monoton vs. beidseitig zyklisch) bei verschiedenen Vertikallasten und Bewährungsgraden zu erhalten. Es zeigt sich, dass zyklische Belastungen, besonders bei gering belasteten Deckenplatten, zu signifikanten Verringerungen der Momententraglast und Verformungskapazität der Verbindung, im Vergleich mit monotonen Lastgeschichten, führen. Dieser Effekt ist für geringe Bewährungsgrade stärker ausgeprägt. Im zweiten Teil wird ein mechanisches Modell zur Berechnung der Momenten-Roationsbeziehung von internen Decken-Stützenverbindungen ohne Querbewährung, die seismisch induzierten Verschiebungen ausgesetzt sind, vorgestellt. Das Modell berücksichtigt auf explizite Art die drei Lastabtragungsmechanismen zwischen Platte und Stütze, die zum Kippmomentenwiderstand beitragen: exzentrischer Schub, Biegung und Torsion. Die Momententraglast und Verformungskapazität der Verbindung werden vom Schneiden der Momenten-Rotationskurve mit einer Versagensbedingung, die auf der ‚Theorie des kritischen Schubrisses‘ basiert, hergeleitet. Es wird zwischen monotonen und zyklischen Lastbedingungen unterschieden. Es zeigt sich, dass das Modell den Momentenwiderstand und die Deformationskapazität von in dieser Arbeit untersuchten und in der Literatur vorhandenen Verbindungen zufriedenstellend vorhersagt.

Der dritte Abschnitt dieser Arbeit behandelt einen Ausbau des zuvor vorgestellten Rechenmodells, um das hysteretische Verhalten und kumulative Schadenseffekte in Decken-Stützenverbindungen, die zyklischen Belastungen ausgesetzt sind, zu berücksichtigen. Eine hysteretische Momenten-Krümmungsbeziehung, basierend auf lokalen Messungen in der Versuchsreihe, wird in radialer Richtung eingeführt. Zyklischer Schadensaufbau wird durch die Zuhilfenahme eines Schadensindexes, basierend auf einer vorhergehenden Arbeit, behandelt. Das erweiterte Modell sagt den Ablauf der zyklischen Versuche präziser voraus als der vereinfachte, zuvor vorgestellte Ansatz.

Abschließend werden, basierend auf den theoretischen Untersuchungen der zwei vorhergehenden Abschnitte, zwei Methoden zur numerischen Berechnung von Gebäuden mit Flachdecken vorgeschlagen, die die Stützenverformungen und Plattendeformationen bis Feldmitte vorhersagen. Die erste, eine ‚Methode der effektiven Plattenbreite‘, wird vorgestellt und mit Versuchsergebnissen von Gebäuden mit Flachdecken und Auskragungen verglichen. Eine zweite, vereinfachte Methode wird für die Berechnung von Decken-Stützenverbindungen die nicht Teil der horizontallast abtragenden Struktur sind, vorge-

schlagen. Dieser Ansatz erlaubt die Abschätzung des Beitrags von Stützen- und Deckenverformung an der horizontalen Geschoßverschiebung.

Stichwörter: Flachdecken aus Stahlbeton, Decken-Stützenverbindung, Erdbebenbelastung, Theorie des kritischen Schubrisses, Geschoßverschiebung, Kippmoment, Belastungsgeschichte, Verformungskapazität, vertikallastabtragende Mechanismen, Methode der effektiven Plattenbreite

Riassunto

Piastre continue in calcestruzzo armato sostenute da pilastri snelli sono frequentemente usate come sistema resistente ai carichi gravitazionali negli edifici. In regioni a media e alta sismicità questi edifici sono tipicamente controventati da muri in calcestruzzo armato, che hanno la funzione di riprendere i carichi orizzontali in caso di terremoto. Il sistema piastra-pilastro non contibuisce significativamente alla rigidezza laterale e alla resistenza della struttura, ma ogni connessione piastra-pilastro deve essere in grado di seguire gli spostamenti dell' edificio dovuti all'azione sismica mantenendo la capacità di trasferire i carichi verticali ai pilastri. In caso contrario, una rottura fragile per punzonamento può manifestarsi e la capacità di deformazione dell'intero edificio é limitata dalla capacità di deformazione della connessione piastra-pilastro se l'edificio non é progettato per resistere attraverso un collasso progressivo.

La prima parte di questo lavoro presenta uno studio sperimentale su 13 connessioni piastra-pilastro interno senza armatura di punzonamento, in scala 1:1. L'obiettivo della campagna sperimentale é di valutare l'influenza della storia di carico (monotonica o ciclica) al variare del carico verticale applicato e delle percentuali di armatura. I risultati mostrano che une storia di carico ciclica comporta una riduzione significativa della resistenza e della capacità di deformazione in confronto a una storia di carico monotonica, soprattutto per carichi verticali bassi. Questo effetto ciclico risulta più pronunciato per piastre con una ridotta percentuale di armatura.

Nella seconda parte viene presentato un modello meccanico per calcolare la relazione momento-rotazione di connessioni piastra-pilastro interno senza armatura di punzonamento soggetti a azioni sismiche. Il modello tiene conto dei tre meccanismi di trasferimento di carico tra piastra e pilastro che contribuiscono alla resistenza (taglio eccentrico, flessione, e torsione) in modo esplicito. La resistenza e la capacità di deformazione sono ottenuti dall'intersezione della curva momento-rotazione con un criterio di rottura basato sulla teoria della fessura critica, e distingue tra condizioni di carico monotoniche e cicliche. Il modello prevede in maniera soddisfacente la resistenza e la capacità di deformazione sia delle piastre testate nell'ambito di questa tesi che di altre presenti in letteratura.

La terza parte di questa tesi propone una estensione del modello meccanico per la relazione momento-rotazione precedentemente mostrato tenendo conto del comportamento isteretico e degli effetti legati al danneggiamento cumulativo di connessioni piastra-pilastro soggette a carico ciclico. Una legge momento-curvatura isteretica viene proposta per la direzione radiale, sulla base di misure di deformazione locali ottenute dalle prove cicliche. Il danneggiamento ciclico é considerato attraverso un indice di danneggiamento proposto in uno studio precedente. Il modello esteso fornisce una previsione più precisa della risposta delle prove cicliche rispetto all'approccio semplificato.

Infine, sulla base dello studio teorico delle due parti precedenti, due metodi per l'analisi numerica di edifici con piastre continue per simulare la deformazione del pilastro e la deformazione della piastra fino alla mezzeria sono proposti. Inizialmente, viene presentato un metodo di trave equivalente, il quale é stato comparato ai dei risultati di prove su edifici con piastre continue. Successivamente, un metodo semplificato per l'analisi di connessioni piastra-pilasto che non fanno parte del sistema resistente ai carichi laterali viene proposto. Il metodo permette di stimare il contributo della deformazione del pilastro e della piastra allo spostamento relativo di interpiano.

Σύνοψη

Οι πλάκες χωρίς δοκούς από οπλισμένο σκυρόδεμα εδραζόμενες επί λυγηρών υποστυλωμάτων χρησιμο-ποιούνται συχνά ως σύστημα ανάληψης κατακόρυφων δράσεων κτιρίων. Σε περιοχές μέσης και ισχυρής σεισμικότητας τα κτίρια αυτά συνήθως ενισχύονται από τοιχεία οπλισμένου σκυροδέματος, τα οποία α-ναλαμβάνουν μεγάλο μέρος των οριζοντίων φορτίων που προκύπτουν από τους σεισμούς. Επομένως, το σύστημα πλάκα-υποστύλωμα δε συνεισφέρει καθοριστικά στην πλευρική δυσκαμψία και στην αντοχή της κατασκευής, αλλά κάθε σύνδεση πλάκας-υποστυλώματος πρέπει να ακολουθεί τις σεισμικές μετακινήσεις του κτιρίου και να διατηρεί την ικανότητα μεταφοράς των κατακόρυφων φορτίων στα υποστυλώματα. Σε αντίθετη περίπτωση, συμβαίνει ψαθυρή αστοχία λόγω διάτρησης και η ικανότητα παραμόρφωσης ολόκλη-ρου του κτιρίου περιορίζεται από την ικανότητα παραμόρφωσης της σύνδεσης πλάκας-υποστυλώματος στην περίπτωση που το κτιρίο δεν έχει σχεδιασθεί έναντι προοδευτικής κατάρρευσης.

Το πρώτο μέρος της παρούσας εργασίας παρουσιάζει μια πειραματική μελέτη 13 εσωτερικών συνδέσεων πλάκας-υποστυλώματος χωρίς οπλισμό διάτρησης, σε πλήρη κλίμακα. Ο σκοπός των πειραμάτων είναι η αξιολόγηση της επιρροής της ιστορίας φόρτισης (μονοτονική/ανακυκλιζόμενη) για διαφορετικά κατα-κόρυφα φορτία και γεωμετρικά ποσοστά οπλισμού. Τα αποτελέσματα δειχνουν ότι η ανακυκλιζόμενη φόρτιση προκαλεί σημαντική απομείωση της αντοχής και της ικανότητας παραμόρφωσης σε σχέση με τα αποτελέσματα μονοτονικών δοκιμών, ιδίως για συνδέσεις υπό μικρά κατακόρυφα φορτία. Η επιρροή της ανακυκλιζόμενης φόρτισης είναι πιο εμφανής σε πλάκες με χαμηλό γεωμετρικό ποσοστό οπλισμού.

Στο δεύτερο μέρος, παρουσιάζεται ένα αναλυτικό προσομοίωμα για το υπολογισμό της σχέσης ροπής-στροφής εσωτερικών συνδέσεων πλάκας-υποστυλώματος χωρίς οπλισμό διάτρησης υπό σεισμικές κατα-πονήσεις. Το προσομοίωμα λαμβάνει ρητώς υπόψιν τους τρεις μηχανισμούς μεταφοράς φορτίου από την πλάκα στο υποστύλωμα (έκκεντρη διάτμηση, κάμψη, και στρέψη). Η αντοχή και η ικανότητα παραμόρ-φωσης προκύπτουν από την τμήση της καμπύλης ροπής-στροφής με το κριτήριο αστοχίας που βασίζεται στην θεωρία κρίσιμης ρωγμής και διακρίνει μονοτονικές και ανακυκλιζόμενες συνθήκες φόρτισης. Το προσομοίωμα προβλέπει με ικανοποιητική ακρίβεια την αντοχή και την ικανότητα παραμόρφωσης δοκιμίων της παρούσας έρευνας καθώς και δοκιμίων από τη βιβλιογραφία.

Το τρίτο μέρος της παρούσας διατριβής προτείνει μία επέκταση του αναλυτικού προσομοιώματος για τη σχέση ροπή-στροφή που παρουσιάστηκε προηγουμένως ώστε να ληφθεί υπόψιν η υστερητική συμπεριφορά και φαινόμενα συσσώρευσης βλάβης σε συνδέσεις πλάκας-υποστυλώματος υπό ανακυκλιζόμενη φορτιση. Ένας υστερητικός νόμος ροπής-καμπυλότητας προτείνεται για την ακτινική διεύθυνση βάσει τοπικών μετρήσεων παραμορφώσεων από τα πειράματα ανακυκλιζόμενης φόρτισης. Η βλάβη λόγω ανακύκλισης εισάγεται μέσω ενός δείκτη βλάβης που έχει προταθεί σε μια προηγούμενη μελέτη. Το προσομοίωμα ανακυκλιζόμενης φορτισης προβλέπει την απόκριση των αντίστοιχων πειραμάτων με μεγαλύτερη ακρίβεια από το απλοποιητικό προσομοίωμα που βασίζεται στο προσομοίωμα μονοτονικής φορτισης.

Τελικώς, επί τη βάσει της ως άνω θεωρητικής μελέτης, προτείνονται δύο μέθοδοι για την αριθμητική προσομοίωση κτιρίων χωρίς δοκούς ώστε να ληφθεί υπόψιν η παραμόρφωση του υποστυλώματος και της πλάκας έως το μέσον του ανοίγματός της. Αρχικά, προτείνεται μία μέθοδος ισοδύναμης δοκού και συγκρίνεται με πειραματικά αποτελέσματα συστημάτων χωρίς δοκούς. Υστερα, προτείνεται μια απλο-ποιητική μέθοδος για την ανάλυση συνδέσεων πλάκας-υποστυλώματος που δε συμμετέχουν στο σύστημα ανάληψης σεισμικών δράσεων. Αυτή η μέθοδος επιτρέπει τον υπολογισμό της συνεισφοράς τόσο της

παραμόρφωσης του υποστυλώματος όσο και της παραμόρφωσης της πλάκας στη σχετική μετακίνηση του ορόφου.

Λέξεις-κλειδιά: πλάκες χωρίς δοκούς από οπλισμένο σκυρόδεμα, σύνδεση πλάκας-υποστυλώματος, ανακυκλιζόμενη φόρτιση, θεωρία κρίσιμης ρωγμής, σχετική μετακίνηση ορόφου, ροπή σύνδεσης πλάκας-υποστυλώματος, ιστορία φόρτισης, ικανότητα παραμόρφωσης, μηχανισμοί αντίστασης στα πλευρικά φορτία, μέθοδος ισοδύναμης δοκού

Contents

Notations

The following symbols are used in this thesis:

A_c	area enclosed by the critical perimeter
B	slab specimen size; Chapter 2: subscript designating tension in the bottom reinforcement [Bro09]
b	Chapter 2: diameter of a circle with the same surface as the region inside the basic control perimeter [Fib11] Chapter 7: effective beam width;
b_1	dimension of the critical section measured in the direction of the span for which moments are determined
b_2	dimension of the critical section measured orthogonal to the span for which moments are determined
b_o	perimeter of the critical section at $d/2$ from the column
c	size of a square column
c_1	perimeter of the critical section at $d/2$ from the column
c_2	perimeter of the critical section at $d/2$ from the column
D	damage index
D_c	damage index due to cyclic loading
D_δ	damage index due to maximum deformation
d	slab effective depth (distance from the tension reinforcement to the extreme compressed fibre)
dE	incremental absorbed hysteretic energy
d_g	maximum diameter of the aggregate
$d_g.0$	reference aggregate size (16 mm, 0.63 in)
E_c	modulus of elasticity of concrete
E_s	modulus of elasticity of reinforcing steel
EI	rotational stiffness of the slab-column connection (Effective Beam Width method)
EI_0	initial stiffness of the moment-curvature relationship (before cracking)
EI_1	stiffness of the moment-curvature relationship after cracking
EI_{eff}	effective stiffness of the column
EI_{gr}	uncracked (gross) stiffness of the column
e	ratio of unbalanced moment to applied vertical load on the slab-column connection (eccentricity)
f_c	average compressive strength of concrete (cylinder)

$f_{j.cyc}(\phi_i)$	radial flexibility of the sector element at angle ϕ_i for cyclic loading (j^{th} peak)
f_o	yield flexibility in the radial direction (inverse of yield stiffness)
$f_{u.mono}(\phi_i)$	radial flexibility of the sector element at angle ϕ_i at failure under monotonic loading
f_y	yield stress of reinforcing steel (flexural reinforcement)
$H_{st.n}$	storey height of the nth floor
H_{tot}	height of building to roof level
h	slab thickness – beam height (Effective Beam Width method)
I_{cr}	moment of inertia of cracked concrete section (equivalent beam)
I_g	moment of inertia of uncracked concrete section (equivalent beam)
i	index designating a sector element of the slab
J_c	property analogous to the polar moment of inertia of the critical section [ACI14]
j_d	distance between the centroid and the the edge of the critical perimeter
K_d	coefficient to take into account the stiffness degradation due to increasing imposed storey drift [Gro97]
k	index designating the load step for the calculation of the moment-rotation relationship
k_e	reduction factor for the length of the control perimeter [Fib11]
L	distance between the axes of the columns in a continuous slab (slab span)
l_1	distance between supports orthogonal to the unbalanced moment vector ($= L$)
l_2	distance between supports parallel to the unbalanced moment vector
M	unbalanced moment introduced to the slab-column connection
M_{cr}	cracking moment
M_{el}	unbalanced moment according to the theory of elasticity
M_{max}	moment capacity/strength (maximum unbalanced moment introduced to the slab-column connection before failure)
$M_{rad}(\phi_i, r)$	radial bending moment of the sector element at angle ϕ_i and distance r from the column centre
$M_{tan}(\phi_i)$	tangential bending moment of the sector element at angle ϕ_i
$M_{tor}(\phi_i, r)$	torsional moment of the sector element at angle ϕ_i and distance r from the column centre
m	slab moment per unit width
m_R	moment capacity of the slab [Fib11]
m_S	average moment demand on the column strip [Fib11]
max	subscript indicating a value corresponding to the peak moment (M_{max})
N	number of specimens
n	number of sector elements; Chapter 7: subscript designating the floor number
non	Chapter 5: subscript designating non-reversed cyclic loading
n_c	number of performed cycles per rotation level (load step)

pl	Chapter 5: subscript designating the plastic portion of generalised strain (displacement, rotation, curvature, strain)
r	distance from the column centre
r_0	radius of the critical shear crack
r_1	radius of the zone where cracking is stabilised
r_c	radius of the column
r_{cr}	radius of the cracked zone
r_q	distance between the centre of the column and the point of application of load
r_y	radius of the yielded zone
rad	subscript designating the radial direction of the slab
rev	Chapter 5: subscript designating reversed cyclic loading
T	fundamental period of the structure; Chapter 2: subscript designating tension in the top reinforcement [Bro09]
tan	subscript designating the tangential direction of the slab
u	subscript designating punching failure; Chapter 3: subscript designating loss of vertical load bearing capacity
V	vertical load acting on the slab-column connection
V_M	fictitious column reaction [Bro09]
V_{Rc}	punching shear capacity
$V_{R.hog}$	shear resistance of the hogging slab half
$V_{R.\pi/2}$	shear resistance of the sector element subjected to the maximum rotation ψ_{max}
V_b	base shear
$V_{y.1}$	column reaction at the onset of reinforcement yielding
$V_{y.2}$	column reaction at overall yielding of the specimen's top reinforcement
v_E	shear stress acting on the critical section
x	height of the compression zone; horizontal axis
y	subscript designating the onset of yielding; Chapter 5: subscript designating the first post-yield peak

Greek letters

α	width reduction coefficient for the Effective Beam Width method
β	stiffness reduction coefficient for the Effective Beam Width method; Chapter 3: shear retention factor
β_c	empirical coefficient accounting for the effect of cyclic loading
γ	shear strain
γ_f	contribution of flexure mechanism on the total unbalanced moment
γ_m	material partial factor
γ_v	contribution of eccentric shear force mechanism on the total unbalanced moment
γ_t	contribution of torsion mechanism on the total unbalanced moment
Δ	slab deflection (vertical displacement); Chapter 7: lateral displacement of flat slab building
ΔV_i	shear force acting on the ith sector element

Δh	thickness variation
Δr	distance from the column face
Δ_{roof}	roof displacement
Δ_{st}	storey displacement
$\Delta\phi$	angle of a slab sector
$\varepsilon_{c.lim}$	limit concrete strain in the tangential direction [Bro09]
$\varepsilon_{c.r}$	radial concrete strain
$\varepsilon_{c.t}$	tangential concrete strain
ε_s	strain of the flexural reinforcement
$\varepsilon_{s.top}$	strain of the top (hogging) flexural reinforcement
$\varepsilon_{s.bot}$	strain of the bottom (sagging) flexural reinforcement
$\varepsilon_{s.y}$	yielding strain of the flexural reinforcement
ν	normalised shear force acting on the slab-column connection
ν_{ref}	normalised shear force at punching failure
ρ	top flexural reinforcement ratio (hogging reinforcement)
ρ'	bottom flexural reinforcement ratio (sagging reinforcement)
ϕ	angle with respect to the bending axis
χ	curvature
ψ_{col}	contribution of column deformation to the interstorey drift
ψ_{max}	maximum slab rotation
ψ_{min}	minimum slab rotation
ψ_{os}	contribution of slab deformation outside $0.22L$ to the interstorey drift
ψ_{scc}	connection rotation (contribution of slab deformation inside $0.22L$ to the interstorey drift)
ψ_{slab}	contribution of slab deformation to the interstorey drift
$\psi_{slab.0}$	residual rotation due to slab deformation (at $M = 0$)
ψ_{st}	interstorey drift
$\psi(\phi)$	local slab rotation with respect to the bending axis

Other symbols

$\varnothing$	bar diameter

Acronyms

CP	Collapse Prevention (Performance criterion)
CSCT	Critical Shear Crack Theory
EBW	Effective Beam Width
EF	Equivalent Frame
GFRS	Gravity force-resisting system
GSR	Gravity Shear Ratio
LFRM	Lateral force-resisting mechanism
LFRS	Lateral force-resisting system
LL	Live Load [Hwa00]
LS	Life Safety (Performance criterion)
MFDR	Modified Flexural Damage Ratio
IO	Immediate Occupancy (Performance criterion)
RC	Reinforced Concrete
SLS	Serviceability Limit State
ULS	Ultimate Limit State

Chapter 1

Introduction

1.1 Motivation and Problem Statement

In many countries around the world including Switzerland, reinforced concrete (RC) flat slabs supported on columns are one of the most widely used floor systems for office and industrial buildings. This system has the advantage to result in large open floor spaces (Fig. 1.1) as well as short construction times and therefore low construction costs.

(a)   (b)
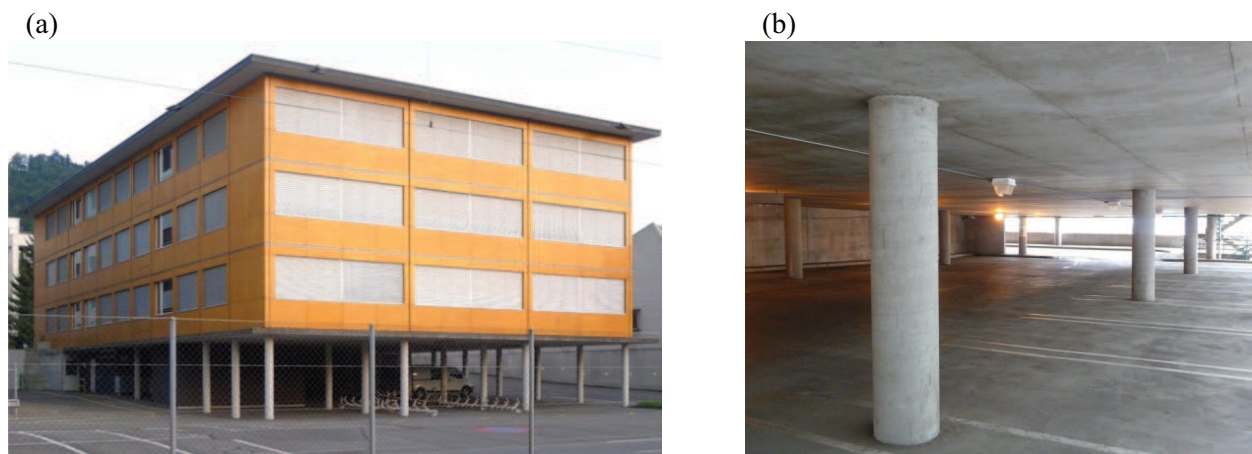
Figure 1.1 – Typical office building in Switzerland with flat slabs supported on columns (courtesy of Thomas Wenk).

For an inner column in a regular slab (same geometric properties and reinforcement content for all sides) with equal spans in both horizontal directions, the shear stresses induced by gravity loads are symmetric. Consequently, the distribution of the shear force and the bending moment is uniform along the perimeter of the column and no moment is transferred from the slab to the column.
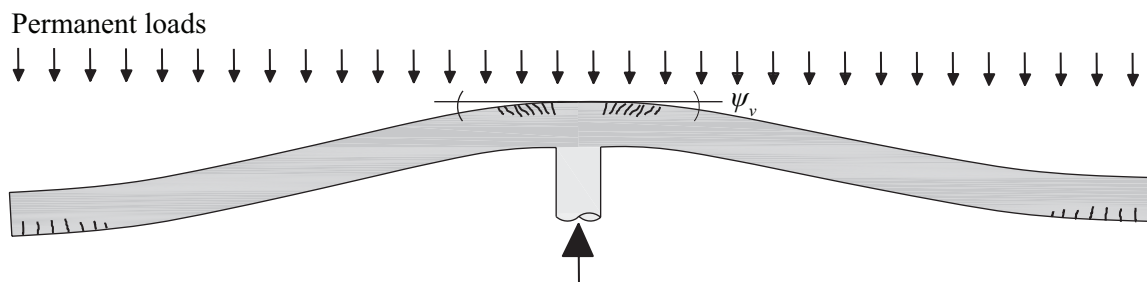
Figure 1.2 – Flat slab subjected to permanent vertical loads.

When a building is subjected to a seismic excitation, each floor is subjected to a different inertial force resulting in a different lateral displacement (Fig. 1.3a). The relative displacement between two adjacent floors divided by the storey height is referred to as interstorey (or storey) drift ψ_{st}. For flat slab systems both the column and the slab contribute, proportionally to their relative stiffness, to the storey drift (Fig. 1.3b).

Slab-column connections may be adequate as the primary lateral force-resisting system of low-rise buildings in regions of low and moderate seismicity. However, in regions of high seismic risk slab-column frames are considered inadequate as the primary lateral force-resisting system because of problems associated with excessive lateral drift and inadequate shear and unbalanced moment capacity of the connection [ACI11]. To increase the horizontal stiffness and strength of the structural system, RC walls such as core walls around lift shafts and staircases are typically added to the structural system (Fig. 1.3a) and the largest portion of the horizontal loads generated during earthquakes will be carried by the walls rather than the columns. However, each slab-column connection must have the capacity to follow the lateral displacements imposed on the building by the earthquake loading while maintaining the capacity to transfer the vertical loads from the slab to the columns.
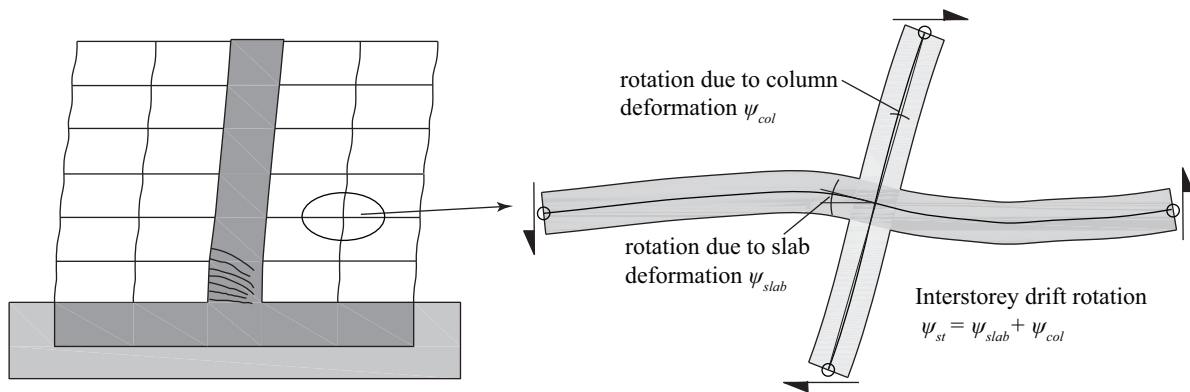
Figure 1.3 – Deformation state due to seismically induced drift: (a) global level (prototype building), and (b) local level (slab-column connection).

The storey drift imposed on the slab-column connection causes moment transfer from the slab to the column, often termed as unbalanced moment (Fig. 1.4). Hence, the final slab moment distribution for combined seismic and gravity loading results in an asymmetric distribution of the vertical shear forces in the slab around the column perimeter and a larger opening of the critical cracks in the slab on the side of the column where the shear forces are larger (hogging slab half).
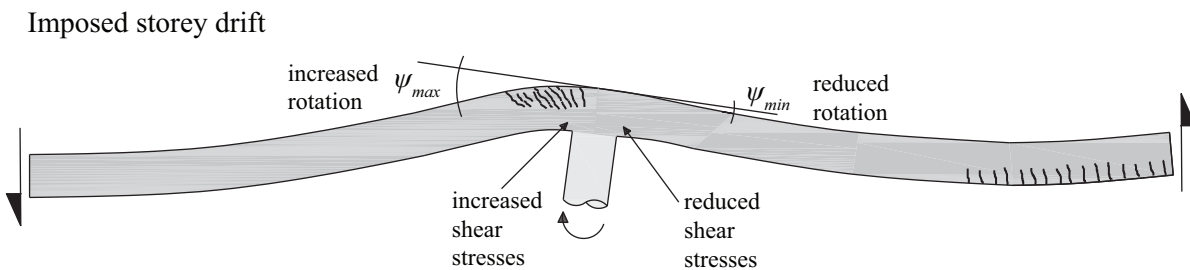
Figure 1.4 – Flat slab subjected to imposed storey drift.

As the seismically induced deformations increase, the capacity of the slab to transfer the vertical loads to the column decreases. If the connection can no longer transfer the vertical loads from the slab to the columns, brittle punching failure of the slab occurs and the deformation capacity of the entire building might be limited by the deformation capacity of the slab-column connection. If the building

is not designed to resist progressive collapse, punching failure of a slab-column connection can lead to pancake-type collapse of the building, as has been observed after several earthquakes (Fig. 1.5).

(a) (b)
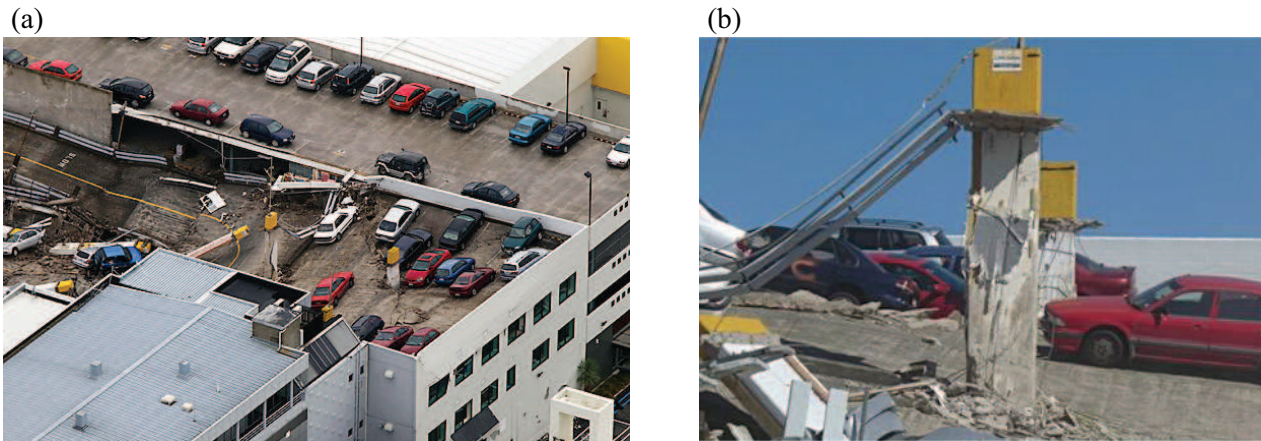
Figure 1.5 – Punching shear failure of the Smiths City Car Parking Building after the 2011 Christchurch earthquake (a, photo: http://www.stuff.co.nz/business/rebuilding-christchurch/5494408/Smiths-City-to-reopen-for-Cup-Week - b, photo: courtesy of Sri Sritharan).

To design and assess buildings with flat slabs and columns, the estimation of the moment-rotation relationship of slab-column connections and their rotation capacity are essential. Codes of practice determine the moment capacity of slab-column connections either using the eccentric shear transfer model [ACI14, Eur04] or by reducing the control perimeter [Fib11]. The deformation capacity is estimated from empirical formulas [ACI14] derived from past experimental works [Pan89].

The following paragraphs discuss open issues with regard to the seismic behaviour of slab-column connections and highlight research needs.

Lack of experimental data on thick slabs and slabs under monotonic or cyclic loading

Until today, research efforts on slab-column connections with unbalanced moment concentrated on the derivation of empirical relationships between the normalised shear force acting on the slab and the rotation capacity of the slab-column connection [Pan89, Hue99]. Empirical formulae have always the drawback that they are limited to the element configurations against which they were calibrated. The empirical relationships were derived from experimental data obtained from tests on relatively thin slabs (effective depth $d < 150$ mm), which have been theoretically shown to be less prone to brittle punching failure than thicker slabs ($d \geq 150$ mm) [Bro09], the latter being more common in Switzerland.

Past experimental studies investigated the seismic response of slab-column connections subjected to monotonic loading (e.g. [Gha74, Gha76, Elg87]) or to cyclic loading with increasing rotation amplitudes (e.g. [Pan89, Rob02, Rob06, Bu09]). Until today, only three pairs of slabs were tested which investigated the impact of the loading history (monotonic vs. reversed cyclic) [Han68, Isl76, Rha14]. The tests were performed on relatively thin slabs (slab thickness $h = 76$–90 mm) and their results were not conclusive regarding the impact of the load history on the force and deformation capacity. Understanding the effect of the loading history is important when developing mechanical models for the moment-rotation relationship of slab-column connections including their rotation capacity.

Past campaigns investigating the seismic behaviour of slab-column connections mainly focused on the global moment-rotation response. For slabs subjected to cyclic unbalanced moments, no experimental data are reported on local slab rotations. Moreover, no experimental campaign focused on the relation between local slab rotations and the rotation due to slab deformation, which represents the portion

of interstorey drift contributed by slab deformation. Local deformation is, however, necessary when developing analytical models on a mechanical basis.

Need for a model for computing the moment-rotation relationship of slab-column connections

When a slab-column connection is subjected to a combination of unbalanced moment and shear force and is responding in the elastic range, three different mechanisms are contributing to the moment resistance [Mas70]: (i) shear force eccentric to the column axis, (ii) flexure and (iii) torsion. As the behaviour of the slab-column connection subjected to an unbalanced moment becomes non-linear—even if this non-linearity results only from cracking—an accurate and realistic estimation of the contribution of the resisting mechanisms to the overall capacity of the slab-column connection is rather difficult. This is accentuated by the fact that the aforementioned lateral force-resisting mechanisms are associated with different failure modes.

Although experimental evidence on the different contributions of the lateral force-resisting mechanisms (eccentric shear force, flexure, and torsion) to the total unbalanced moment is limited, the design equations in codes of practice [ACI14,Eur04] are based on estimating the contribution of the eccentric shear and flexure mechanisms on the basis of empirical works while neglecting the contribution of the torsion mechanism. Another important assumption of these equations is the fact that the distribution of shear stresses on the critical perimeter is linear according to ACI-318 [ACI14] (Fig. 1.6a) or uniform according to Eurocode 2 [Eur04] (Fig. 1.6b). As a result, due to the non-linear distribution of shear stresses on the control perimeter and depending on the actual contribution of the resistance-providing mechanisms at failure the code equations underpredict/overpredict the moment capacity of slab-column connections. Moreover, current codes (e.g. [ACI14]) adopt different approaches for calculating the unbalanced moment capacity of a slab-column connection and its deformation capacity under seismic actions. A generally accepted method for calculating the moment that is transferred to the connection and a model for capturing the relationship between moment strength and deformation capacity are lacking.
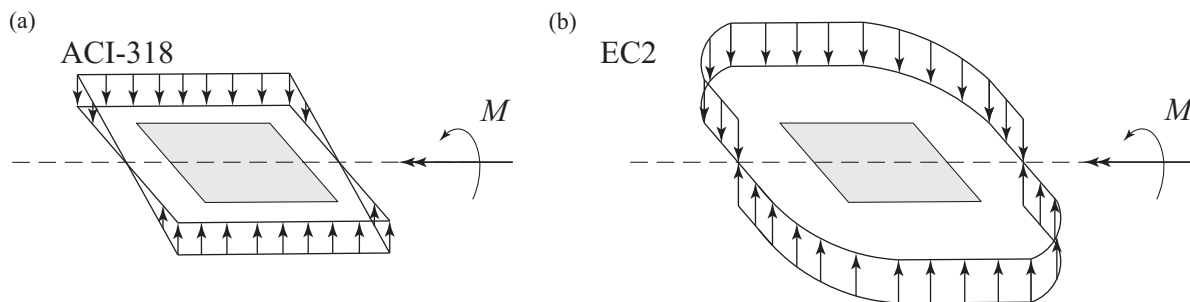
Figure 1.6 – Assumed distribution of shear stresses due to unbalanced moment in the control perimeter according to (a) ACI-318 [ACI14] and (b) EC2 [Eur04].

The only mechanical model for calculating the critical connection rotation that leads to punching failure and the corresponding unbalanced moment is proposed by Broms [Bro09]. Broms assumes that punching occurs when the concrete compression strain in the tangential direction at the column face reaches a critical value that depends on the height of the compression zone and the concrete compressive strength. The model satisfies equilibrium and strain compatibility in both the slab and the column. Broms' method provides only estimates of rotation and unbalanced moment at failure and not the entire moment-rotation relationship. Broms' model is limited to slab-column connections subjected to monotonic loading.

Need for a model to predict the cyclic moment-rotation response of slab-column connections

Past research on RC members has shown that cyclic loading may lead to a significant increase of crack widths when compared to monotonic loading. Thus, for the same gravity load acting on the slab-column connection, the unbalanced moment under earthquake conditions may be smaller compared to monotonic conditions. In the codes of practice the influence of cyclic loading on the deformation capacity is accounted for empirically [ACI14], while its influence on the moment capacity is overlooked. Broms assumes, based on the developed monotonic model [Bro09] (see above), that under cyclic shear stress reversals the tangential concrete strain capacity reduces by 25% compared to monotonic loading [Bro09]. To date, no suitable model to assess the increase of crack widths on slab-column connections when they are subjected to cyclic unbalanced moments has been proposed.

Need for analytical calculation of the width reduction coefficient of the Effective Beam Width method

Previous research with regard to two-dimensional analysis methods for buildings with slab-column connections focused on the Effective Beam Width method and the Equivalent Frame method. For the Effective Beam Width method, the slab action is represented by an equivalent beam with the same thickness as the slab and an effective width that is equal to the midspan-to-midspan distance in the transverse direction times a width reduction coefficient α. Cracking is accounted for through the use of a stiffness reduction factor β. The choice of both α and β influences significantly the obtained results. Past studies proposed formulations for the factors either based on finite element calculations or to fit experimental results. Accurate estimation of α requires the rotational stiffness of the slab-column joint to be known. For this reason, the unbalanced moment and the corresponding rotation due to slab deformation are necessary input parameters, while the contribution of both the slab regions until $0.22L$ (defined as slab-column connection region, L corresponds to the distance from midspan to midspan) and outside $0.22L$ on the moment-rotation response should be accounted for. The influence of various parameters, such as material and geometric properties, vertical and lateral load level, reinforcement ratio, etc. on the rotational stiffness should also be captured.

1.2 Objectives

The overarching aim of this thesis is to increase the understanding of the seismic behaviour of internal slab-column connections without transverse reinforcement. In addition, it is aimed to develop tools for the calculation of the moment-rotation response of slab-column connections which can be used for seismic design and assessment, as well as for the numerical analysis of flat slab buildings. The tools should have a sound mechanical basis so as to provide reasonably accurate predictions without impeding the user's understanding. More specifically, the main objectives of this dissertation are:

- Development of a mechanical model for predicting the moment-rotation relationship of slab-column connections subjected to monotonically increasing deformations, which permits to compute the contribution of the different lateral force-resisting mechanisms in the elastic and post-elastic range of response, considering the influence of both the slab regions until $0.22L$ and outside $0.22L$ on the response

- Development of a relationship between the local rotation ψ and the rotation due to slab deformation ψ_{slab}, which represents the slab deformation contribution to the interstorey drift ψ_{st}

- Development of a model for predicting the moment strength and the rotation capacity of slab-column connections

- Extension of the existing experimental database for thick slabs and test unit pairs subjected to monotonic and cyclic loading, respectively, and assessment of the effect of gravity load, flexural reinforcement ratio and cyclic loading on the rotation capacity and on the punching strength degradation

- Development of a mechanical model that accounts for the effect of cyclic loading on the moment-rotation relationship

- Development of methods for the numerical analysis of buildings with slab-column connections which can be used by structural engineers for design and assessment

1.3 Methodology

In order to achieve the aforementioned objectives, experimental, analytical, and numerical tools are employed, with greater focus on the two first ones.

First, an experimental investigation is conducted to provide both global understanding of, and local insight into, the seismic behaviour of slab-column connections, in particular with regard to the influence of loading history (montonic vs cyclic) for different vertical loads and reinforcement ratios. Moreover, the experimental investigation provides evidence related to the assumptions to be adopted during the analytical model development. For the design of the experimental programme and the adopted setup configuration numerical tools were used, including mainly non-linear finite element simulations.

Then, analytical studies are carried out to develop a physical model for calculating the moment-rotation relationship as well as the moment strength and the deformation capacity of slab-column connections. These studies are based on an analytical axisymmetric model proposed by Muttoni [Mut08] for the derivation of the load-rotation relationship of slab-column connections subjected to vertical load alone and on the failure criterion of the Critical Shear Crack Theory (CSCT) [Mut08]. Afterwards, both the results of experimental and numerical studies are used for validating the proposed analytical model.

Afterwards, local deformation data from the performed cyclic tests are used to get a deeper insight into the degradation exhibited by slab-column connections due to cyclic loading. This information is then used to extend the analytical model to cyclic loading and cumulative damage effects. The model is validated against results of cyclic tests.

The last part of the thesis shows how the proposed analytical model can be combined with linear finite element models to analyse entire flat slab buildings under seismic excitation.

1.4   Scope

This thesis treats only interior slab-column connections, excluding all types of edge or corner configurations. Only isolated specimens are considered (compressive membrane action is neglected). It is assumed that the column is monolithically connected to the slab (cases of prefabricated columns are not treated in the following). Slab-wall connections are also not treated within this research.

Although previous studies have shown the use of shear capitals increases the strength, the stiffness and the energy dissipation of the connection [Wey92], this research focuses on flat slabs, i.e. slabs without increased thickness around the column.

Only non-axisymmetric loading conditions are treated in this thesis with the focus on earthquake-induced loading conditions. RC slabs subjected to constant eccentricity are treated only for validation purposes. This thesis focuses on slabs subjected to uni-directional loading (uniaxial unbalanced moment). Specimens subjected to bi-directional loading (biaxial unbalanced moment) are therefore excluded, independently of the adopted loading protocol type (sequential, clover-leaf, etc.).

Several research projects have shown that the deformation capacity of slab-column connections can be significantly improved if transverse reinforcement is introduced [Meg00a, Rob02, Bro07]. However, as a first step, this research is limited to slabs without transverse reinforcement. Such slabs constitute a large portion of slabs constructed in the past and today. Therefore, use of any type of internal non-horizontal reinforcement (shear reinforcement, cables for post-tensioning) or external reinforcement (e.g. FRP) is not considered in this thesis.

Regarding the involved materials, all slab specimens are made of normal weight, normal aggregate, normal or high strength concrete. Specimens fabricated with fibre-reinforced concrete, ultra-high-performance concrete, or self-compating concrete are therefore disregarded. The reinforcing steel of the specimens has sufficient ductility, as prescribed in the codes of practice. Any failure modes associated with the interface between concrete and reinforcing steel (bond or anchorage failures) are neglected. Moreover, repaired or strengthened slab specimens are not treated in this dissertation.

Concerning the predictions according to the developed analytical models and the code provisions, mean strength values are used for the materials (concrete and reinforcing steel), while all safety factors are set to unity.

1.5   Organisation of the thesis

This dissertation is organised as follows:

- Chapter 2 gives an overview of the state of the art. The key elements of past experimental and theoretical research are presented. The provisions of several codes of practice are also presented.

- Chapter 3 presents an experimental campaign conducted within the current research. The objective of the test campaign is to assess the influence of the loading history (monotonic vs. reversed cyclic) for different gravity loads and reinforcement ratios. The experimental results are discussed and compared to the predictions of several codes of practice. This chapter is based on an article published in *Engineering Structures* [Dra16].

- Chapter 4 proposes a mechanical model for the derivation of the moment-rotation relationship of slab-column connections under monotonic loading conditions. The presented approach considers only the slab region until $0.22L$ from the column axis. The influence of the region outside $0.22L$ on the moment-rotation response is considered by combining the proposed model with an Effective Beam Width model. Drift-induced punching failure is determined by combination of the proposed model with the failure criterion of the CSCT which distinguishes between monotonic and cyclic loading. Then, the results of parametric studies on the impact of various parameters on the contribution of the lateral force-resisting mechanisms and on the seismic rotation capacity are discussed. Afterwards, the model predictions are compared to the results of the performed tests (Chapter 3).

- Chapter 5 presents an extension of the monotonic analytical model (Chapter 4) to account for cyclic loading when calculating the moment-rotation relationship. Based on local deformation measurements from the cyclic tests presented in Chapter 3, the required assumptions in addition to the ones of the monotonic model are presented (shear crack inclination, hysteretic moment-curvature relationship) as well as the adopted seismic damage model. The model predictions are then compared to the results of the performed cyclic tests. Finally, the results of parametric studies on the influence of various parameters (including loading history) on the contribution of the lateral force-resisting mechanisms and on the seismic rotation capacity are presented and discussed.

- Chapter 6 presents a detailed validation of the mechanical model proposed in Chapter 4 and its extension for cyclic loading conditions (Chapter 5). First, the main assumptions of the analytical model are evaluated though comparisons with the tests performed within this thesis. Then, the performance of the analytical model (combined with the failure criterion) in predicting the moment strength and the deformation capacity of isolated specimens and continuous specimens is assessed through comparison with experimental results found in the literature.

- Chapter 7 proposes two analysis methods for buildings with slab-column connections, on the basis of the proposed model. The first method is based on the Effective Beam Width approach and can be applied to connections that belong to the lateral force-resisting system or not. The method is validated against experimental results on multi-storey flat slab systems. The second method is suitable for slab-column connections that do not belong to the lateral force-resisting system.

- Chapter 8 presents the conclusions of this dissertation as well as recommendations for further research.

1.6   Personal contributions

The main personal contributions of the author were:

- Carrying out a series of full-scale tests on isolated slab specimens without transverse reinforcement under combined vertical load and monotonically or cyclically increasing unbalanced moment, analysing the obtained measurement data, and comparing the obtained results to the predictions of several codes of practice;

- Developing an analytical model for the calculation of the moment-rotation relationship of slab-column connections under monotonic loading conditions, which allows to calculate the contribution of the lateral force-resisting mechanisms in an explicit manner, and comparing its predictions with test results from the test campaign and the literature;

- Developing a method to account for the contribution of the slab region outside $0.22L$ when calculating the moment-rotation response of slab-column connections, based on the Effective Beam Width approach, and validating it through comparisons with test results from the literature and finite element calculations;

- Developing an analytical model for the calculation of the moment-rotation relationship of slab-column connections under cyclic loading conditions, which adopts a hysteretic moment-curvature relationship for the radial direction, assumes a fixed shear crack to govern the post-yield behaviour of each sector element, and incorporates cyclic damage using a model proposed previously [Rou87], and validating its performance through comparisons with results of cyclic tests;

- Performing parametric studies on the influence of various parameters such as the slab effective depth, the reinforcement ratio, the slab slenderness, the loading history, on the seismic rotation capacity of slab-column connections, based on the predictions of the developed analytical models;

- Proposing two methods for the numerical analysis of flat slab buildings based on the developed analytical models: (a) an Effective Beam Width method with the width reduction coefficient calculated analytically, and (b) the method for calculating the contribution of column and slab deformation to the interstorey drift for slab-column connections belonging only to the gravity force-resisting system.

Chapter 2

State of the Art

Section 2.1 gives an overview of the previous experimental research carried out on slab-column connections with combined vertical load and unbalanced moment and is divided in three subsections. Firstly, the test setups used for the various experimental campaigns are presented, whereas comparisons of the observed behaviour for slabs tested under monotonically and cyclically increasing moment are presented in the second subsection. The third subsection covers experimental investigation aiming to uncouple the lateral force-resisting mechanisms that are contributing to the moment resistance of slab-column connections.

In Section 2.2, an overview of the theoretical research is presented, divided in two subsections. Firstly, an overview of proposed analytical models is given, followed by the presentation of proposed empirical models. The first subsection is divided in three; firstly, proposed mechanical models for estimating the moment strength of slab-column connections are presented, followed by models for estimating both the moment strength and the deformation capacity of slab-column connections and models for the numerical analysis of buildings with slab-column connections.

In Section 2.3, several current code provisions are presented.

2.1 Experimental research on slab-column connections with unbalanced moment

2.1.1 Test setup configurations

Space limitations in the laboratory are often a determinant constraint when designing test setups for slab-column connections. For this reason, most experimental campaigns studied the behaviour of isolated slab-column connections that comprise one column and the surrounding slab and only few research groups opted for testing subassemblies [Rob92, Dur95] (Fig. 2.1a) of one interior and two exterior slab-column connections or large-scale tests on single-storey [Pan92, Rha14] and multi-storey buildings [Fic08, Moe85] (Fig. 2.1b) with slab-column connections.
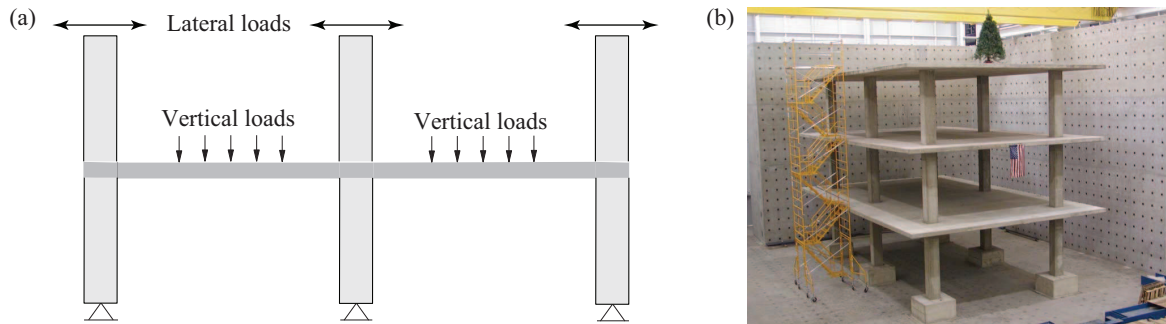
Figure 2.1 – Large-scale configurations chosen for experimental investigation on the seismic behaviour of slab-column connections: (a) Subassembly of one interior and two exterior slab-column connections, and (b) Multi-storey building (photo from [Fic08]).

The configurations shown in Figure 2.1 provide significant information with respect to the seismic behaviour of actual flat slabs and the interaction between external and internal slab-column connections. Nevertheless, since the present research is focused on the seismic behaviour of internal slab-column connections, this section treats only test programmes on isolated specimens. Internal slab-column connections are considered more critical concerning punching shear failure during seismic loading, since they tend to be much stiffer than edge or corner slab-column connections. As a result, for the same interstorey drift, the moment to be transferred by an internal slab-column connection is much larger than the seismically induced moment to be transferred by edge or corner columns [Rob92, Dur95, Rha14]. Moreover, large-scale experimental investigations aimed to evaluate the response of slab-column connections as part of the lateral force-resisting system of the building and the potential of progressive collapse after the first connection failure. However, the present research aims at investigating the behaviour of internal slab-column connections subjected to seismically-induced drifts, often imposed by stiff vertical spines that consist the lateral force-resisting system of the structure (see Chapter 1).

Most test programmes on the behaviour of slab-column connections subjected to an unbalanced moment considered test specimens representing a single interior column and the surrounding slab. The dimensions of the specimens for the monotonic tests were typically chosen as $0.44L$ x $0.44L$ where L is the distance between column axes [Gha76, Elg87, Haw89]. The distance $0.22L$ corresponds for an elastic slab with constant stiffness and equal spans subjected to an evenly distributed vertical load to the distance of the point of contraflexure to the column axis. Most experimental campaigns focusing on the seismic response of slab-column connections used slab elements of the size $1.0L$ x $1.0L$, i.e., from midspan to midspan of adjacent bays (e.g. [Pan89, Rob02, Rob06] with few exceptions where larger elements were tested [Han68, Haw74]).

All past monotonic tests used one of the following test setups, which differed with regard to the kinematic boundary conditions and the way the vertical load was applied:

- Setup (a): the unbalanced moment is introduced by an eccentric vertical load and by restraining the vertical dispalcement of the slab ends [Els56, Moe61, Kru99, Bin05] (Fig. 2.2).

- Setup (b): the unbalanced moment is introduced by applying additional vertical loads to the edges of the slab and by fixing the column stub ends [Han68, Isl76, Haw89] (Fig. 2.2). The only programme where the opposite loads were unequal so as to maintain the same eccentricity was that of Hawkins et al. [Haw89].

- Setup (c): the unbalanced moment is introduced by applying a horizontal force to the top column stub and by restraining the vertical displacement of the slab edges [Gha76, Elg87, Pan89, Rob02, Rob06, Bu09, Tia08, Cho07, Cho09b] (Fig. 2.2) or specific locations on the slab surface [Tia08] determined through finite element analysis to reproduce the internal actions of the prototype building [Tia07]. The vertical load is applied either by jacks underneath the column stub [Bu09, Tia08] or by weights on the slab surface [Rob02, Rob06], with several campaigns combining both aforementioned ways of vertical load introduction [Pan89, Par07].

Setup (a) is predominantly adopted to simulate unbalanced moments due to unequal spans. The test setup is simple and easy to implement but when applied to simulate seismic loading, it is somewhat unrealistic as the ratio of inserted moment to applied vertical load on the slab-column connection (subsequently referred to as eccentricity) remains constant. As a result, the applied vertical load changes throughout the test.

Depending on the control of the actuators inducing the forces at the slab edges, setup (b) can be used to simulate constant eccentricity [Haw89], constant vertical load [Han68] or equal but opposite slab deflections at the two opposite edges [Isl76]. Since column deformation induces significant rigid body rotations to the slab-column connection that are in turn increasing the displacement demand on the actuators applying the force couple at the slab edges, the column is typically post-tensioned [Haw89]. No additional reinforcement is provided to the slab edges perpendicular to the unbalanced moment to account for the slab part between $0.22L$ and $0.5L$.

Setup (c) is predominantly used for cyclic tests on slab-column connections. It is based on the assumption that for seismic actions the contraflexure points are located at midspan of the slab. The test unit size and the reaction structure for the lateral load application impose significant space requirements for laboratories and therefore the specimens are often tested at reduced scale, i.e. specimens with thin slabs, with very few exceptions [Elg87, Bu08, Cho09b].
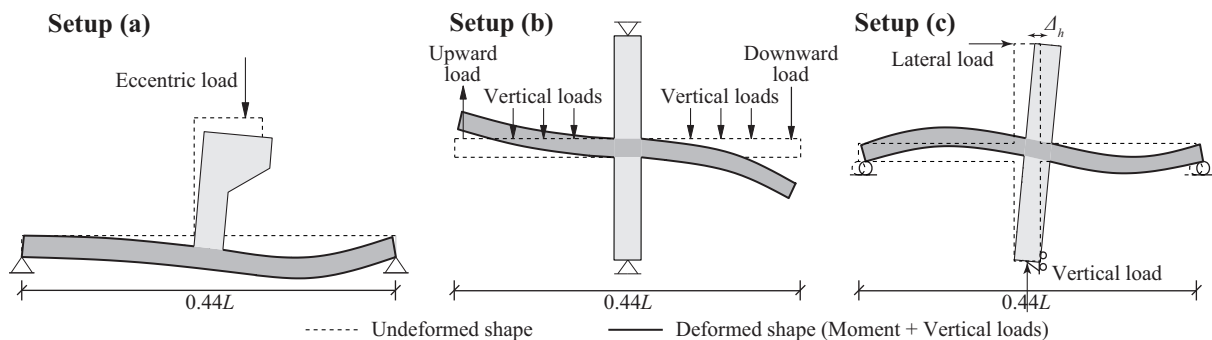
Figure 2.2 – Test setup configurations used in previous experimental campaigns for slab-column connections subjected to combined vertical load and monotonic moment transfer.

The superimposed gravity load is simulated by placing extra weight on the slab [Isl76], by applying constant forces on the slab by means of vertical actuators [Haw89], or by jacking the column to deliver the gravity load to the slab [Gha76]. For test setups (b) and (c), the height of the column stubs was typically chosen as the height of the point of contraflexure of the column, i.e., half the storey height (e.g. [Pan89]), with few exceptions (e.g. [Far93]).

13

For the test programmes addressing the effect of seismically induced storey drifts on the slab-column connection by means of quasi-static cyclic tests either setup (b) or setup (c) was used. In these tests, the imposed vertical loads on the slab edges (setup (b)) and the imposed horizontal displacement on the top of the column (setup (c)) were subjected to a history of cycles with increasing amplitude (Fig. 2.3).
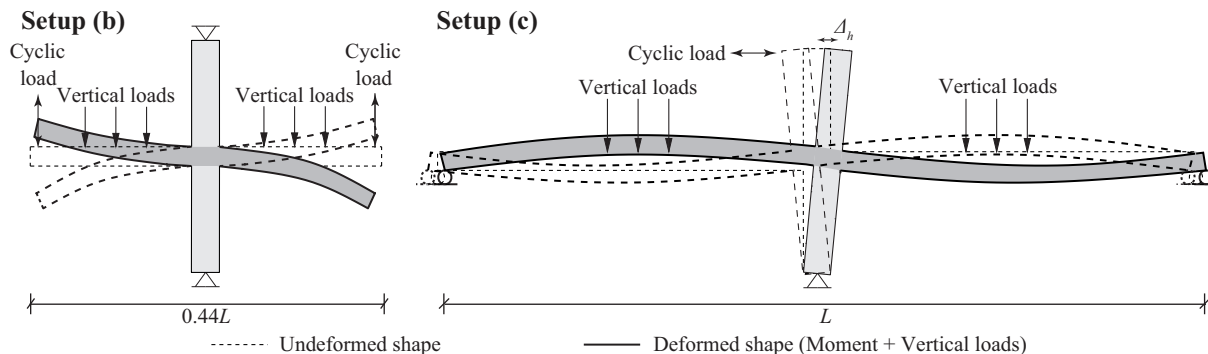
Figure 2.3 – Test setup configurations used in previous experimental campaigns for slab-column connections subjected to combined vertical load and cyclic moment transfer.

For cyclic tests using setup (b), the specimen size was either $1.00L$ [Han68, Isl76] or $0.60L$ [Haw74, Sym76]. Concerning setup (c), the slab was typically modelled until midspan for cyclic tests [Pan89, Rob02, Rob06], rather than $0.22L$ that was the predominant case for monotonic tests. It should though be noted that several researchers adopted specimen sizes equal to $0.44L$ (Fig. 2.2) for experimental investigation under cyclic loading conditions [Bu09]. For the vertical load application for setup (c), since slab cracking often resulted in redistribution of the vertical load from the column to the roller supports [Rob02, Rob06], in many experimental campaigns extra weight on the slab was often combined with an upward jacking force at the column base to keep the shear force acting on the slab-column connection constant throughout the test [Pan89].

2.1.2 Punching of slabs with monotonic or cyclic unbalanced moment

Although the first experimental campaigns of slabs under eccentric vertical loads were carried out during the 1950's, it was not until the mid-1970's that the seismic behaviour of slab-column connections became a subject of research.

Tables 2.1 and 2.2 summarise existing test series on slab-column connections subjected to monotonic and cyclic moment transfer, respectively. The tables include information on the number of test specimens per test series (only square specimens without transverse reinforcement were counted), the slab thickness h, the normalised shear strength, the top slab reinforcement ratio ρ over the column, and the test setup. The normalised shear strength is defined as the shear strength at failure divided by $b_o\, d\, \sqrt{f_c}$ where b_o is the control perimeter located at $d/2$ from the face of the column, calculated with rounded corners [Fib11], d is the effective depth of the slab, and f_c is the concrete compressive strength. More information on the selected tests is provided in Appendix A. In several research programmes using test setups (a) or (c) not only the slab edges perpendicular to the direction of loading but also those parallel to the imposed deformation were restrained. In Tables 2.1 and 2.2 these test setups are annotated as $(a)_R$ and $(c)_R$, respectively.

Table 2.1 – Experimental programmes imposing monotonically increasing drifts on slab-column specimens

Author(s)	h [mm]	ρ [%]	$\dfrac{V_{test}}{b_o\,d\,\sqrt{fc}}$ $[\sqrt{MPa}]$	Test setup	Loading parameter
Elstner and Hognestad [Els56] (2)	152	2.47	0.50-0.52	(a)$_R$	e
Moe [Moe61] (9)	152	1.34-1.50	0.21-0.40	(a)$_R$	e
Anis [Ani70] (5)	102	2.19	0.15-0.43	(c)	e
Narasimhan [Nar71] (1)	178	1.11	0.29	(a)$_R$	e
Ghali et al. [Gha74] (2)	152	1.39	0.10-0.11	(c)	V
Stamenkovic and Chapman [Sta74] (4)	76	1.17	0.11-0.37	(c)$_R$	V
Ghali et al. [Gha76] (3)	152	0.50-1.35	0.11-0.12	(c)$_R$	V
Islam and Park [Isl76] (2)	89	0.83	0.09	(b)	V
Elgabry and Ghali [Elg87] (1)	152	1.10	0.16	(c)	V
Hawkins et al. [Haw89] (22)	114-152	0.60-1.26	0.13-0.41	(b)	e
Kamaraldin [Kam90] (4)	80	0.55-1.00	0.17-0.36	(b)	e
Marzouk et al. [Mar96] (5)	150	0.50-1.00	0.17-0.38	(c)$_R$	e
Kruger [Kru99] (2)	150	1.00	0.26-0.28	(a)$_R$	e
Binici and Bayrak [Bin05] (1)	75	1.38	0.44	(a)	e
Ben Sasi [Ben12] (2)	80	1.40	0.14-0.23	(c)$_R$	e
Average (65)	**130**	**1.15**	**0.25**		
V = **const (12)**	**116**	**1.09**	**0.16**		
e = **const (53)**	**134**	**1.16**	**0.27**		

Table 2.1 shows that for most of the monotonic tests performed under constant eccentricity the normalised shear force at failure was relatively high (ν_{avg} = 0.27 / GSR = 0.81) in comparison to monotonic tests under constant vertical load (ν_{avg} = 0.16 / GSR = 0.48). This can be attributed to the fact that researchers using setup (a) were primarily aiming to evaluate the punching strength of slab-column connections under relatively small eccentricities when, for instance, slabs with unequal spans are subjected to vertical load alone.

Table 2.2 – Experimental programmes imposing cyclically increasing drifts on slab-column specimens

Author(s)	h [mm]	ρ [%]	$\dfrac{V_{test}}{b_o\,d\,\sqrt{fc}}$ $[\sqrt{MPa}]$	Test setup
Kanoh and Yoshizaki [Kan75] (3)	100	0.70-1.10	0.11-0.24	(c)
Islam and Park [Isl76] (1)	89	0.83	0.09	(b)
Morrison et al. [Mor83] (1)	76	1.03	0.09	(c)
Zee and Moehle [Zee84] (1)	61	0.80	0.14	(c)
Pan and Moehle [Pan89] (2)	122	0.76	0.08-0.13	(c)
Cao [Cao93] (3)	150-155	1.29	0.18-0.29	(c)
Robertson et al. [Rob02] (1)	115	0.75	0.09	(c)
Stark et al. [Sta05] (1)	115	1.42	0.21	(c)
Robertson and Johnson [Rob06] (5)	114	0.45-1.03	0.08-0.18	(c)
Choi et al. [Cho07] (3)	120	1.05-1.59	0.09-0.17	(c)
Park et al. [Par07] (1)	132	0.78	0.12	(c)
Kang and Wallace [Kan08] (1)	152	0.49	0.11	(c)$_R$
Tian et al. [Tia08] (1)	152	0.61	0.13	(c)$_R$
Bu and Polak [Bu09] (2)	120	1.25	0.17-0.23	(c)$_R$
Cho [Cho09] (1)	150	1.00	0.11	(c)
Choi et al. [Cho09b] (1)	152	1.27	0.08	(c)$_R$
Park et al. [Par12] (2)	135	1.06	0.16-0.17	(c)
Average (30)	**121**	**0.95**	**0.14**	

Tables 2.1 and 2.2 show that the tests found in the literature are performed on relatively thin slabs for both monotonic and cyclic loading conditions ($h_{avg} = 130$ mm and 121 mm, respectively). The average normalised shear force ν for tests under constant vertical load was equal to 0.16 (GSR $= 0.48$) for monotonic tests and 0.14 (GSR $= 0.42$) for cyclic tests. The average flexural reinforcement ratio over the column was 1.09% for monotonic tests and 0.95% for cyclic tests.

Figure 2.4 shows the measured drift at peak moment $\psi_{st.p}$ as a function of the normalised shear force ν at peak moment for the tests found in the literature for which drift measurements are reported (setups (b) and (c)). The figure distinguishes between monotonic and cyclic tests and between tests on slabs with effective depths smaller and larger than 100 mm.
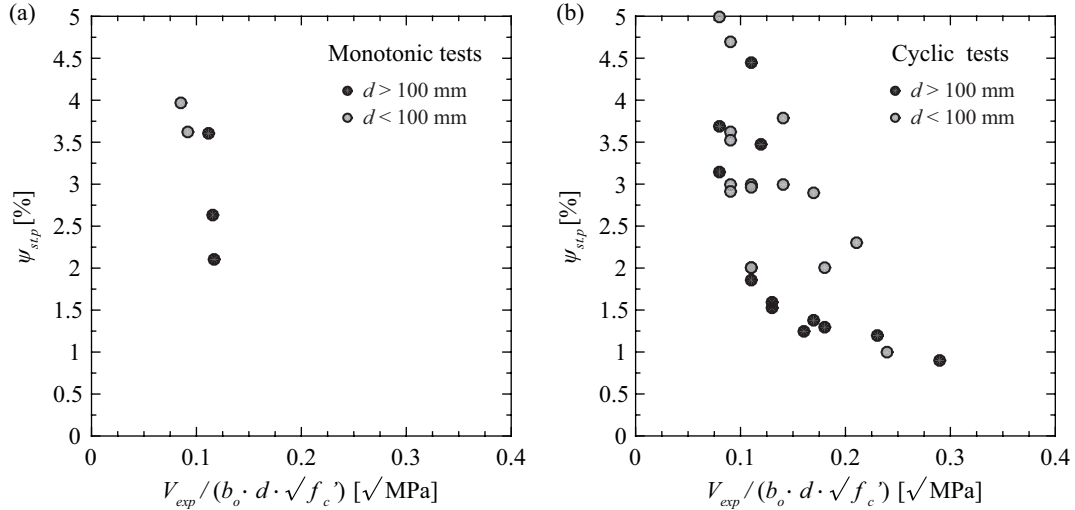
Figure 2.4 – Normalised shear force vs measured drift at peak moment for slab-column connections subjected to: (a) monotonically increasing moment, and (b) cyclically increasing moment.

As can be seen in Figure 2.4 increased gravity load-induced shear force results in lower deformation capacity of the slab-column connection, in particular for cyclic tests. Due to size effect slabs with effective depths smaller than 100 mm typically feature larger normalised shear strengths than thicker slabs. In addition, slabs with small thicknesses might also be subjected to large uncertainties due to, for example, variations in the slab effective depth. Figure 2.4 shows that a large number of monotonic and cyclic tests have been conducted on slab specimens with effective depths smaller than 100 mm. This can be attributed to the fact that slab specimens are often tested at reduced scales due to laboratory constraints, which results in reduced slab thickness for most of the existing tests (see Tables 2.1 and 2.2). Since cyclic tests focus on the seismic behaviour of slab-column connections more data are available for the imposed drift at peak moment in comparison with monotonic tests, but the scatter is relatively large. The difference between cyclic and monotonic behaviour has already been examined for very thin slabs [Isl76].

Although experimental investigations on continuous flat slabs supported on columns are not treated in the present chapter, useful information on the significance of cyclic degradation exhibited by interior slab-column connections of actual flat slabs can be provided by testing identical continuous flat slab specimens to monotonic and cyclic lateral loads. To date, the only campaign investigating the cyclic loading effect on single-storey continuous flat slabs is performed by [Rha14]. Figure 2.5 shows the response comparison between the monotonic and the cyclic test for the entire tested specimen and the interior slab-column connection.
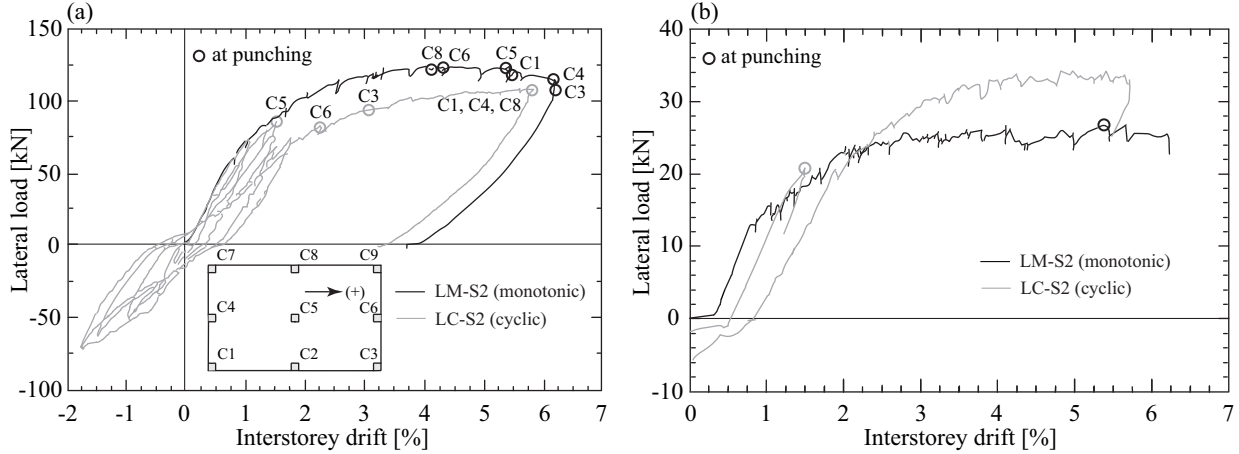
Figure 2.5 – Comparison of the response of: (a) the tested continuous flat slab, and (b) the interior slab-column connection (C5) under monotonic and cyclic loading conditions.

The obtained results showed that cyclic application of lateral loads resulted in strength reduction of approximately 13% in comparison to monotonic lateral load application. The corresponding interstorey drift was found to be 6.1% and 5.9% for monotonic and cyclic loading conditions, respectively (Fig. 2.5a). Nevertheless, for the cyclic test after reaching an interstorey drift of 1.5% monotonic loading was applied in the positive direction. Hence, the influence of cyclic degradation on the global moment strength and the deformation capacity of the structure could be underestimated. For the internal slab-column connection C5, which was proved to be determinant for the response of the cyclically tested specimen, cyclic application of lateral loads resulted in a dramatic decrease of the interstorey drift at punching from 5.38% to only 1.50% and a decrease of moment strength from 37.5 kNm to 28.9 kNm (Fig. 2.5b).

To assess effectively through experimental investigation the influence of cyclically increasing deformations on the stiffness, moment and deformation capacity of slab-column connections pairs of identical slab specimens should be tested under monotonic and cyclic loading conditions. Although existing experimental research on slab-column connections under both monotonically and cyclically increasing deformations is rather extensive, the database of identical specimens subjected to monotonic and cyclic loading is extremely limited and covers only thin slabs [Isl76]. The main reason for such lacking is related to differences in the slab specimen dimensions that are typically chosen for setup configurations aiming to reproduce the effects of monotonically increasing and cyclically increasing moments. While the size of slabs tested under monotonically increasing moments is most times $0.44L$, the size of slabs for cyclic tests is typically L. Therefore comparisons between monotonic and cyclic tests are rather difficult and rely on accidental coincidence of a large number of parameters for tests conducted in different experimental campaigns [Elg87, Cao93].

2.1.3 Contribution of the lateral force-resisting mechanisms

When a slab-column connection is subjected to a combination of unbalanced moment and shear force, three different slab actions are contributing to the moment resistance [Mas70] (Fig. 2.6): (a) eccentric shear force, (b) flexure, and (c) torsion. In the present work these slab actions are denoted as lateral force-resisting mechanisms (LFRM). As soon as the behaviour of the slab-column connection subjected to an unbalanced moment becomes non-linear, an accurate and realistic estimation of the contribution of the resisting mechanisms to the overall capacity of the slab-column connection is rather difficult. This is accentuated by the fact that the LFRM are associated with different failure modes.
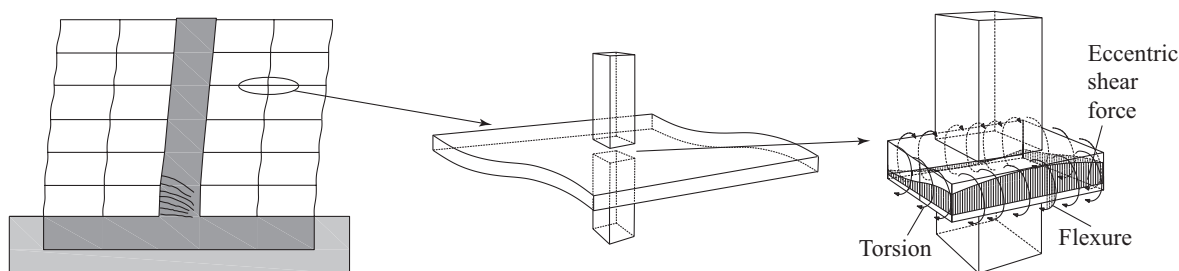
Figure 2.6 – Mechanisms providing resistance in slab-column connection under gravity and lateral loads.

Since experimental investigations on the moment capacity of slab-column connections subjected to lateral loads cannot provide any information on the contribution of the aforementioned resisting mechanisms, various researchers attempted to isolate them by testing slab sub-specimens or specimens with slots at the column vicinity. Although less numerous than the tests presented in the previous section, their results are particularly interesting since their impact on the current code provisions is still visible.

The most typical configuration consists in cutting slots in the column proximity aiming to set the contribution of torsion or flexure (Fig. 2.7) to zero [Han68, Sta74, Bu11]. Depending on the test campaign, the researchers opted for curtailing the slab flexural reinforcement running through the holes [Sta74, Bu11] or not [Han68]. Hanson and Hanson [Han68] conducted tests on relatively thin rectangular slabs ($h = 76$ mm). One of the aims of the campaign was to determine the relative contribution of flexure and torsion on the moment capacity of slab-column connections either by slots parallel to the moment vector (similar to Fig. 2.7a) or perpendicular to the moment vector. It was observed that setting the contribution of torsion to zero resulted in rather insiginificant drop of the moment capacity, whereas setting the contribution of flexure to zero reduced the moment capacity by 30-35% compared to specimens without slots. Stamenkovic and Chapman [Sta74], conducted tests on relatively thin slabs ($h = 76$ mm) under unbalanced moment alone. The adopted setup is shown in Figure 2.2 (with vertical loads set to zero). The experimental results suggested that 70% of the total moment is contributed by flexure and the remaining 30% is contributed by torsion. To date, the only test campaign addressing the moment capacity and deformation capacity of medium thickness ($h = 120$ mm) square slabs with slots under reversed cyclic loading has been carried out by Bu [Bu11]. The plan view of the slab specimen is shown in Figure 2.7a. Figure 2.7b shows the comparison of the hysteresis loops for the reference test unit (SW5 – no slots) and the test unit with slots parallel to the inserted moment vector (SW6). The slab SW6 failed at 30% lower moment and 45% lower drift than its counterpart SW5.
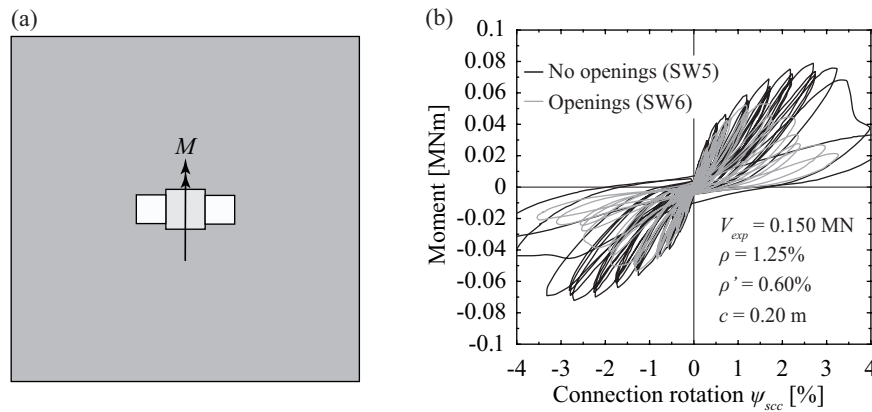
Figure 2.7 – Test performed by Bu [Bu11] to evaluate the influence of slots parallel to the moment vector on the moment resistance of slab-column connections: (a) Plan view of the slab specimen SW6, and (b) comparison of the hysteretic response between SW6 and SW5 (drawn after Bu [Bu11]).

Kanoh and Yoshizaki [Kan79] evaluated experimentally the torsion contribution by performing pure torsion tests (without gravity loading) on half slab specimens connected to the column stub only at one face (Fig. 2.8). Based on the test results, the authors claimed that the contribution of torsion to the total unbalanced moment is rather large. However, observation of the cracking patterns suggests that also flexure and eccentric shear contributed to a significant extent to the resistance of the tested half slab specimens.
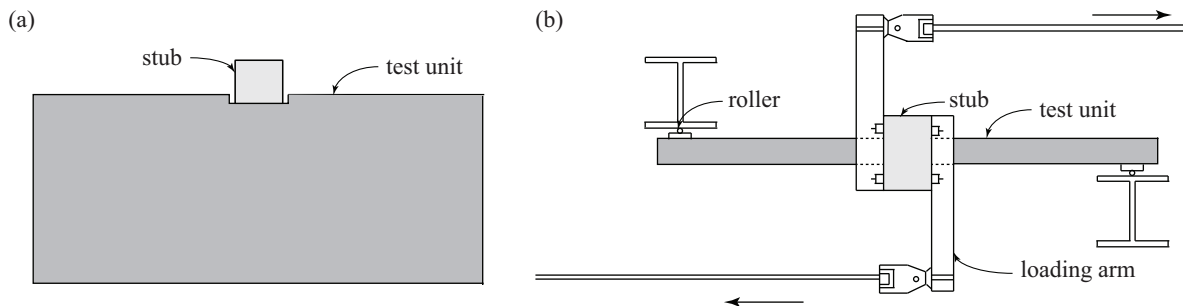
Figure 2.8 – Test campaign performed by Kanoh and Yoshizaki [Kan79] to evaluate the contribution of torsion to the moment resistance of slab-column connections: (a) Plan view of the slab specimens, and (b) Torsion introduction into the slab-column connection (drawn after Kanoh and Yoshizaki [Kan79]).

Although rather useful for assessing the effect of openings in the column proximity on the moment capacity of slab-column connections, the above-mentioned experimental attempts did not provide consistent information on the relative contribution of the LFRM to the applied moment. The assumption behind such attempts is that the slab is responding as a beam under pure torsion and pure flexure in the two orthogonal directions. Nevertheless, the slab behaviour is rather planar than linear (as assumed for beams) and consequently these two components do not add up to the total moment resisted by the slab-column connection (without slots). This is largely due to the fact that floor systems are characterised by redundancy and alternative load paths can be activated when a local disturbance is caused, as has been shown by finite element calculations [Far92a]. For this reason, the arrangement of slots in the proximity of interior slab-column connections to determine the relative contribution of torsion and flexure to the total resisted moment was criticised by some researchers [Far92a, Far92b].

2.2 Theoretical research on slab-column connections with unbalanced moment

2.2.1 Proposed analytical models

Various approaches based on equilibrium have been proposed for the calculation of the moment transferred from slabs to columns and the corresponding deformation. They can be distinguished into two categories depending on the target of analysis, which can be either the capacity or the demand; estimation of the capacity of slab-column connections requires more local study of the mechanisms that are contributing to the resistance that is most times performed at the level of the slab-column connection. For structural systems composed of slab-column connections the estimation of the seismic demand is a procedure performed at the global level, i.e. the level of the structure. As the demand in terms of unbalanced moment or interstorey drift depends on the characteristics of the structural system (mass, stiffness, damping) and the ground motion characteristics, a numerical model is usually set up by the structural engineer.

The present section is divided in three parts. The first two parts focus on the resistance side. Firstly, a review of proposed mechanical models for calculating the moment capacity of slab-column connections is presented. Afterwards, mechanical models for estimating both the moment and deformation capacity of slab-column connections are reviewed. The third part adresses the demand side and presents an overview of models for the numerical analysis of buildings with slab-column connections.

Mechanical Models for estimating the moment capacity of slab-column connections

In 1960, Di Stasio and Van Buren proposed a working stress method for the design of slab-column connections under combined vertical load and unbalanced moment [DiS60]. The shear stresses due to vertical load were superposed to the shear stresses due to unbalanced moment, which were assumed to vary linearly about the centroid of the critical section:

$$v_E = \frac{8\,h}{7\,d} \left(\frac{V_E}{A_c} \pm \frac{(M_E - m_{AB} - m_{CD})\,j_d}{J_c} \right) \frac{1}{1 + (E_s/E_c - 1)\,\rho} \tag{2.1}$$

where $m_{AB} + m_{CD}$ is the moment resisted by flexure in the faces perpendicular to the direction of excitation and the term $M_E - m_{AB} - m_{CD}$ respresents the part of the unbalanced moment M_E resisted by eccentric shear stresses (see Fig. 2.6). The last term of Eq. (2.1) was added to account for the dowel action of the reinforcement. To consider punching shear, Di Stasio and Van Buren proposed to limit the vertical shear stress calculated from Eq. (2.1) to $1/16\,\sqrt{f_c}$, assuming a critical section directly adjacent to the column faces. The method proposed by Di Stasio and Van Buren [DiS60] for calculating the shear stresses due to combined vertical load and unbalanced moment (Eq. (2.1)), also known as the eccentric shear stress method, forms the basis of the current ACI Building Code [ACI14].

The first moment strength model for slab-column connections was proposed by Moe in 1961 [Moe61]. According to this model which is based on the eccentric shear stress model, the vertical shear stress due to combined vertical load and unbalanced moment acting on the critical section (assumed to be directly adjacent to the column faces) was calculated as

$$v_E = \frac{V_E}{A_c} \pm \frac{\gamma_v\,M_E\,j_d}{J_c} \tag{2.2}$$

For the factor γ_v, which represents the part of the moment resisted by eccentric shear forces, Moe proposed a value of 0.33. This value was determined experimentally by assuming that the vertical shear stress at failure is equal to the vertical shear stress at failure for concentric punching. In 1968, Hanson and Hanson proposed a value of γ_v equal to 0.40 on the basis of tests performed on relatively thin rectangular slabs [Han68].

In 1970, Mast [Mas70] proposed a strength model based on the elastic plate theory. Closed-form relationships were used to describe quantitatively the stresses that are developed in the column proximity. The results suggested that for square columns one third of the unbalanced moment is carried by flexure, 15% is carried by torsion and the remaining approximatively 50% is carried by the eccentric shear force mechanism. Although neglecting the vertical load that is acting on the slab as well as the slab cracking due to increasing unbalanced moment, the model of Mast has been approved for accurately describing the contribution of the LFRM under elastic conditions and has significantly influenced later theoretical works.

The results of the aforementioned theoretical studies influenced significantly the changes that were introduced in the 1971 ACI Building Code [ACI71] for the design of slab-column connections in presence of seismic moments. Firstly, the design was based on ultimate strength rather than on working stresses, which was the case for earlier versions of the same Standard. The factored shear stresses at the critical section due to gravity and unbalanced moment were limited to $0.33\sqrt{f_c}$. Moreover, an empirical expression for the fraction of unbalanced moment that induces shear stress on the control perimeter (subsequently referred to as γ_v) was developed as a function of the critical section dimensions. The expression to calculate γ_v has remained unchanged since then. The remainder portion of the unbalanced moment was assumed to be resisted by flexure in the critical section faces perpendicular to the direction of excitation.

In 2014, Choi et al. proposed a shear strength model for the case of slab-column connections subjected to combined vertical load and unbalanced moment [Cho14], based on a strain-based shear strength model for slender beams [Par06b]. The unbalanced moment capacity was derived as the sum of flexure, torsion and eccentric shear force. For flexure, it was assumed that in both the front and the back of the critical section (side under hogging moment and sagging moment, respectively) the flexural reinforcement is yielding before punching failure. For the contribution of the eccentric shear force to the unbalanced moment capacity, it was calculated based on the difference between the shear stress at punching failure v_{Rc} (concentric punching) and the shear stresses due to gravity loads v_E that are acting on the slab-column connection. For the calculation of the shear stress at punching failure v_{Rc} only the compression zone was considered while the contribution of aggregate interlocking and dowel action were neglected.

Mechanical Models for estimating the moment and deformation capacity of slab-column connections

To date, the only mechanical model estimating both the moment and deformation capacity of slab-column connections with unbalanced moment was suggested by Broms [Bro05]. A simplified model based on the same principles was proposed some years later [Bro09]. The approach is limited to slabs without transverse reinforcement.

The initially proposed model for eccentric punching is a direct extension of the model for the punching shear capacity of slabs subjected to concentric loads [Bro05]. For a given gravity shear force ratio, the model allows estimating the ultimate unbalanced moment and rotation capacity of the slab. Two failure criteria are considered: The first criterion is strain-based and limits the concrete strain tangential to the column. The second criterion is stress-based and limits the compressive stress in the fictitious internal compression strut. The proposed failure criteria are, among other parameters, a function of the stress state of the slab reinforcement. The stress state of the reinforcement being function of the reinforcement ratio, two reinforcement ratios should be calculated to compute the punching resistance for concentric punching corresponding to the critical concrete tangential strain; ρ_1 corresponds to punching without any reinforcement yielding and ρ_2 corresponds to punching after all reinforcement has reached the yield limit.

First, the reinforcement ratio limit ρ_1 is calculated solving the following non-linear system of equations:

$$\epsilon_{c.lim} = 0.001 \left(\frac{25}{f_c{}'} \right)^{0.1} \left(\frac{0.15}{x_{lim}} \right)^{1/3} \tag{2.3}$$

$$x_{lim} = \frac{\epsilon_{c.lim}}{\epsilon_{c.lim} + \dfrac{f_y}{E_s}} \, d \tag{2.4}$$

$$\rho_1 = \frac{\epsilon_{c.lim} \, x_{lim} \, 0.5 \, E_c}{d \, f_y} \tag{2.5}$$

Then, the reinforcement ratio limit ρ_2 is calculated solving the following non-linear system of equations:

$$\epsilon_{c.pu} = 10^{-6} \sqrt{ \left(\frac{25}{f_c{}'} \right)^{0.3} \frac{E_c}{f_y} \frac{0.075}{d} \frac{10^3}{\rho_2} } \tag{2.6}$$

$$x_{pu} = d \, \frac{2 \, \rho_2}{\epsilon_{c.pu}} \frac{f_y}{E_c} \tag{2.7}$$

$$\frac{f_y}{E_s \, (d - x)} \left(1 - 0.5 \left(1 + \frac{B}{c} \right) \right) = \frac{B}{c} \left(\frac{\epsilon_{c.pu}}{x_{pu}} - \frac{f_y}{E_s \, (d - x)} \right) \tag{2.8}$$

with

$$x = d \, \frac{E_s}{E_c} \, \rho_2 \left(\sqrt{ 1 + \frac{2 \, E_c}{E_s \rho_2} } - 1 \right) \tag{2.9}$$

The yield moment is

$$m_{y1} = \rho \, d^2 \, f_y \left(1 - \frac{x}{3 \, d} \right) \tag{2.10}$$

and the flexural capacity is

$$m_{y2} = \rho \, d^2 \, f_y \left(1 - 0.59 \frac{\rho \, f_y}{f_c{}'} \right) \tag{2.11}$$

Then, the column reaction corresponding to the start of reinforcement yielding at the column is calculated:

$$V_{y1} = m_{y1} \frac{8 \, \pi}{2 \ln \left(\dfrac{B}{2 \, r_c} \right) + 1 - \left(\dfrac{2 \, r_c}{B} \right)^2} \tag{2.12}$$

and the column reaction corresponding to overall yielding of the specimen's top reinforcement is

$$V_{y2} = m_{y2} \frac{2 \, \pi}{1 - \left(\dfrac{2 \, r_c}{B} \right)} \tag{2.13}$$

Then, the radius r_y from the column centre within which yielding of the top reinforcement occurs is calculated using the following relationship:

$$\frac{V_{y1}}{8\pi} \left[2 \ln \frac{r_s}{r_y} + 2 - \left(\frac{r_c}{r_y} \right)^2 - \left(\frac{2 \, r_c}{B} \right)^2 \right] + (\phi_u - \phi_y) \frac{r_c}{r_y} EI = m_{y1} \tag{2.14}$$

If $r_y < r_s$ the shear strength is given by the following formula

$$V_u = \frac{2 \, V_{y1}}{m_y \, B} \left[m_y \, r_y + \int_{r_y}^{r_s} \frac{V_{y1}}{8\pi} \left(2 \ln \frac{r_s}{r} + 2 - \left(\frac{r_c}{r} \right)^2 - \left(\frac{2 \, r_c}{B} \right)^2 \right) + (\phi_u - \phi_y) \frac{r_c}{r} EI] \mathrm{d}r \right] \tag{2.15}$$

whereas if $r_y > r_s$ then

$$V_u = V_{y2} \tag{2.16}$$

Then the deflections δ_{y1}, δ_{y2} and δ_u corresponding to start of reinforcement yielding at the column, overall yielding of the top reinforcement and punching failure, respectively, are calculated using the following formulas:

$$\delta_{y1} = \frac{V_{y1}}{4\,\pi} \left(1 - \frac{r_c}{r_s}\right)^2 \frac{B}{2\,EI} \frac{B - 2\,r_c}{2} \tag{2.17}$$

$$\delta_{y2} = \delta_{y1} + \phi_y \frac{(B - 2\,r_c)^2}{4} \tag{2.18}$$

$$\delta_u = \delta_{y1} + (\phi_u - \phi_y) \frac{2\,r_c}{2} \frac{B - 2\,r_c}{2} \tag{2.19}$$

Afterwards, the deflection due to the vertical load V can be calculated. If $V < V_{y1}$, substitution of V_{y1} by V in (2.17) gives

$$\delta_V = \frac{V}{4\,\pi} \left(1 - \frac{r_c}{r_s}\right)^2 \frac{B}{2\,EI} \frac{B - 2\,r_c}{2} \,,\; V < V_{y1} \tag{2.20}$$

If $V > V_{y1}$, then substitution of ultimate values of deflection and curvature (δ_u and ϕ_u) in (2.19) with the values corresponding at the applied vertical load V gives

$$\delta_V = \delta_{y1} + (\phi_V - \phi_y) \frac{2\,r_c}{2} \frac{B - 2\,r_c}{2} \,,\; V > V_{y1} \tag{2.21}$$

In this case, as apart from the deflection δ_V neither the corresponding curvature ϕ_V nor the radius r_y that defines the zone with reinforcement yielding occurs are known, the system of equations (2.21), (2.15) and (2.14)(substituting V_u and ϕ_u by V and ϕ_V, respectively) should be solved.

Then, an initial guess of the additional overall deflection $2\Delta_M$ due to the imposed ultimate column rotation should be provided. According to [Bro05] half of this deflection (i.e. Δ_M) is assumed to occur before column rotation and the other half after full column rotation is developed. Afterwards, the maximum additional slab deflection Δ is calculated as follows:

$$\Delta = \delta_u - \delta_V - 2\,\Delta_M \tag{2.22}$$

The reaction of each sector element subjected to hogging moment due to seismic loading depends on the state of deflections.

$$\delta_t(i) = \delta_V + \Delta_M + \Delta \sin\phi(i) \tag{2.23}$$

For elastic deflection ($\delta_t(i) < \delta_{y1}$) the reaction of each sector element due to moment is

$$V_t(i) = \frac{\delta_t(i)}{\delta_{y1}} V_{y1} - V \tag{2.24}$$

For the sector elements with $\delta_t(i) > \delta_{y1}$, to calculate the column reaction, the curvature ϕ_V due to vertical load reaction of each sector element should be first computed for the following relationship:

$$\delta_t(i) = \delta_{y1} + (\phi_V - \phi_y) \frac{c}{2} \frac{B - c}{2} \tag{2.25}$$

Then, the radius r_y defining the zone within which yielding occurs should be calculated by solving the following equation:

$$m_{y1} = \frac{V}{8\pi}\left[2\ln\frac{r_s}{r_y} + 2 - \left(\frac{2\,r_c}{2\,r_y}\right)^2 - \left(\frac{2\,r_c}{B}\right)^2\right] + \left(\phi_v - \phi_y\frac{V}{V_{y1}}\right)\frac{c}{2\,r_y}EI \tag{2.26}$$

The reaction of each sector element is, for this case, calculated using the following formula:

$$
\begin{aligned}
V_t(i) = \frac{2\,V_{y2}}{m_{y1}\,B}\left[m_{y1}\,r_y + \int_{r_y}^{r_s}\frac{V_{y1}}{8\pi}\left[2\ln\frac{B}{2\,r} + 2 - \left(\frac{2\,r_c}{2\,r}\right)^2 - \left(\frac{2\,r_c}{B}\right)^2\right]\mathrm{d}r\right] + \\
+ \frac{2\,V_{y2}}{m_{y1}\,B}\frac{V_{y1}}{8\pi}\left[\int_{r_y}^{r_s}(\phi_v - \phi_y)\frac{2\,r_c}{2\,r}EI\mathrm{d}r\right] - V
\end{aligned}
\tag{2.27}
$$

If the slab is divided in n sector elements, the total reaction of the slab half subjected to hogging moment due to seismic loading is

$$V_t = \sum_{i=1}^{n/2}\frac{V_t(i)}{n/2} \tag{2.28}$$

The part of the total unbalanced moment that is carried by the hogging slab half is calculated as follows:

$$M_t = \sum_{i=1}^{n/2}\frac{V_t(i)}{n/2}\,r_s\,\sin\phi(i) \tag{2.29}$$

Likewise, the reaction of each sector element subjected to sagging moment due to seismic loading depends on the state of deflections.

$$\delta_b(i) = \delta_V + \Delta_M - \Delta\,\sin\phi(i) \tag{2.30}$$

For elastic deflection ($\delta_b(i) < \delta_{y1}$) the reaction of each sector element is

$$V_b(i) = V - \frac{\delta_b(i) + \dfrac{1 - \sqrt{EI_1/EI}}{\sqrt{EI_1/EI}}\delta_V}{\delta_{y1}}\,V_{y1}\,\frac{\rho'}{\rho}\,\sqrt{EI_1/EI} \tag{2.31}$$

with

$$V_b(i) \leq V_{b.max} = V + \frac{\rho'}{\rho}\,V_{y2} \tag{2.32}$$

The total reaction of the slab half subjected to sagging moment due to seismic loading is

$$V_b = \sum_{i=1}^{n/2}\frac{V_b(i)}{n/2} \tag{2.33}$$

The part of the total unbalanced moment that is carried by the sagging slab half is calculated as follows:

$$M_b = \sum_{i=1}^{n/2}\frac{V_b(i)}{n/2}\,r_s\,\sin\phi(i) \tag{2.34}$$

The final stage, before calculating the ultimate moment that is transferred to the slab-column connection, is the check of the equilibrium, that is satisfied when the sum of the sector element reactions due to moment at the sagging slab half is approaximately equal to the one of the hogging slab half plus the column reaction due to the deflection Δ_M that is assumed to occur before column rotation, as shown in the following equation:

$$V_b - V_t - \Delta_M \frac{V_{y1}}{\delta_{y1}} \approx 0 \qquad (2.35)$$

The moment capacity of the slab-column connection can therefore be calculated by summing the contribution of the hogging and sagging slab half, as follows:

$$M_u = M_t + M_b \qquad (2.36)$$

The rotation capacity of the slab is

$$\theta_u = \theta_1 + \theta_2 \qquad (2.37)$$

where

$$\theta_1 = \frac{1}{\sqrt{EI_1/EI}} \frac{\delta_u - \delta_V - 2\Delta_M}{r_s - r_c} \qquad (2.38)$$

and

$$\theta_2 = \frac{12\,M_u}{\pi\,E_c\,h^3} \left(\ln \frac{B}{2\,r_c} - 1 + \frac{2\,r_c}{B} \right) 10^{-3} \qquad (2.39)$$

To provide a non-iterative and less laborious model than the model presented above (Eqs. (2.3) - (2.39) - [Bro05]) in terms of calculations, a simplified version was proposed some years later [Bro09]. No reinforcement limits ρ_1 and ρ_2 are calculated. If the reinforcement is still elastic, it is assumed that only one-third of the unbalanced moment is transferred as bending moment on the column edges parallel to the vector of the unbalanced moment [Mas70]. The remaining two-thirds are assumed to be carried by eccentric shear forces and torsional moments on the column edges that are perpendicular to the vector of the unbalanced moment; these are not examined further. Hence, the rotation capacity of the slab is limited by the bending moments induced on the column edges parallel to the vector of the unbalanced moment. If the slab reinforcement yields, it is assumed that the mechanisms of eccentric shear force and torsional moments no longer contribute to the resistance of the connection. Instead, a strut and tie model develops, which is shown in Figure 2.9. The proposed model takes into consideration the size effect as well as the concrete brittleness with increasing strength.
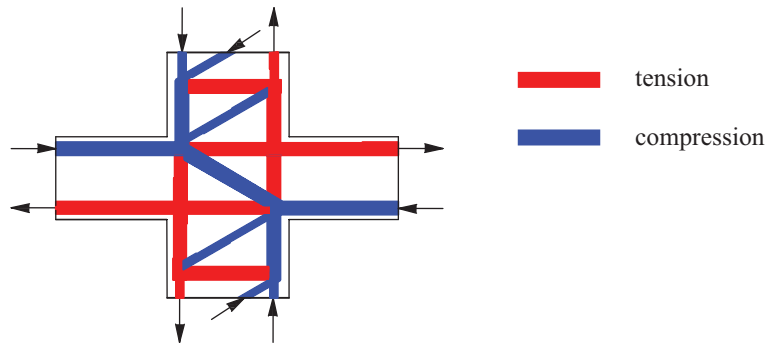
Figure 2.9 – Mechanical model according to Broms [Bro09] for the transfer of the moment after the onset of slab reinforcement yielding at the column face.

First, the critical bending moment at the column edge is calculated:

$$m_u = \rho \left(\frac{\epsilon_y}{\epsilon_s} \right)^{0.2} d^2\,E_s\,\epsilon_s \left(1 - \frac{x}{3\,d} \right) \qquad (2.40)$$

The corresponding critical total reaction force is:

$$V_u = m_u \frac{8\,\pi}{2\ln\left(\dfrac{B}{2\,r_c}\right) + 1 - \left(\dfrac{2\,r_c}{B}\right)^2} \tag{2.41}$$

If $V_u < V_{y1}$ (Eq. (2.12)) then the slab behaves elastically. The moment capacity of the hogging slab half is

$$M_{el.T} = \left(1 - \frac{V}{V_u}\right) \frac{3\,c\,m_u}{1 - \dfrac{c}{B}} \tag{2.42}$$

while the moment capacity of the sagging slab half is:

$$M_{el.B} = \begin{cases} M_{el.T} - m_{y1} \dfrac{1 - \dfrac{V}{V_u}}{1 - \dfrac{c}{B}} \dfrac{\rho - \rho'}{\rho}\, c\,\ln\left(\dfrac{2\,r_0}{c}\right), & \text{if } V/V_u < 0.5 \\[4mm] M_{el.T}, & \text{if } V/V_u > 0.5 \end{cases} \tag{2.43}$$

wher $r_0 = \dfrac{c}{2} \dfrac{1 - (V/V_u)}{(V/V_u)}$.

Therefore, the moment capacity of the slab-column connection is

$$M_u = M_{el} = M_{el.T} + M_{el.B} \tag{2.44}$$

The corresponding rotation for elastic behaviour is calculated as follows:

$$\theta_u = \theta_{el} = \frac{2\,M_{el.T}}{EI\left(2.8 + 26\,\dfrac{c}{B}\right)} \left(1 - \frac{V}{V_u}\right) \phi_u\,(2\,d + c) \tag{2.45}$$

When $V_{y1} < V_u < V_{y2}$ partial or overall yielding of the rebars occurs and therefore inelastic deformations are expected. The ultimate rotation is calculated as follows:

$$\theta_u = \begin{cases} \theta_{el} + (\phi_u - \phi_y)\dfrac{6\,c}{EI\left(2.8 + 26\,\dfrac{c}{B}\right)}\dfrac{1}{1 - \dfrac{c}{B}}, & \text{if } V < V_{y1} \\[6mm] \left[\theta_{el} + (\phi_u - \phi_y)\dfrac{6\,c}{EI\left(2.8 + 26\dfrac{c}{B}\right)}\dfrac{1}{1 - \dfrac{c}{B}}\right]\left[1 - \left(\dfrac{V - V_{y1}}{V_u - V_{y1}}\right)^4\right], & \text{if } V > V_{y1} \end{cases} \tag{2.46}$$

with the elastic portion of the rotation θ_{el} being calculated by substituting V_u and ϕ_u by V_{y1} and ϕ_y, respectively, in Eq. (2.45).

The elastic moment carried by the hogging slab half ($M_{el.T}$ is calculated by substituting V_u and m_u by V_{y1} and m_{y1}, respectively, in Eq. (2.42), while the elastic moment carried by the sagging slab half

$M_{el.B}$, is given by the following formula:

$$
M_{el.B} = \begin{cases} M_{el.T} - m_{y1} \dfrac{1 - \dfrac{V}{V_u}}{1 - \dfrac{c}{B}} \dfrac{\rho - \rho'}{\rho} \, c \, \ln\left(\dfrac{2\,r_0}{c}\right), & \text{if } V/V_u < 0.5 \\[2em] M_{el.T}, & \text{if } V/V_u > 0.5 \end{cases}
\tag{2.47}
$$

The ultimate moment corresponding to the rotation θ_u is, similarly to the case of elastic conditions, the following:

$$
M_u = M_{u.T} + M_{u.B}
\tag{2.48}
$$

The ultimate moment that can be carried by tension of the top reinforcement is

$$
M_{u.T} = \frac{V_M - V}{2\pi}\left(1 - \frac{2\,r_c}{B}\right)\frac{B}{1 - \dfrac{c}{B}}
\tag{2.49}
$$

where V_M is an equivalent concentric column reaction for which punching occurs, giving the same total bending moment over the width r_s as the acting vertical load V plus the unbalanced moment. To satisfy this condition, the radius r_y from the column centre within which yielding of the top reinforcement occurs is calculated to give the moment corresponding to yielding m_{y1} at this section:

$$
\frac{V}{8\pi}\left[2\ln\frac{r_s}{r_y} + 2 - \left(\frac{2\,r_c}{2\,r_y}\right)^2 - \left(\frac{2\,r_c}{B}\right)^2\right] + \left(\phi_u - \phi_y \frac{V}{V_{y1}}\right)\frac{c}{2\,r_y}EI = m_{y1}
\tag{2.50}
$$

Equation (2.50) should be solved numerically to obtain r_y. If r_y is larger than r_s then the equivalent concentric column reaction V_M is equal to V_{y2}, otherwise it is calculated by moment integration along the radius r:

$$
\begin{aligned}
V_M = {} & \frac{4\pi}{B\left(1 - \dfrac{2\,r_c}{B}\right)}\left[m_{y1}\,r_y + \int_{r_y}^{r_s}\frac{V}{8\pi}\left[2\ln\frac{r_s}{2\,r} + 2 - \left(\frac{2\,r_c}{2\,r}\right)^2 - \left(\frac{2\,r_c}{B}\right)^2\right]\mathrm{d}r\right] + \\[1em]
& + \frac{4\pi}{B\left(1 - \dfrac{2\,r_c}{B}\right)}\left[\int_{r_y}^{r_s}\left(\phi_u - \phi_y\frac{V}{V_{y1}}\right)\frac{c}{2\,r}EI\mathrm{d}r]\right]
\end{aligned}
\tag{2.51}
$$

The behaviour of the opposite slab half remains elastic as the bending moment along the radius decreases. The ultimate positive moment that is transferred to the slab-column connection is

$$
M_{u.B} = M_{u.Ba} + M_{u.Bb}
\tag{2.52}
$$

where $M_{u.Ba}$ is the unbalanced moment caused by reduction of the stress of the top reinforcement to zero and $M_{u.Bb}$ the additional moment caused by tension to the bottom reinforcement. Upper bound estimation of $M_{u.Ba}$ is provided by the following formula:

$$
M_{u.Ba} = \frac{\theta_u}{\theta_{0B}}\,M_{0B} \leq \frac{V}{2\pi}\frac{1 - \dfrac{2\,r_c}{B}}{1 - \dfrac{c}{B}}\,B
\tag{2.53}
$$

where

$$
M_{0B} = \frac{V}{V_{y1}}\frac{3\,c\,m_{y1}}{1 - \dfrac{c}{B}}
\tag{2.54}
$$

and

$$\theta_{0B} = \frac{2\,M_{0B}}{EI\left(2.8 + 26\,\dfrac{c}{B}\right)}\,\frac{V}{V_{y1}}\,\phi_y\,2\,d \tag{2.55}$$

Similarly, for the additional moment $M_{u.Bb}$ due to tension of the bottom reinforcement

$$M_{u.Bb} = \frac{\theta_u - \theta_{0B}}{\theta_{yB}}\,M_{yB} \leq \frac{V_{y2}\,\dfrac{\rho'}{\rho}}{2\pi}\,\frac{1 - \dfrac{2\,r_c}{B}}{1 - \dfrac{c}{B}}\,B \tag{2.56}$$

where the moment causing onset of yielding in the bottom reinforcement at the column is

$$M_{yB} = \frac{\rho'}{\rho}\,\frac{3\,c\,m_{y1}}{-\dfrac{c}{B}} \tag{2.57}$$

corresponding to an additional rotation of

$$\theta_{yB} = \frac{2\,M_{yB}}{\dfrac{\rho'}{\rho}\,EI\left(2.8 + 26\,\dfrac{c}{B}\right)} + \phi_y\,(2\,d + c) \tag{2.58}$$

Models for the numerical analysis of buildings with slab-column connections

In any building construction involving floor slabs connected with columns in a monolithic way, the determination of the mechanical properties of the floor members is less direct than for the columns when earthquake-type loading should be considered. Consequently, obtaining realistic values of the unbalanced moment and the corresponding deformation of the slab is rather difficult. The development of finite element codes for the analysis of structures enabled structural engineers to compute the unbalanced moment and the corresponding slab deformation using numerical analysis software. However, the computation complexity of a connection of the slab (shell-type member) with the column (beam-type member) together with the needed computation time became important shortcomings, especially when the non-linear behaviour of the joint had to be considered.

Various approaches have been proposed to address these shortcomings, most commonly by substituting the slab with linear beam-type members combined in some cases with torsional members and bond-slip members. The vast majority of these approaches are based either on the equivalent frame method or the effective beam width method, which consist in analysing the slab-column connection as part of a bi-dimensional frame. In the following, these two methods are discussed first. The last category of models that is presented comprises models based on the beam analogy method. Yield line methods and strip methods are not covered in the following, since the focus is drawn on the frame analysis concept.

1. Equivalent Frame Models

The Equivalent Frame (EF) method consists in representing the three-dimensional slab-column system by series of two-dimensional frames consisting of slab members and equivalent column members that in turn consist of column and transverse torsional members (Fig. 2.10a). The slab and column members have the same geometric properties with the prototype structure. For the transverse torsional member, the proposed formulas for the torsional stiffness were typically calibrated using experimental results on slabs under gravity load alone [Cor70, Van83], assuming that the distribution of the twisting moment per unit length is triangular (Fig. 2.10b), which is valid only for slab-column systems subjected to gravity loads.
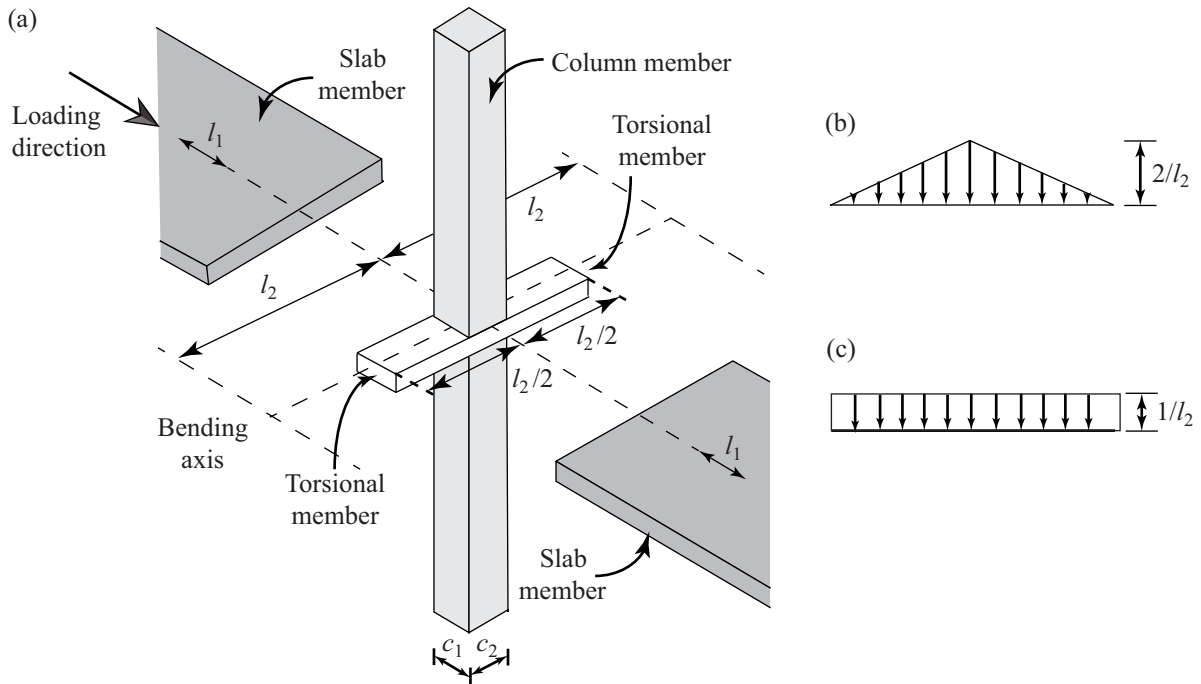
Figure 2.10 – (a) Illustration of the Equivalent Frame method for lateral loads [ACI14], and distribution of unit twisting moment along the axis of the torsional member according to (b) ACI-318 [ACI14], and (c) Park et al. [Par09].

The application of the method is relatively simple and is recommended since 1971 by ACI-318 [ACI71] for the analysis under loads acting in the plane of frames, i.e. under gravity loads and/or lateral loads. However, several studies showed that the predictions of the method in terms of slab moments and deflections are rather inaccurate since the method was developed to capture the mechanical behaviour of frames with slab-column connections subjected to gravity loads only [Can88,Hwa00,Par09]. In addition, the presence of transverse torsional members renders the method unsuitable for three-dimensional analysis of flat slab buildings [Rob97]. According to [Hwa00], this method was found to underestimate the lateral stiffness of the slab-column system.

In 1983, Vanderbilt and Corley proposed to use an equivalent slab member which consists of a slab member and two torsional members connected in series, rather than an equivalent column member. This modification is based on the principle that, unlike the case of gravity loads, for which the load is transferred from the slab to the torsional member and in turn to the column, when lateral loads are applied to the system, the column is restrained by both the torsional stiffness of the transverse torsional member and the flexural stiffness of the slab member. Moreover, a stiffness reduction factor equal to one-third was recommended to take into account cracking.

In 1988, Cano and Klingner proposed to use explicitly transverse torsional members for the connection of the column members with the beam-equivalent slab members [Can88]. Although the resulting structure is not planar, the modelling process is rather simple and requires very few hand calculations.

In 2009, Park et al. [Par09] used the equivalent slab member as proposed by [Van83] with the only difference that for the case of lateral loads alone, the distribution of twisting moments along the transverse torsional member was assumed to be uniform (Fig. 2.10c) instead of triangular [ACI14]. This modified EF method was compared against experiments and was found to offer similar accuracy with finite element analyses and the Effective Beam Width method proposed by Hwang and Moehle [Hwa00], which will be presented in the following.

2. Effective Beam Width Models

In the Effective Beam Width method (EBW) slab action is represented by a flexural slab-beam framing directly between columns that are modelled with their actual properties. The slab-equivalent beam (Fig. 2.11b) has the same thickness as the slab (Fig. 2.11a) and an effective width that is a portion of the distance from midspan to midspan in the transverse direction (subsequently referred to as l_2 - see Fig. 2.11). The width reduction coefficient α is the parameter that is largely influencing the prediction of slab moments and deflections and is defined as the required coefficient so that the rotational stiffness of the slab-equivalent section equals the rotational stiffness of the full width section of the flat slab panel. This equality is obtained if the areas under the moment (or rotation) diagrams of the real system (non-uniform distibution) and the fictitious system (uniform distribution) (Fig. 2.11) are equal.
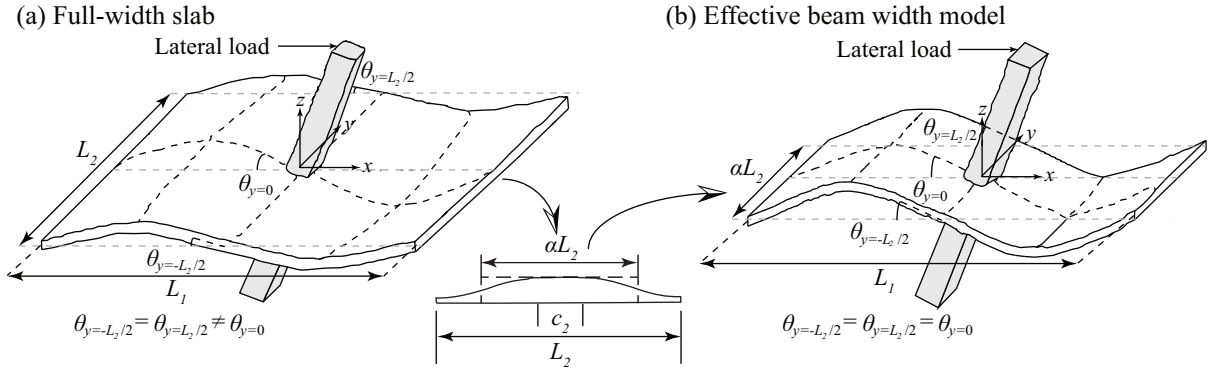
Figure 2.11 – Illustration of the Effective Beam Width method: (a) Full-width slab (real case), and (b) Effective Beam Width Model (simplified case)

Initially, Westergaard and Slater [Wes21] calculated the rotational stiffness of the slab using the infinite plate solution. By equating the rotational stiffness of the slab with the rotational stiffness of a simply supported equivalent beam subjected to an unbalanced moment M at midspan, the width reduction coefficient α was derived:

$$\alpha = \frac{l_1}{l_2} \frac{\pi}{3 \left[ln\left(\frac{l_1}{c\sqrt{2}}\right) + \left(\frac{c}{l_1}\right)^2 - \frac{1}{2}\right]} \left(1 - \frac{c}{l_1}\right)^3 \tag{2.59}$$

where the last term represents the effect of joint flexibility.

The moment that is inserted to an internal support of a continuous beam due to a rotation θ of all supports if the inflection lines appear at midspan is given by the theory of elasticity as follows:

$$M = \frac{12\,EI}{l_1}\,\theta \tag{2.60}$$

where l_1 is the distance between supports, and EI is the section stiffness.

Substituting the moment of inertia I of the beam section by $\alpha\,l_2\,h^3/12$ in the above formula, the effective beam width coefficient α is obtained:

$$\alpha = \frac{M}{\theta}\,\frac{l_1}{l_2}\,\frac{1}{E_c\,h^3} \tag{2.61}$$

The definition of Eq. (2.61) served only as background for the closed-form equations for the width reduction coefficient proposed by various researchers. These equations, in view of the lack of an analytical model that correlates the unbalanced moment with the rotation due to slab deformation

were either based on finite element analyses or on experimental observations and are summarised in Table 2.3 for interior slab-column connections and square columns.

Table 2.3 – Proposed width reduction coefficients α for interior slab-column connections using the EBW method

Source	α
Pecknold [Pec75]	$\dfrac{1}{1-\nu^2}\,\dfrac{c_2}{l_1}\,\dfrac{l_1}{l_2}\,\dfrac{1}{f_b + 6\sum_{m=1}^{\infty}\left(\dfrac{1}{m\,\pi}\right)^3 Q_m\,A_m}$
Banchik [Ban87]	$\left(5\,\dfrac{c_1}{l_2} + \dfrac{l_1}{4\,l_2}\right)\dfrac{1}{1-\nu^2}$
Pan and Moehle [Pan92]	$1/3$
Luo and Durrani [Luo95]	$\dfrac{\left(-0.0221\left(\dfrac{c_1}{c_2}\right)^4 + 0.0281\left(\dfrac{c_1}{c_2}\right)^3 + 0.1535\left(\dfrac{c_1}{c_2}\right)^2 + 0.773\left(\dfrac{c_1}{c_2}\right) + 0.0845\right)\left(\dfrac{c_1}{l_2}\right)}{0.05 + 0.002\left(\dfrac{l_1}{l_2}\right)^4 - 2\left(\dfrac{c_1}{l_1}\right)^3 - 2.8\left(\dfrac{c_1}{l_1}\right)^2 + 1.1\left(\dfrac{c_1}{l_1}\right)}$
Grossman [Gro97]	$K_d\left(0.3\,\dfrac{l_1}{l_2} + \dfrac{c_1}{l_2}\,\dfrac{l_1}{l_2} + \dfrac{c_2 - c_1}{2\,l_2}\right)\left(\dfrac{d}{0.9\,h}\right)^{*}$
Hwang and Moehle [Hwa00]	$\left(2\,\dfrac{c_1}{l_2} + \dfrac{l_1}{3\,l_2}\right)$

* $K_d = 1.1$, 1.0, 0.8, 0.5 if $\psi_{st} = 0.125\%$, 0.25%, 0.50%, and 1.00%, respectively, with $0.2K_d \leq \alpha \leq 0.5K_d$.

In 1975, Pecknold proposed a formula for the width reduction coefficient using the theory of elasticity and a standard Levy-type solution for a slab-column connection subjected to lateral loading alone [Pec75]. In 1977, Allen and Darvall arrived to identical results with Pecknold using a Fourier series technique [All77]. Nevertheless, due to the complexity of the numerical equations and the neglecting of the gravity loads, they have not been used in engineering practice. In 1987, Banchik proposed a simpler formula based on finite element analyses considering the same geometric parameters as proposed by Pecknold (column size c_1 parallel to the moment vector and distance l_1 between inflection points) [Ban87]. As shown above, a number of methods have been used to arrive at a value for α but generally they rely on an elastic finite element analysis of the slab-column connection [Van83] while the effect of stiffness reduction due to cracking was generally incorporated through a factor that is function of the Poisson ratio ν. In 1992, Pan and Moehle proposed a value of one-third for the α coefficient only for a lateral drift of 0.2%, based on experimental results on isolated slab-column specimens [Pan92]. In 1995, Luo and Durrani proposed a simpler formulation for the α coefficient calibrating the elastic solution proposed by Pecknold [Dur95]. Moreover, a stiffness reduction factor β (ratio of the cracked stiffness and the gross stiffness of the slab) was proposed for the beam-equivalent member, which is dependent on the moment and vertical load applied to the slab. Later, Grossman [Gro97] proposed a formula for the width reduction coefficient that depends on geometric properties and the imposed drift value. K_d was introduced to take into account stiffness degradation for increasing drift levels (see Table 2.3), based on test results of a flat slab system [Hwa93]. In 2000, Hwang and Moehle [Hwa00]

proposed a formula similar to the formula of Banchik [Ban87] for the α coefficient. Analytical and experimental data treatment led to different formulation for the β coefficient, which depends upon geometric properties (c_1/l_1) and the service live load acting on the slab. In 2009, Han et al. proposed an alternative formula for the stiffness reduction factor with only parameter the ratio of applied to cracking moment based on non-linear regression analysis using test results [Han09]. Table 2.4 resumes the β factors that have been proposed for interior slab-column connections.

Table 2.4 – Proposed stiffness reduction factors β for interior slab-column connections using the Effective Beam Width Method

Source	β
Luo and Durrani [Luo95]	$\left(1 - 0.4 \dfrac{V_E}{4 \, A_c \, \sqrt{fc}}\right) \left[\left(\dfrac{M_{cr}}{M_E}\right)^3 + \left(1 - \left(\dfrac{M_{cr}}{M_E}\right)^3\right) \dfrac{I_{cr}}{I_g}\right]$
Hwang and Moehle [Hwa00]	$\max\left[5 \, \dfrac{c_1}{l_1} - 0.1 \left(\dfrac{LL}{40} - 1\right), \dfrac{1}{3}\right]^{*}$
Han et al. [Han09]	$0.4 + 0.32 \left[\left(\dfrac{M_E}{M_{cr}}\right)^{-0.5} - \left(\dfrac{M_E}{M_{cr}}\right)^{0.5}\right]$

* LL= Service live load [lb/ft^2]

In 1997 Robertson proposed a modified EBW method [Rob97] based on results from a subassembly composed of two exterior and one interior slab-column connections (Fig. 2.1a) tested previously [Rob92]. The approach consisted in substituting the equivalent beam member by two beam members representing the slab regions subjected to hogging and sagging moments, since the latter one was observed to be significantly less damaged than the first one. The stiffness reduction factor β was derived for the drift levels of 0.5% and 1.5% (representing the serviceability and ultimate limit state) to match the experimentally measured slab moment distribution. For the beam under hogging moment a value of 0.1 was proposed for both drift levels, while for the beam subjected to sagging moment it was proposed $\beta = 1.0$ for 0.5% drift and $\beta = 0.5$ for 1.5% drift. A value of 0.4 for the width reduction coefficient α was found to give the best estimate of both examined interstorey drifts. In 2005, Dovich and Wight [Dov05] proposed an EBW model with beam width $b = l_2/2$ and $b = l_2/3$ for initial stiffness and strength, respectively, based on test results of two-storey, two-bay flat slab frame tested earlier [Dov94].

3. Beam Analogy Methods

The beam analogy approach derives the strength of the connection by describing all the actions in the critical perimeter of the connection and satisfying equilibrium both for the shear force and the moment. For the shear force the following equation is used:

$$V_E = V_{back} - V_{front} + V_{side.1} + V_{side.2} \tag{2.62}$$

where V_{front} and V_{back} are the shear forces at the front and the back face of the examined critical section (hogging and sagging slab half, respectively) and $V_{side.1}$ and $V_{side.2}$ are the shear forces at the side faces 1 and 2 (Fig. 2.12a).

Equilibrium of shear forces about the bending axis gives

$$M_u = M_{front} + M_{back} + T_1 + T_2 + M_{v.front} + M_{v.back} \tag{2.63}$$

where $M_{v.front}$ and $M_{v.back}$ are the moments due to shear force at the front and the back face of the examined critical section (shear force times the distance from the column axis), respectively, M_{front} and M_{back} are the moments due to flexure at the front and the back face, respectively, and T_1 and T_2 are the torsional moments at the two side faces (Fig 2.12a).
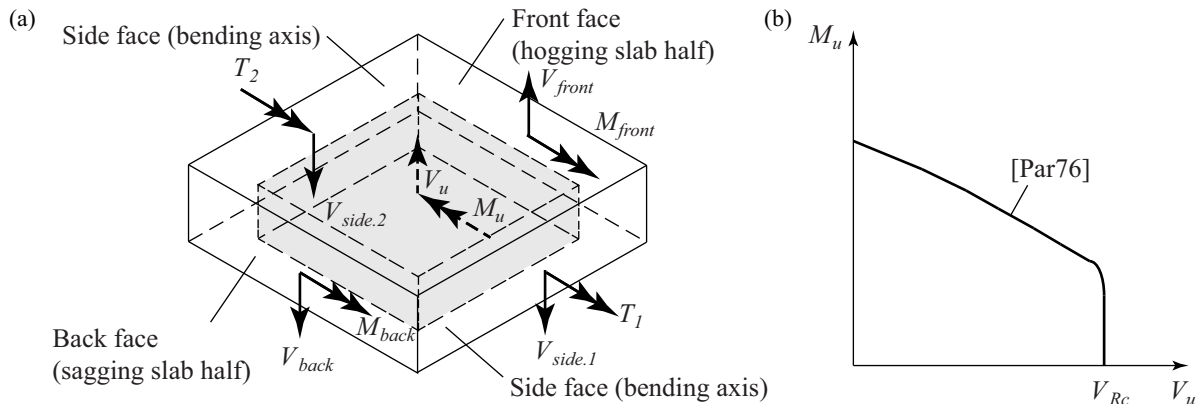
Figure 2.12 – (a) Illustration of the Beam Analogy Method, and (b) Interaction diagram according to [Par76].

In 1976, Park and Islam [Par76] proposed an equation for the unbalanced moment-shear force interaction diagram (Fig. 2.12b) aiming to reduce the conservativeness of the strength predictions by [ACI71] on the basis of the beam analogy concept.

Although being the most rational, the beam analogy method is difficult to be applied for design purposes as multiple failure modes are associated with the various actions that are considered (shear force, flexure, torsion). Therefore, this concept served only as basis for the development of lumped plasticity models for consideration of both slab non-linearity and punching failure. Since during the last decades non-linear analysis has been widely used by structural engineers for both performance-based design and seismic assessment of buildings, these approaches gained significant popularity. Moreover, as the analysis results can be compared to the experimental ones not only in terms of moment and deformation capacity but also in terms of the overall moment-rotation response, considerable research has been carried out and various modelling approaches were proposed. The main aspects of such works are discussed in the following.

In 1984, Akiyama and Hawkins proposed a model for non-linear analysis of flat slabs composed of flexural, torsional and bond-slip elements and forcing deformation compatibility using rigid connecting bars [Aki84]. The most important parameters were calibrated using tests from literature [Haw74].

Later, Tian et al. developed a 2D non-linear model based on the beam analogy concept for use in non-linear static analysis of flat slab buildings [Tia09]. The resistance offered by flexure and shear was modelled using an equivalent beam while the resistance offered by torsion was modelled by a spring element. The stiffness parameters of the model were calibrated from results of cyclically tested specimens [Tia08] to capture the effect of gravity load and reinforcement ratio on the connection stiffness.

In 2015, Choi and Kim [Cho15] proposed a method for non-linear static analysis of flat slabs on the basis of test results, assuming that structural damage is concentrated at the slab-column connection. Non-linearity was introduced by the use of zero-length flexural and shear hinges at the front and back faces of the critical section and torsional hinges at the side faces. The backbone curves of the hinges were introduced separately while the column and the rest of the slab were modelled elastically.

2.2.2 Proposed empirical models

During an earthquake, buildings are subjected to horizontal deformations, which can be expressed on a global level in terms of the interstorey drift ψ_{st}. In buildings with flat slabs supported on columns, seismically induced drifts result in imposed rotations to the slab-column connections and therefore to transferred moments between the slab and the column. While considerable theoretical work has been conducted with respect to analytical methods for calculating the maximum moment that is resisted by a slab-column connection (§2.2.1), developing theoretically admissible models for the deformation capacity of slab-column connections when subjected to earthquake loading is rather difficult and therefore significantly less analytical investigation has been performed. On the other hand, the significant amount of experimental data (Section 2.1) allowed several researchers to propose empirical models for the deformation capacity of slab-column connections. Moreover, non-linear analysis has gained significant popularity during the last decades, both for assessment of the seismic vulnerability of existing structures and for performance-based design of new structures. This requires the estimation of both the strength and the deformation capacity of the involved structural members by the structural engineer. For this reason, empirical approaches for the deformation capacity of slab-column connections date only since the end of the 1980's. In the following, the most important aspects of such works are briefly presented.

Based on monotonic and cyclic tests on slab-column connections, Pan and Moehle [Pan89, Pan92] showed that the rotation capacity of the slab is strongly dependent on the gravity shear ratio V_E/V_{Rc} with V_E being the vertical load acting on the slab-column connection during the seismic event and $V_{Rc} = 0.33\,b_o\,d\,\sqrt{f_c}$ (nominal punching strength according to ACI-318 [ACI14]). Pan and Moehle proposed to limit the gravity shear ratio in new designs to 0.40 (Fig. 2.13a) since slabs with higher gravity shear ratios did not display an inelastic displacement capacity. The influence of other parameters such as the reinforcement ratio and the geometry of the slab and the column was disregarded, on the basis of previous experimental observations [Pan88].

Adequate seismic behaviour of a structural member is characterised, in addition to sufficient moment and deformation capacity, by large ductility, i.e. post-elastic deformation prior to failure. The definition of the ductility of a structural member requires the yield point of the force-displacement relationship to be identified. For slab-column connections, although gradual yielding of the flexural reinforcement leads to softening of the moment-rotation curve, no clear yield point can be identified. Nevertheless, in 1989, Pan and Moehle proposed an empirical method for calculating the ductility factor μ of a slab-column connection when subjected to earthquake loading [Pan89]. According to the proposed method, the secant stiffness at two-thirds of the maximum moment corresponds to the elastic stiffness of the connection while the displacement (or equally the rotation) when the elastic branch reaches the maximum moment is considered to correspond to yielding (Fig. 2.13b). Therefore, the ductility can be calculated as the ratio of the displacement at peak to the displacement at yielding.

(a)

(b)
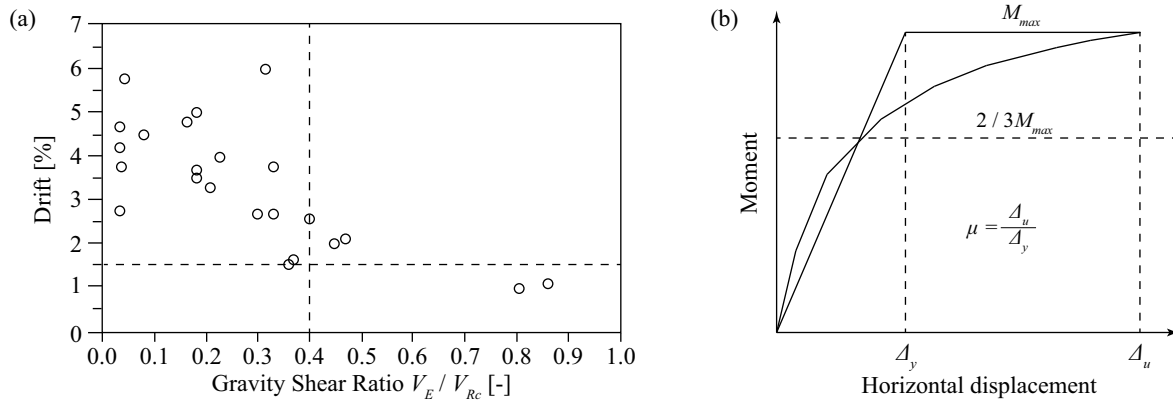
Figure 2.13 – (a) Dependency of the drift at failure on the gravity shear ratio (drawn after [Pan89]), and (b) Displacement ductility definition according to Pan and Moehle [Pan89].

In 1999, Hueste and Wight [Hue99] proposed a trilinear empirical model between interstorey drift and gravity-induced shear (Fig. 2.14a), based on an extended test database compared to Pan and Moehle [Pan89]. Moreover, a method was proposed to account for punching shear failures of internal slab-column connections when performing non-linear analysis for the assessment of regular RC buildings [Hue99], based on lumped plasticity. The slab is substituted by a beam element with two non-linear rotational springs at a specified distance from the column face, while rigid end zones are assigned to the slab-column connection region. Based on prior experimental investigations and on the model proposed by Pan and Moehle [Pan89], Hueste and Wight proposed as failure criterion a trilinear model to relate the gravity shear ratio V_E/V_{Rc} with the member-end rotation θ (Fig. 2.14b), which consists a relatively easy output to be extracted from most commercial software for non-linear analysis. The only parameter that must be computed beforehand is the critical beam-end rotation θ_{cr} corresponding to a shear ratio V_E/V_{Rc} equal to 0.4 (elbow in Figure 2.14b). For this purpose, it was proposed to carry an initial non-linear static (pushover) analysis of the building until 1.5% of roof drift and vertical loads corresponding to a gravity shear ratio equal to 0.4 and assign to each slab-column connection the negative rotation (corresponding to hogging moment) that results from this initial analysis as θ_{cr}. Once the critical rotation θ_{cr} is determined for each slab-column connection, a second non-linear analysis (static or dynamic) with the required gravity loads is conducted. Then, the demand in terms of negative beam-end rotations can be readily compared to the allowable negative beam-end rotation for each slab-column connection.

(a)

(b)
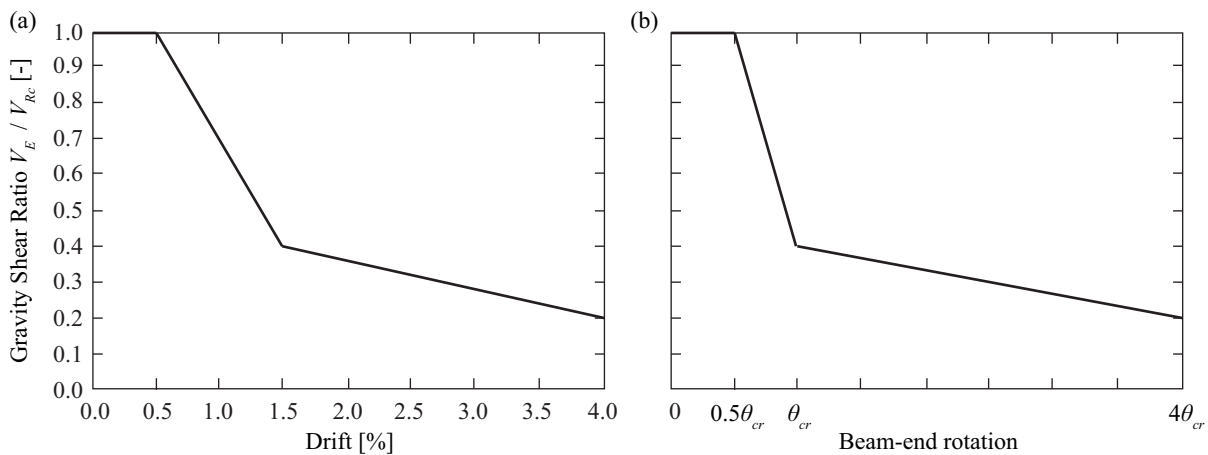
Figure 2.14 – Model proposed by Hueste and Wight [Hue99]: (a) Dependency of the drift at failure on the gravity shear ratio (drawn after [Hue99]), and (b) Beam-end rotation as function of the gravity shear ratio (drawn after [Hue99]).

In 2005, the model proposed by Pan and Moehle was introduced into the American concrete design standard when designing for interstorey drift and remained unchanged since then. While the interstorey drift capacity proposed in [ACI14] are lower bound estimates, Hueste et al. [Hue07] showed that the mean storey drift capacity of slab-column connections is approximately 50% higher than the values prescribed in the code and can be described by a linear function with capacities of 5.0% and 0.8% for gravity shear ratios of zero and 0.6, respectively. Based on these findings, a procedure for performance-based design was also provided:

$$\psi_{st.IO} = \frac{1}{3}\left(0.05 - 0.07\frac{V_E}{V_{Rc}}\right) \tag{2.64}$$

$$\psi_{st.LS} = \frac{2}{3}\left(0.05 - 0.07\frac{V_E}{V_{Rc}}\right) \tag{2.65}$$

$$\psi_{st.CP} = 0.05 - 0.07\frac{V_E}{V_{Rc}} \tag{2.66}$$

where $\psi_{st.IO}$, $\psi_{st.LS}$ and $\psi_{st.CP}$ are the interstorey drifts corresponding at the Immediate Occupancy (IO), Life Safety (LS) and Collapse Prevention (CP) performance criteria, respectively.

In 2009, Kang et al. proposed a model for the non-linear analysis of buildings with slab-column connections [Kan09], combining the principles of distributed plasticity for column modelling and lumped plasticity for the modelling of the slab and the slab-column connection. Column response both in the elastic and inelastic range was incorporated by the use of fibre elements. For the slab, the elastic behaviour was modelled by the EBW method proposed by Pecknold [Pec75] (see §2.2.1). For the inelastic behaviour of the slab, plastic hinges were arranged at the ends of the beam-equivalent member. The flexural capacity of the beam plastic hinges corresponds to reinforcement yielding within a width equal to the column strip. The slab-column connection was modelled by a connection spring that links the beam to the column. The arrangement of the members is shown in Figure 2.15. The flexural moment of the connection spring corresponds to the sum of the flexural capacities of the sagging and hogging reinforcement over the critical section width, assumed to be equal to $c + 3\,h$ by [Kan09] (see §2.3.1 in the following section). All springs and plastic hinges were assumed to follow a rigid-plastic law with hardening. Concerning the post-yield stiffness of the connection spring, a value equal to 10% of the elastic (cracked) stiffness of the slab was proposed, on the basis of shake table test results performed by the authors [Kan04]. For the plastic hinges instead, a very low value of post-yield stiffness was proposed to avoid convergence problems. The following three cases were distinguished:

- (a): stress-induced punching failure without plastic rotation neither for the connection spring nor for the plastic hinges of the beams. In this case the moment at punching is determined using the eccentric shear stress model of [ACI14] (similar to Eq. (2.2)).

- (b): attainment of the moment capacity for the connection spring after the appearance of plastic rotation in the connection spring but without plastic rotations in the plastic hinges of the beams. The moment capacity of the connection spring corresponds to the plastic rotation capacity of the connection, which was approximated as $1.5\,\chi_{y.c+3h}\,h$ (χ_{c+3h} is the yield curvature over the width $c + 3\,h$ and h is the slab thickness), based on shake table test results [Kan04].

- (c): drift-induced punching failure after the appearance of plastic rotations both in the connection spring and the plastic hinges of the beams. To do so, a limit state incorporating the empirical model proposed by Pan and Moehle [Pan89] was introduced.

Cases (a) and (b) correspond to failure at the connection level (connection spring), while the case (c) corresponds to failure at the slab level (plastic hinge). It should also be noted that drift-induced punching failure is possible prior to reaching the moment capacity of the connection spring. However, for non-prestressed slab-column connections yielding of the connection spring ($c + 3h$) typically occurs

before yielding of the plastic hinge (column strip). Moreover, other empirical models that link the gravity shear ratio to the drift at punching failure can be used as limit state (e.g. [Hue99]).
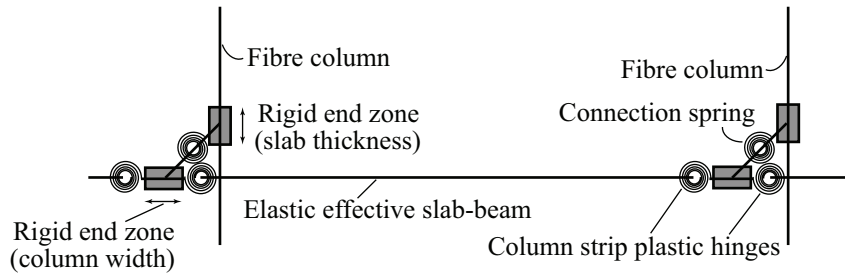
Figure 2.15 – Model for non-linear analysis of buildings with slab-column connections proposed by Kang et al. (drawn after [Kan09])

2.3   Design code provisions

2.3.1   ACI-318

For the case of moment transfer between column and slab it is assumed that a fraction of moment (equal to the coefficient γ_v) is resisted by the eccentric shear force mechanism. The shear stresses due to moment transfer M_E are superposed to the shear stresses due to vertical loads V_E as shown in the following equation:

$$v_E = \frac{V_E}{b_{o.ACI}\, d} \pm \frac{\gamma_v\, M_E\, j_d}{J_c} \tag{2.67}$$

where $b_{o.ACI}$ is the length of the control perimeter (located at a distance of $d/2$ from the column face), j_d is the distance between the centroid and the edge of the critical perimeter, and J_c is a property analogous to the the polar moment of inertia of the critical section:

$$J_c = \frac{d\, b_1^{\,3}}{6} + \frac{d^3\, b_1}{6} + \frac{d\, b_1^2 b_2}{2} \tag{2.68}$$

The fraction of the moment resisted by the eccentric shear force mechanism is (Section 13.5.3.2 [ACI14]):

$$\gamma_v = 1 - \frac{1}{1 + \dfrac{2}{3}\,\sqrt{\dfrac{b_1}{b_2}}} \tag{2.69}$$

where b_1 and b_2 are the dimensions of the critical section measured in the direction of the span for which moments are determined and perpendicular to it, respectively.

For unbalanced moments at interior slab-column it is permitted to increase the value of the fraction γ_f of the moment resisted by flexure (complementary of γ_v) by 25% (but $\gamma_f \leq 1.0$), provided that V_E does not exceed $0.4\, V_{Rc}$.

The total maximum shear stress v_R acting on the control perimeter is:

$$v_R = \min\left(0.17\left(1 + \frac{2}{\beta_c}\right), 0.083\left(2 + \frac{\alpha_s\, d}{b_{o.ACI}}\right), \frac{1}{3}\right)\,\sqrt{f_c} \tag{2.70}$$

where β_c is the ratio of long to short side of the column and α_s is a parameter equal to 40 for interior slab-column connections, 30 for exterior slab-column connections, and 20 for interior slab-column connections.

According to the same standard the unbalanced moment cannot be more than the moment resisted by flexure by the hogging and sagging reinforcement ($m_{R.hog}$ and $m_{R.sag}$, respectively) over a width equal to $c + 3\,h$. The maximum inserted moment can therefore be calculated using the following formula:

$$
M_{max} = \min \left(\frac{v_R - \dfrac{V_E}{b_{o.ACI}\,d}}{\gamma_v\,j_d}\,J_c, \; \frac{(m_{R.hog} + m_{R_s ag})\,(c + 3\,h)}{1 - \gamma_v} \right)
\tag{2.71}
$$

ACI-318 [ACI14] is the only standard that poses drift limitations for slab-column connections. Based on the study of Pan and Moehle [Pan89] the maximum admissible drift (in radians) is function of the applied shear force on the slab-column connection:

$$
\psi_{st.u} = \max \left(0.005, 0.035 - 0.05\,\frac{V_E}{V_{Rc}} \right)
\tag{2.72}
$$

where V_{Rc} is the punching strength of the slab-column connection according to Eq. (2.70). For design, V_{Rc} should be multiplied by the strength reduction factor $\phi = 0.75$.

2.3.2 Eurocode 2

As ACI-318, EC2 [Eur04] uses the eccentric shear transfer model for predicting the maximum unbalanced moment. While ACI-318 [ACI14] assumes a linear shear stress distribution along the control perimeter, EC2 assumes that it is uniform. Therefore, for a given shear force V and moment M, the shear stress v_E acting on the control perimeter of the slab-column connection is:

$$
v_E = \frac{V}{b_{o.EC2}\,d} + \frac{k\,M}{W_1\,d}
\tag{2.73}
$$

where $b_{o.EC2}$ is the length of the control perimeter (located at a distance of $2\,d$ from the column face), k is the column aspect ratio factor that is equal to 0.60 for square columns, and W_1 is a geometric parameter calculated by taking moments about the centroid of the control perimeter which for internal square columns under uniaxial bending is:

$$
W_1 = 2.5\,c^2 + 4\,c\,d + 16\,d^2 + 2\,\pi\,c\,d
\tag{2.74}
$$

The maximum permissible shear stress v_R acting on the control perimeter is:

$$
v_R = 0.18\,\zeta\,(100\,\rho_l\,f_c)^{1/3}
\tag{2.75}
$$

where ζ is a coefficient to take into account the size effect (equal to $1 + \sqrt{200/d} \leq 2.0$) and ρ_l is the flexural reinforcement ratio of the slab. The moment capacity for a given V can therefore be calculated by substituting v_E by v_R in Eq. (2.73) and solving for M.

2.3.3 Model Code 2010

The punching formulation of Model Code 2010 [Fib11] is based on the Critical Shear Crack Theory [Mut08], which uses the following failure criterion:

$$
v_R = \frac{1}{1.5 + 0.9\,\psi\,d\,k_{dg}}\,\sqrt{f_c}
\tag{2.76}
$$

where $k_{dg} = 2/(1 + d_g/d_{g0}) \geq 0.75$, d_{g0}=16 mm. For Level of Approximation II (recommended for a typical design of new structures), the slab rotation can be estimated with a simplified parabolic relationship, which is a function of the ratio of moment demand to capacity [Mut13]:

$$\psi = 1.5 \, \frac{r_s}{d} \, \frac{f_y}{E_s} \, \left(\frac{m_s}{m_R} \right)^{3/2} \tag{2.77}$$

where r_s is the radius of an isolated slab or $0.22L$ in case of a continuous slab with regular span lengths, f_y and E_s are the yield stress and modulus of elasticity of flexural reinforcement, respectively. m_R is the moment capacity of the slab and m_S the average moment demand on the column strip. For interior columns in slabs with sufficiently regular geometry, m_S can be estimated as $m_S = V \left(\frac{1}{8} + \frac{e}{2 \, b_s} \right)$, where $e = \dfrac{M_d}{V_d}$ is the load eccentricity and b_s is the width of the support strip.

Unbalanced moments are accounted for by reducing the length of the control perimeter (situated at a distance of $d/2$ from the column face) by the factor:

$$k_e = \frac{1}{1 + e/b} \tag{2.78}$$

where b is the diameter of a circle with the same surface as the region inside the basic control perimeter. The shear strength can therefore be computed using the following formula:

$$V_R = v_R \, b_0 \, d \tag{2.79}$$

Chapter 3

Experimental Campaign

Although a significant amount of experimental research on the seismic behaviour of slab-column connections without transverse reinforcement has been conducted over the last decades, the state of the art (Chapter 2) reveals several gaps; (a) existing experimental research covers relatively thin slabs, (b) the database of pairs of slabs tested under both monotonically and cyclically increasing unbalanced moment is very limited, and (c) no experimental data are reported on the relation between local slab rotations and the rotation due to slab deformation, which gives an estimate of the interstorey drift part contributed by slab deformation.

To address the aforementioned needs, an experimental campaign was performed within this research, comprising 13 full-scale slab specimens. Two slabs were tested under monotonically increasing vertical loads, six slabs were tested under constant vertical load and monotonically increasing moment and five slabs were tested under constant vertical load and cyclically increasing moment. All specimens had the same plan dimensions (3.00 m x 3.00 m), slab thickness (250 mm) and column size (390 mm x 390 mm). The investigated parameters were the gravity loads applied to specimens subjected to combined vertical load and moment, the flexural reinforcement ratio and the loading type (monotonic against cyclic). The present chapter is based on an article by Drakatos et al. [Dra16].

Section 3.1 presents the prototype building that served as reference for the design of the experimental campaign.

In Section 3.2, the test setup that was adopted for the experimental investigation is presented, followed by the presentation of the response comparison between the test setup and the prototype building using NLFEA (Section 3.3). For comparison purposes the setup configurations used in past experimental campaigns (Chapter 2) are compared to the adopted test setup and the prototype building in terms of the moment-rotation response. Then, the specimen properties, the instrumentation and the adopted loading procedure are presented (Sections 3.4, 3.5, and 3.6, respectively).

Section 3.7 comprises the main results of the experimental study with respect to the influence of gravity loads, cyclic loading and reinforcement content on the moment strength and the deformation capacity of the tested slab-column connections. In Section 3.8, the effect of each of the above-mentioned factors on the initial siffness, the peak moment, the rotation capacity and the cracking pattern are discussed.

In Section 3.9, the tests results are compared with the requirements of the codes of practice presented in Chapter 2 both for the moment strength and the rotation capacity.

3.1 Prototype building

A five-storey office building typical for Central European construction served as reference for the design of the test specimens of the performed experimental campaign. The slabs had a thickness of 250 mm and internal spans of 6.8 m. The storey height was 3.0 m. The primary lateral load-resisting system comprised two RC C-shaped cores providing lateral strength and stiffness in both directions (Figure 3.1), whereas slab-column connections were designed to carry only vertical loads. The design was performed according to fib-Model Code [Fib11] for moderate seismic zone. The columns were square and cast-in-place with a size of 390 mm. The top reinforcement ratio in each direction was equal to 0.75% in the zone of the slab near the column (grey zones) and 0.5% in the middle strip (white zones), as shown in Figure 3.1. Bottom reinforcement was provided in both directions over the whole slab, with a ratio equal to 0.38% around the column (dark grey zones) and 0.5% elsewhere. The provided bottom flexural reinforcement was continuous over the slab-column connections, complying with the integrity rules of ACI-318 [ACI14]. The quasi-permanent vertical loads consisted of 6.25 kN/m^2 of self-weight of the slab, 1.00 kN/m^2 superimposed load and 0.60 kN/m^2 quasi-permanent live load. Under this load combination, the unfactored vertical load acting on an interior slab-column connection was approximately 40% of the punching strength according to ACI-318 [ACI14] and Eurocode 2 [Eur04] and 50% of the punching strength according to fib-Model Code [Fib11] using mean strength values without applying any safety factors. The assumed concrete compressive strength was 32 MPa and the yield and maximum tensile stress of the reinforcing steel were 550 MPa and 680 MPa, respectively.

■ Reinforcement ratio 0.75% in both directions
▨ Reinforcement ratio 0.5% in X direction and 0.75% in Y direction
▨ Reinforcement ratio 0.75% in X direction and 0.5% in Y direction
□ Reinforcement ratio 0.5% in both directions
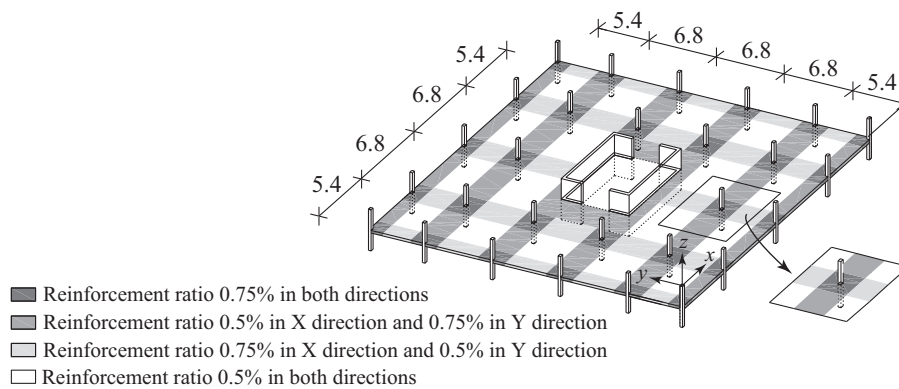
Figure 3.1 – Typical storey of the building that served as reference for the experimental campaign and top reinforcement ratios (dimensions in m).

3.2 Test setup

Figure 3.2 shows a drawing of the setup that was chosen for this test campaign, which is subsequently denoted as setup (b)$_{\mathrm{mod}}$ since it is an evolution of setup (b). When compared to setup (b), the unbalanced moment is introduced by additional upward and downward loads located at approximately $0.50L$ from the column axis. The slab had only dimensions of $0.44L$ while the distance between the slab edge and $0.50L$ was bridged by steel beams. A photo of the test setup is shown in Figure 3.3.
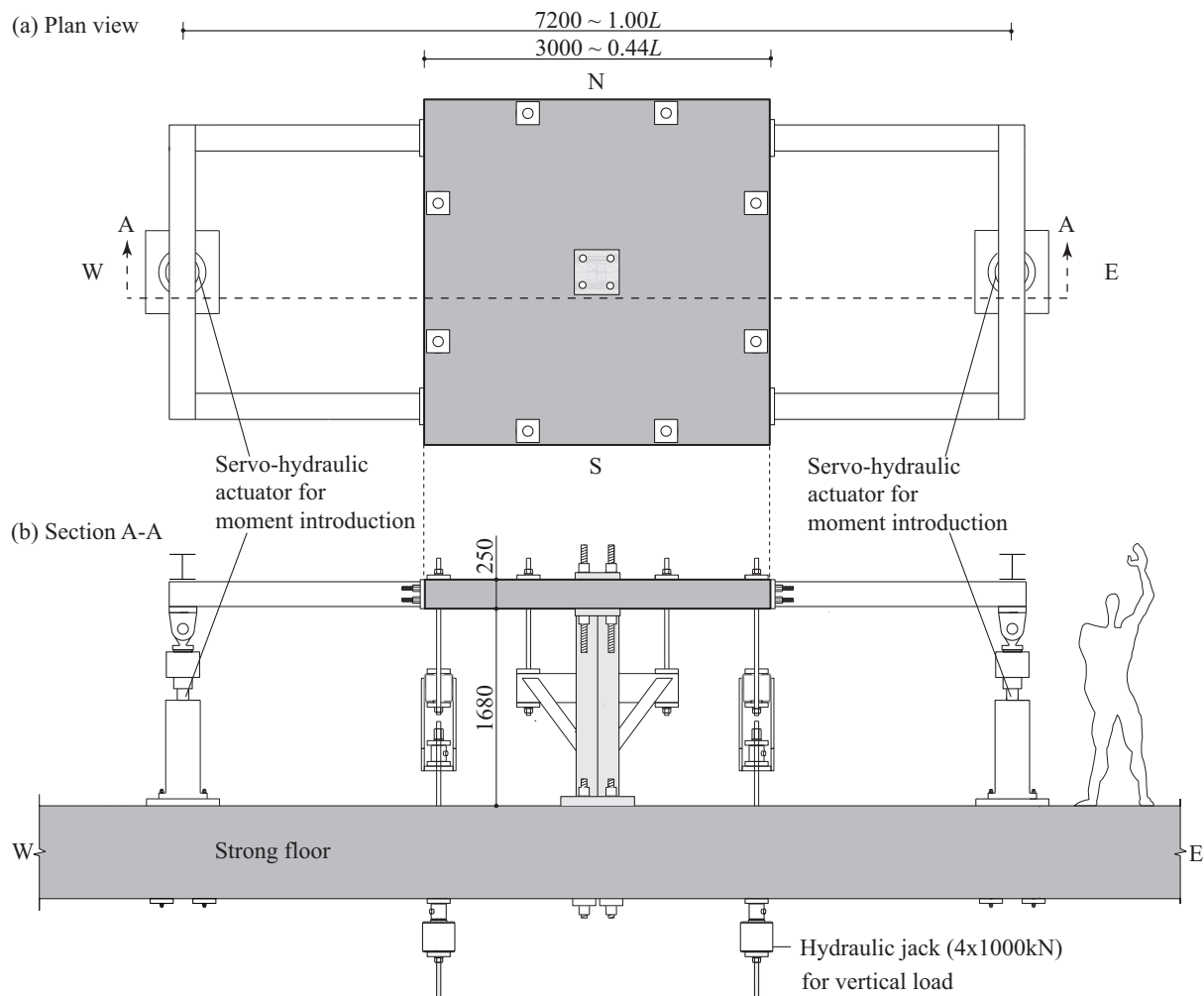
Figure 3.2 – Drawing of the setup (dimensions in mm): (a) plan view and (b) section A-A.

The column consisted of a welded steel profile and was clamped to the strong floor. Before the zero measurements, the slab was clamped down onto the column by means of four threaded bars Ø50 mm. They were each post-tensioned to a force of 1.2 MN in order to limit separation of the slab-column interface. Prestressing of the slab-column connection is necessary for setup (b) to provide stability to the system [Haw89,Isl76]. Use of steel instead of RC does not affect the behaviour of the connection as in both cases the column is designed to remain elastic during the test [Sta05]. As long as failure occurs outside the threaded bar-reinforced region, it is not expected that this region affects the behaviour of the specimen [Bin05].

The vertical load was applied using four hydraulic jacks, each one connected to a steel beam that distributed the load to two points on the slab surface. Its magnitude was kept constant by controlling the oil pressure in the vertical loading jacks. The vertical loads were applied at a radius of 1.504 m, which corresponds to $0.22L$, i.e. the radius where the radial moment of an elastic homogenous slab subjected to a uniformly distributed vertical load is zero. These vertical loads modelled all superimposed loads and the gravity loads of the slab part that was not included in the test setup (0.22-$0.50L$).

The effects of seismically induced drifts were simulated by applying two equal and opposite vertical forces by means of two servo-hydraulic actuators (Fig. 3.2). The lever arm of the force couple was increased from 6.8 m, which corresponds to the bay length of the prototype building, to 7.2 m due to laboratory constraints. The actuators were connected to steel beams that were in turn connected to the slab. Since the forces applied by the two servo-hydraulic actuators were equal and opposite, the shear force applied to the slab-column connection remained constant.

In real structures subjected to drifts, horizontal forces are transferred from the slab to the column combined with vertical shear. However, the column of the adopted setup is subjected to a constant moment along the height, but since the horizontal forces are transmitted in the flexural compression zone, their omission should not significantly affect the experimental results.

For the quasi-static monotonic tests, the forces applied by the servo-hydraulic actuators were monotonically increased until failure. For the quasi-static cyclic tests, rotation cycles of increasing amplitude were applied. The monitoring of the slab rotation was performed using inclinometers that were installed on the east and west slab edge (ψ_{max} and ψ_{min}). To obtain the slab-column connection rotation due to slab deformation alone (ψ_{scc}), the rotation due to column deformation and possible separation of the slab-column interface was measured using rotation readings at the middle of the top surface of the slab (ψ_{col}) and then subtracted from the measured slab rotation:

$$\psi_{scc} = \frac{\psi_{max} - \psi_{min}}{2} - \psi_{col} \tag{3.1}$$

The slab edges were reinforced with additional bars to account for the part of the slab that is not represented by the test setup and to connect the slab to the steel beams for the moment application. It will be shown in the following section that this additional reinforcement was crucial in order to obtain a good comparison between the moment-rotation relationship of the prototype building and that of the test unit.
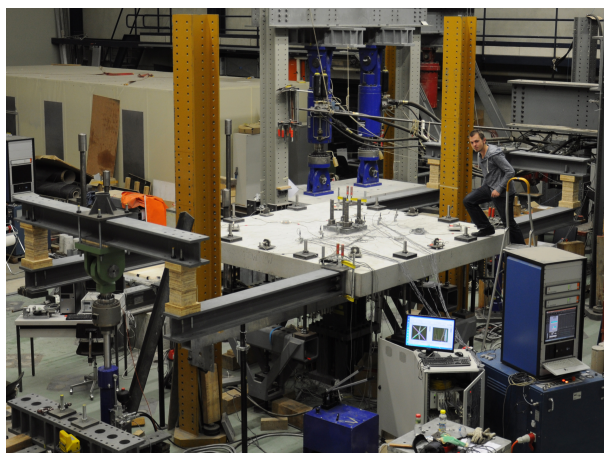
Figure 3.3 – Slab specimen in test setup.

The main differences between the chosen setup and setup (a) are related to the introduction of vertical loads and unbalanced moment as well as the boundary conditions. For the proposed setup the vertical loads are introduced in the slab perimeter whereas for setup (a) they are introduced in the column. Likewise, the kinematic boundary conditions of the two configurations are different, the slab being clamped to the column for the adopted setup and simply supported on the slab perimeter for setup (a). Moreover, for setup (a) the unbalanced moment is introduced by an eccentric vertical whereas for setup (b)$_{\mathrm{mod}}$ the unbalanced moment is introduced by a force couple (Fig. 3.2).

Setup (b) is the configuration which is most similar to setup (b)$_{\mathrm{mod}}$. The only differences lie in the simulation of the unbalanced moment and the reinforcement pattern. Setup (b) can simulate increasing moment both under constant eccentricity or constant vertical load whereas setup (b)$_{\mathrm{mod}}$ can only simulate increasing moment under constant vertical load. For the reinforcement pattern of the chosen setup, the strips with additional reinforcement that are arranged in the edges parallel to the direction of excitation account for the slab portion that is not modelled (outside $r = 0.22L$). On the other hand, since the reinforcement pattern of setup (b) is orthotropic the slab region outside $r = 0.22L$ cannot be accounted for but the reinforcement placing is significantly easier, in particular for relatively thin slabs.

The differences of setup (b)$_\text{mod}$ comparing to setup (c) can be distinguished in the following four categories: (a) regarding the boundary conditions, for setup (c) the slab is simply supported at its perimeter and the column is pinned at its base whereas for the proposed configuration the slab is free at its perimeter and clamped to the column at their interface, (b) the slab is modelled until midspan ($r = 0.50L$) for setup (c) whereas for setup (b)$_\text{mod}$ is modelled until $r = 0.22L$, (c) the seismically-induced drift is introduced through horizontal load at column midheight for setup (c) whereas for the chosen setup it is introduced through vertical loads at slab midspan, and (d) the monitoring parameter of cyclic tests is for setup (c) the horizontal displacement at column midheight whereas for the proposed setup is the connection rotation, using measurements on the slab surface.

3.3 Response comparison between proposed test setups and prototype building

Since there are only very few tests on subassemblies and flat slab buildings (§2.1.1), mechanical models have to be validated mainly against tests on isolated slab-column connections. For this reason, it is important to understand the approximations related to the testing of such isolated connections. To do so, the slab-column connection of the prototype building (Section 3.1) is analysed and its moment-slab rotation relationship is used as benchmark for the curves obtained from different experimental setups. These comprise setup configurations of previous experimental campaigns (§2.1.1) and the adapted setup configuration that is used in the experimental study presented in this chapter (Section 3.2).

The setup configurations presented in Chapter 2 (§2.1.1) and Section 3.2 are simplifications of the boundary conditions imposed on a flat slab in an actual building subjected to seismic excitation. The influence of the boundary conditions on the deformation capacity of slab-column connections has been demonstrated by previous numerical studies, under both vertical load [Ein15] and combined vertical load and transferred moment [Par06]. It is therefore essential to evaluate the capacity of each setup to reproduce the behaviour of slab-column connections of the prototype building (presented in Section 3.1). To this end, the response of an internal slab-column connection of the prototype building and the response of isolated slab-column connections tested in setups (b), (c) and the chosen (b)$_\text{mod}$ were simulated using the program SAP2000 [CSI14]. As discussed in Chapter 2, setup (a) is not suitable for reproducing the seismic response of slab-column connections. Setup (a) was therefore only used for the validation of the numerical model but not included in the evaluation of test setups. The slab was modelled using non-linear layered shell elements with a Mindlin-Reissner formulation to include transverse shear deformations. Only elastic shear deformations were included; the model could therefore only predict the non-linear flexural response. The layered shell formulation adopted for the numerical investigation uses smeared reinforcement. Fourteen integration points were used over the height of the slab. The unconfined concrete model by Mander et al. [Man88] and the model by Park and Paulay [Par75] were used for modelling the non-linear behaviour of concrete and reinforcing steel, respectively. The tensile strength of the concrete was assumed to be zero.

For evaluating the seismic performance of buildings in terms of displacements, structural engineers use typically the interstorey drift ψ_{st}, i.e., the relative horizontal displacement between two adjacent floors divided by the storey height. In structural systems of flat slabs and columns both the deformation of the slab and the column contribute to the interstorey drift:

$$\psi_{st} = \psi_{col} + \psi_{slab} \tag{3.2}$$

where ψ_{col} and ψ_{slab} are respectively the contributions of column deformation and slab deformation to the interstorey drift. Since the present study focuses on the contribution of slab deformation to the interstorey drift, the columns were modelled as rigid ($\psi_{col} = 0$).

In laboratory tests, often only the hogging moment area under gravity loads is represented. It is usually assumed that the limit of this area is located at a distance of $r = 0.22L$ from the column axis,

where L is the midpan-to-midspan distance. In reality, the slab region inside and outside $r = 0.22L$ are contributing to the rotation due to slab deformation:

$$\psi_{slab} = \psi_{scc} + \psi_{os} \tag{3.3}$$

where ψ_{scc} and ψ_{os} are respectively the rotation due to deformation of the slab-column connection (slab region inside $0.22L$) and the rotation due to the deformation of the outer portion of the slab (outside $r = 0.22L$ up to $r = 0.50L$).

3.3.1 Verification of the numerical method

To verify the numerical model, slab specimens tested in previous experimental campaigns were analysed and numerical results compared against experimental results. More details on the properties of the analysed specimens can be found in Chapter 2 (§2.1.2) and in Appendix A. Figure 3.4 shows the comparisons of the experimental and calculated curves for tests using setups (a) and (b) [Kru99, Isl76] while Figure 3.5 shows the same for tests using setup (c) [Pan89, Rob02, Tia08]. For each test campaign, the contribution of the slab deformation to the interstorey drift was measured differently and the comparison uses the deformation quantity reported. This is the central deflection for test units P16A and P32A by Krüger [Kru99], who used setup (a) (Fig. 3.4a, b). These test units were chosen because of their high slenderness. Islam and Park [Isl76], who used setup (b) (Fig. 3.4c) for the test IP2, reported the slab-column connection rotation ψ_{scc}. It was computed from the deflections of the two slab edges orthogonal to the lateral load. Pan and Moehle [Pan89], Robertson et al. [Rob02] and Tian et al. [Tia08] used setup (c) (Fig. 3.5). For all these tests the deformations were described using the slab-column connection rotation, computed as the horizontal displacement of the rigid column divided by the storey height. Test units AP1 [Pan89] and 1C [Rob02] were chosen since they represent cases with limited and increased deformation capacity, respectively, and similar reinforcement ratio with the prototype building. Test unit L0.5 [Tia08] was chosen since its column size is very close to the one adopted for the prototype building and the experimental campaign. The reinforcement layers of all test units were modelled explicitly both over the thickness (four reinforcement layers) and in plan to account for eventual reinforcement concentration within the column strip (e.g. [Pan89, Rob02, Tia08]).
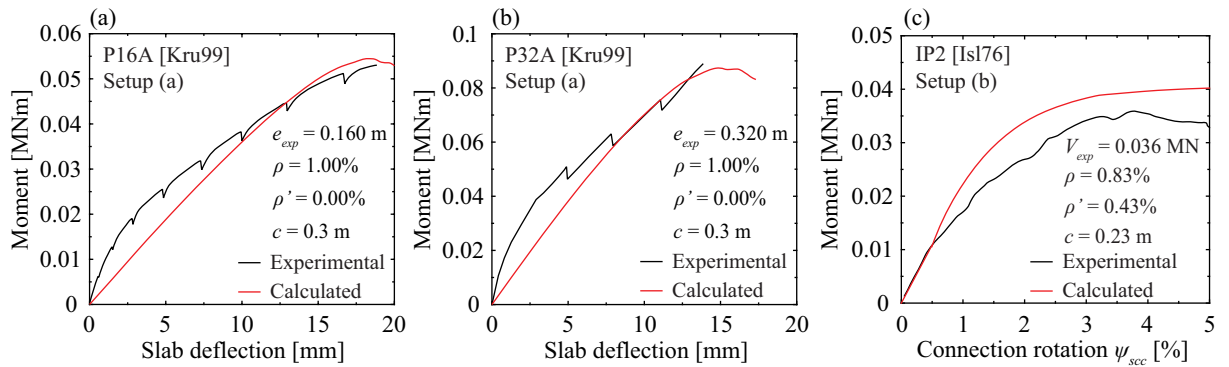
Figure 3.4 – Comparison of test results and numerical analyses for setup (a) and setup (b).
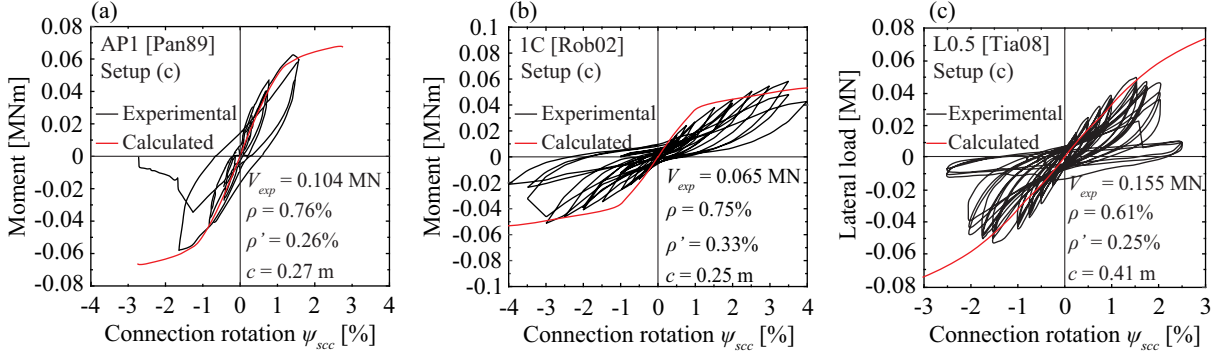
Figure 3.5 – Comparison of test results and numerical analyses for setup (c).

It should be noted that the finite element model captures only the non-linear flexural response but cannot account for premature punching failure of the slab-column connections that can occur at a moment substantially lower than the yield moment. After punching failure, the shear deformations become significant, which is not accounted for in the numerical simulation. Finite element modelling that accounts for punching failure of the slab-column connection would necessitate the use of brick elements for the modelling of the slab. On the other hand, shell elements do not explicitly incorporate features to account for such type of failure. For this reason, the comparison of numerical and experimental response focuses on the prediction up to the experimental peak strength. A constant shear retention factor $\beta = 0.1$ was chosen for the shear stiffness reduction before and after cracking since the focus was on the ultimate response rather than the initial response. Figures 3.4 and 3.5 show that, although the loading and boundary conditions of the specimens differed substantially between the different setups (2.1.1), the numerical analysis predicted the moment-deformation response between cracking and peak load rather well (note that the aim of the simulation was not to predict the ultimate strength but the moment-rotation response).

3.3.2 Moment-rotation response comparison between prototype building and test setups

To simulate the behaviour of an internal slab-column connection in the prototype building (Fig. 3.1), an element L x L with continuity boundary conditions (Fig. 3.6a) was analysed. The moment at the slab-column connection was inserted through incrementally increasing lateral loads at the top of the column stub while monitoring the rotation at the slab-column node. A uniform gravity pressure q_V was applied at the slab surface to simulate the vertical loads specified in Section 3.1. The column member was modelled as rigid and was pinned at the base ($\delta_{x,y,z} = 0$) and free at the top. The slab edges parallel to the x axis were restrained against rotation about the same axis ($\theta_x = 0$) whereas the other edges were constrained to have the same vertical displacement (δ_z) and rotation about the y axis (θ_y) as shown in Figure 3.6a. Since the column is rigid ($\psi_{col} = 0$, Fig. 3.6a), the slab rotation ($\psi_{scc} + \psi_{os}$) is equal to the interstorey drift ψ_{st}. The geometric and material properties as well as the slab reinforcement of the element L x L with continuity boundary conditions are specified in Section 3.1. For consistency reasons, the models representing the test units for setups (b)$_{\text{mod}}$, (b) and (c) were assigned the same material properties and reinforcement ratios. The slab dimensions of setups (b) and (b)$_{\text{mod}}$ were $0.44L$ and that of setup (c) $1.0L$.

The numerical model for setup (b)$_{\text{mod}}$ is shown in Figure 3.6b. The moment at the slab-column connection was introduced through a couple of incrementally increasing vertical forces with amplitude F_V applied to steel members that were in turn connected to the slab edges. The steel members were modelled using elastic beam elements. The model of setup (b)$_{\text{mod}}$ included also the additional reinforcement at the slab edges parallel to the x-axis (see Section 3.2). The numerical model for setup (b) is similar to the one of the chosen setup, the only differences being the absence of the additional reinforcement along the slab edges and the smaller lever arm of the applied vertical force couple ($0.44L$

vs $1.0L$). Since for these two setups the column rotation was zero, the analysis result is shown in terms of the slab-column connection rotation computed from the deflections at a distance of $0.22L$ from the column centre (ψ_{scc}), which corresponds to the slab edge for these setup configurations. The same definition will be used for the presentation of the test results of the experimental campaign.

The numerical model of setup (c) is similar to the numerical model established to simulate an internal slab-column connection of the prototype building (Fig. 3.6a). The only differences lie in the boundary conditions. For setup (c), the edges parallel to the y-axis were restrained only against vertical displacement whereas the edges parallel to the x-axis were unrestrained. The connection rotation for setup (c) and the continuous flat slab was computed as for setups (b) and (b)$_{\mathrm{mod}}$.
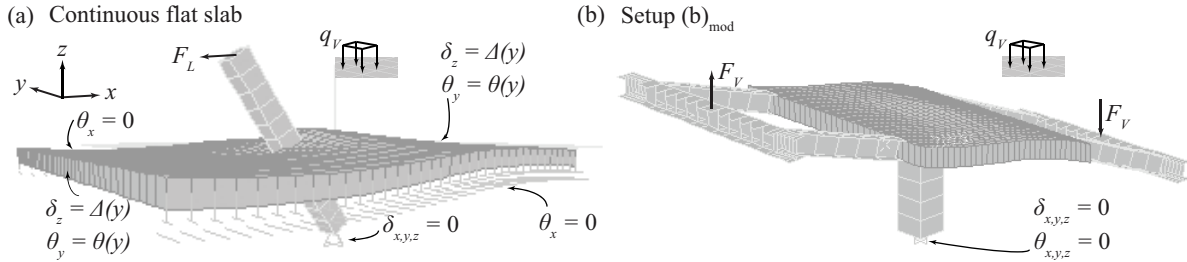
Figure 3.6 – Deformed shape of the established numerical models: (a) element L x L with continuity boundary conditions, and (b) setup (b)$_{\mathrm{mod}}$.

The influence of the adopted setup on the moment-rotation relationship of the slab-column connection is shown in Figure 3.7. Since punching failure is not captured by the numerical analysis, the comparison should be based on the moment-rotation relationship up to the moment capacity predictions according to ACI-318 [ACI14] and Eurocode 2 [Eur04] (dashed lines in Figs. 3.7a and b). Modelling the slab only until $0.22L$ (setup (b) and setup (b)$_{\mathrm{mod}}$) results in a softer flexural behaviour than the continuous slab; this has already been demonstrated for the case of vertical loads alone [Ein15]. The difference in stiffness beween setup (b) and setup (b)$_{\mathrm{mod}}$ results from the additional edge reinforcement that is provided in setup (b)$_{\mathrm{mod}}$. This effect is smaller for larger reinforcement ratios (Fig. 3.7b) since the edge reinforcement was not scaled with reinforcement content. Comparison between the continuous flat slab (Fig. 3.6a) and the setup (c) shows that for the same specimen size ($1.0L$), the boundary conditions significantly affect the moment-rotation response: The continuous flat slab is significantly stiffer than the simply supported slab (setup (c)). Figure 3.7 shows that for the two reinforcement ratios that were investigated within the experimental campaign, setup (b)$_{\mathrm{mod}}$ yields from all investigated setups the best estimate of the stiffness of the slab-column connection of the prototype building.
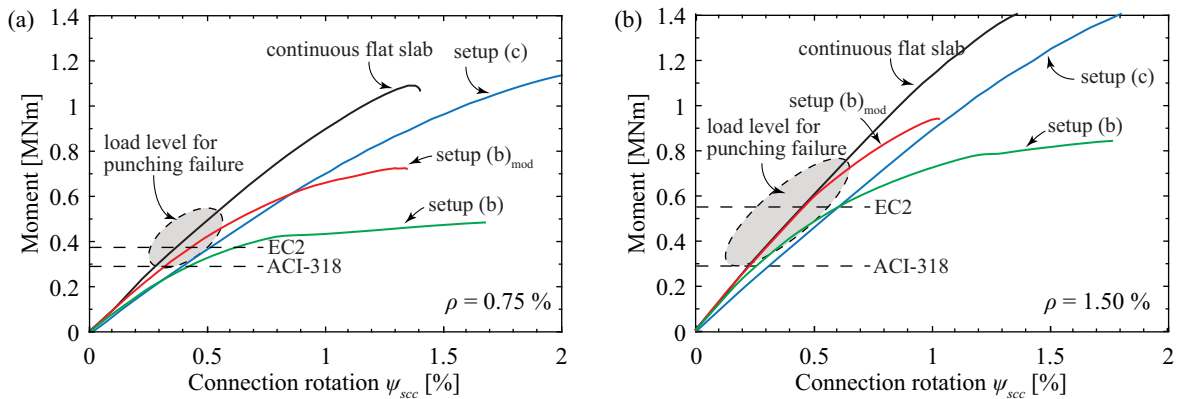
Figure 3.7 – Influence of the adopted setup on the estimation of the moment – rotation response of the continuous flat slab for flexural reinforcement ratio equal to: (a) 0.75%, and (b) 1.50%.

3.4   Specimen properties

Table 3.1 summarises the geometric and material properties as well as the value of the loading parameter. The dimensions of each isolated specimen were 3.00 m x 3.00 m (B x B) and the slab thickness was 250 mm. The column size was equal to 390 mm x 390 mm (c x c) for all tested slabs. Three different types of loading are distinguished: "V" stands for the application of symmetrical vertical loads, whereas "M" and "C" represent the introduction of monotonically and cyclically increasing unbalanced moments, respectively. The slab's top reinforcement ρ consisted of 16 mm deformed bars per direction with 125 mm spacing for slabs with 0.75% nominal reinforcement ratio, whereas for 1.50% nominal reinforcement ratio 20 mm deformed bars were spaced at 100 mm in each direction. For the bottom mat 10 mm and 14 mm deformed bars were spaced at 100 mm in each direction for slabs with $\rho' = 0.38\%$ and 0.75% nominal bottom reinforcement ratio, respectively. The reinforcement layer with the biggest lever arm was positioned perpendicularly to the moment vector for both top and bottom mat. The effective depth d for each slab, taken as the average value for both reinforcement directions until the rebar centre, was measured a posteriori after saw cuts had been performed along the slab thickness. The nominal concrete cover was 20 mm for both top and bottom mat and the maximum aggregate size d_g was 16 mm. The compressive strength of concrete f_c (determined by compression tests on concrete cylinders 160 x 320 mm at the day of testing) and the mean yield stress of reinforcing steel f_y (average values measured on 0.90 m bars) are also reported in Table 3.1. The fourth column gives the normalised shear force:

$$\nu = \frac{V_{test}}{b_o \, d \, \sqrt{f_c}} \tag{3.4}$$

where b_o is the length of the control perimeter situated at a distance of $d/2$ from the column face, calculated with rounded corners [Fib11]. It should be noted that the gravity shear ratio (GSR) defined according to ACI-318 [ACI14] is obtained when the normalised shear force ν according to Eq. (3.4) (expressed in $\sqrt{\text{MPa}}$) is multiplied by three (expressed in SI units). For tests PD7 and PD9, which were subjected to increasing vertical loads alone ("V"), V_{test} corresponds to the maximum applied force which caused punching of the slab. For the other tests ("V+M", "V+C"), V_{test} was kept constant throughout the test and is the vertical load that was applied before applying the seismic moment. The fifth column gives the ratio of the applied normalised shear force ν to the normalised shear force ν_{ref} of the reference slab ("V").

Table 3.1 – Summary of properties of interior slab-column specimens tested within the present research (ordered by loading type, ν, and reinforcement ratio)

Loading type	Slab	V_{test} [MN]	ν [$\sqrt{\text{MPa}}$]	ν/ν_{ref} [-]	f_c [MPa]	d_g [mm]	f_y [MPa]	ρ [%]	ρ' [%]	d [mm]	B [m]
V	PD7	0.983	0.359	1.00	39.2	16	507	0.80	0.35	200	3.00
V	PD9	1.040	0.419	1.00	34.3	16	593	1.61	0.74	195	3.00
V+M	PD1	0.253	0.092	0.26	37.9	16	559	0.79	0.35	204	3.00
V+M	PD4	0.376	0.137	0.38	39.0	16	507	0.80	0.35	201	3.00
V+M	PD5	0.517	0.195	0.54	37.5	16	507	0.81	0.35	198	3.00
V+M	PD3	0.734	0.288	0.80	34.9	16	558	0.81	0.34	198	3.00
V+M	PD12	0.517	0.205	0.49	35.5	16	546	1.61	0.72	195	3.00
V+M	PD10	0.734	0.301	0.72	32.3	16	593	1.60	0.72	197	3.00
V+C	PD8	0.376	0.152	0.42	32.7	16	575	0.81	0.29	198	3.00
V+C	PD6	0.517	0.192	0.53	38.3	16	507	0.81	0.30	199	3.00
V+C	PD2	0.734	0.288	0.80	36.9	16	558	0.81	0.34	198	3.00
V+C	PD13	0.517	0.201	0.48	36.5	16	546	1.61	0.72	196	3.00
V+C	PD11	0.734	0.299	0.71	33.1	16	593	1.60	0.71	196	3.00

The vertical loads that were applied to slabs subjected to combined vertical load and unbalanced moment were chosen based on the predictions of several codes of practice. Figure 3.8 shows the design vertical loads for Ultimate Limit State (ULS) according to ACI-318 [ACI14] and fib-Model Code 2010 [Fib11], as well as the strength predictions of the Critical Shear Crack Theory (CSCT) [Mut08] for different reinforcement ratios (continuous lines). Moreover, the design vertical loads for the Serviceability Limit State (SLS) according to ACI-318 [ACI14] and fib-Model Code 2010 [Fib11] are also represented in the same graph (dashed lines). The normalised experimental punching strengths for the reference tests (see Table 3.1) for both $\rho = 0.75\%$ and $\rho = 1.50\%$ are shown in the same graph (diamond markers). As can be seen, the CSCT predicts very accurately the experimental punching strength of the reference tests for both reinforcement ratios. Based on the graph of Figure 3.8 the vertical load levels of the tests under combined vertical load and unbalanced moment were chosen for both monotonic loading conditions (circular markers) and cyclic loading conditions (x markers).
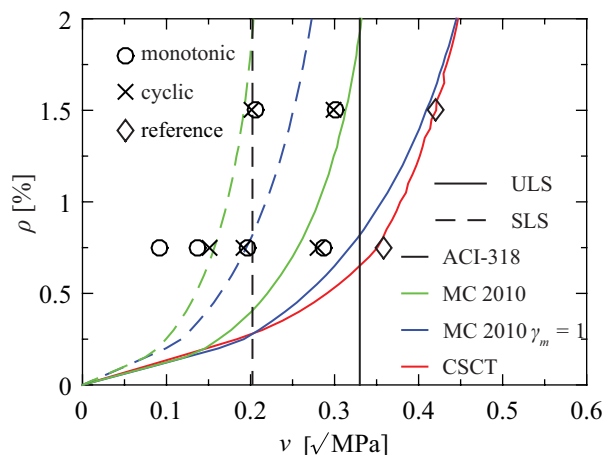
Figure 3.8 – Design against vertical loads according to fib-Model Code 2010 [Fib11] and ACI-318 [ACI14] and punching strength preditions according to CSCT [Mut08].

For $\rho = 0.75\%$, the slab pair loaded at relatively high vertical loads ($\nu = 0.29$) was tested to assess the moment strength and the deformation capacity of slab-column connections loaded at the ULS gravity loads according to fib-Model Code 2010 [Fib11]. Although such a choice of vertical loads during a seismic excitation is rather overestimating, an eventual change of building use may increase the vertical loads acting on the slab-column connections compared to the initial design. On the other hand, the test performed at very low vertical loads ($\nu = 0.09$) is rather representative of building usage change resulting in decrease of the gravity-induced shear force on the slab-column connection. For the same reinforcement ratio the slab pairs loaded at intermediate vertical loads were tested to assess the moment strength and deformation capacity of slab-column connections designed for gravity loads at the SLS according to the same standard ($\nu = 0.14$ and 0.19 as lower-bound and upper-bound limits, respectively). These cases are valuable also from the engineering practice point of view.

For $\rho = 1.50\%$, the slab pairs loaded at $\nu = 0.30$ and 0.20 are representative of slab-column connections loaded at the ULS and SLS, respectively, if the design is performed according to fib-Model Code 2010 [Fib11] with material partial factors γ_m. The lowest vertical load level ($\nu = 0.20$) is also representative of the shear force corresponding to the SLS according to ACI-318 [ACI14].

3.5 Instrumentation

The bottom face of all specimens was instrumented with 26 displacement transducers and 16 strain gauges to measure slab deflections and concrete strains along the axis perpendicular to the moment vector direction (EW direction – see Fig. 3.9b). On the top face, nine inclinometers recorded slab

rotations in different directions (Fig. 3.9b). One of these inclinometers was positioned on the middle of the specimen to measure the rotation of the slab due to column deformation and a possible slab-column separation. The inclinometers that were monitoring the quasi-static cyclic tests are shown in Figure 3.9c. In addition, strain gauges were attached on selected rebars of the top and bottom mat in the EW direction to measure strains at various locations. Since the present chapter focuses on the global response, only the results of the inclinometers are used in the following.
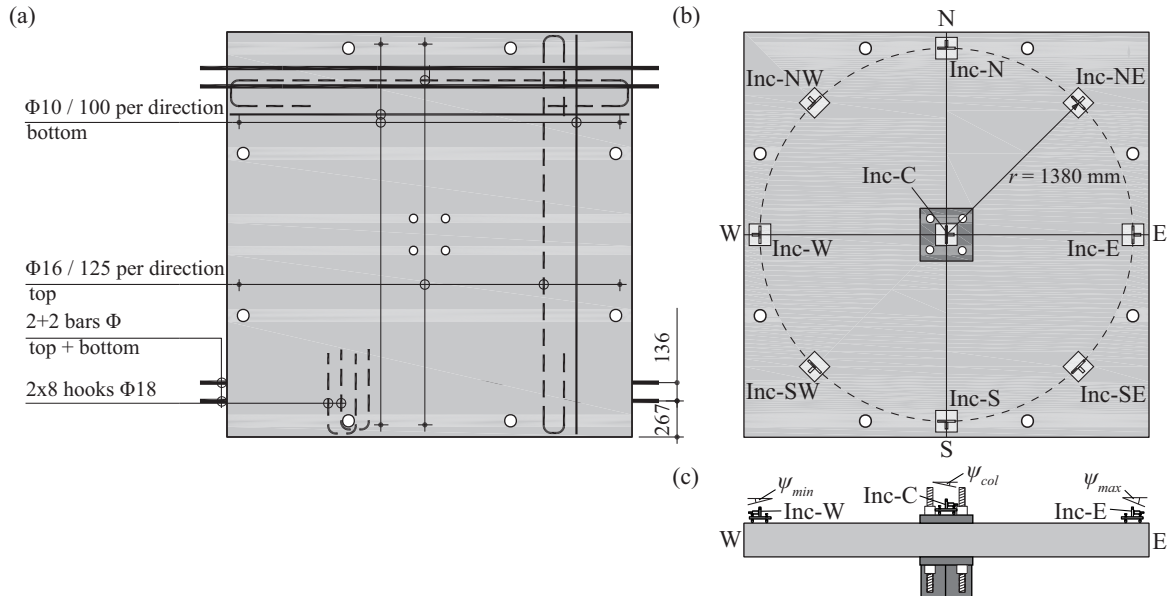
Figure 3.9 – (a) Reinforcement plan for slabs with $\rho = 0.75\%$ (dimensions in mm), (b) position of inclinometers for measuring slab rotations and middle steel plate rotation, and (c) elevation view of the inclinometers monitoring the cyclic tests.

3.6 Loading procedure

After the zero measurements, the vertical load was applied with a velocity of 20 kN/min at eight points arranged on a radius of 1.504 m ($= 0.22L$). The slab was charged by means of four hydraulic jacks, which applied each the same load on two points on the slab (Fig. 3.2). The unbalanced moment was introduced by the two servo-controlled hydraulic actuators, of which the master actuator was displacement-controlled and the other force-controlled. For the specimens subjected to constant vertical load and monotonically increasing moment (V+M – Table 3.1), the master actuator imposed a monotonically increasing downward displacement with a velocity of 0.2 mm/s until failure. The other actuator was imposing an upward displacement and was force-controlled applying the same force amplitude as the master actuator but in opposite direction. In this way, a force couple was introduced to the slab-column connection and the connection rotation was monotonically increasing. For the specimens subjected to a constant vertical load and a cyclic moment (V+C – Table 3.1), the displacement-controlled and force-controlled actuators were alternated at each half cycle with the same displacement velocity of the master actuator as for monotonic tests. The actuator applying the downward force was always the displacement-controlled master actuator. The control parameter was the slab-column connection rotation, defined as the mean value of the inclinometers west and east minus the value of the column rotation (measured using an inclinometer on the top plate, Fig. 3.9b). Two cycles were applied per rotation level. Since a minimum number of eight cycles before failure were desired, a different loading protocol was followed for tests with increased deformation capacity (Fig. 3.10a) and limited deformation capacity (Fig. 3.10b). Throughout the moment application, the vertical load was manually controlled to remain constant.
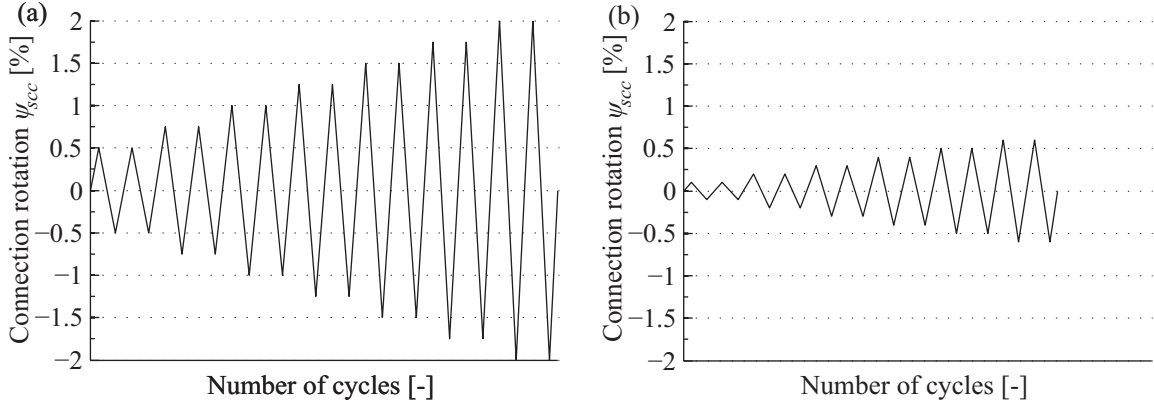
Figure 3.10 – Displacement routine applied for cyclic testing of specimens with (a) increased deformation capacity (PD6, PD8 and PD13), and (b) limited deformation capacity (PD2 and PD11)

3.7 Results

The normalised vertical load-slab rotation curves for the reference tests PD7 and PD9 (without unbalanced moments) are shown in Fig. 3.11. Rotation ψ_v is the average of rotation measurements on the east and west side of the slab. Fig. 3.11 shows also the vertical load levels applied to those slabs that were also subjected to an unbalanced moment.
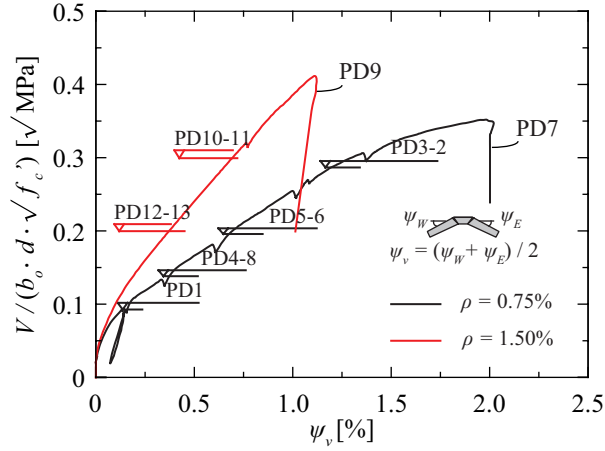
Figure 3.11 – Vertical load levels of tested slab specimens with respect to reference tests (concentric punching).

Table 3.2 summarises for the slabs that were subjected to a vertical load and an unbalanced moment the obtained moment and slab-column connection rotation at peak load (M_{max} and $\psi_{scc.max}$, respectively), at loss of vertical load bearing capacity, referred to as ultimate (M_u and $\psi_{scc.u}$, respectively), as well as at 20% drop of unbalanced moment strength ($M_{80\%}$ and $\psi_{scc.80\%}$, respectively) for slabs with $M_{80\%}$ higher than M_u.

Table 3.2 – Summary of results of tests on slab-column specimens subjected to combined vertical load and moment

Slab	Loading type	Moment [kNm]			Slab-column connection rotation [%]		
		M_{max}	$M_{80\%}$	M_u	$\psi_{scc.max}$	$\psi_{scc.80\%}$	$\psi_{scc.u}$
PD1	V+M	525	-	503	*	-	*
PD3	V+M	200	-	177	0.45	-	0.60
PD4	V+M	527	-	458	2.01	-	2.44
PD5	V+M	462	-	435	2.19	-	2.39
PD10	V+M	290	-	285	0.49	-	0.52
PD12	V+M	469	-	461	1.21	-	1.27
PD2	V+C	196	157	124	0.36	0.37	0.42
PD6	V+C	372	297	287	0.86	0.84	0.84
PD8	V+C	384	307	307	1.30	1.66	1.66
PD11	V+C	286	-	231	0.43	-	0.50
PD13	V+C	410	-	345	0.86	-	0.88

*   inconsistent rotation measurement

Fig. 3.12 shows the interaction diagrams to facilitate the comparisons between the performed tests in terms of normalised moment resistance ($M_{max}/b_o\, d^2\, \sqrt{f_c}$ [$\sqrt{\text{MPa}}$]) and corresponding slab-column connection rotation ($\psi_{scc.max}$ – Table 3.2).
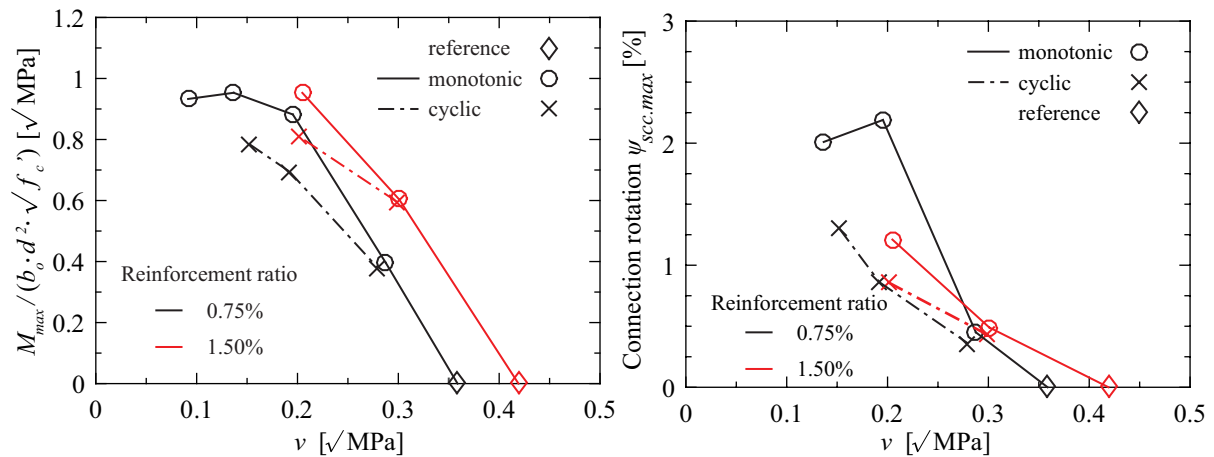
Figure 3.12 – Interaction diagrams resulting from the performed tests: (a) Moment capacity, and (b) corresponding connection rotation.

The measured relationships between the introduced moment, slab-column connection rotation and maximum and minimum local slab rotations for the slabs tested to investigate the influence of gravity load and reinforcement ratio are shown in Figure 3.13. A discussion of these effects follows in Section 3.8.
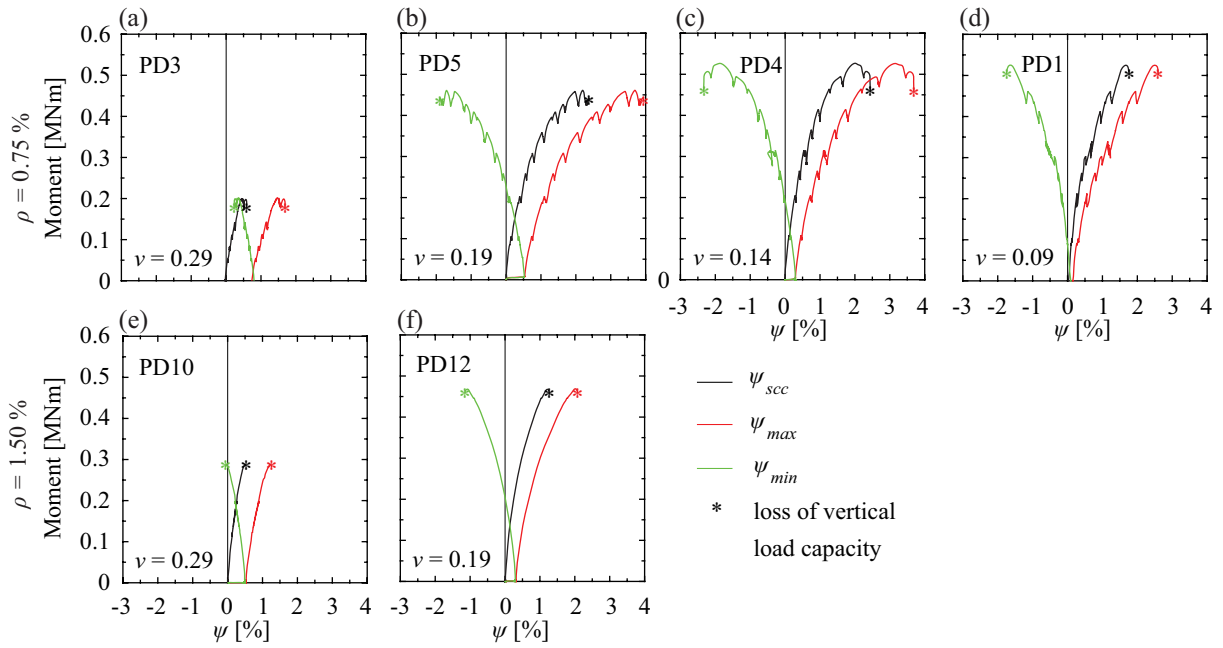
Figure 3.13 – Relationship between introduced moment, connection rotation and maximum and minimum local slab rotations for monotonic tests at different reinforcement ratios and vertical loads (ν [$\sqrt{\text{MPa}}$] according to Eq. (3.4)).

The comparisons of the moment-connection rotation response for the slabs tested to investigate the cyclic loading effect are shown in Figure 3.14 for all three vertical load levels that were considered and for both flexural reinforcement ratios.

Figure 3.14 – Moment–connection rotation relationship for cyclic and monotonic tests at different reinforcement ratios and vertical loads (ν [$\sqrt{\text{MPa}}$] according to Eq. (3.4)).

The cracking pattern of the top slab surface is illustrated in Figures 3.15 and 3.16 for selected cases of slabs with $\rho = 0.75\%$ and 1.50%, respectively. Cracks shown in black were drawn after the application of vertical loads. Cracks shown in red were caused by the unbalanced moment and were drawn after the end of each test. The slab half where the shear force due to the unbalanced moment acts downwards

(i.e. in the direction of the vertical forces) is referred to as hogging slab half. The other slab half where the shear force due to unbalanced moment acts opposite to the shear force due to the vertical loads, is denoted as sagging slab half. The cracking pattern of all tested slabs can be found in Appendix B. In Figures 3.15 – 3.19, the hogging slab half is represented by positive x values. Moreover, since the y axis ($x = 0$) is parallel to the vector of the applied moment, the y axis will be subsequently referred to as bending axis. All specimens failed due to punching of the slab. For the reference specimens, which had been subjected to gravity loads only, the punching was concentric; for the specimens subjected to combined gravity loads and unbalanced moment, the punching-shear-related damage concentrated in the hogging slab half. This concentration was naturally stronger for monotonic tests than for cyclic tests.
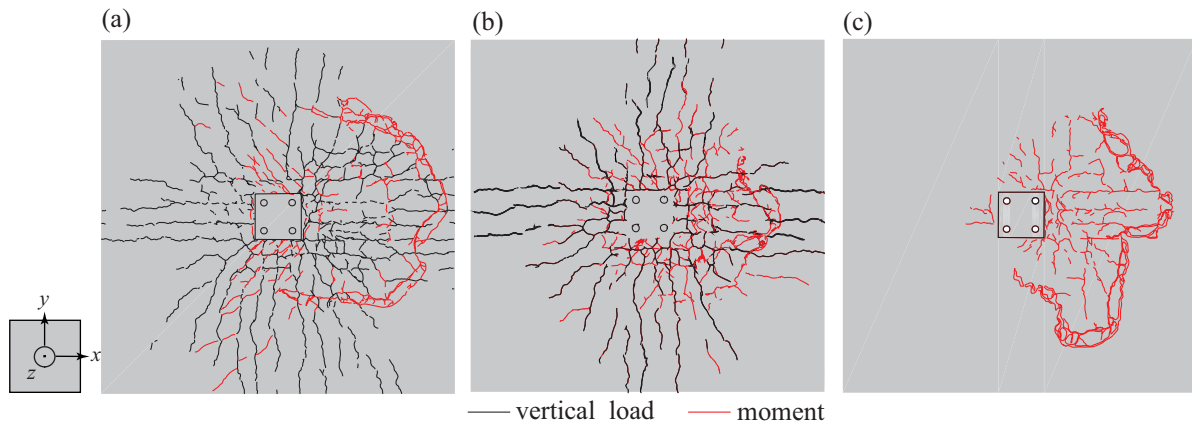
Figure 3.15 – Top surface cracking pattern for tested slabs with 0.75% flexural reinforcement ratio: (a) $\nu = 0.14$ $\sqrt{MPa}$ (monotonic loading), (b) $\nu = 0.14$ $\sqrt{MPa}$ (cyclic loading), and (c) $\nu = 0.09$ $\sqrt{MPa}$ (monotonic loading).
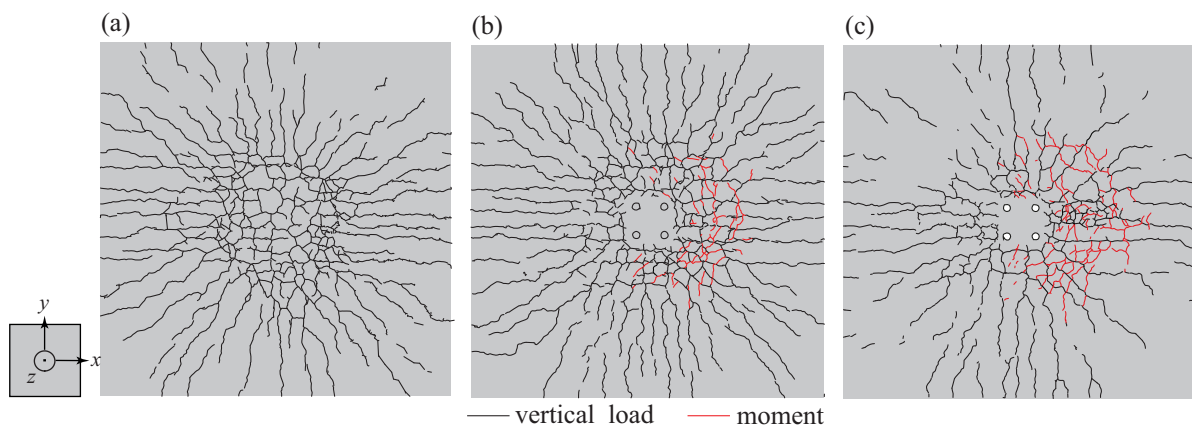
Figure 3.16 – Top surface cracking pattern for monotonically tested slabs with 1.50% flexural reinforcement ratio: (a) reference slab ($\nu = 0.42$ $\sqrt{MPa}$), (b) $\nu = 0.29$ $\sqrt{MPa}$, and (c) $\nu = 0.19$ $\sqrt{MPa}$.

To obtain information on the inclination of the shear crack at failure, saw cuts were performed after each test. The saw cuts show the surface perpendicular to the unbalanced moment vector (parallel to the x direction). They illustrate the effect of the gravity load (Fig. 3.17), the loading history (Fig. 3.18) and the reinforcement ratio (Fig. 3.19) on the crack angle. Note that PD11 ($\rho = 1.50\% - \nu = 0.29$ $\sqrt{MPa}$) was reloaded after a first drop in moment, which resulted in complete punching of the slab and provoked additional cracks over the slab thickness. These cracks are shown with grey colour in Figures 3.17, 3.18, and 3.19.
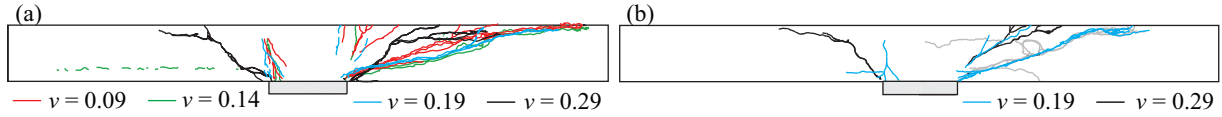
Figure 3.17 – Saw cut comparison for slabs tested under monotonically increasing moments to investigate the gravity load effect, with: (a) 0.75%, and (b) 1.50% reinforcement ratio.
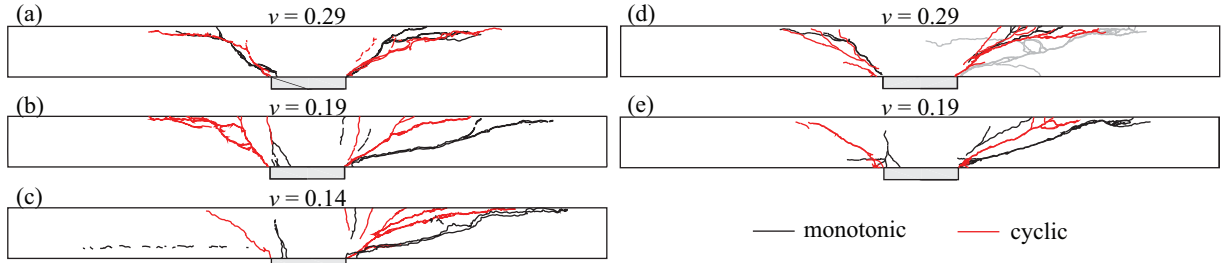
Figure 3.18 – Saw cut comparison for slabs tested under monotonically and cyclically increasing moments: (a) $\rho = 0.75\%$ – $\nu = 0.29$, (b) $\rho = 0.75\%$ – $\nu = 0.19$, (c) $\rho = 0.75\%$ – $\nu = 0.14$, (d) $\rho = 1.50\%$ – $\nu = 0.29$, and (e) $\rho = 1.50\%$ – $\nu = 0.19$.
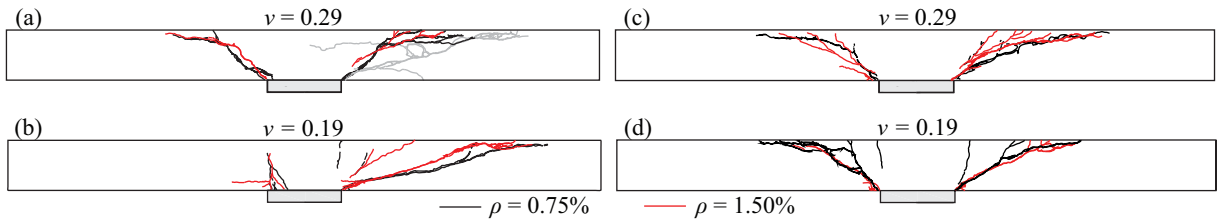
Figure 3.19 – Saw cut comparison for slabs with 0.75% and 1.50% reinforcement ratio under ν [$\sqrt{\text{MPa}}$] equal to (a) 0.29 (monotonic loading), (b) 0.19 (monotonic loading), (c) 0.29 (cyclic loading), and (d) 0.19 (cyclic loading).

Fig. 3.20 shows the slab rotations that were measured at peak moment at varying angles with regard to the bending axis ($\phi = 0$ and $\phi = \pi$) for the slabs subjected to monotonically increasing moments. As can be seen, the slab rotations follow approximately a sinusoidal law with ψ_{max} for $\phi = \pi/2$ and ψ_{min} for $\phi = 3\pi/2$.
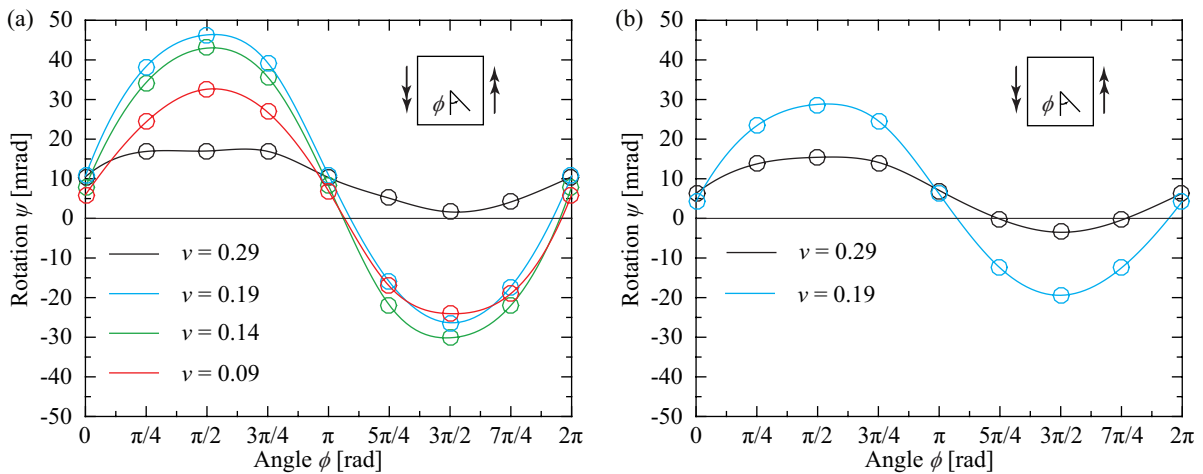
Figure 3.20 – Measured slab rotations at peak moment at varying angles from the bending axis ($\phi = 0$ and $\phi = \pi$) for slabs with: (a) 0.75% reinforcement ratio, and (b) 1.50% reinforcement ratio.

3.8   Discussion of the results

The discussion focuses on the influence of three factors on the seismic behaviour of slab-column connections, i.e., the influence of gravity loads, reinforcement ratio and loading history (monotonic vs cyclic). The first two factors are discussed with regard to the monotonic test results (§3.8.1 and 3.8.2). In the third subsection (§3.8.3), cyclic and monotonic test results are compared. For each factor the effect of the initial stiffness, the peak moment, the rotation capacity and the cracking pattern is discussed. The initial stiffness is defined as the secant stiffness up to 75% of the peak moment and the rotation capacity as the rotation at peak moment since punching failure occurs typically shortly after reaching the peak moment.

3.8.1   Gravity load effect

The effect of the gravity load on the stiffness, strength and deformation capacity of slab-column connections without shear reinforcement has been extensively investigated by [Pan89, Rob06, Bu09, Cho07]. The results of the present campaign are shown in Figure 3.21 and largely confirm previously observed trends. They provide, however, a more differentiated view with regard to the gravity load effect on the rotation capacity (see discussion below).
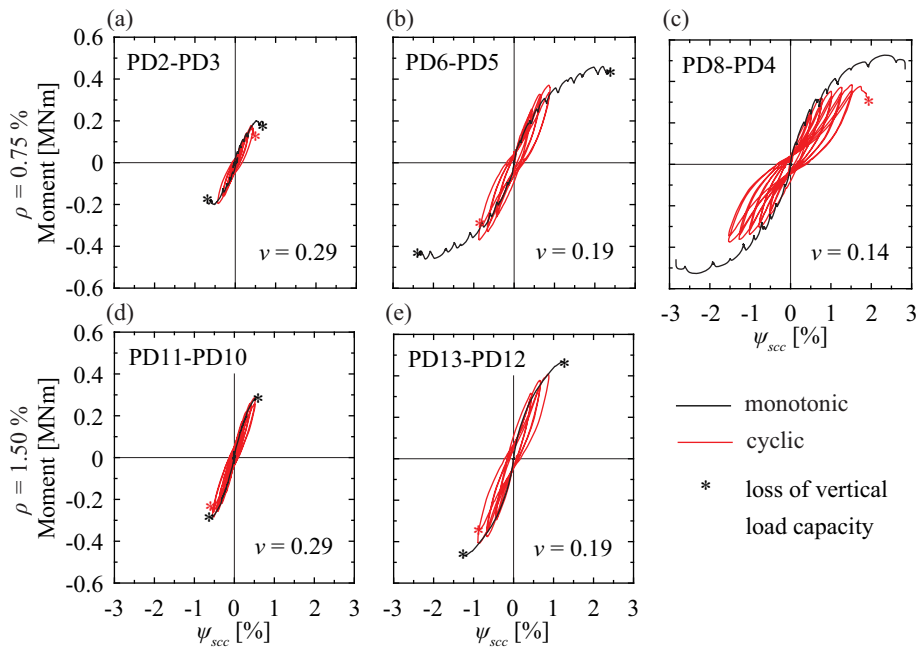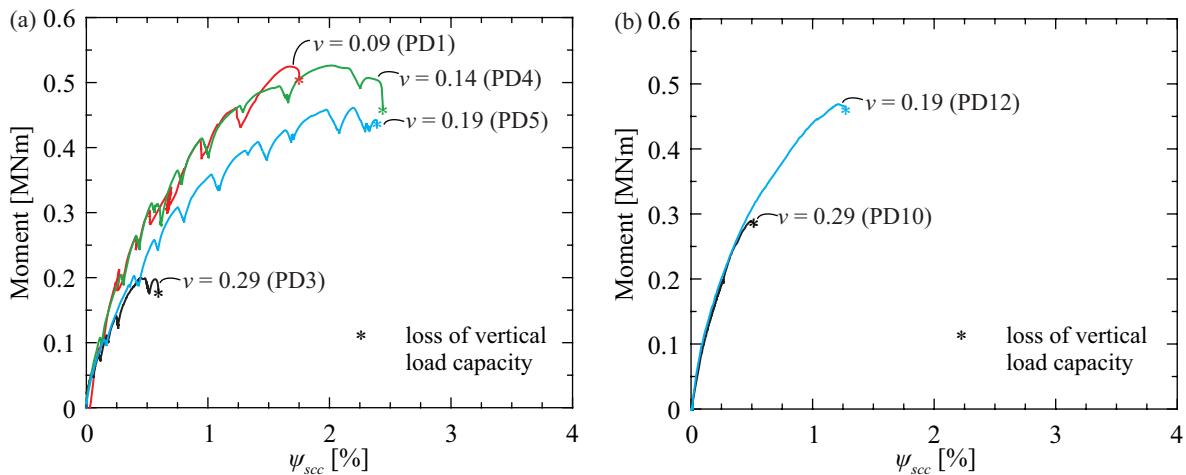

Figure 3.21 – Moment-connection rotation relationship for cyclic and monotonic tests at different reinforcement ratios and vertical loads, performed within this research.

Stiffness

The test campaign comprised slabs subjected to normalised shear forces ν equal to 0.09, 0.14, 0.19 and 0.29 $\sqrt{\text{MPa}}$. Figure 3.21a shows that an increase in vertical loads results in a decrease of the connection stiffness. The sensitivity of the stiffness is largest when increasing ν from 0.14 to 0.19 $\sqrt{\text{MPa}}$, while it is rather small for $\nu < 0.14$ $\sqrt{\text{MPa}}$ and $\nu > 0.19$ $\sqrt{\text{MPa}}$ (Fig. 3.21a and b).

Moment capacity

The effect of vertical loads on the moment capacity of a slab-column connection depended on the vertical load level (Fig. 3.12a and 3.21). In general, decreasing the vertical load, increased the peak moment. Similar trends have been shown by previous studies [Pan89, Rob06, Bu09]. This study showed that the trend was stronger for slabs with $\nu \geq 0.19$ $\sqrt{\text{MPa}}$ and less strong for $\nu < 0.19$ $\sqrt{\text{MPa}}$. A gravity load of 0.19 $\sqrt{\text{MPa}}$ corresponds to half the punching shear strength without unbalanced moment.

Rotation at peak moment

It is generally assumed that the rotation at peak moment decreases with increasing vertical load (e.g. ACI-318 [ACI14] and Pan and Moehle [Pan89]). This experimental campaign confirmed this trend for $\nu > 0.19 \sqrt{\text{MPa}}$ (Fig. 3.21). For lower vertical loads, however, the rotation at peak moment increased slightly with increasing vertical loads (Fig. 3.21a). This is attributed to the fact that higher vertical loads lead to more cracks and therefore to a reduced stiffness, which increases the deformation capacity since the moment capacity remained almost unchanged. In fact, the same observation can be inferred from results of previous tests [Rob06, Cho07, Bu09].

Cracking pattern

The cracking pattern of the top slab surface was strongly influenced by the vertical load level: the larger the vertical load level, the more cracks due to vertical loads and the fewer cracks due to the unbalanced moment. This applied for both reinforcement ratios (Figs. 3.15a, c and 3.16). Concrete spalling of the top slab surface was observed only for slabs with $\rho = 0.75\%$ (Fig. 3.15a, c).

The saw cuts of slabs subjected to monotonic loading showed that if the maximum eccentricity M_{max}/V was lower than $c/2+d$ ($\nu = 0.29 \sqrt{\text{MPa}}$ in Fig. 3.17), the shear crack inclination was approximately 45 degrees for both hogging and sagging slab half. For higher maximum eccentricities ($\nu < 0.29 \sqrt{\text{MPa}}$ in Fig. 3.17) the shear crack of the hogging slab half was flatter, whereas no significant cracking was observed over the thickness of the sagging slab half.

3.8.2 Reinforcement ratio effect

The influence of the flexural reinforcement ratio on the moment-rotation response of slab-column connections without transverse reinforcement has been thoroughly investigated in several experimental campaigns [Gha76, Haw89, Rob06, Cho07]. This test campaign varied not only for one reinforcement ratio the gravity load but for two ($\rho = 0.75$ and 1.50%). It therefore allows to investigate the sensitivity of the gravity load effect with regard to the reinforcement ratio (Fig. 3.22).
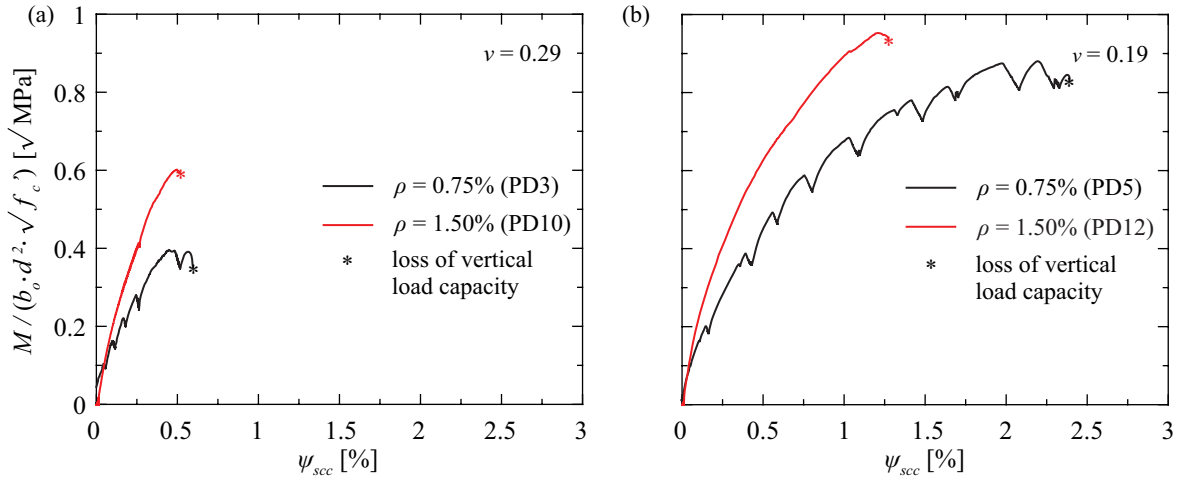
Figure 3.22 – Influence of reinforcement ratio on moment-rotation response for monotonically tested connections with ν equal to (a) 0.29 $\sqrt{\text{MPa}}$, and (b) 0.19 $\sqrt{\text{MPa}}$.

Stiffness

Fig. 3.22 shows that doubling the flexural reinforcement ratio resulted in a significant stiffness increase for both gravity load ratios.

Moment capacity

The effect of the flexural reinforcement ratio on the moment capacity depended on the applied vertical load: For $\nu = 0.29$ $\sqrt{\text{MPa}}$ (Fig. 3.22a), doubling the reinforcement increased significantly the peak moment; for lower vertical loads ($\nu = 0.19$ $\sqrt{\text{MPa}}$, Fig. 3.22b), doubling the reinforcement ratio had little effect on the peak moment.

Rotation at peak moment

As for the moment capacity, the effect of the flexural reinforcement ratio on the deformation capacity depended on the applied vertical load: For $\nu = 0.29$ $\sqrt{\text{MPa}}$, when increasing ρ from 0.75% to 1.50% (Fig. 3.22a), the deformation capacity remained almost constant. For $\nu = 0.19$ $\sqrt{\text{MPa}}$, however, doubling the reinforcement reduced the deformation capacity by more than a factor of two (Fig. 3.22b).

Cracking pattern

The saw cuts showed that for high vertical loads ($\nu = 0.29$ $\sqrt{\text{MPa}}$) the shear crack inclination was not significantly affected by the reinforcement ratio (Fig. 3.19a). For lower vertical loads ($\nu = 0.19$ $\sqrt{\text{MPa}}$), an increase in the reinforcement ratio from 0.75% to 1.50% resulted in a slightly steeper shear crack in the hogging slab half (Fig. 3.19b).

3.8.3 Cyclic loading effect

Although existing experimental research on slab-column connections under both monotonically and cyclically increasing deformations is rather extensive, before this campaign only three pairs of specimens had been subjected to monotonic and cyclic moment to investigate the effect of the loading history. Out of these three pairs two investigated isolated slab specimens [Han68, Isl76] and one a continuous flat slab [Rha14]. These tests showed that cyclic loading had only a small effect on the moment strength. Deformation measurements are only available for [Isl76] and [Rha14] and the effect of cyclic loading on the deformation capacity was non-conclusive: For [Rha14], the cyclic loading reduced the rotation capacity by more than a factor of three but it had almost no effect for [Isl76]. All three pairs investigated very thin slabs ($h = 76$-90 mm). For such thin slabs, small variations in the thickness of the concrete cover can have a large influence on the effective depth and therefore on the slab behaviour. The present test campaign provides results for five pairs of slabs with $h = 250$ mm (Fig. 3.14), which allows to investigate the influence of the loading history in more depth.

Stiffness

The initial stiffness of slabs tested under monotonically and cyclically increasing moments were similar (Fig. 3.14a, b, d, e), small discrepancies being attributed to differences in the material properties between monotonic and cyclic counterparts (Fig. 3.14c – Table 3.1).

Moment capacity

The moment capacity of cyclically loaded slabs was smaller than the moment capacity of monotonically loaded slabs. This difference decreased for increasing gravity loads:

- $\rho = 0.75\%$: $\nu = 0.14$ $\sqrt{\text{MPa}}$: -27%, $\nu = 0.19$ $\sqrt{\text{MPa}}$: -19%, $\nu = 0.29$ $\sqrt{\text{MPa}}$: -2%

- $\rho = 1.50\%$: $\qquad\qquad\qquad\qquad\qquad$ $\nu = 0.19$ $\sqrt{\text{MPa}}$: -13%, $\nu = 0.29$ $\sqrt{\text{MPa}}$: -1%

Rotation at peak moment

As for the moment capacity, the rotation capacity of cyclically loaded slabs is smaller than for mono-tonically loaded slabs. The difference varies between 12 and 61%:

- $\rho = 0.75\%$: $\nu = 0.14$ $\sqrt{\text{MPa}}$: -35%, $\nu = 0.19$ $\sqrt{\text{MPa}}$: -61%, $\nu = 0.29$ $\sqrt{\text{MPa}}$: -20%

- $\rho = 1.50\%$: $\nu = 0.19$ $\sqrt{\text{MPa}}$: -29%, $\nu = 0.29$ $\sqrt{\text{MPa}}$: -12%

For $\nu = 0.19$ $\sqrt{\text{MPa}}$ and $\nu = 0.29$ $\sqrt{\text{MPa}}$ the following trends can be observed: The larger the gravity loads, the smaller the difference in rotation capacity between monotonic and cyclic tests. This is confirmed by measurements of the top reinforcement strain (Fig. 3.23). The difference is larger for $\rho = 0.75\%$ than for $\rho = 1.50\%$. For these tests, the envelope of the moment-rotation curve of the cyclic test corresponded very well to the moment-rotation curve of the monotonic test, with the difference that failure occurred earlier.
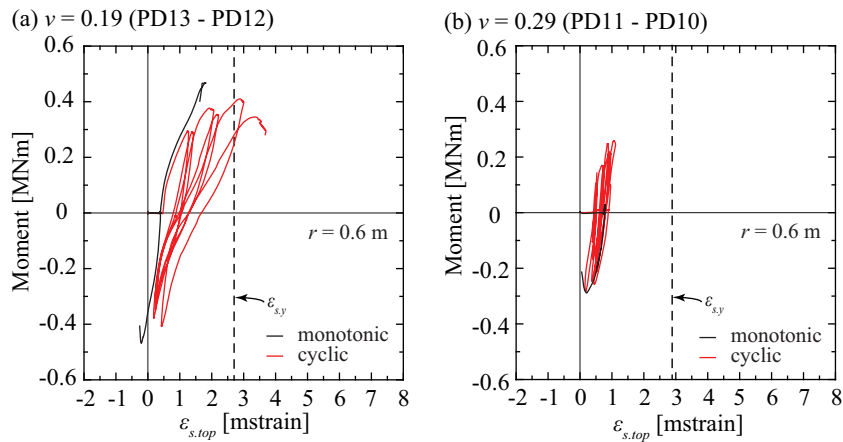
Figure 3.23 – Measured strains of the top reinforcing bars at a distance $r = 0.6$ m from the column axis for monotonically and cyclically tested slabs ($\rho = 1.50\%$), for ν equal to (a) 0.19 $\sqrt{\text{MPa}}$, and (b) 0.29 $\sqrt{\text{MPa}}$.

When $\nu = 0.14$ $\sqrt{\text{MPa}}$ and $\nu = 0.19$ $\sqrt{\text{MPa}}$ are compared ($\rho = 0.75\%$), the trend is different: The monotonic rotation capacity is almost the same for both values of ν but the cyclic rotation capacity is significantly larger for $\nu = 0.14$ $\sqrt{\text{MPa}}$ than for $\nu = 0.19$ $\sqrt{\text{MPa}}$. This is because for $\nu = 0.14$ $\sqrt{\text{MPa}}$ the cyclically loaded specimen yields for $M > 0.80 M_{max,cyc}$ a considerably softer response than the monotonically loaded specimen.

Cracking pattern

The cyclic loading led naturally to a more symmetric cracking pattern than the monotonic loading. This applies to the cracking pattern on the surface (Fig. 3.15) and saw cuts (Fig. 3.19). Moreover, it was observed that for low vertical loads ($\nu \leq 0.19$ $\sqrt{\text{MPa}}$), the shear crack at failure was significantly steeper for cyclic tests than for their monotonic counterparts, both for $\rho = 0.75\%$ (Fig. 3.18b and c) and 1.50% (Fig. 3.18e). Steep shear cracks due to load reversals indicate severe concrete degradation that limits the deformation capacity of the connection, as has been observed by other researchers [Mat15]. For higher vertical loads, the shear crack inclination at failure was not significantly influenced by the loading type (Fig. 3.18a and d).

3.9   Comparison to codes of practice

In the following, the results of the tests are compared with the requirements of some codes of practice. The provisions for the design of slab-column connections in the presence of seismic moments according to ACI-318 [ACI14], Eurocode 2 (EC2) [Eur04]] and fib-Model Code (MC2010) [Fib11] are presented in Chapter 2 (Section 2.3). The performance of the aforementioned standards in predicting the peak moment and the corresponding connection rotation is assessed for the slabs tested in the present campaign. To this aim, mean strength values are used for both concrete and reinforcing steel and the partial factors γ_m and ϕ are set to unity. The resulting code predictions are shown in Table 3.3 in the form of ratio of predicted to observed values both for the maximum moment M_{max} and the corresponding slab-column connection rotation $\psi_{scc.max}$. As can be seen from Table 3.3, ACI-318 [ACI14] and fib-Model Code (MC2010) [Fib11] provide the most conservative predictions for the moment capacity of the tested slabs (ratio of predicted to observed values: 0.485 ± 0.317 and 0.478 ± 0.294, respectively), followed by EC2 [Eur04] (0.723 ± 0.200).

Table 3.3 – Ratios of predicted to experimental values of moment capacity M_{max} according to ACI-318, EC2 and fib-MC2010 and corresponding connection rotation $\psi_{scc.max}$ according to the drift limit of ACI-318 for the slabs tested under combined vertical load and moment (Mean and CoV values are represented in bold)

Slab	Loading type	$M_{max.pred}/M_{max.exp}$ [-]			$\psi_{scc.pred}/\psi_{scc.max.exp}$ [%]
		ACI-318	EC2	MC2010	ACI-318
PD1	V+M	0.710	0.903	0.655	-
PD3	V+M	0.440	0.495	-	-
PD4	V+M	0.581	0.721	0.464	-
PD5	V+M	0.463	0.530	0.283	-
PD10	V+M	0.231	0.721	0.362	-
PD12	V+M	0.407	0.778	0.562	-
PD2	V+C	0.515	0.561	-	1.389
PD6	V+C	0.597	0.728	0.372	0.721
PD8	V+C	0.659	0.857	0.565	0.938
PD11	V+C	0.241	0.731	0.367	1.163
PD13	V+C	0.488	0.924	0.668	0.581
Mean	(all tests)	**0.485**	**0.723**	**0.478**	**0.958**
CoV		**0.317**	**0.200**	**0.294**	**0.340**
Mean	(V + M)	**0.472**	**0.691**	**0.465**	-
CoV		**0.344**	**0.223**	**0.321**	-
Mean	(V + C)	**0.500**	**0.760**	**0.493**	**0.958**
CoV		**0.319**	**0.183**	**0.302**	**0.340**

The normalised moment-shear force interaction diagrams according to ACI-318 [ACI14], EC2 [Eur04] and fib-MC2010 [Fib11] are shown in Figure 3.24a and b for nominal flexural reinforcement ratios equal to 0.75% and 1.50%, respectively. Since discrepancies among the material properties and the effective depth d of the tested slabs do not influence to a significant degree the code predictions, the curves are drawn for the average experimental values of f_c, f_y and d (see Table 3.1). The experimental results of the presented campaign are also shown (represented with markers). Figure 3.24 shows that an increase of reinforcement ratio from 0.75% to 1.50% increases the conservatism of the predictions of ACI-318 [ACI14]. The predictions of EC2 [Eur04] and fib-MC2010 [Fib11] are also conservative but appear to follow the experimental trend.
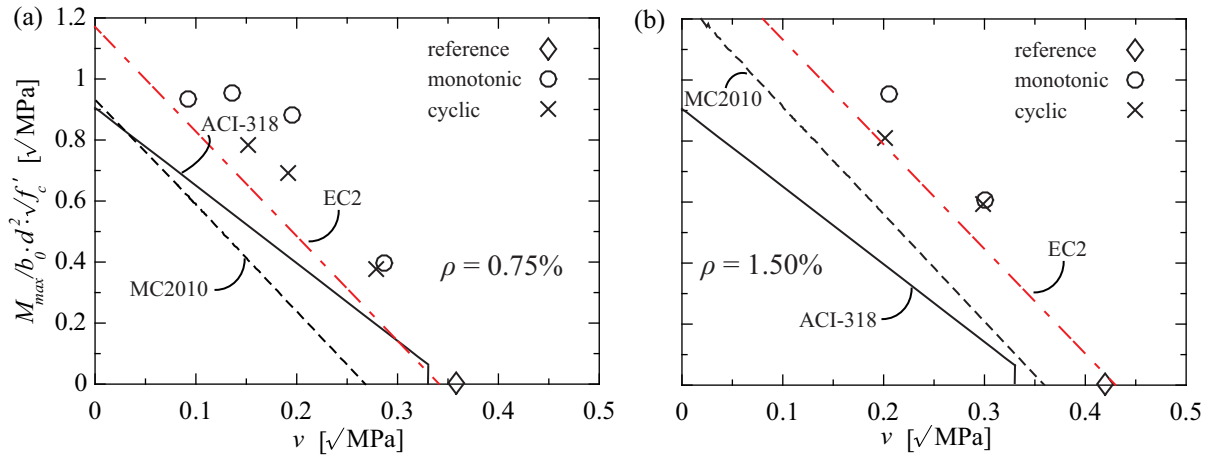
Figure 3.24 – Code predictions for the moment capacity of the tested slab specimens: (a) $\rho = 0.75$ %, and (b) $\rho = 1.50$ %.

Only ACI-318 [ACI14] provides a lower-bound limit for the deformation capacity of slab-column connections subjected to reversed cyclic loading in terms of interstorey drift. The drift limit of ACI-318 [ACI14] along with the connection rotation at peak moment for the cyclic tests of the present campaign are shown in Fig. 3.25, as function of GSR (according to [ACI14]) in the bottom abscissa, and ν (according to Eq. (3.4)) in the top abscissa. In average, the deformation capacity is predicted rather well (0.958 ± 0.340). Assuming the contribution of column deformations to interstorey drifts is small, ACI-318 [ACI14] provides deformation capacity estimates on the unsafe side for GSR > 0.80. This has already been reported by other researchers [Bro09].
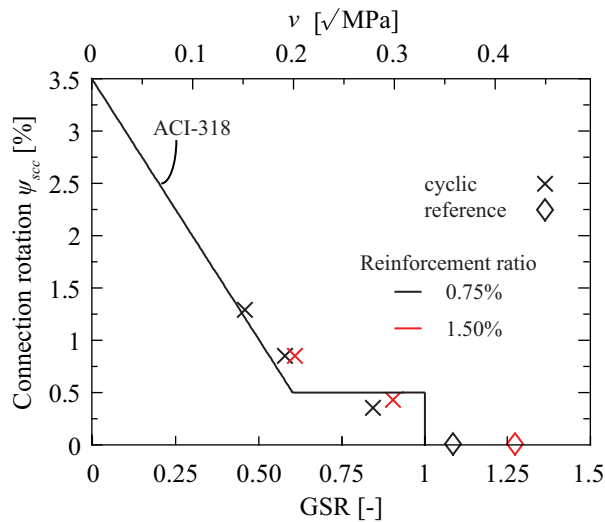
Figure 3.25 – Connection rotation at peak moment for the cyclic tests of the present campaign and allowable drift limit according to ACI-318.

3.10 Conclusions

This chapter presents the results of an experimental campaign on the seismic behaviour of internal reinforced concrete slab-column connections without transverse reinforcement with main objective to investigate the effect of cyclic loading on the moment-rotation response. The campaign comprised 13 full-scale isolated slab-column specimens. The adopted setup configuration is presented and compared to setup configurations used in past experimental studies. The results were discussed with regard to the effect of gravity loads, reinforcement ratio and loading history (monotonic vs cyclic) on the stiffness, strength, deformation capacity and cracking pattern of the slab-column connection. The obtained experimental results were also compared to the predictions of ACI-318 [ACI14], Eurocode 2 (EC2) [Eur04] and fib-Model Code (MC2010) [Fib11] for moment strength and deformation capacity. The main conclusions of this chapter are:

1. Non-linear finite element analyses showed that stiffness and deformation capacity of slab-column connections depend on the chosen experimental setup. The setup configuration adopted for the present study reproduces well the moment-connection rotation response of an internal slab-column connection of a typical building configuration.

2. Reversed cyclic loading reduces the moment capacity and the deformation capacity of slab-column connections. This effect is more pronounced for smaller gravity loads and smaller reinforcement ratios. In general, the envelope of the cyclic response corresponded to the curve of the monotonic test, with the difference that failure occurred earlier for the cyclic test. However, for very low gravity loads, cyclic loading resulted in a softer moment-rotation response than for monotonic loading for moments higher than 80% of the peak cyclic moment.

3. For slabs subjected to cyclically increasing moments, the shear crack at failure is steeper than for slabs subjected to monotonically increasing moments. This effect is more marked for smaller gravity loads than for larger gravity loads.

4. Increasing gravity load reduces the stiffness and the moment capacity of slab-column connections as observed by others. With regard to the deformation capacity a more differentiated trend was identified: For gravity loads larger than a threshold value, the deformation capacity decreases with increasing gravity load. For gravity loads smaller than this threshold value, however, the trend did not continue but smaller gravity loads led to a reduced deformation capacity. This was attributed to the smaller extent of cracking for small vertical loads. From the present experimental campaign this threshold value was found to correspond to approximately half the punching strength under concentric gravity loads ($V_{test}/b_o\, d\, \sqrt{f_c} = 0.19\, \sqrt{\mathrm{MPa}}$). Note that such a change in trend was not observed for cyclic tests for which the deformation capacity always increased with decreasing gravity loads.

5. Increasing reinforcement content resulted in general in higher stiffness and lower deformation capacity, as has been noted by previous studies. For low gravity loads, increasing the reinforcement ratio had however little influence on the moment capacity. For high gravity loads, increasing the reinforcement ratio had little influence on the deformation capacity.

6. ACI-318 [ACI14] and fib-MC2010 [Fib11] provide the most conservative estimates of the moment capacity, followed by EC2 [Eur04] with respect to both accuracy and precision.

7. The allowable drift limit of ACI-318 [ACI14] estimates rather accurately the connection rotation capacity of the cyclic tests. However, ACI-318 appears to overestimate the rotation capacity for high vertical loads (GSR > 0.8).

Chapter 4

Analytical model for monotonically increasing drifts

In this chapter, a mechanical model is proposed for computing the entire moment-rotation relationship of slab-column connections subjected to seismic loading. This model allows to compute the contribution of each resisting mechanism, i.e., eccentric shear, flexure and torsion. To do so, the slab is divided into n sector elements and equilibrium is first formulated for each sector element and then for the entire slab. This permits to connect local deformations of each sector element to the global rotation of the slab-column connection. The presented approach considers only the slab region until $0.22L$ from the column axis (defined as slab-column connection region, L corresponds to the distance from midspan to midspan). The proposed method can be combined with an effective beam width model for the slab region outside $0.22L$ in order to transform the connection rotation to the interstorey drift. Drift-induced punching failure is determined by combination of the proposed model for computing the moment-rotation relationship with the failure criterion of the Critical Shear Crack Theory (CSCT) [Mut08]. The failure criterion distinguishes between monotonic loading, for which shear stress redistribution between sector elements is considered, and cyclic loading, for which shear stress distribution is neglected.

Section 4.1 treats the slab deformation related to interstorey drift, using NLFEA. The goal of this section is to assess the contribution of ψ_{scc} and ψ_{os} to the slab deformation ψ_{slab} (see definitions in Chapter 3) and to provide a simple mechanical approach for estimating ψ_{os}.

Section 4.2 presents the development of the analytical model for the calculation of the moment-rotation relationship of slab-column connections without transverse reinforcement subjected to monotonically increasing drifts. The model is based on the axisymmetric model developed by Muttoni [Mut08] that considers both the load and the deformation of the slab.

Section 4.3 addresses the failure criterion that is combined with the moment-rotation relationship to determine the unbalanced moment and the corresponding slab rotation at punching failure. Two approaches for the failure criterion are proposed in this chapter to distinguish between monotonic and cyclic loading conditions, since the analytical model presented in this chapter does not account for the effect of the loading history on the moment-rotation relationship.

Section 4.4 presents a parametric study on the influence of drift level, gravity load, reinforcement ratio and slab slenderness on the contribution of the three resisting mechanisms (flexure, torsion and eccentric shear) according to the presented model.

Section 4.5 examines the influence of cyclic loading, reinforcement ratio, slab effective depth and slab slenderness on the calculated rotation capacity of slab-column connections.

Section 4.6 compares the model predictions with the results of the experimental campaign in terms of the moment-rotation response, moment strength and deformation capacity.

4.1 Slab deformation related to interstorey drift

To assess the contribution of ψ_{scc} and ψ_{os} to the slab deformation ψ_{slab} (Eq. (3.3) in Section 3.3), a slab element with continuity boundary conditions, subjected to horizontal loads, was analysed using the finite element program SAP2000 [CSI14]. In this model, the column is modelled by a rigid beam element and the slab by layered shell elements to which non-linear material laws are assigned. The analysis yields the moment-rotation relationship due to flexural deformations of the slab but cannot account for punching failure. Details with respect to the numerical modelling can be found in Chapter 3 (§3.3.2). Figure 4.1 illustrates both contributions to the slab rotation ψ_{slab} for flexural reinforcement ratios in the hogging moment area equal to 0.75% and 1.50%. Since the model captures only flexural failure, Figure 4.1 also shows horizontal lines that correspond to the unbalanced moment at punching failure according to ACI-318 [ACI14]. For this horizontal load level, the slab-column connection rotation ψ_{scc} contributes approximately 75% - 80% to the total slab rotation ψ_{slab}, the remaining part being contributed by the slab region outside $r = 0.22L$.
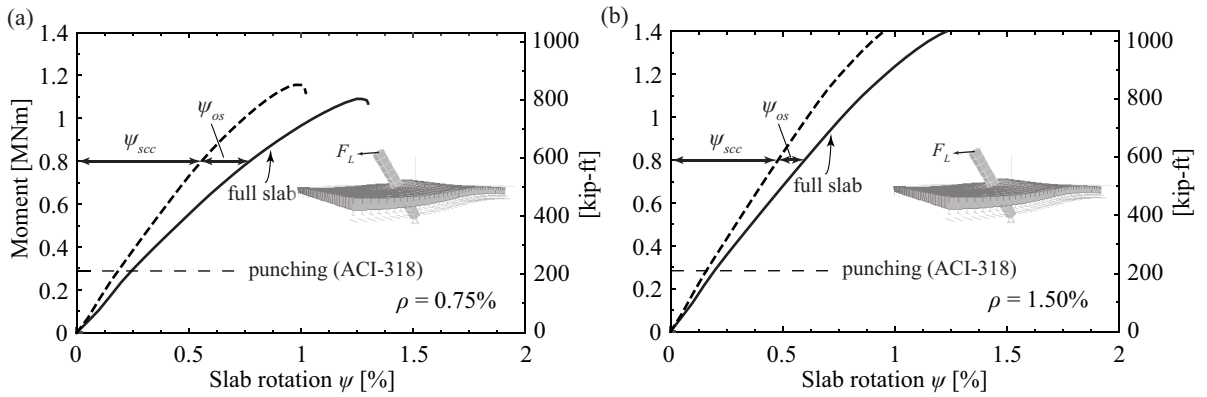
Figure 4.1 – Contribution of the slab deformation inside and outside $r = 0.22L$ to the total slab contribution to the interstorey drift for flexural reinforcement ratio equal to: (a) 0.75%, and (b) 1.50% ($L = 6.8$ m, $h = 0.25$ m, $c = 0.39$ m – Note 1 m = 3.28 ft).

4.1.1 Contribution of slab-column connection to the slab deformation

This section analyses characteristics of the slab deformations inside $0.22L$ using the numerical model presented in Section 3.3. When a slab-column connection is subjected to an unbalanced moment, the local slab rotations vary along the perimeter $r = 0.22L$. The location of the investigated points is described by the angle ϕ, which is measured with regard to the bending axis y (Fig. 4.2a). Figure 4.2a shows the variation of the slab rotation with ϕ for vertical loads alone (black line) and for three different horizontal load levels (colored lines). When only vertical loads are applied, the system is approximately axisymmetric and the slab rotation is almost constant. When an unbalanced moment about the y-axis is introduced, the slab rotation varies with ϕ and the relationship between maximum local slab rotation (for $\phi = \pi/2$) and minimum slab rotation (for $\phi = 3\pi/2$) follows approximately a sinusoidal law. This observation has been confirmed experimentally by measurements on slab-column connections subjected to constant shear force and increasing moment (Chapter 3). This relationship will be assumed in the mechanical model to connect the local slab rotations to the global rotation of the slab-column connection.

Figure 4.2b shows the profile of slab deflections along the x-axis for the same load levels as in Figure 4.2a. It shows that the profile of slab deflections is approximately linear between $r = d$ (slab effective depth) and $r = 0.22L$. This means that the curvature in radial direction of the slab-column connection in the region $r > d$ can be neglected. The assumption of a rigid behaviour of this region taken

by [Kin60, Mut08] is thus confirmed also for the case of slab-column connections with unbalanced moment.
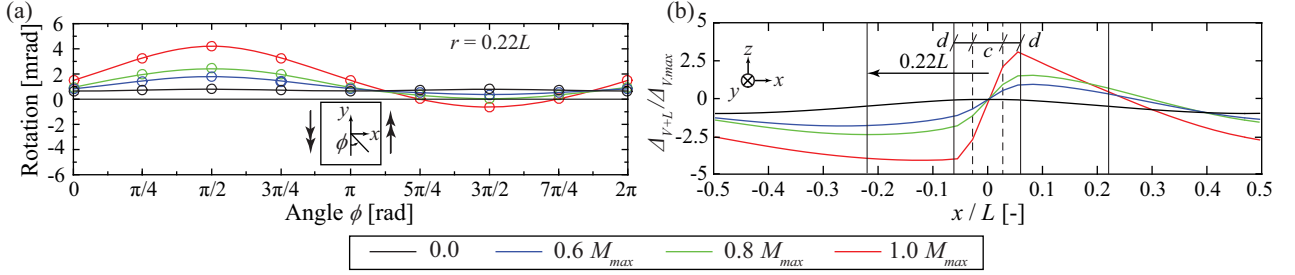
Figure 4.2 – (a) Local slab rotations at varying angles and (b) slab deflections along the x-axis for different lateral load levels.

4.1.2 Contribution of the slab region outside $0.22L$ to the slab deformation

The slab part outside $r = 0.22L$ contributes about a quarter to the total slab rotation (dashed-dotted lines, Fig. 4.1). To estimate this contribution using a simple mechanical approach, an effective beam width model is employed. In this model, the column is modelled as rigid but with its actual dimensions. The slab is modelled by a beam to which a width αl_2 is assigned, where l_2 is the transverse span [Pan92]. The width reduction coefficient α can be derived assuming the same rotational stiffness for the full-width slab (real system) and the equivalent beam (fictitious system) (same as Eq. (2.61)):

$$\alpha = \frac{M}{\psi_{slab}} \frac{l_1}{l_2} \frac{1}{E_c \, h^3} \qquad (4.1)$$

where M is the moment transferred to the slab-column connection, l_1 is the distance between columns (equal to L), E_c is the modulus of elasticity of concrete and h is the slab thickness. The slab rotation ψ_{os} is then obtained from a simple beam model where the column and the slab inside $r = 0.22L$ are modelled as rigid. Figure 4.3 shows the established effective beam width model to calculate the contribution of the slab region outside $0.22L$ to the slab deformation rotation ψ_{slab}. The slab outside $r = 0.22L$ is modelled as an elastic beam with a width αl_2 and height h. For the calculation of the reduction coefficient α (Eq. (4.1)), the unbalanced moment M and the corresponding rotation due to slab deformation ψ_{slab} are obtained from the moment-rotation relationship of the slab-column connection, which is presented in the next section. The only differences between the models shown in Figures 4.1 (close-up) and 4.3 lie on the use of beam members instead of shell elements, distribution of the gravity loads per unit length instead of unit area and modelling of the beam part inside $0.22L$ with high stiffness. Note that cracking is directly accounted for by the width reduction coefficient α. For validation, M and ψ_{slab} were taken from the layered shell element model and the rotation ψ_{os} obtained by the effective beam model was compared to that of the finite element model (Fig. 4.1). The difference in rotations was smaller than 10%.
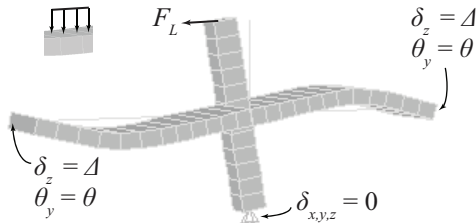
Figure 4.3 – Deformed shape of the established effective beam width model with high stiffness for $r < 0.22L$.

The slab outside $r = 0.22L$ has also an effect on the moment capacity by providing a confining effect [Par06]. This is, however, not considered in the analytical model presented in this chapter.

4.2   Moment-rotation relationship

This section presents the theoretical background of the proposed model for the moment-rotation relationship of a slab-column connection subjected to a seismically-induced moment. The model is derived from the axisymmetric model developed by Kinnunen and Nylander [Kin60] and Muttoni [Mut08] for slabs subjected to gravity loads. In the original model, the slab is divided into an even number n of sector elements and the region inside the shear crack. Since that model is axisymmetric, the equilibrium formulation can be reduced to one sector element (Fig. 4.5a). For the case of a seismically-induced moment, several modifications of the axisymmetric analytical model are introduced which are presented first. Next, equilibrium is formulated for a sector element and then for the entire slab specimen until $r = 0.22L$. It follows the approach for computing the slab-column connection rotation. To compute the total slab rotation, also the deformation of the slab part outside $r = 0.22L$ needs to be considered, which is presented in the final part of this section.

4.2.1   Assumptions

As already shown in Figure 4.2a, the slab rotation of the sector elements follows approximately a sinusoidal law with regard to the location described by angle ϕ. The slab rotation of the sector element at angle ϕ with regard to the bending axis y is therefore:

$$\psi(\phi) = \frac{\psi_{max} + \psi_{min}}{2} + \frac{\psi_{max} - \psi_{min}}{2} \sin(\phi) \tag{4.2}$$

where ψ_{max} and ψ_{min} are the maximum slab rotation for $\phi = \pi/2$ and the minimum slab rotation for $\phi = 3\pi/2$, respectively.

Moreover experimental evidence shows that radial curvatures concentrate in the slab area between column axis and shear cracks [Mut08]. In case of slab-column connections with unbalanced moment M, the tests presented in Chapter 3 showed that the inclination of critical shear cracks depends on the ratio of unbalanced moment M to the shear force V (Fig. 4.4), subsequently referred to as eccentricity e. Based on these observations it is assumed that the radius r_0 of the critical shear crack is equal to $e = M / V$, but not smaller than $r_c + d$ as assumed by Muttoni [Mut08]:

$$r_0 = e \geq r_c + d \tag{4.3}$$
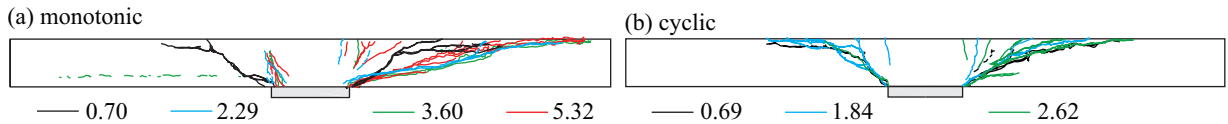
Figure 4.4 – Critical shear crack inclination for drift-induced punching under (a) monotonic and (b) cyclic loading conditions for different ratios of maximum eccentricity to column size [Dra16].

Past experimental evidence showed that reversed cyclic loading affects the ultimate rotation capacity but does not affect to a significant degree the moment-rotation relationship of slab-column connections before failure [Rha14, Dra16]. For this reason, the present chapter assumes that the response envelope under cyclic loading is represented by the monotonic moment-rotation curve.

4.2.2 Equilibrium of sector elements (local level)

The assumption of different rotations at different angles (Fig. 4.2a) from the bending axis implies that the moment is introduced from the column to the slab not only by a flexural moment but also by a torsional moment and an eccentric shear force. This can be demonstrated by formulating equilibrium for a sector element as shown in Figure 4.5.
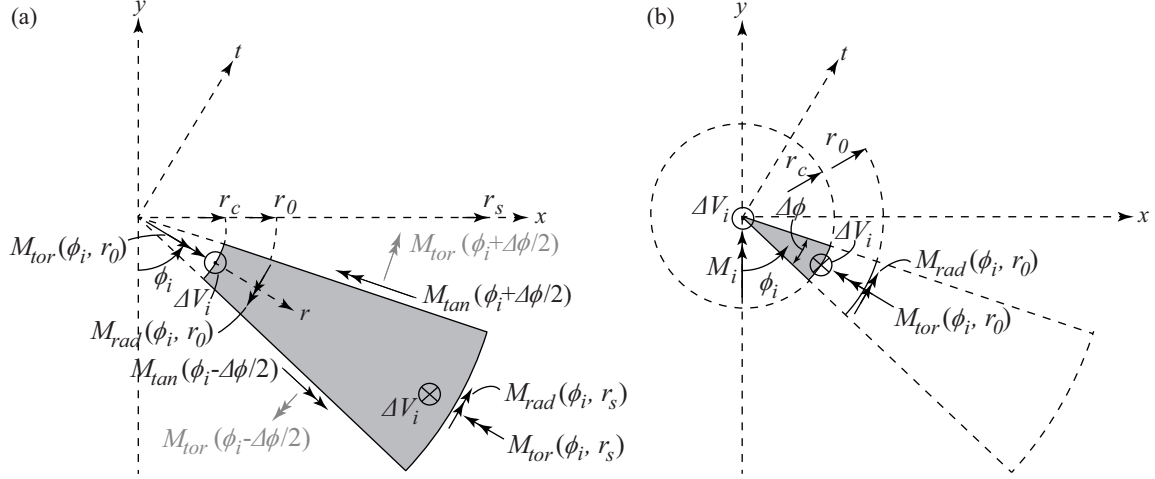
Figure 4.5 – Internal forces acting on the slab region: (a) outside the shear crack (hogging slab half), and (b) inside the shear crack.

During the model development it was identified that the torsional moments acting on each face of the sector element are highly dependent on the assumed torsional stiffness. For this reason, this study neglects the moments $M_{tor}(\phi - \Delta\phi/2)$ and $M_{tor}(\phi + \Delta\phi/2)$ (shown in grey in Fig. 4.5a) and the associated shear forces. An axonometric view of the sector element shown in Figure 4.5a can be seen in Figure 4.6.
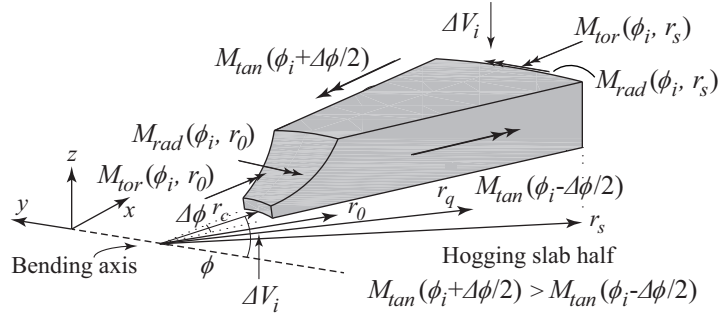
Figure 4.6 – Axonometric view of a sector element of the hogging slab half and internal forces acting on it.

$M_{tan}(\phi - \Delta\phi/2)$ and $M_{tan}(\phi + \Delta\phi/2)$ are the integrals of the tangential moments at the faces of each sector element (Fig. 4.5a). These moments can be determined directly as a function of the assumed rotation and a quadri-linear moment-curvature relationship [Mut08]:

$$\left(\begin{array}{c} M_{tan}(\phi) = m_R \left\langle r_y - r_0 \right\rangle + EI_1\, \psi(\phi) \left\langle ln\,(r_1) - \, ln\,(r_y) \right\rangle + EI_1\, \chi_{TS} \left\langle r_1 - \, r_y \right\rangle + \\ + m_{cr} \left\langle r_{cr} - r_1 \right\rangle + EI_0\, \psi(\phi) \left\langle ln\,(r_s) - \, ln\,(r_{cr}) \right\rangle \end{array} \right) \tag{4.4}$$

where EI_0 and EI_1 are the slab stiffness before and after cracking, m_{cr} and m_R are the cracking moment and moment capacity respectively per unit width, χ_{TS} is the curvature due to the tension stiffening effect, and r_0, r_y, r_1, r_{cr} and r_s are the radii of the critical shear crack, of the yielded zone,

of the zone in which cracking is stabilised, of the cracked zone and of the circular isolated slab element respectively. The operator $\langle x \rangle$ is x for $x > 0$ and 0 for $x < 0$. Equation (4.4) for the calculation of the tangential moment $M_{tan}(\phi)$ is taken directly from the CSCT [Mut08]. For the case of seismically induced deformations, the local slab rotation ψ depends on the angle ϕ of the sector element with regard to the direction of seismic loading and the radius r_0 of the critical shear crack is updated as function of the eccentricity (see Eq. (4.2)) to take into account the fact that the shear force becomes less determinant as eccentricity increases. Therefore, the integral of the radial moment for a sector element at angle ϕ at $r = r_0$ is:

$$M_r(\phi) = m_r(\phi) \, r_0 \, \Delta\phi \tag{4.5}$$

where $m_r(\phi)$ is the radial moment per unit width at $r = r_0$ as function of the radial curvature [Mut08].

If ϕ_i is the angle formed by the axis of bending and the bisector of the ith sector element, the shear force that can be carried by the compression strut of this sector element is derived by moment equilibrium in the radial direction with respect to the centre of the column with radius r_c:

$$\Delta V_i = \frac{1}{r_q - r_c} \left[M_{rad}(\phi_i, r_0) - M_{rad}(\phi_i, r_s) + \left[M_{tan}(\phi_i + \frac{\Delta\phi}{2}) + M_{tan}(\phi_i - \frac{\Delta\phi}{2}) \right] \sin\left(\frac{\Delta\phi}{2}\right) \right] \tag{4.6}$$

The moment equilibrium in the tangential direction gives the torsional moment that is carried by the connection for the ith sector element:

$$M_{tor}(\phi_i, r_0) = \left[M_{tan}(\phi_i + \frac{\Delta\phi}{2}) - M_{tan}(\phi_i - \frac{\Delta\phi}{2}) \right] \cos\left(\frac{\Delta\phi}{2}\right) + M_{tor}(\phi_i, r_s) \tag{4.7}$$

The radial and torsional moments at the perimeter of each sector element $M_{rad}(\phi_i, r_s)$ and $M_{tor}(\phi_i, r_s)$ (Eq. (4.5) and (4.7)) are obtained using an Effective Beam Width Method, as will be shown in the following (§4.2.5).

Equilibrium of shear forces at the column edge gives the total shear force acting on the connection for the load step k:

$$V_k = \sum_{i=1}^{n} \Delta V_i \tag{4.8}$$

Moment equilibrium at the column edge gives the total moment acting on the connection (parallel to the unbalanced moment) for the load step k:

$$M_k = \sum_{i=1}^{n} \left[M_{rad}(\phi_i, r_0) \sin(\phi_i) + M_{tor}(\phi_i, r_0) \cos(\phi_i) + \Delta V_i \, r_c \sin(\phi_i) \right] \tag{4.9}$$

The three terms of Eq. (4.9) represent the contribution of flexure, torsion and eccentric shear force to the total unbalanced moment.

4.2.3 Equilibrium of slab specimen (global level)

For the case of uniformly distributed vertical loading alone, formulating the equilibrium for one sector element is equivalent to formulating the equilibrium for the entire circular slab since $\psi_{max} = \psi_{min} = \psi_v$ (Fig. 4.7a). If a seismic moment is added, the slab rotations vary between sector elements and therefore equilibrium has to be formulated locally for each sector element and globally for the entire circular slab (Fig. 4.7b).
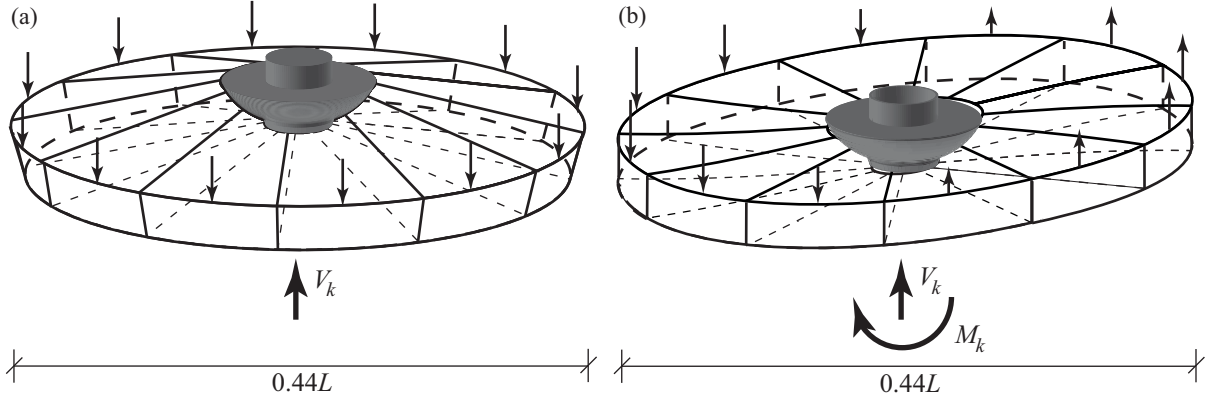
Figure 4.7 – Assumed deformed shape of slab specimen under (a) vertical load [Mut08] and (b) vertical load and imposed lateral deformation.

The unbalanced moment is applied about the y-axis. The adoption of the kinematic law of Eq. (4.2) implies symmetry about the x-axis ($\phi = \pi/2$ and $\phi = 3\pi/2$) and therefore the moment about the x-axis is always zero. To ensure global equilibrium about the y-axis, the following procedure is adopted: For each load step k, a new value of ψ_{max} is chosen. To determine all local slab rotations by means of the sinusoidal law one needs to choose a value ψ_{min}, which is iterated such that the sum of all shear forces ΔV_i is equal to the shear force V that is applied to the slab-column connection. The shear force V is assumed as constant since it results from gravity loads. In order to obtain the moment-rotation curve, the radius r_0 of the shear crack is adapted at each load step k as it is assumed to be equal to the attained eccentricity:

$$e_k = M_k/V_k \tag{4.10}$$

The aforementioned iterative procedure can also be used if M_k or e_k rather than V_k is constant, situations which can be found when constant horizontal loads act on columns or when slabs with unequal spans are subjected to vertical load alone.

4.2.4 Slab-column connection rotation

The previous section yields a relationship between the unbalanced moment M and the local slab rotations $\psi(\phi)$. To determine a relationship between unbalanced moment and slab-column connection rotation ψ_{scc}, a relationship between the local rotations $\psi(\phi)$ and the connection rotation ψ_{scc} is needed.

Figure 4.8a shows the deformed shape of the slab analysed previously until midspan ($0.50L$). Since the proposed model assumes that only the cone inside the shear crack deforms and each element outside the shear crack behaves as a rigid body, the deformed shape of the top slab surface is linear only outside the shear crack (Fig. 4.7b). The connection rotation ψ_{scc} can be defined using either local slab rotations ($\psi_{scc.rot}$) or local slab deflections ($\psi_{scc.defl}$). If the definition is based on rotations, $\psi_{scc.rot}$ can be calculated as the average of the maximum and minimum local rotations ψ_{max} and ψ_{min} (Fig. 4.8a):

$$\psi_{scc.rot} = \frac{\psi_{max} - \psi_{min}}{2} \tag{4.11}$$

If the connection rotation is computed from deflections, one obtains:

$$\psi_{scc.defl} = \frac{\Delta_{max} - \Delta_{min}}{2\,\Delta r + c} \tag{4.12}$$

where Δ_{max} and Δ_{min} are respectively the maximum and minimum local slab deflections at a distance $\Delta r + c/2 = 0.22L$ from the column centre along the x-axis (points A and A' in Figure 4.8a), where c is the column size.
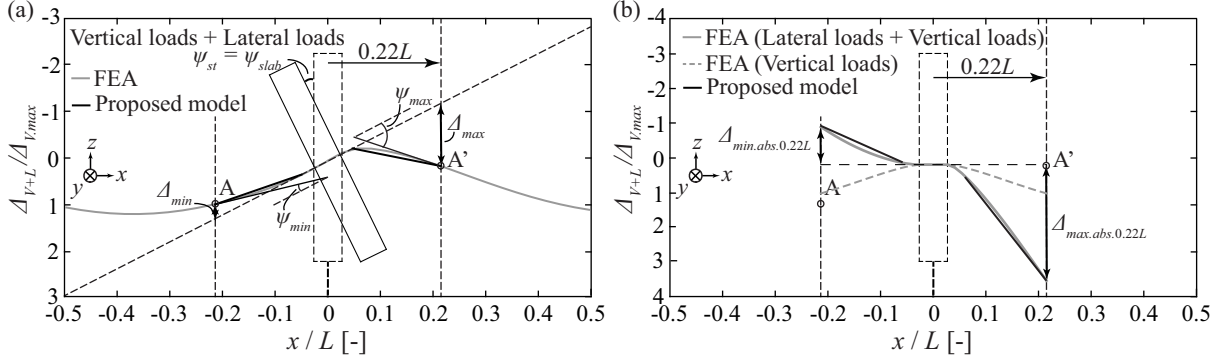
Figure 4.8 – Deformed shape of (a) continuous flat slab until midspan, and (b) setup (b) according to FEA and the proposed model for combined vertical and lateral loads.

In the following, the definition of the slab-column connection rotation for the setups that are most suitable for simulating seismically-induced deformations (setups (b) and (c) - see §2.1.1) is briefly discussed. The deformed shape of the slab for each setup is also shown. The adopted numerical method is presented in Chapter 3 (Section 3.3).

Setup (b)

For setup (b), the deformed shape of the slab under vertical loads and combined vertical and lateral loads is shown in Figure 4.8b. The deformed shape assumed by the proposed model is also shown in the same figure. Finite element analyses have shown that, for this setup configuration, calculation of the slab-column connection rotation on the basis of deflections provides more realistic estimation of the interstorey drift of an internal connection of the reference slab-column frame (Chapter 3). This definition was therefore used both for the experimental peak connection rotations (Appendix A) and the predicted peak connection rotations (Appendix D) for the slabs tested using this setup.

Setup (c)

For setup (c), the deformed shape of the slab depends on the way the vertical loads are applied: For vertical loads applied by jacks underneath the column stub (Fig. 4.9a) the deformed shape resembles the deformed shape of setup (b) (Fig. 4.8b); for vertical loads applied on the slab surface (Fig. 4.9b) the deformed shape is significantly different since the slab region between $r = 0.22L$ and $0.50L$ contributes to the slab deformation.
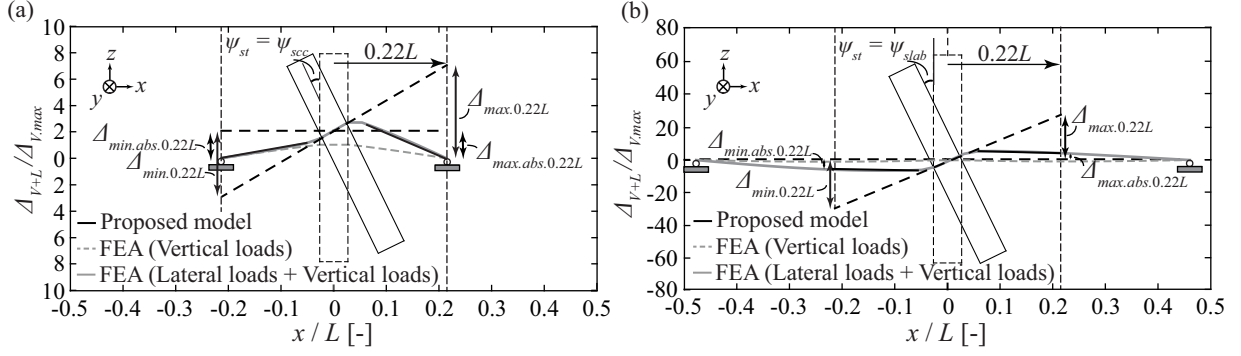
Figure 4.9 – Setup (c) - Deformed shape of slab according to FEA and the proposed model for: (a) vertical load applied on the column, and (b) vertical load applied on the slab surface.

According to the proposed model the slab-column connection rotation based on rotations is:

$$\psi_{scc.rot} = \frac{\Delta_{max} - \Delta_{max.abs}}{2\,\Delta r} - \frac{\Delta_{min} - \Delta_{min.abs}}{2\,\Delta r} = \frac{\Delta_{max} - \Delta_{min}}{2\,\Delta r} - \frac{\Delta_{max.abs} - \Delta_{min.abs}}{2\,\Delta r} \qquad (4.13)$$

where $\Delta_{max.abs}$ and $\Delta_{min.abs}$ are respectively the deflection of the tip of the hogging slab half and the sagging slab half relative to the column centre.

The connection rotation based on deflections is:

$$\psi_{scc.defl} = \frac{\Delta_{max} - \Delta_{max.abs}}{2\,\Delta r + c} - \frac{\Delta_{min} - \Delta_{min.abs}}{2\,\Delta r + c} = \frac{\Delta_{max} - \Delta_{min}}{2\,\Delta r + c} - \frac{\Delta_{max.abs} - \Delta_{min.abs}}{2\,\Delta r + c} \qquad (4.14)$$

In both Equations (4.13) and (4.14) the first term represents the total rotation due to slab deformation ψ_{slab} and the second term represents the contribution of the outer slab part (ψ_{os}) to the rotarion ψ_{slab}.

For setup (c) with the vertical load applied on the column, since $\Delta_{max.abs} = \Delta_{min.abs}$, the connection rotation that is calculated according to the proposed model is equal to ψ_{slab} (i.e. $\psi_{os} = 0$).

For setup (c) with the vertical load applied on the slab surface, since the slab part between $0.22L$ and $0.50L$ contributes to the rotation due to slab deformation ψ_{slab} (i.e. $\psi_{os} > 0$), the connection rotation that is calculated according to the proposed model is smaller than the rotation ψ_{slab}. For this case, the following subsection proposes an Effective Beam Width model in order to calculate the contribution of the slab part outside $0.22L$ to the interstorey drift.

Based on finite element analyses of setup (c) with the vertical load applied on the column, the connection rotation based on rotations was adopted, since it provides better estimate of the interstorey drift than the definition based on deflections. It should be noted that both definitions yield similar results for $\Delta r >> c$, i.e. for slab specimens much larger than the column size.

4.2.5 Rotation due to slab deformation outside the slab-column connection

The presented model for the moment-rotation relationship considers only the slab region inside $0.22L$ (ψ_{scc}). To obtain an accurate prediction of the total slab deformation ψ_{slab}, the rotation ψ_{os} should also be accounted for. This can be performed by calculating the radial and tangential moments $M_{rad}(\phi_i, r_s)$ and $M_{tor}(\phi_i, r_s)$ at the perimeter of each sector element. For this purpose, a beam that connects the perimeter of the considered sector element with the perimeter of the sector element of the opposite column (Fig. 4.10) is used. When the beam is subjected to a rotation $\psi(\phi_i)$ at Node 1 and $\psi(2\,\pi - \phi_i)$ at Node 2, the moment at Node 1 can be found using the elastic solution:
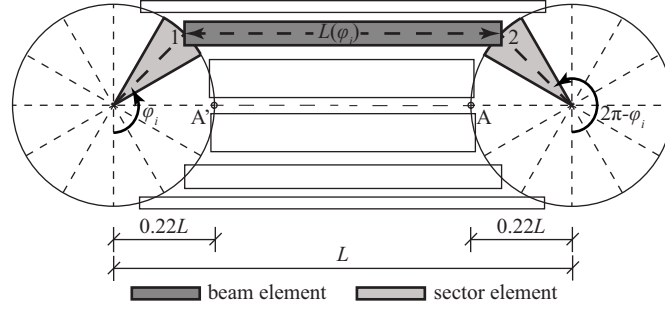
Figure 4.10 – Effective Beam Method for calculating the contribution of the outer slab part to the total deformation.

$$M_{y.EBW}(\phi_i) = \frac{2\,EI_{k-1}(\phi_i)}{L(\phi_i)}\left[\psi(\phi_i)\sin(\phi_i) + \frac{\psi_{max}-\psi_{min}}{2}\left(2+\cos^2(\phi_i)\,(1-3\frac{r_c}{r_s})\right)\right] \qquad (4.15)$$

where the bracketed term represents the projection of the slab rotation to the y-axis (perpendicular to the axis of each beam), $L(\phi_i)$ is the length of the beam that connects the sector element at angle ϕ_i with the sector element at angle $2\pi-\phi_i$ and $EI_{k-1}(\phi_i)$ is its stiffness calculated using the Effective Beam Width Method:

$$EI_{k-1}(\phi_i) = \frac{M_{k-1}}{\psi_{slab.k-1}}\,\frac{L(\phi_i)}{12}\,\frac{\sin(\Delta\phi)\,|\sin(\phi_i)|}{4} \qquad (4.16)$$

where M_{k-1} and $\psi_{slab.k-1}$ is the unbalanced moment and the total rotation due to slab deformation at the load step k-1. The last fraction of Eq. (4.16) is inserted so that the sum of the width of all effective beams yields the width of one single effective beam that represents the slab action (Eq. (4.1) - §4.1.2).

The radial and torsional moments $M_{rad}(\phi_i, r_s)$ and $M_{tor}(\phi_i, r_s)$ at the perimeter of each sector element can be found by projecting the moment calculated using Eq. (4.15) to the radial and tangential direction, respectively:

$$M_{tor}(\phi_i, r_s) = M_{y.EBW}(\phi_i)\cos(\phi_i) \qquad (4.17)$$

$$M_{rad}(\phi_i, r_s) = M_{y.EBW}(\phi_i)\sin(\phi_i) \qquad (4.18)$$

If the beam is simply supported at midspan, as is typically chosen for tests using setup (c) (§2.1.1), the moment at Node 1 can be calculated using the following formula instead of Equation 4.15:

$$M_{y.EBW}(\phi_i) = \frac{3\,EI_{k-1}(\phi_i)}{L(\phi_i)}\left[\psi(\phi_i)\sin(\phi_i) + \frac{\psi_{max}-\psi_{min}}{2}\cos^2(\phi_i)\left(1-\frac{r_c}{r_s}\right)\right] \qquad (4.19)$$

4.3 Failure criterion

In the following, two failure criteria for drift-induced punching are proposed, which are both based on the failure criterion of the CSCT [Mut08]. One failure criterion is applied to slabs subjected to monotonic loading and the other to slabs subjected to cyclic loading. The criteria differ with regard to the assumed shear force redistribution. Shear redistribution from sector elements with higher rotations to sector elements with smaller rotations has been previously found to influence significantly the punching strength and corresponding rotation of slabs loaded and/or reinforced in a non-axisymmetric manner [Sag11].

For slabs subjected to monotonic loading, it is assumed that failure occurs when the shear force reaches the shear resistance for the hogging slab half. This criterion is denoted by CSCT(mono). For slabs subjected to cyclic loading, shear redistribution is neglected and failure is assumed to occur when the

sector subjected to the largest slab rotation reaches the CSCT-failure criterion. This is denoted by CSCT(cyc). In the following, the two failure criteria are described.

The failure criterion CSCT(cyc) applied to cyclically loaded slabs predicts smaller rotation capacities than the failure criterion CSCT(mono) applied to monotonically loaded slabs. Cyclic loading leads to an accumulation of plastic strains and therefore to an increase in crack opening with each cycle. If symmetric cycles are applied, ψ_{min} increases with increasing number of cycles. For the same slab rotation ψ_{scc}, ψ_{max} is therefore larger and so are the crack widths of the hogging slab half, which in turn lead to a reduced shear force redistribution between adjacent sector elements. To account for this phenomenon implicitly, different failure criteria are applied to monotonically and cyclically loaded slabs. This implicit approach is chosen since the analytical model developed in this chapter does not account for the effect of the loading history on the moment-rotation relationship. The next chapter proposes an extension of the analytical developed herein to account for cyclic loading and cumulative damage effects on the moment-rotation relationship.

4.3.1 Approach accounting for shear stress redistribution (CSCT(mono))

Based on the work of Sagaseta et al. on non-axisymmetric punching [Sag11], it is assumed that failure of monotonically loaded slabs occurs when the sum of the shear forces acting on the sector elements of the hogging slab half ($0 \leq \phi \leq \pi$) is equal to the sum of the shear resistance of these sector elements:

$$V_{R.hog} = \int_0^\pi v_R(\phi) \ (r_c{}' + d(\phi)) \ d\phi \tag{4.20}$$

where $r_c{}'$ is the nominal radius for shear calculations, which for square columns is adjusted to give the same perimeter, and $v_R(\phi)$ is the shear resistance per unit length in MN/m:

$$v_R(\phi) = \frac{0.75 \, d(\phi) \, \sqrt{f_c}}{1 + 15 \, \dfrac{\psi(\phi) \, d(\phi)}{d_g + d_{g.0}}} \qquad \text{(SI Units; N, mm)} \tag{4.21}$$

where f_c is the concrete compressive strength, d_g is the maximum aggregate size and $d_{g.0}$ is the reference aggregate size, which is assumed to be equal to 16 mm (0.63 in). For imperial units (psi, in.) factor 0.75 has to be replaced by 9. Note that the effective depth d changes with ϕ to account for the different effective depths for bending around the x-and y-axis. One can either apply a cosinusoidal interpolation for intermediate angles or use an average value for all angles. The former is applied for the calculations presented in this chapter and in Chapter 6, for validation purposes.

4.3.2 Approach based on the maximum rotation (CSCT(cyc))

In this chapter, the CSCT(cyc) approach is used for slabs subjected to cyclically increasing moment. This approach neglects a possible redistribution of the shear force to adjacent sector elements, which are subjected to smaller rotations than the maximum rotation ψ_{max}. It is assumed that punching failure occurs when the shear that is carried by the compression strut (that is developed along the shear crack) of the sector element with the maximum rotation ψ_{max} is equal to the shear resistance of this sector element. According to the CSCT [Mut08], the shear resistance of the sector element subjected to the maximum rotation ψ_{max} can be computed as:

$$V_{R.\pi/2} = \frac{0.75 \, b_o(\Delta\phi) \, d(\pi/2) \, \sqrt{f_c}}{1 + 15 \, \dfrac{\psi_{max} \, d(\pi/2)}{d_g + d_{g.0}}} \qquad \text{(SI Units; N, mm)} \tag{4.22}$$

where $b_o(\Delta\phi)$ is the part of the critical section that belongs to the sector element with the maximum rotation. The critical section is assumed to be at a distance of $d/2$ from the column face.

4.4 Lateral force-resisting mechanisms

A realistic estimation of the contribution of the three resisting mechanisms (eccentric shear force, flexure and torsion) to the overall capacity of the slab-column connection is rather difficult because of the non-linear behaviour of the slab-column connection and the fact that each resisting mechanism is associated to a different failure mode. As shown in §4.2.2 the proposed analytical model allows to predict the contribution of all resistance-providing mechanisms at any drift level (Eq. (4.9)). Figure 4.11 shows the influence of the gravity load and the reinforcement ratio on the predicted γ factors for the case of a flat slab panel with slenderness $L/d = 35$, as a function of the connection rotation ψ_{scc}. The predicted failure points are also represented in the same graphs (CSCT(cyc)). The assumed γ_f value according to ACI-318 (equal to 0.4 - [ACI14]) and the solution of an elastic homogeneous isotropic slab (equal to 0.33 - [Mas70]) are also shown in the same figure.
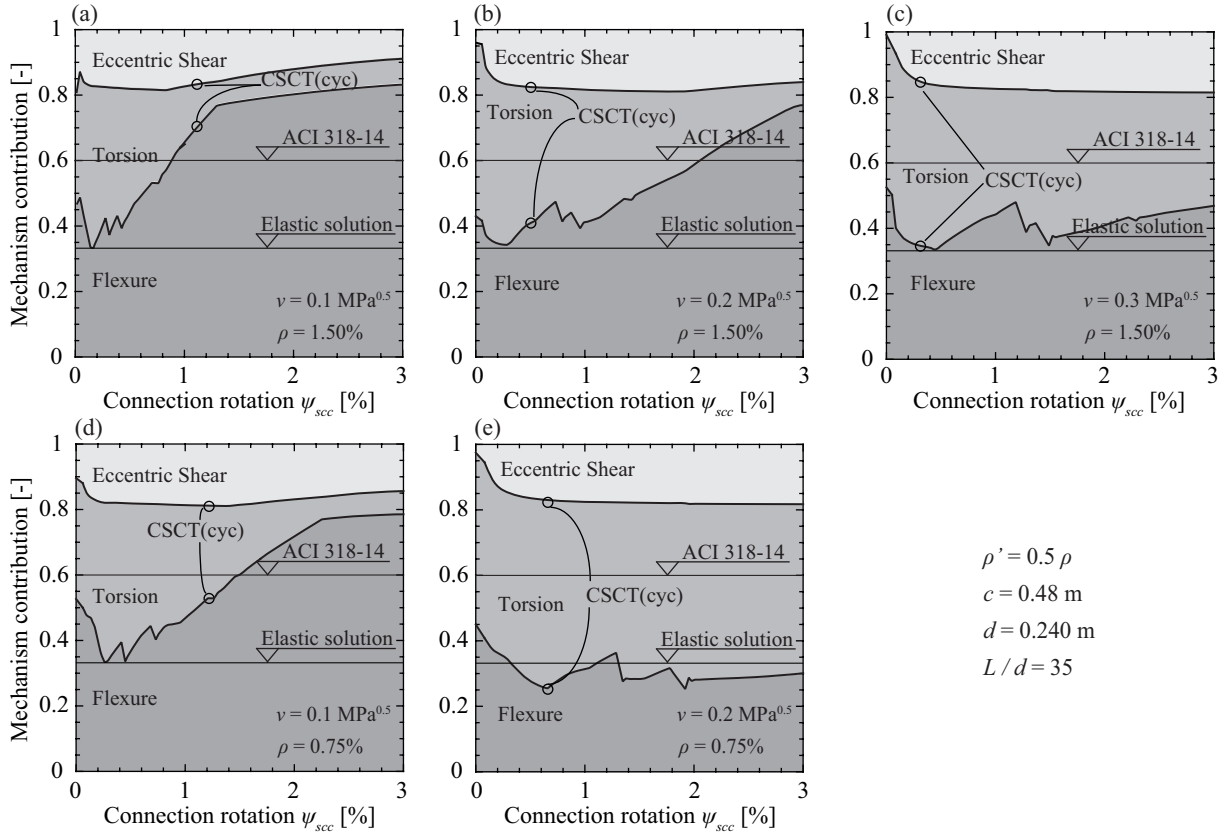
Figure 4.11 – Predicted contribution of flexure, torsion and eccentric shear force according to the proposed model ($\rho = 0.5\rho'$; $d = 240$ mm; $c = 2d$; $L = 35d$; $f_c = 30$ MPa; $d_g = 16$ mm and $f_y = 460$ MPa) for $\rho = 1.50\%$: (a) $\nu = 0.1$ $\sqrt{\text{MPa}}$; (b) $\nu = 0.2$ $\sqrt{\text{MPa}}$; (c) $\nu = 0.3$ $\sqrt{\text{MPa}}$; and for $\rho = 0.75\%$: (d) $\nu = 0.1$ $\sqrt{\text{MPa}}$; and (e) $\nu = 0.2$ $\sqrt{\text{MPa}}$.

As can be seen from Figure 4.11, large connection rotations ψ_{scc} lead to larger contribution of the flexure mechanism (i.e. higher γ_f values) compared to small ψ_{scc}. For the same ψ_{scc}, large gravity loads lead to smaller γ_f values and larger γ_v and γ_t values than low gravity loads. Moreover, γ_f attains larger values for higher flexural reinforcement ratio (Fig. 4.11a, b) than for smaller flexural reinforcement ratio (Fig. 4.11d, e). It can be observed that the predicted γ_f can reach values higher than the value assumed by ACI-318 [ACI14]. For large vertical loads (Fig. 4.11b, c, and e) the predicted γ_f value at failure is close to the elastic solution by Mast [Mas70].

In this chapter the effect of cyclic loading is accounted for only in the failure criterion (Section 4.3). Since the CSCT(cyc) predicts smaller connection rotation at failure than the CSCT(mono), cyclic

loading leads to smaller γ_f values than monotonic loading. On the other hand, the γ_v and γ_t values increase with cyclic loading.

In the following, the results of a parametric study on the influence of the flexural reinforcement ratio ρ and the slab slenderness L/d on the contribution of eccentric shear force (γ_v), flexure (γ_f) and torsion (γ_t) to the maximum unbalanced moment are presented. The results correspond to the intersection of the moment-rotation relationship (Section 4.2) and the failure criterion CSCT(cyc) (§4.3.2). The calculations were performed for the case of a continuous flat slab ($B = 0.44L$ and the same rotation and deflection at $r = 0.5L$). Since the gravity load is the parameter with the largest influence on the contribution of the different resisting mechanisms at failure (Fig. 4.11), the abscissas of all the following graphs of this section represent the normalised shear force applied to the slab-column connection (as defined in Section 3.4). The predictions are plotted until the gravity load that corresponds to zero rotation capacity ψ_{slab} at punching (dashed lines). Other parameters such as the boundary conditions and the slab thickness were found to affect the predicted γ values only to a minor extent.

4.4.1   Reinforcement ratio effect

Figure 4.12 shows the influence of the reinforcement ratio on the γ factors predictions at failure (CSCT(cyc)). As can be seen, higher reinforcement ratio leads to increased flexure contribution while the eccentric shear force contribution remains almost unaffected, as has been observed by others [Meg00]. It is also shown that for high gravity loads (GSR > 0.60), high ρ leads to γ_f values that are closer to the elastic solution by [Mas70] than small ρ.
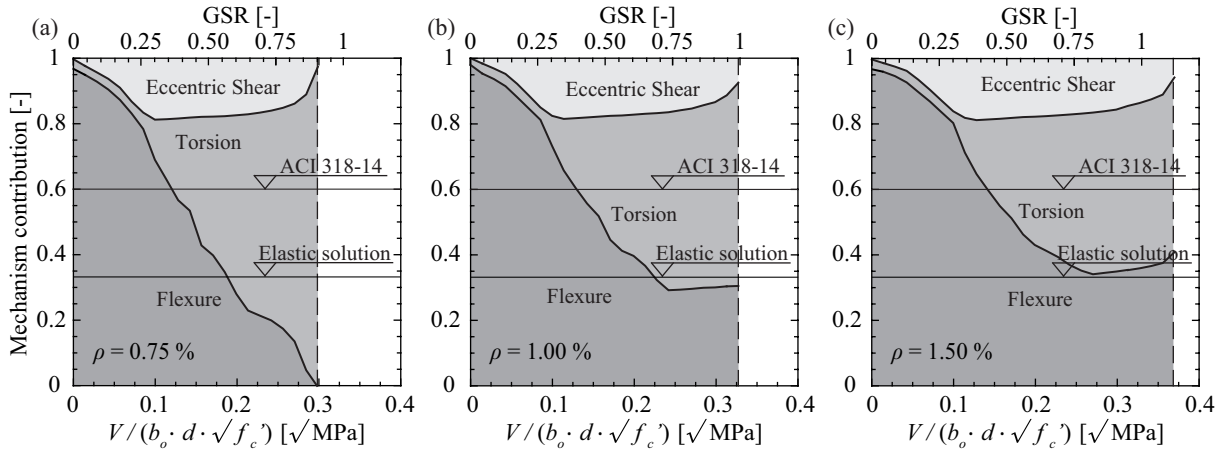
Figure 4.12 – Predicted contribution of flexure, torsion and eccentric shear force as a function of the applied gravity load ($d = 240$ mm; $c = 2d$; $f_c = 30$ MPa; $L = 35d$; $d_g = 16$ mm and $f_y = 460$ MPa) for ρ equal to: (a) 0.75%, (b) 1.00%, and (c) 1.50%.

4.4.2   Slenderness

Figure 4.13 shows the influence of the slab slenderness L/d on the contribution of flexure, torsion and eccentric shear force. It is shown that for the same normalised shear force ν, higher slenderness results in significantly smaller γ_v and γ_f values which are counterbalanced by higher γ_t values.
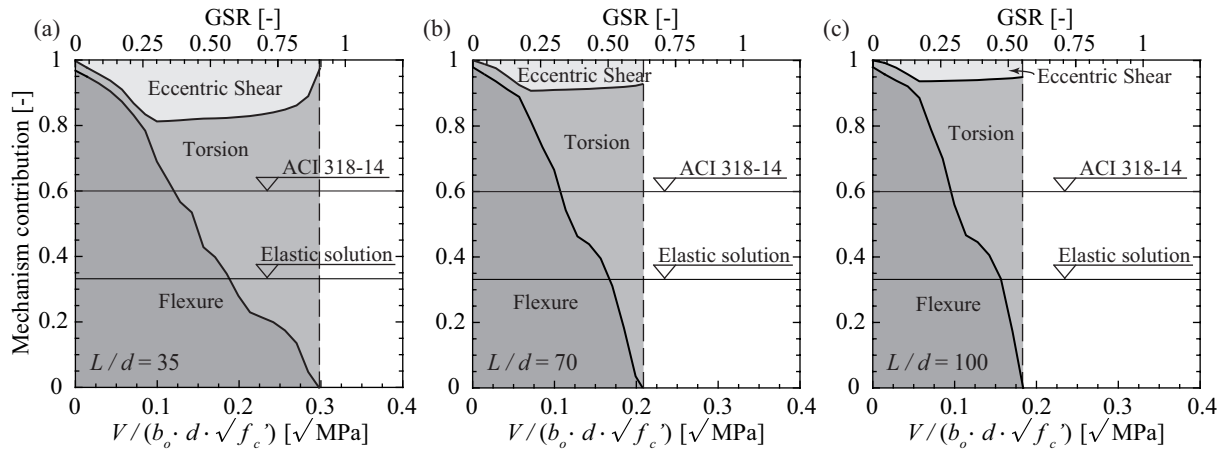
Figure 4.13 – Predicted contribution of flexure, torsion and eccentric shear force as a function of the applied gravity load ($d = 240$ mm; $c = 2d$; $f_c = 30$ MPa; $\rho = 0.75\%$; $d_g = 16$ mm and $f_y = 460$ MPa) for slenderness L/d equal to: (a) 35, (b) 70, and (c) 100.

4.5 Seismic rotation capacity

Figure 4.14 shows the predicted slab rotation ψ_{slab} at peak moment according to the analytical model. The drift limit of ACI-318 [ACI14] and the drift limit proposed by Hueste and Wight [Hue99] are also shown in the same graphs. All graphs of Figure 4.14 show that the larger the gravity induced shear the smaller the rotation capacity of slab-column connections, as has been observed by others [Pan89, Hue99, Bro09, Cho14]. The model proposed in this chapter accounts for the effect of cyclic loading through the failure criterion (CSCT(cyc) against (CSCT(mono)). Figure 4.14a shows that the predicted deformation capacity under cyclic loading is approximately 5-45% smaller than for monotonic loading. The reduction in rotation capacity due to cyclic loading is more important for smaller gravity loads, confirming prior experimental observations [Dra16].

The model confirms Broms' observation that the rotation capacity decreases with increasing depth of the slab (Fig. 4.14b). Although the top reinforcement ratio influences significantly the local slab rotations, its effect on the rotation capacity of the slab-column connection is less pronounced (Fig. 4.14b). The slenderness ratio L/d of the slab has only a smaller effect on the rotation capacity. For smaller gravity loads, higher slenderness confers higher rotation capacity but the trend inverses for higher gravity loads.

The drift limit of ACI-318 [ACI14] for flat slabs represents a safe approach for a slab with $d = 120$ mm. However, a slab with $d = 240$ mm reaches the rotation capacities predicted by ACI-318 [ACI14] only for a gravity load ratio GSR between 0.55 and 0.7 (Fig. 4.14b). This is expected since the drift limit of ACI-318 [ACI14] is based on experimental research on slabs with thickness $h \leq 152$ mm.

If a minimum rotation capacity, for instance 0.5%, is required for the slab-column connection, the 120 mm slab meets this requirement for every gravity load value (as long as GSR < 1). For the 240 mm slab, the gravity load ratio GSR has to be limited to 0.7 in order to reach a drift of 0.5%. If the building is designed for a drift value of 2.0%—a value that is often quoted as drift limit for RC wall buildings—the GSR must be smaller than 0.35 for slabs with $d = 120$ mm, which is close to the value proposed by Hueste and Wight [Hue99] (GSR < 0.36). For slabs with $d = 240$ mm, the GSR must be limited to 0.22. This discussion accounted only for the contribution of the slab deformations to the interstorey drift. The effective interstorey drift capacity will be larger than the calculated slab rotation since also the column deformation will contribute to the interstorey drift capacity (Eq. (3.2)). The column deformation contribution to the interstorey drift is typically smaller than 10% when the column is assumed uncracked but can increase over 20% when column cracking is accounted for.
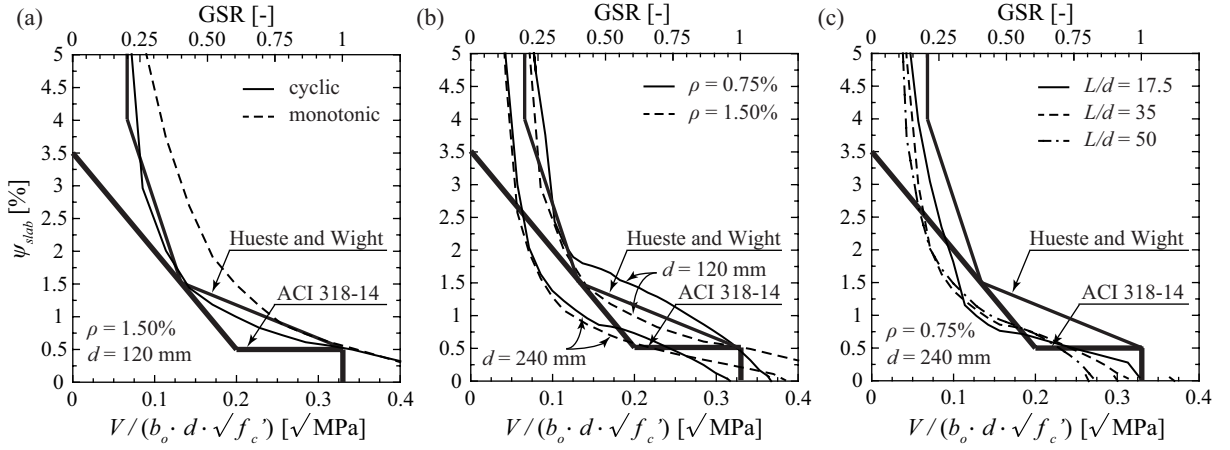
Figure 4.14 – Predicted slab rotation at peak moment and allowable drift limit according to ACI-318 [ACI14] and Hueste and Wight [Hue99] ($c = 2d$; $f_c = 30$ MPa; and $f_y = 460$ MPa): (a) Influence of loading conditions (cyclic vs monotonic) ($L = 35d$; $d_g = 16$ mm); (b) Influence of slab effective depth and reinforcement ratio on the seismic rotation capacity ($L = 35d$; $d_g = 16$ mm); and (c) Influence of slenderness ratio L/d on the seismic rotation capacity ($d_g = 16$ mm).

Figure 4.15 shows the influence of column size on the predicted rotation capacity. For the same level of gravity loads larger column results in higher rotation capacity. This effect is more pronounced for small reinforcement ratios (Fig. 4.15a) than for high reinforcement ratios (Fig. 4.15b).
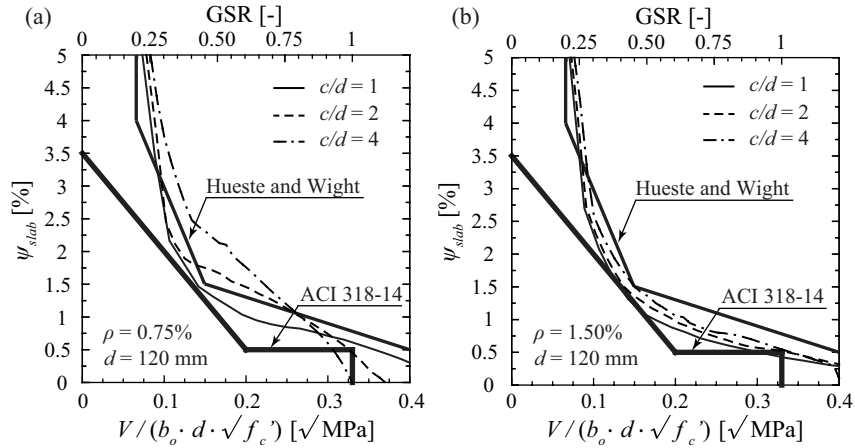
Figure 4.15 – Predicted slab rotation at peak moment and allowable drift limit according to ACI-318 [ACI14] and Hueste and Wight [Hue99] ($d = 120$ mm; $L = 35d$; $f_c = 30$ MPa; $d_g = 16$ mm; and $f_y = 460$ MPa) - Influence of column size for: (a) $\rho = 0.75\%$; and (b) $\rho = 1.50\%$.

4.6 Comparison with the performed tests

This section compares the experimental moment-rotation response of the monotonically and cyclically tested slabs (Chapter 3) with the predicted moment-rotation response according to the proposed analytical model (Figs. 4.16 and 4.17, respectively). Figure 4.16 shows that the predicted moment-rotation curves follow the experimental trend rather well. The moment strength is predicted accurately enough by the combination of the proposed model with the CSCT(mono) failure criterion. For the corresponding connection rotation, if PD1 is excluded (due to inconsistent rotation measurement) the model predictions are rather on the safe side. More detailed comparisons of the model predictions with the results of the monotonic tests performed within the current research as well as monotonic tests found in the literature are presented in Chapter 6.
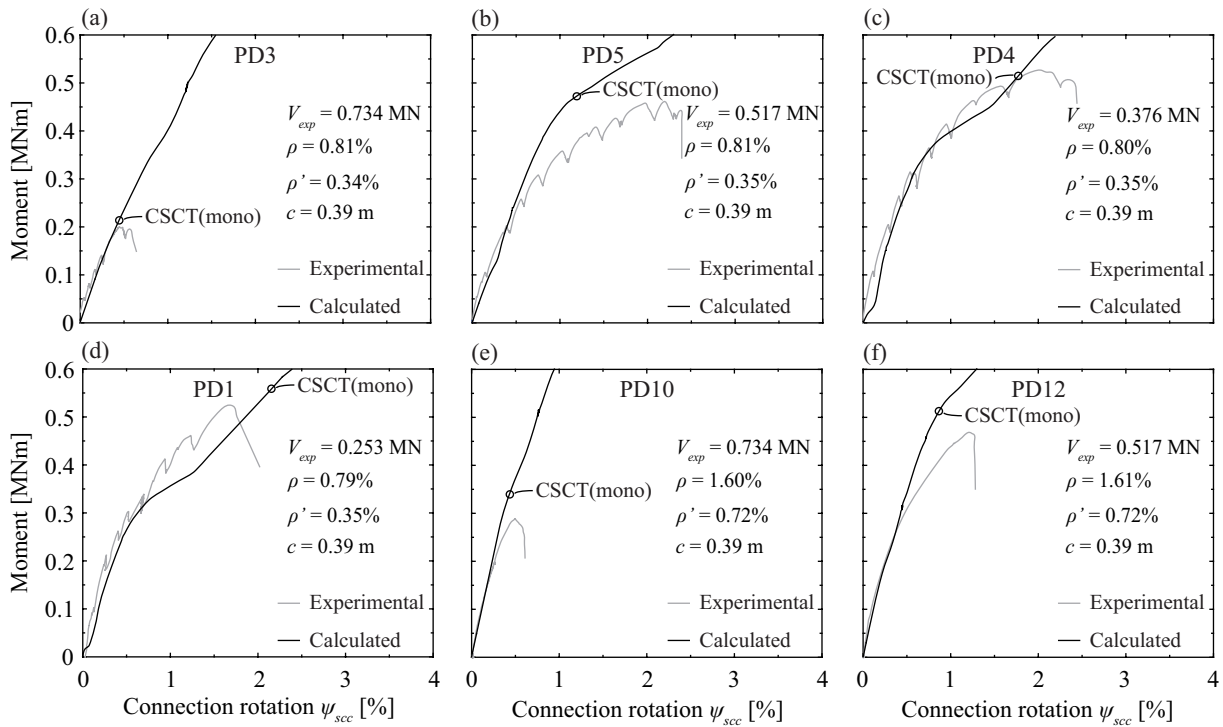
Figure 4.16 – Comparison between experimental and calculated moment-connection rotation curves for the monotonic tests performed within the present research: (a) PD3, (b) PD5, (c) PD4, (d) PD1, (e) PD10, and (f) PD12.
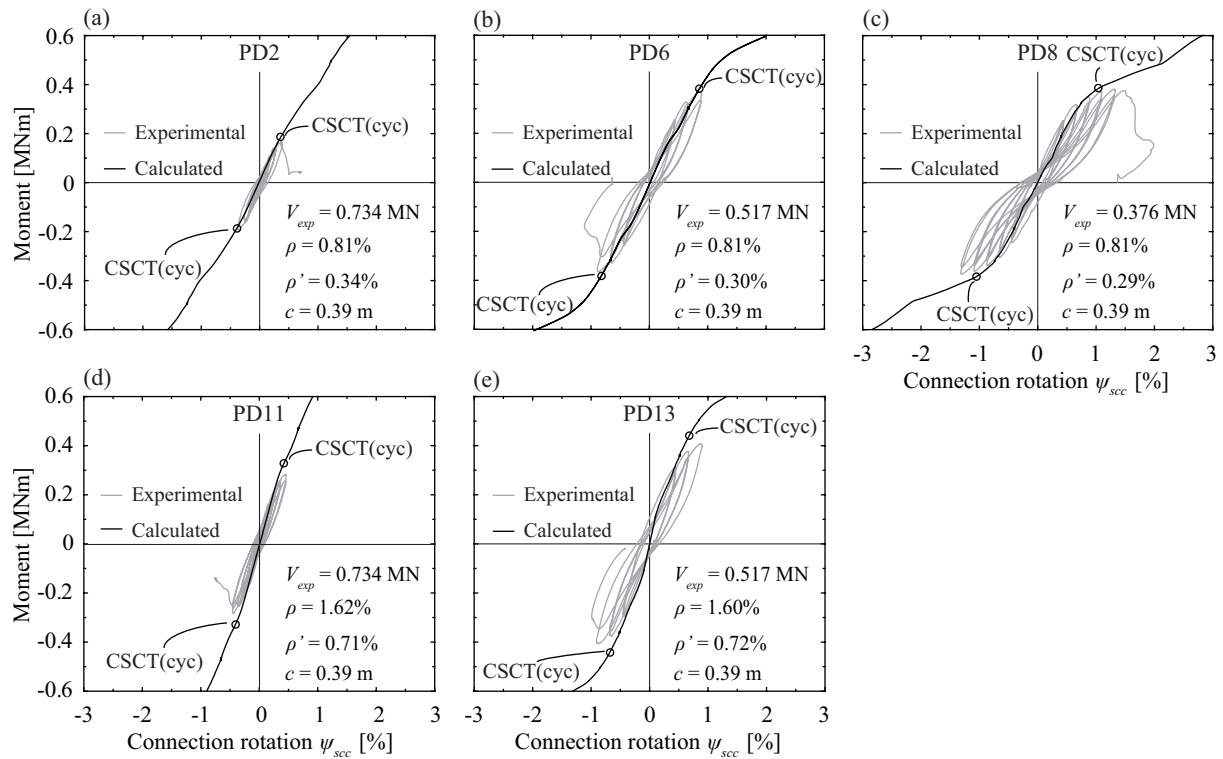
Figure 4.17 – Comparison between experimental and calculated moment-connection rotation curves for the cyclic tests performed within the present research: (a) PD2, (b) PD6, (c) PD8, (d) PD11, and (e) PD13.

Figure 4.17 shows that the monotonic analytical model predicts the envelope of the experimental response of most performed cyclic tests rather well. For low gravity loads acting on the slab-column connection, the predicted response is slightly stiffer than the experimental response. Combination of the analytical model with the CSCT(cyc) failure criterion gives the moment strength (M_{max}) and the corresponding connection rotation ($\psi_{scc.max}$) of the slab-column connection for cyclic loading conditions. As can be seen from Figure 4.17, both M_{max} and $\psi_{scc.max}$ are predicted accurately enough for most performed cyclic tests, in particular for large gravity loads. For low gravity loads acting on the slab, the deformation capacity predictions become conservative (PD8 - Fig. 4.17c). Figure 4.16c shows that the moment-rotation response, the M_{max} and the $\psi_{scc.max}$ are predicted very well for the monotonic counterpart of PD8. The influence of cyclic loading on the moment-rotation response of slabs with low gravity loads was already pointed out in the previous chapter (§3.8.3). Therefore, the discrepancy between calculated and measured deformation capacity for PD8 (Fig. 4.17c) could be attributed to the influence of the loading history on the moment-rotation curve. The following chapter presents an extension of the monotonic analytical model for the moment-rotation relationship to account for the effect of cyclic loading.

4.7 Conclusions

The present chapter proposes a mechanical model to describe the moment-rotation relationship of slab-column connections without transverse reinforcement subjected to seismically-induced deformations. The model accounts explicitly for the three different load transfer actions between slab and column, i.e., eccentric shear, flexure and torsion. The failure criterion of the Critical Shear Crack Theory (CSCT) [Mut08] is adapted to predict the moment and rotation capacity. The effect of cyclic loading is considered by neglecting shear force redistribution between sector elements of the hogging slab half. In the present chapter the effect of cyclic loading on the moment-rotation relationship is neglected. The main points of this chapter are:

1. When an unbalanced moment is introduced to a slab-column connection, the value of the rotation of the sector elements outside the shear crack (or local rotation) changes at varying angles with respect to the direction of excitation. Finite element analyses and experimental work (Chapter 3) show that the local rotations follow approximately a sinusoidal law.

2. To obtain the moment-rotation relationship the equilibrium is formulated both locally for each sector element and globally for the entire slab until $0.22L$. The influence of the slab part between $0.22L$ and $0.50L$ on the moment-rotation response is considered using the Effective Beam Width method. The calculation is iterative with regard to the maximum and the minimum local slab rotations.

3. According to the proposed model the contribution of flexure (γ_f) to the total moment resisted by the slab-column connection increases for increasing connection rotation and can attain values higher than the value assumed by ACI-318 [ACI14]. The predicted γ values at failure were found to depend primarily on the load history (cyclic vs monotonic), the reinforcement ratio ρ, and the slab slenderness: (a) Cyclic loading results in smaller γ_f values at failure than monotonic loading; (b) High ρ leads to larger γ_f values than small ρ; (c) Increasing slab slenderness L/d results in smaller γ_f and γ_v values which are counterbalanced by larger γ_t values.

4. The model confirms what has been shown experimentally (Chapter 3) that cyclic loading leads to smaller slab rotation capacities than monotonic loading. It is confirmed that the smaller the gravity loads, the larger the reduction in rotation capacity due to cyclic loading.

5. It is shown that the seismic rotation capacity of flat slabs is primarily influenced by the gravity induced shear and the slab effective depth but also by the column size, top reinforcement ratio and to a smaller extent by the slab slenderness. Since increasing slab effective depth leads to

decreasing rotation capacity, empirical models should not be applied to slabs with larger depths than those used for the calibration of the model.

6. The predictions of the proposed model combined with the CSCT(mono) failure criterion in terms of moment capacity are in good agreement with the results of the monotonic tests performed within this research (Chapter 3), while the deformation capacity predictions are on the safe side. For the cyclic tests, combination of the analytical model with the CSCT(cyc) failure criterion gives good overall predictions of the moment strength and the corresponding connection rotation for high and intermediate gravity loads. The deformation capacity predictions for slabs subjected to low gravity loads are slightly conservative.

Chapter 5

Analytical model for cyclically increasing drifts

The seismic design and assessment of structures with flat slabs and columns requires as input estimates of the moment-rotation relationship and the rotation capacity of slab-column connections. Until today, research efforts on slab-column connections with unbalanced moment concentrated on the derivation of empirical relationships between the normalised shear force acting on the slab and the rotation capacity of the slab-column connection [Pan89, Hue99].

The cyclic tests carried out within the present research have shown that cyclic loading can lead to significant degradation and consequently reduction of the moment strength and the corresponding connection rotation determined through monotonic tests (Chapter 3). Moreover, the monotonic analytical model presented in Chapter 4 tended to be rather conservative with respect to the deformation capacity of slabs subjected to low gravity loads. This chapter presents a more detailed model for considering the degradation due to cyclic loading when calculating the moment-rotation relationship of internal slab-column connections without transverse reinforcement. The developed model is an extension of the mechanical model proposed in Chapter 4.

Section 5.1 presents correlations regarding the strength degradation, the shear crack inclination, the shape of the hysteresis loops, and the shear crack opening/closing process through local deformation measurements from the cyclic tests performed within this thesis. This information provides more in-depth understanding of the cyclic behaviour of slab-column connections and can be very valuable for developing hysteretic models and seismic damage models for slab-column connections.

In Section 5.2, the monotonic mechanical model for the moment-rotation relationship presented in the previous chapter is extended to cyclic loading. This section focuses on the assumptions that are required in addition to those of the monotonic model (shear crack inclination, moment-curvature relationship, and seismic damage). Section 5.3 presents the adopted failure criterion, while the Section 5.4 compares the predictions of the cyclic model (combined with the failure criterion) with the results of the experimental campaign.

Next the effect of the loading history on the response of slab-column connections is discussed (Section 5.5), while Section 5.6 discusses the effect of loading history on the contribution of the different lateral force-resisting mechanisms to the total unbalanced moment.

Section 5.7 describes an extension of the Effective Beam Width method proposed in Chapter 4 (to calculate the contribution of the outer slab part to the total slab deformation) for cyclic loading.

The last section presents the effect of gravity load, seismicity level, slab depth, reinforcement ratio and slab slenderness on the seismic rotation capacity of slab-column connections according to the proposed cyclic model.

5.1   Local deformation measurements from tests

This section presents several local deformation measurements from the experiments carried out within this research. The main objective is to identify trends and correlations that are valuable for developing hysteretic models and damage models for slab-column connections subjected to combined vertical load and unbalanced moment. This information will be used later in this chapter to extend the analytical model presented in Chapter 4 (monotonic loading conditions) to account for the effect of cyclic loading. First, a correlation is attempted between the moment strength degradation and the maximum slab rotation reduction due to cyclic loading, while §5.1.2 aims at correlating the shear crack inclination with the onset of flexural reinforcement yielding. §5.1.3 aims at identifying specific features of the hysteretic slab response related to the shape of the loading-unloading loops.

5.1.1   Correlation between moment strength degradation and maximum slab rotation reduction due to cyclic loading

Figure 5.1 shows the correlation between the peak unbalanced moment reduction due to cyclic loading and the maximum slab rotation reduction due to cyclic loading for the five slab pairs that were tested under monotonic and cyclic loading within the current research (Chapter 3).
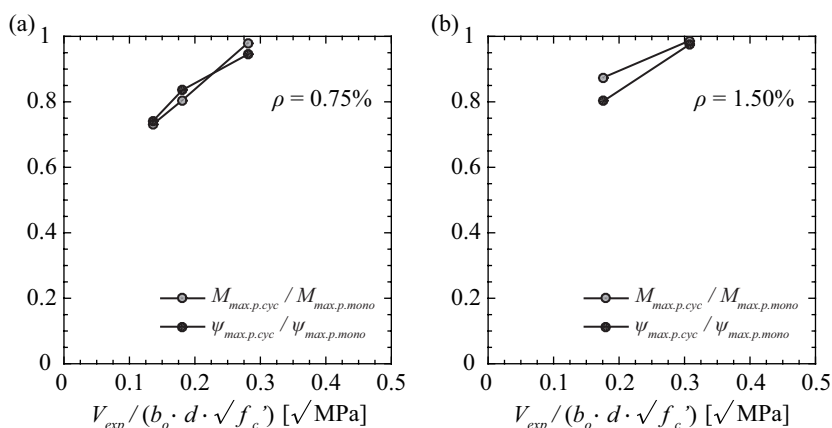
Figure 5.1 – Comparison between moment strength degradation and reduction of maximum slab rotation due to cyclic loading as function of the normalised shear force for slabs with (a) $\rho = 0.75\%$, and (b) $\rho = 1.50\%$.

It can be seen that the ratio $\psi_{max.p.cyc}/\psi_{max.p.mono}$ gives a rather good estimate of the strength degradation exhibited by the tested slab-column connections. In addition, the strength degradation decreases with increasing gravity load acting on the slab. This is in agreement with what has been shown experimentally on the global level (Chapter 3). Local information regarding the influence of cyclic loading on the behaviour of the tested specimens was provided by strain measurements at selected locations on the reinforcing bars and on the concrete surface, and by crack opening measurements. The latter ones provide direct measurement of the shear crack opening during unbalanced moment reversals and are therefore very valuable for assessing the effect of loading history on the crack opening-closing process. Figures 5.2 and 5.3 compare the measured crack opening - unbalanced moment relationship for monotonically tested slabs (black curves) and cyclically tested slabs (red curves) with $\rho = 1.50\%$.
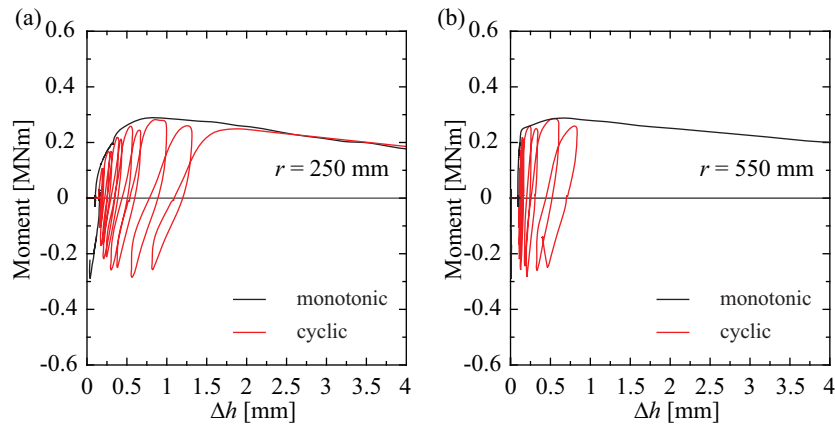
Figure 5.2 – Measured thickness variation for monotonic and cyclic tests with $\rho = 1.50\%$ ($\nu = 0.29$) along the x-axis (see Fig. 5.4): (a) $r = 0.25$ m and (b) $r = 0.55$ m.
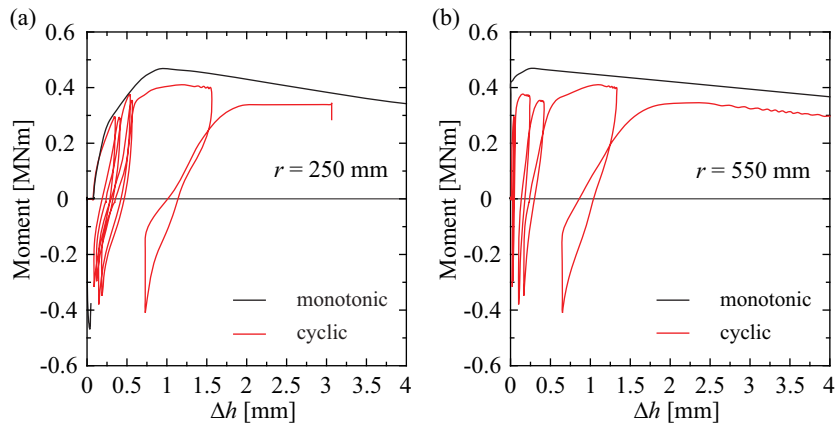
Figure 5.3 – Measured thickness variation for monotonic and cyclic tests with $\rho = 1.50\%$ ($\nu = 0.19$) along the x-axis (see Fig. 5.4): (a) $r = 0.25$ m and (b) $r = 0.55$ m.

The crack opening measurements confirm that cyclic degradation is more important for low gravity loads acting on the slab (Fig. 5.3) than for high gravity loads (Fig. 5.2).

Regarding the effect of loading history on the deformation capacity, cyclic loading leads to more pronounced reduction of the connection rotation at peak $\psi_{scc.max}$ than the moment strength M_{max}, as discussed in Chapter 3. This is attributed to significantly larger minimum slab rotations at peak for the cyclic tests compared to their monotonic counterparts due to accumulation of plastic rotations during moment reversals.

5.1.2 Correlation between shear crack inclination and top reinforcement yielding

Figure 5.4 shows the shear crack inclination for monotonic and cyclic tests performed within the experimental campaign. In the same figure, the locations where top reinforcement strains were measured are also indicated (circular markers). Strains measured at specified locations of the top reinforcement along the x-axis (strong axis) are shown in Figures 5.5 and 5.6 for slabs with $\rho = 0.75\%$ and 1.50%, respectively, as function of the unbalanced moment.
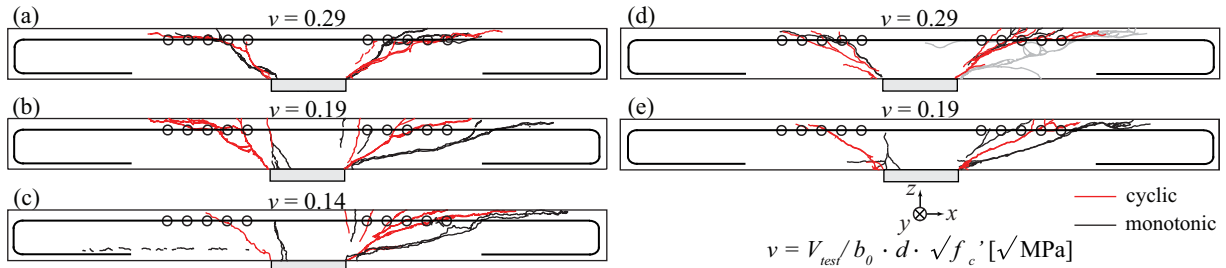
Figure 5.4 – Saw cuts for slabs tested under monotonically and cyclically increasing moments and locations where reinforcement strains where measured: (a) $\rho = 0.75\% - \nu = 0.29$, (b) $\rho = 0.75\% - \nu = 0.19$, (c) $\rho = 0.75\% - \nu = 0.14$, (d) $\rho = 1.50\% - \nu = 0.29$, and (e) $\rho = 1.50\% - \nu = 0.19$.
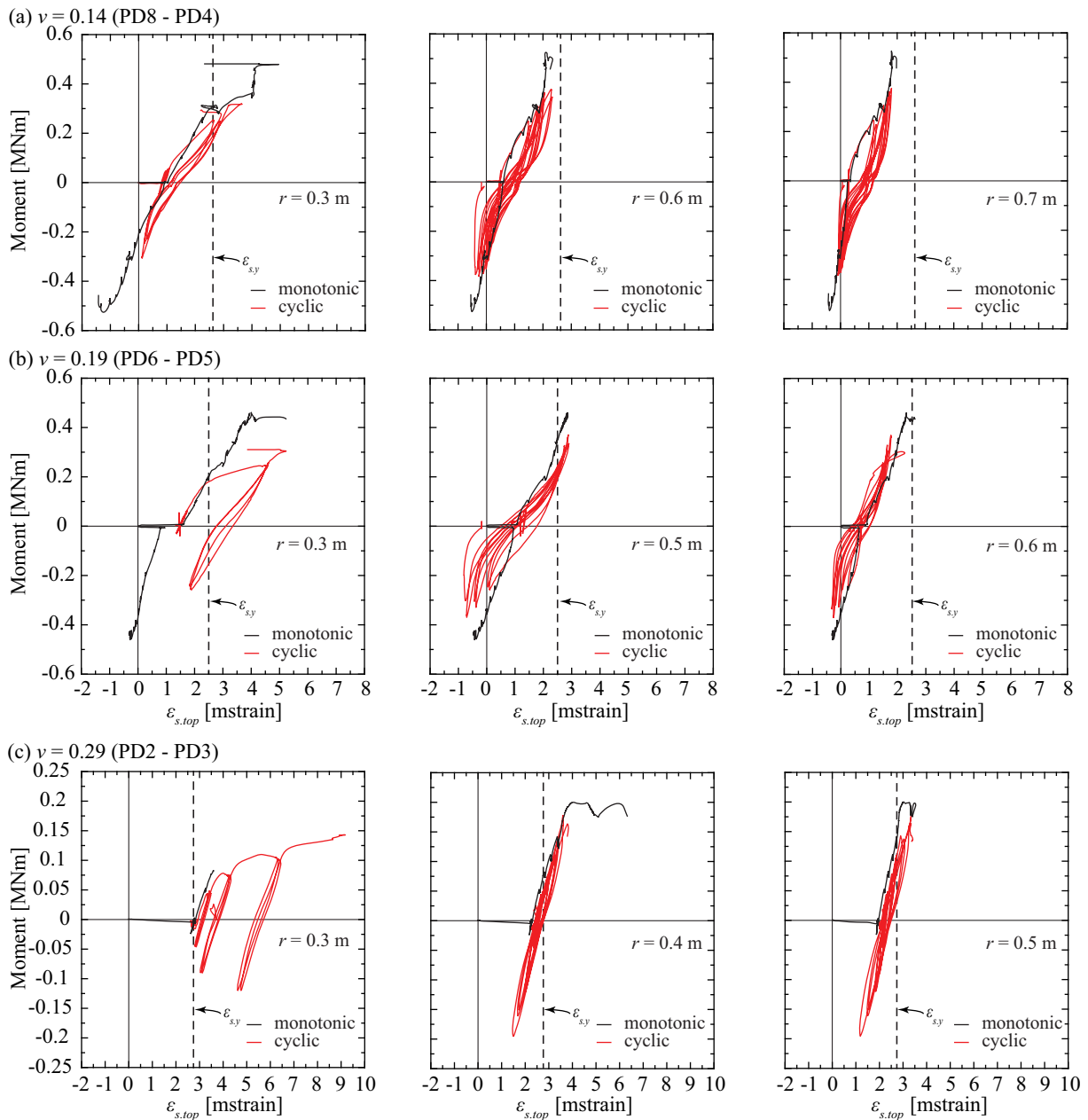
Figure 5.5 – Strain gauge measurements at specified locations of top reinforcing bars along the x-axis for monotonic and cyclic tests with $\rho = 0.75\%$, for ν equal to (a) 0.14, (b) 0.19, and (c) 0.29.

Figure 5.4 shows that cyclic loading results in steeper cracking angles than monotonic loading. This is more pronounced for low gravity loads (Fig. 5.4b, c, and e) than for high gravity loads (Fig. 5.4a, and d).

Figure 5.5b and c shows that for relatively small distances from the column centre ($r = 0.3$ m) the top reinforcement is yielding rather early. Figure 5.4a and b indicates that flexural cracks cross the top rebar at approximately this location ($r = 0.3$ m - circular markers closest to the column). For steel strains larger than the yield strain, cyclic loading resulted in significant concentration of permanent inelastic strains in the slab half subjected to hogging moments. For this reason, cyclic loading (i.e. alternation of hogging and sagging slab halves) did not lead to appearance of compressive strains in the sagging slab half (red curves, Figure 5.5). On the other hand, monotonic loading (black curves, Figure 5.5) for slabs with $\nu \leq 0.19$ led to compressive strains on the top reinforcing bars of the sagging slab half at the column proximity ($r = 0.3$ m). This section focuses on the correlation between flexural reinforcement yielding and shear crack inclination. For this purpose, only strain gauge data in the proximity of shear cracks will be discussed in the following, while measurement of reinforcement strains in the proximity of flexural cracks will not be discussed any further in this chapter.
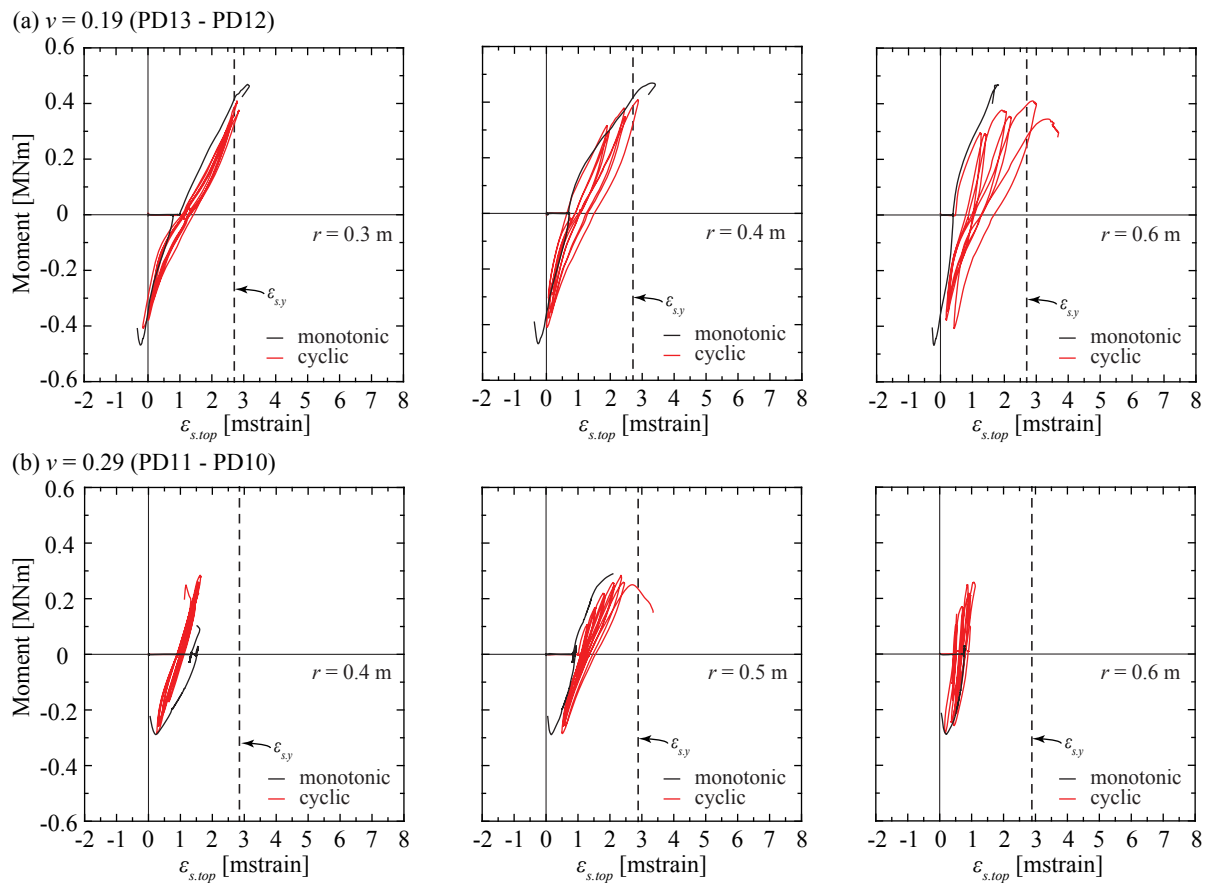
Figure 5.6 – Strain gauge measurements at specified locations of top reinforcing bars along the x-axis for monotonic and cyclic tests with $\rho = 1.50\%$, for ν equal to (a) 0.19, and (b) 0.29.

For slab PD2 that responded in the inelastic range already under vertical load, Figure 5.5c shows that the shear crack was already open after the vertical load application and, therefore, no steeper shear crack could appear during the unbalanced moment introduction. Figure 5.4a shows that for both monotonic and cyclic tests the radius at which the shear crack crosses the top reinforcement is $r_0 \approx r_c + d$ (see also Chapter 4), where r_c is the column radius and d the slab effective depth. Shear cracks steeper than 45 degrees were not observed from the saw cuts prepared after the tests have been completed.

For slabs that responded in the elastic range under vertical load but in the post-elastic range (i.e. the range where the top reinforcement in the vicinity of the shear crack reached the yield strain) during the introduction of unbalanced moment, a correlation trend was identified between shear crack inclination and eccentricity at first post-yield peak. For slab PD6 ($\rho = 0.75\%$ - $\nu = 0.19$), Figure 5.5b shows that vertical load induced only elastic strains while first unloading from post-elastic reinforcement strains occurred at eccentricity $e = M/V = 0.62$ m, which is rather close to the experimentally observed shear crack inclination at failure from Figure 5.4b ($r_0 = 0.56$ m). For slab PD8 ($\rho = 0.75\%$ - $\nu = 0.14$), which also responded in the elastic range under vertical load, it was not possible to establish such a correlation because the strain gauges did not record any plastic strains (Fig. 5.5a). This can be probably attributed to the fact that the shear crack crosses the rebar between two adjacent strain gauges (Fig. 5.4c). For slab PD13 ($\rho = 1.50\%$ - $\nu = 0.19$), first unloading from post-elastic reinforcement strains occurred at eccentricity $e = 0.75$ m (Fig. 5.6a). This eccentricity is close to the experimentally observed radius where the shear crack crosses the reinforcement, which can be taken from Figure 5.4e ($r_0 = 0.68$ m). For slab PD11 ($\rho = 1.50\%$ - $\nu = 0.29$), careful observation of the saw cut (Fig. 5.4d) indicates that the shear crack crosses the reinforcement at $r_0 \approx 0.45$ m, i.e. between two adjacent strain gauges (Fig. 5.6b). Since $e_{max} = 0.39 < r_c + d$, even unloading from the maximum attained eccentricity did not result in shear crack steeper than 45 degrees, like for slab PD2.

Based on these observations, one can conclude that the cyclic behaviour of slab-column connections responding into the inelastic range is dominated by the opening-closing of a fixed shear crack rather than a rotating crack, which was observed for monotonic tests and adopted by the analytical model for monotonically increasing drifts (Chapter 4 and [Dra14]). The radius at which this single shear crack crosses the top flexural reinforcement correlates rather well with the eccentricity of the slab-column connection at first unloading from the post-elastic range. The lower-bound radius at which the top reinforcement is crossed by the shear crack is $r_c + d$ (i.e. distance d from the column edge, Fig. 5.4).

5.1.3 Shape of the hysteresis loops

The cyclic flexural behaviour of beam-type RC members with asymmetrical reinforcement subjected to moment loading is characterised by asymmetric hysteresis loops due to the different top and bottom reinforcement contents ($\rho > \rho'$). The difference between ρ and ρ' leads to different positive and negative moment capacities. Moreover, compared to symmetrically reinforced RC members ($\rho = \rho'$), a diversified regime in the accumulation process of plastic strains in the reinforcement of each side has been observed experimentally [Ma76]: when ρ goes from tension to compression, ρ' is not sufficient to drive ρ to yielding in compression and therefore the plastic tensile strains developed at positive loading are not compressed. On the other hand, when ρ' has previously yielded in tension and goes from tension to compression it yields soon in compression. Therefore the flexural crack closes soon and the stiffness increases again. This effect, subsequently denoted as "pinching effect", is identified by inverted-S unloading-reloading loops with rather low dissipated energy. For asymmetrically reinforced RC sections, the pinching effect is, therefore, more marked when the smaller reinforcement ratio ρ' is loaded from tension to compression [Far09].

For the shape of the hysteresis loops in symmetrically loaded RC members where shear effects are significant, pinching of the response is associated with the deterioration of the aggregate interlock along diagonal cracks and the appearance of plastic tensile strains in the flexural and shear reinforcement. The response is characterised by steep initial unloading and rather steep final reloading in the opposite direction. The intermediate phase is characterised by lower slope, indicator of less restrained slippage between the two faces of the shear crack until hard contact is achieved again.

RC slabs subjected to combined vertical load and unbalanced moment (as the ones tested within this thesis) present load asymmetry in addition to the reinforcement asymmetry. The application of gravity load prior to the unbalanced moment introduction results in appearance of tensile strains in

the top reinforcement at zero unbalanced moment. In the following, local measures of crack opening, reinforcement strain, and concrete strain are discussed so as to provide better understanding of the shape of the loading-unloading loops.

Crack opening

Crack opening measurements can provide valuable information on the shear crack opening-closing process, the overall shape of the hysteresis loops as well as the gradual stiffness degradation exhibited during the performed cyclic tests. The shear crack opening-closing process was monitored using slab thickness variation measurements. Figures 5.7a and b show the influence of the loading history on the measured crack openings in the connection proximity ($r = 0.25$ m) for different gravity loads and reinforcement ratios. For comparison purposes the shear force-stirrup strain of a cantilever T-beam tested by Ma et al. under cyclic shear [Ma76] is shown in Figure 5.7c.
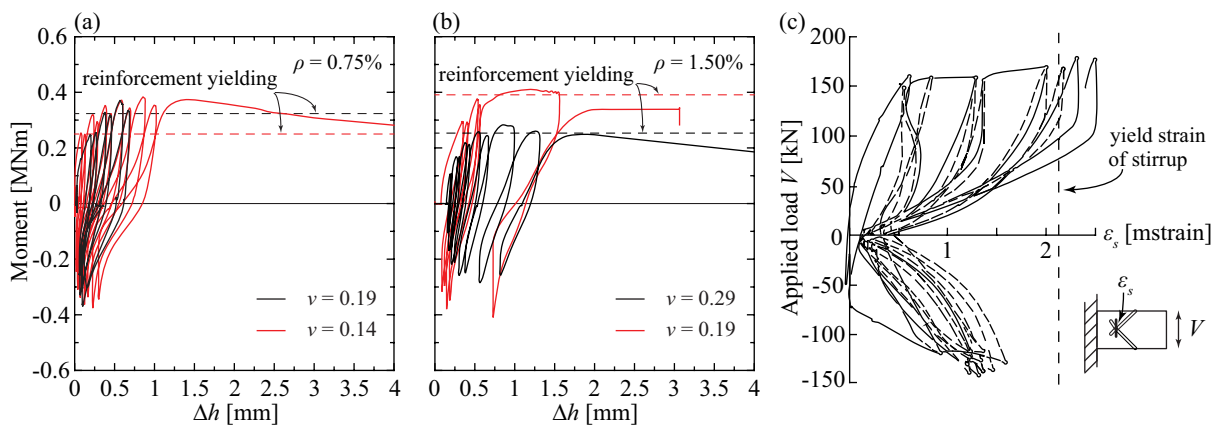
Figure 5.7 – Comparison of measured thickness variation between cyclically tested slabs for different gravity loads along the strong axis ($r = 0.25$ m): (a) $\rho = 0.75\%$ and (b) $\rho = 1.50\%$. (c) Shear force - stirrup strain for a T-beam subjected to cyclic shear [Ma76].

Concerning the shear crack opening-closing process, Figure 5.7c shows that for T-beams subjected to cyclic shear, the recorded stirrup strain attains values close to zero for small applied loads while the $V - \varepsilon_s$ curve has very small stiffness for near zero shear force V. Therefore, it can be deduced that the stirrup strain is suppressed and the shear crack closes. Loading in the reverse direction leads to tension in the reinforcement of the opposite side and opening of a shear crack perpendicularly to the previously closed one. On the contrary, Figures 5.7a and b show that for the tested slabs (Chapter 3) the increase in thickness at zero unbalanced moment is larger than zero. This indicates that the shear crack remains open when loading in the opposite direction.

The measurement of the crack opening can also provide better insight into the accumulation of plastic crack openings and plastic rotations that are associated with them, which influence significantly the cyclic behaviour of slab-column connections. As can be seen from Figures 5.7a and b, during unloading-reloading in the elastic range, crack openings due to moment introduction are recovered, with minor unrecoverable crack openings being attributed to the negative tension stiffening effect. Yield crack opening corresponds to the beginning of reinforcement yielding (§5.1.2). Post-yield behaviour is characterised by appearance of plastic crack openings, which correspond to plastic reinforcement strains. For loading in the post-elastic range, increase of the plastic rotation is assumed to occur after reaching the peak rotation of the previous cycle in the same direction. This assumption is consistent with the definition of plastic crack opening for monotonic loading and has already been adopted by others [Tak70]. Table 5.1 compares the elastic crack opening (or thickness variation) for the cycle before the peak unbalanced moment (Δh_{el}) and the crack opening difference between positive and negative

peak at M_{max} $(\Delta h_p^+ - \Delta h_p^-)$ for the specimens for which crack opening measurements were available. Comparison of columns 2 and 5 of Table 5.1 shows that at M_{max} no compression of plastic crack openings occurred for the tested slab-column connections during unloading and loading in the opposite direction.

Table 5.1 – Elastic crack opening and difference between peak crack openings at M_{max} for the cyclic tests for which crack opening measurements were available (sorted by increasing vertical load and reinforcement ratio)

Slab name	Δh_{el} [mm]	Δh_p^+ [mm]	Δh_p^- [mm]	$\Delta h_p^+ - \Delta h_p^-$ [mm]
PD8	0.57	0.82	0.24	0.58
PD6	0.39	0.57	0.17	0.40
PD13	0.75	1.54	0.74	0.80
PD11*	0.53	1.00	0.56	0.44

* M_y determined through Figure 5.7b

Regarding the shape of the $M - \Delta h$ hysteresis loops, it can be seen that for slabs subjected to relatively low gravity loads (red curves in Figures 5.7a and b), final reloading in both directions is characterised by high stiffness while the intermediate phase exhibits smaller stiffness. Figures 5.5a and b show that final reloading coincides with appearance of very small tensile strains (or even compressive strains) in the top reinforcement of the sagging slab half. It can be therefore deduced that the reloading stiffness of the sagging slab half increases close to $\varepsilon_{s.top} \approx 0$. On the other hand, for slabs subjected to relatively high gravity loads (black curves in Figures 5.7a and b), for which relatively high tensile strains appeared in the top reinforcement of the sagging slab half, the $M - \Delta h$ hysteresis loops did not exhibit such a late increase in stiffness. Similarly, the global moment-rotation response of slabs subjected to high gravity loads did not show any significant stiffness dependency on the unbalanced moment M.

Figures 5.7a and b show that for increasing number of rotation cycles as well as increasing amplitude of rotation levels, the crack opening at the hogging slab half increases. The gradually decreasing reloading stiffness is an indication of the stiffness degradation exhibited by the slab specimens (Chapter 3). Stiffness degradation is more pronounced for low gravity loads (red curves) than for large gravity loads (black curves). As can be seen from the same figure, low gravity load (red curves) confers lower unloading stiffness close to zero unbalanced moment than high gravity load (black curves). As has been shown earlier, no compression of the plastic crack opening occurred during loading in the reverse direction, and therefore the shear crack remained open. Consequently, this stiffness softening close to zero unbalanced moment should not be attributed to less restrained slippage between the two faces of the shear crack, i.e. to pinching effect. Moreover, Figures 5.7a and b indicate that stiffness degradation is more pronounced when loading towards the direction where the top reinforcement goes from compression to tension (from negative to positive unbalanced moment) rather than towards the opposite direction.

Top reinforcement strain

The final stiffening of the $M - \varepsilon_{s.top}$ curves in Figures 5.5 and 5.6 is related to the appearance of close to zero strains in the top reinforcement of the sagging slab half, as explained earlier. Moreover, for slabs where close to zero strains appeared in the top reinforcement of the sagging slab half, the unloading stiffness close to zero unbalanced moment was rather small compared to the unloading stiffness close to peak. This results in hysteresis loops with inverted-S shape, typically for slabs subjected to low gravity loads (Figs. 5.5a, b, and 5.6a). On the other hand, for slabs for which relatively high tensile

strains appeared in the top reinforcement of the sagging slab half, no apparent stiffness dependency on the unbalanced moment was observed. This leads to spindle-shaped hysteresis loops, which are for slabs subjected to high gravity loads (Figs. 5.5c and 5.6b).

The difference in shape between low and high gravity loads can be attributed to the stress state of the slab when the unbalanced moment M approaches zero. Application of high gravity load results in high radial moment m_{rad} in the column proximity, whereas application of low gravity load leads to rather low radial moment m_{rad} in the column proximity. Therefore, for $M \approx 0$, the radial moment m_{rad} is smaller for low gravity loads than for high gravity loads. During unloading, as the action (e.g. bending moment, shear force) approaches zero, the stiffness decreases. This is a rather common feature of RC members [Far09].

For strains at the location of flexural cracks, unloading from the post-elastic range ($\varepsilon_s > \varepsilon_{s.y}$) results in significant permanent tensile strains locked in the reinforcing bars and practically no stiffness dependency on the unbalanced moment M, as shown in Figures 5.5b and c (for $r = 0.3$ m).

Bottom reinforcement strain

The strains measured in the bottom mats were significantly lower in comparison with the strains measured in the top mats for all tested slab pairs apart from the slab pair with $\rho = 0.75\%$ loaded up to $\nu = 0.14$, as shown in Figure 5.8.
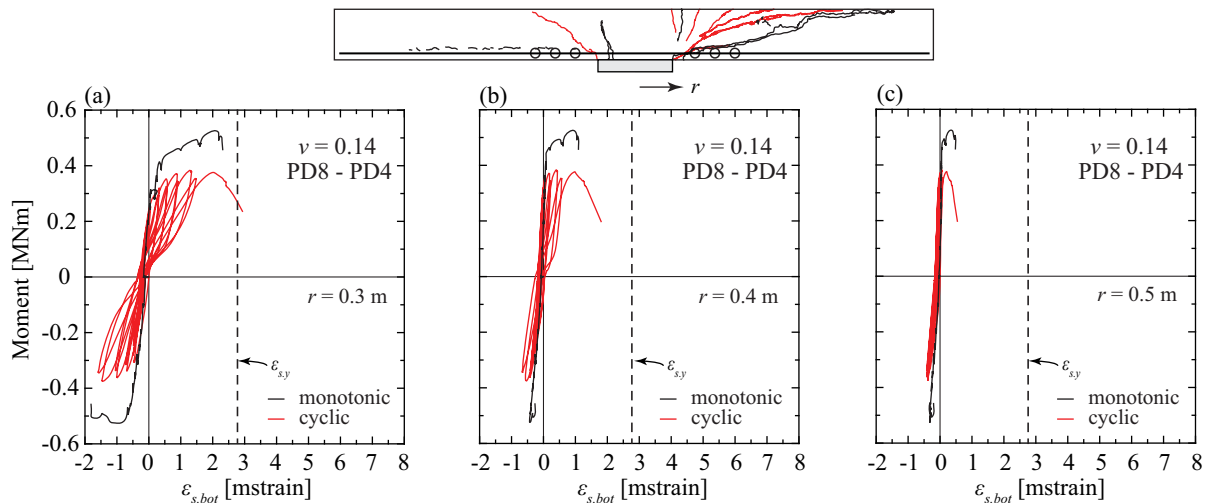
Figure 5.8 – Strain gauge measurements at specified locations of bottom reinforcing bars along the x-axis for monotonic and cyclic test with $\rho = 0.75\%$ and $\nu = 0.14$.

As can be seen in Figure 5.8, for low vertical loads applied on the slab, alternation of tension and compression due to cyclic loading led to significant increase of the strains compared to monotonic loading for the same unbalanced moment. Moreover, for low gravity load, tensile strains appear in the bottom reinforcement. This confirms the appearance of sagging (or negative curvatures). In the same figure it is also shown that since vertical loading results in rather insignificant compressive strains in the bottom reinforcement, the loading-reloading loops due to unbalanced moment are rather symmetric.

Concrete strain

Figure 5.9 shows radial concrete strain measurements at the bottom slab surface as function of M for the slabs with $\rho = 0.75\%$ and 1.50%, in the proximity of the slab-column connection ($r = 0.3$ m).
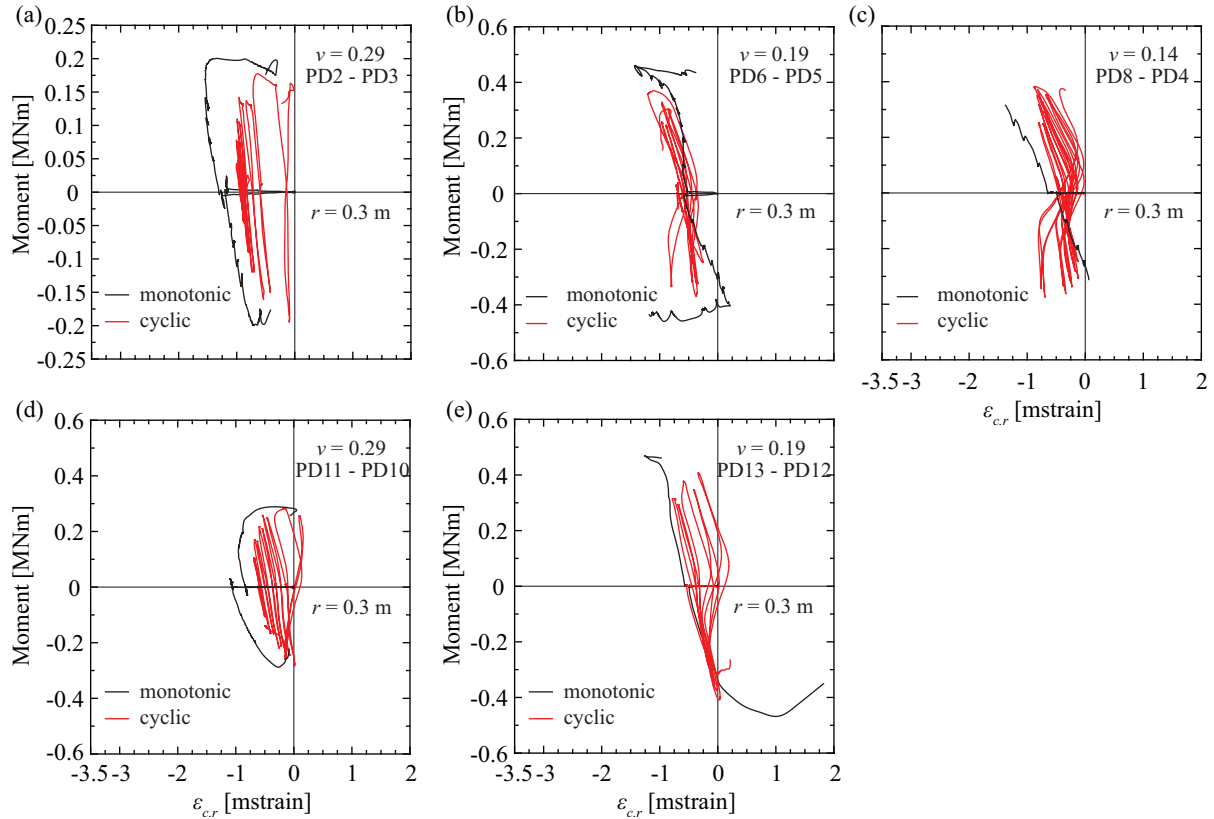
Figure 5.9 – Radial concrete strain measurements of the bottom slab surface along the strong axis ($r = 0.3$ m) for monotonically and cyclically tested slabs with: (a) $\rho = 0.75\%$ - $\nu = 0.29$, (b) $\rho = 0.75\%$ - $\nu = 0.19$ and (c) $\rho = 0.75\%$ - $\nu = 0.14$, (d) $\rho = 1.50\%$ - $\nu = 0.29$, and (e) $\rho = 1.50\%$ - $\nu = 0.19$.

The monotonic $M - \varepsilon_{c.r}$ relationship (black curves in Fig. 5.9) is characterised by increasing compressive strain $\varepsilon_{c.r}$ for increasing unbalanced moment M both for the sagging slab half ($M < 0$) and the early load stages of the hogging slab half ($M > 0$). For the final load stages, an increase of M results in a reduction of $\varepsilon_{c.r}$ of the hogging slab half. This has been theoretically explained by the formation of an elbow-shaped strut which requires a horizontal tie in the slab soffit close to the column [Mut08].

For cyclic loading, the shape of the $M - \varepsilon_{c.r}$ curves in the column vicinity was found to depend on the gravity load level. For high gravity loads, the same behaviour as for monotonic loading was observed, with the exception that cyclic loading results in faster reduction of the compressive strain than monotonic loading (Figs. 5.9a, d). This is probably due to increasing crack opening with the number of cycles. For low gravity loads (Figs. 5.9b, c, and e), although final loading in both directions is characterised by increased compressive strain for increasing M (like for monotonic loading), the intermediate phase ($M \approx 0$) shows an inversed trend, i.e. larger M leads to smaller compressive strain $\varepsilon_{c.r}$. This means that there is a zone close to zero unbalanced moment where decreasing hogging radial curvature corresponds to unbalanced moment increase.

Regarding the stiffness of the $M - \varepsilon_{c.r}$ curves of slabs subjected to high gravity loads (Figs. 5.9a, d), no dependency on the unbalanced moment was observed. For low gravity loads, the intermediate phase between peak moments is marked by smaller stiffness than close to peak moment, which decreases with increasing number of cycles. This confirms the strain gauge measurements presented above.

Figure 5.10 shows radial concrete strain measurements at various distances from the column centre for slabs with $\rho = 1.50\%$. It can be seen that cyclic degradation becomes more significant in the column proximity ($r = 0.3$ m) than farther from it ($r = 0.4$ m and 0.5 m).
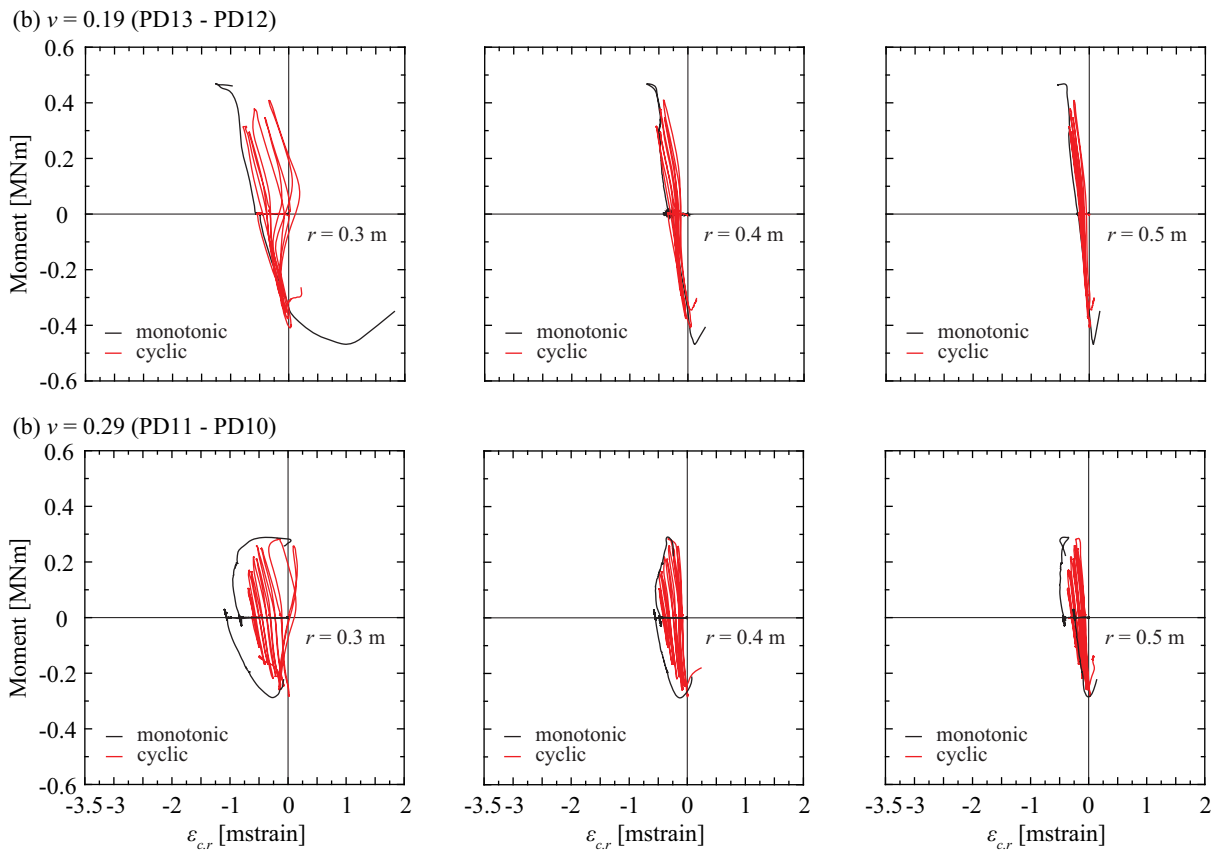
Figure 5.10 – Radial concrete strain measurements of the bottom slab surface at various locations along the strong axis for monotonically and cyclically tested slabs with $\rho = 1.50\%$: (a) $\nu = 0.14$, and (b) $\nu = 0.29$.

Figure 5.11 shows the influence of load history on the measured $M - \varepsilon_{c.t}$ relationship ($\varepsilon_{c.t}$ is the tangential concrete strain) at a distance $r = 0.30$ m from the column centre for slabs with $\rho = 0.75\%$.
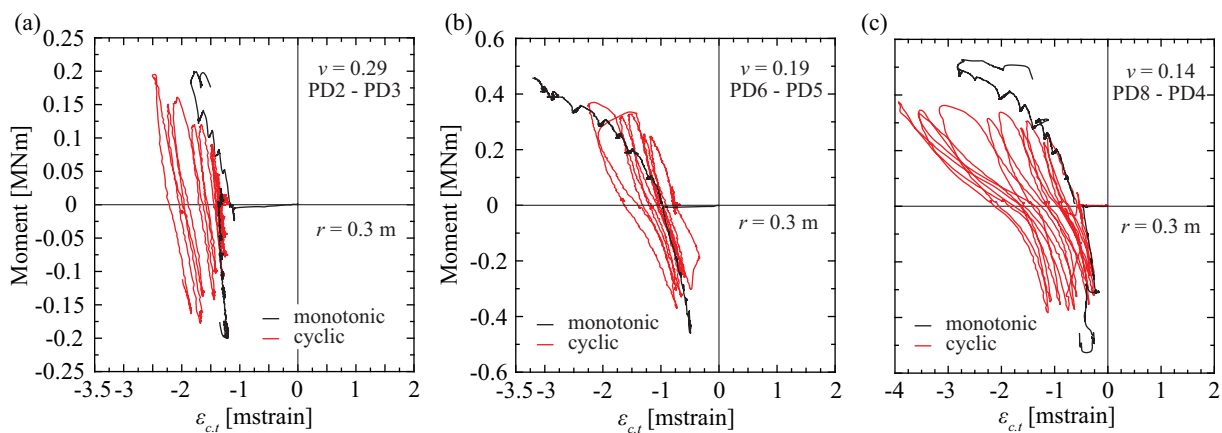
Figure 5.11 – Tangential concrete strain measurements of the bottom slab surface along the strong axis ($r = 0.3$ m) for monotonically and cyclically tested slabs with $\rho = 0.75\%$: (a) $\nu = 0.29$, (b) $\nu = 0.19$, and (c) $\nu = 0.14$.

The obtained measurements were non-conclusive: For $\nu = 0.29$ and $\nu = 0.14$ (Figs. 5.11a and c, respectively), cyclic loading resulted in higher compressive tangential strains at peak unbalanced moment than monotonic loading but for $\nu = 0.19$ the trend was inversed (Fig. 5.11b). For this reason, the influence of the load history on the tangential moments is neglected in the development of the cyclic model, presented in the following.

5.1.4 Main findings

The main findings of the experimental campaign with respect to the influence of cyclic loading on the local behaviour of slab-column connections are summarised in the following:

1. The reduction of the maximum slab rotation ψ_{max} at peak unbalanced moment due to cyclic loading shows good correlation with the observed moment strength degradation due to cyclic loading ($M_{max.cyc}/M_{max.mono}$). The ratio $\psi_{max.p.cyc}/\psi_{max.p.mono}$ decreases for decreasing gravity loads on the slab. This agrees with global experimental observations (§3.8.3) and local deformation data (crack opening measurements).

2. Reversed cyclic loading results in steeper shear cracks than monotonic loading. The impact of cyclic loading on the shear crack inclination is more pronounced for low gravity loads than for high gravity loads.

3. For cyclic tests, the radius of the shear crack (r_0) was found to correlate rather well with the attained eccentricity at first unloading from the post-elastic range. A lower-bound limit for the shear crack inclination was observed to be approximately 45 degrees, like for the performed monotonic tests.

4. The shape of the hysteresis $M - \Delta h$ and $M - \varepsilon_{s.top}$ loops for the tested slab-column specimens is characterised by the following features:

   - Hogging slab half: (a) The loading/reloading branch softens with increasing number of cycles. (b) The unloading stiffness is initially high and gradually decreases as the applied unbalanced moment approaches zero, particularly for low gravity loads acting on the slab.
   - Sagging slab half: (a) The loading/reloading stiffness is approximately equal to the stiffness of the hogging slab half during the unloading branch that preceded, and is characterised by final stiffness increase only for close to zero strains in the top reinforcement. (b) The unloading branch is characterised by very steep initial stiffness. For low gravity loads, the unloading branch close to zero unbalanced moment is marked by lower stiffness, approximately equal to the intermediate loading stiffness ($M \approx 0$) that preceded.

5. For the tested slab-column connections plastic crack openings were not reduced when the loading was reversed.

6. The stiffness of the hogging slab half decreaces as the amplitude of inelastic rotation cycles increases or the number of rotation cycles increases. The stiffness degradation was more marked for the hogging slab half than for the sagging slab half.

7. The shape of the hysteresis $M - \varepsilon_{c.r}$ loops for the tested slab-column specimens is generally characterised by higher compressive strain $\varepsilon_{c.r}$ for increasing M. For low gravity loads, though, for close to zero unbalanced moments, an increase of M resulted in a decrease of compressive strains, indicating that at this stage decreasing positive (or hogging) curvature corresponds to unbalanced moment increase.

8. The cyclic effect on the measured radial concrete strains is more pronounced in the column proximity. No clear trend with respect to the influence of the loading history on the measured tangential concrete strains was identified.

Based on the above experimental findings, the following section proposes a hysteretic model for the calculation of the cyclic moment-rotation relationship of slab-column connections. Seismic damage due to cyclic loading is expected to affect both the failure criterion and the moment-rotation relationship. As has been shown by the experimental observations within the current research, cyclic loading leads to increased crack opening and consequently decrease of the unbalanced moment for the same connection rotation. Therefore, the moment-rotation curve of slab-column connections softens as the number of cycles increases. The shear force resisted by the compression strut is also expected to decrease with cyclic loading triggering a lowering of the failure criterion compared to monotonic loading. This lowering is though difficult to be estimated quantitatively since no test programme includes systems for measuring the slab stresses in the column vicinity. Therefore, seismic damage due to cyclic loading is only incorporated in the hysteretic moment-rotation relationship of the slab-column connection, while its influence on the failure criterion is neglected in this chapter.

5.2 Hysteretic moment-rotation relationship

As observed by Vaz Rodriguez [Vaz07], specimens subjected to concentrated loads may significantly increase their crack widths when they are subjected to cyclic loading. The amount of shear force that can be carried by a slab (for the same level of gravity loads) may thus be reduced under earthquake conditions. To date, there is no suitable model to assess the increase of crack widths on RC slab-column connections when they are subjected to cyclic unbalanced moments.

Under load reversals in the inelastic range, the stiffness of RC members decreases due to concrete cracking, concentration of plastic strains and bond deterioration at the steel-concrete interface. In order to describe adequately the cyclic behaviour of RC members the exact stress and deformation state of the materials should be known at each point of the hysteresis loops. This is typically modelled using a hysteretic stress-strain relationship for the concrete and the reinforcing steel (e.g. [Ken69, Vec99]). Alternatively, a hysteretic moment-curvature relationship is adopted (e.g. [Rou87]). When the shear force equals zero, a sectional analysis gives the monotonic (or primary) moment-curvature $(M - \chi)$ relationship of the section. When the shear force is non-zero, any acceptable procedure can be applied to obtain the monotonic $M - \chi$ relationship and the monotonic shear force-shear strain $(V - \gamma)$ relationship, such as the Modified Compression-Field Theory [Vec86]. However, for the derivation of the hysteretic $M - \chi$ and $V - \gamma$ relationships, strength degradation with higher drift levels and increasing number of cycles, often termed as seismic (or cyclic) damage, should be incorporated. Moreover, members subjected to cyclic flexure and/or shear may exhibit lower stiffness as the applied moment approaches zero. For flexure-dominated members, high deformation demand results in the appearance of large flexural cracks that remain open at zero applied moment. Loading in the opposite direction results in opening of new flexural cracks at the opposite side of the member. If the flexural cracks of the newly compressed side remain open, stiffness is provided only by the reinforcing steel. The stiffness increases again once the flexural cracks of the newly compressed side close. In members where shear effects become significant, sliding between the two faces of a shear crack is less restrained for close to zero loads than for higher loads, leading to softening of the $V - \gamma$ curve as V approaches zero. Upon closing of the shear crack, the member exhibits stiffer response. This particular feature of RC members subjected to inelastic loading cycles, often termed as pinching effect, should also be considered when calculating the hysteretic $M - \chi$ and $V - \gamma$ relationships. Due to the involved complexity, a hysteretic moment-curvature relationship is typically adopted to descibe the flexural behaviour of the member (e.g. [Tak70]), while the effects of strength degradation and pinching on the flexural hysteresis loops are usually modelled in an empirical manner [Rou87, Ozc89].

The analytical model for the load-rotation relationship of slabs subjected to vertical loads alone [Mut08] is based on a quadrilinear moment-curvature relationship for both the radial and the tangential moments accounting for the influence of the shear crack on the flexural behaviour in a computationally efficient way. This model forms the basis of the analytical model for the moment-rotation

relationship of slabs under monotonically increasing drifts (Chapter 4). Extending this model for cyclic loading conditions is considerably facilitated if a hysteretic moment-curvature relationship is adopted. This simplified extension to predict the increase of crack widths in the proximity of slab-column connections when subjected to cyclic loading is presented in the following. The assumptions regarding the shear crack inclination are presented first, followed by the assumptions related to the hysteretic moment-curvature relationship. Finally, the adopted approach for the seismic damage consideration is presented. It should be noted that the same formulas used for the calculation of the monotonic moment-rotation curve (Eqs. (4.2), (4.4) - (4.9)) apply also for the calculation of the cyclic moment-rotation curve and, therefore, are not repeated in the following.

5.2.1 Shear crack inclination

If during loading and reloading no yielding occurs, no plastic radial curvatures appear and the shear crack opening due to unbalanced moment is assumed to be recovered completely during the unloading that follows. Therefore, for this case, the radius of the shear crack (r_0) is assumed to be equal to the attained eccentricity at that load step, like for monotonic loading conditions (Chapter 4).

Concerning the shear crack inclination of cyclically loaded slab-column connections responding beyond the yield limit, a fixed value for the radius r_0 is assumed, which corresponds to the shear crack inclination at the first post-yield peak. This assumption is based on experimental observations of the slab saw cuts and recorded reinforcement strains (§5.1.2 - Point 2 in §5.1.4). For subsequent loading and unloading in both directions, it is assumed that all additional plastic curvatures of the considered sector element are concentrated at this fixed shear crack. Since this crack is assumed to govern the behaviour of each sector element of the slab-column connection during all subsequent cycles, no flatter or steeper shear crack can appear.

Figure 5.12a illustrates the assumed shear crack inclination at the elastic and plastic domain of slab PD8 for the loading protocol shown in Figure 5.12b. The shear crack at the pre-yield range (continuous lines in Fig. 5.12a) is rotating and r_0 depends on the attained eccentricity e (but $r_0 \geq r_c + d$). Once the first unloading in the plastic domain (grey-shaded area in Fig. 5.12b) of the sector element subjected to ψ_{max} ($\phi = \pi/2$) occurs, a fixed r_0 value equal to the eccentricity e at the first inelastic peak (dashed line in Fig. 5.12a) is assumed to govern the behaviour of all sector elements. Although this assumption neglects the fact that sector elements with smaller rotations (as for instance parallel to the bending axis) have not yet reached their yield limit, Chapter 4 has shown that adopting the same value of r_0 for all sector elements simplifies significantly the calculation.
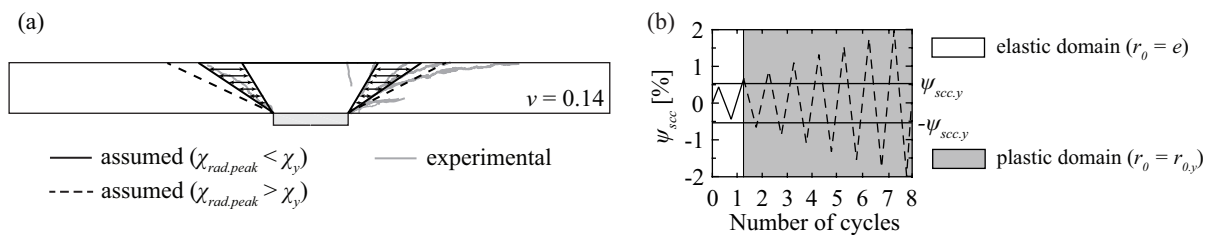
Figure 5.12 – Assumption related to the shear crack inclination for cyclic loading conditions.

5.2.2 Moment-curvature relationship

Radial concrete strain measurements have shown that cyclic degradation (decrease of concrete compressive strain due to cyclic loading) is more significant in the column vicinity. Since no clear trend on the influence of cyclic loading on the tangential concrete strains was identified (Point 7 in §5.1.4), the hysteretic behaviour of slab-column connections is accounted for by adopting a hysteretic moment-curvature relationship only for the radial moments acting on the shear crack ($r = r_0$). Unlike for the case of monotonic loading, for which the radial moment of each sector element depends only on the corresponding radial curvature (Chapter 4), for cyclic loading it is assumed that the radial moment depends also on the loading history as will be shown in the following. Both the axisymmetric model for slabs subjected to vertical load alone [Mut08] and the analytical model for slabs subjected to combined vertical load and monotonically increasing unbalanced moment (Chapter 4) adopt a piece-wise linear (quadri-linear) moment-curvature relationship for the sector elements. Likewise, the hysteretic $M - \chi$ relationship presented in the following adopts a piece-wise linear form (polygonal shape). Adoption of a smooth hysteretic model would add significant and unjustified complexity to the calculation and would be inconsistent with the above-mentioned analytical models (Chapter 4 and [Mut08]). An additional assumption to describe the increase-decrease of the developed plastic radial curvature to simulate the opening-closing process of the shear crack is necessary and will be presented in the following, based on experimental observations (§5.1.3).

Figure 5.13 shows the assumed hysteretic moment-curvature relationship (colored lines) and the primary moment-curvature relationship (black line). The shape of the unloading-reloading branches is based on a hysteretic shear model for concrete members by Ozcebe and Saatcioglu [Ozc89] and the findings on the previous section (Points 3, 5, and 6 in §5.1.4). Positive and negative directions correspond to increasing tension in the top reinforcement and decreasing compression in the bottom reinforcement, respectively (see Fig. 5.13). To facilitate understanding, the hysteresis loops are shown for four post-elastic scenarios depending on the sign of the radial moment at negative peak and the sign and value of the corresponding curvature. It should be noted that the moment-rotation curve represents the global behaviour of the slab-column connection, whereas the shown radial $m_{rad} - \chi_{rad}$ relationship is formulated for each sector element. Therefore the loading and unloading branches of the $m_{rad} - \chi_{rad}$ curve do not necessarily correspond to the loading and unloading branches of the moment-rotation curve.
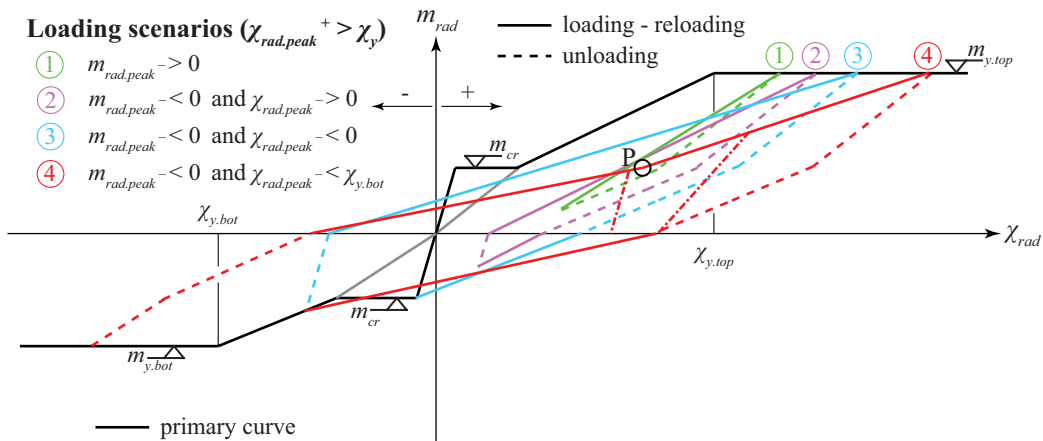
Figure 5.13 – Proposed hysteretic radial moment-curvature relationship for each sector element of the slab (based on Ozcebe and Saatcioglu [Ozc89]).

In the following, rules are given for the loading/reloading branch and the unloading branch of the $m_{rad} - \chi_{rad}$ relationship under different conditions.

Unloading branches

The following rules are applied for the loop segments that correspond to unloading:

1. Unloading follows the primary curve (black line in Fig. 5.13) if $\chi < \chi_y$ at the beginning of unloading and m_{cr} has not been previously exceeded in either direction.

2. If m_{cr} has been exceeded at least once in the considered direction and the yield curvature has not been previously exceeded in the opposite direction ($\chi < \chi_y$), unloading from $m_{rad.peak} > m_{cr}$ follows the elastic post-cracking stiffness (grey line in Fig. 5.13) up to the zero radial moment axis. If $m_{rad.peak} < m_{cr}$ unloading follows the initial stiffness up to zero radial moment. If the yield curvature has already been exceeded in the opposite direction, unloading follows the initial stiffness up to zero radial moment independently from the value of $m_{rad.peak}$.

3. If the yield curvature has been exceeded at least once in the considered quadrant, unloading from curvature higher than the maximum previously attained curvature follows the elastic post-cracking stiffness until m_{cr}. Unloading for $m_{rad} < m_{cr}$ follows a line connecting m_{cr} with the plastic radial curvature χ_{pl} of the considered sector element (zero radial moment). If the peak curvature is smaller than the maximum previously attained curvature, unloading follows the initial stiffness up to $m_{rad} = 0$ if $\chi < \chi_{pl}$, otherwise a line connecting $\chi_{rad.peak}$ with χ_{pl} is followed (dash-dotted lines in Fig. 5.13).

   The plastic radial curvature $\chi_{pl.i}(\phi_i)$ of the sector element at angle ϕ_i is calculated according to the following rules:

   • For the first unloading from the post-yield curvature:

   $$\chi_{pl.i}(\phi_i) = \chi_{peak.i}(\phi_i) - \chi_y(\phi_i) \tag{5.1}$$

   where χ_y is the yield curvature of the sector element, calculated according to [Mut08].

   • If the yield curvature has been previously exceeded in the considered direction, increase of the plastic radial curvatures due to tensile strains in the top or bottom reinforcement during loading in the positive direction ($m_{rad} > 0$) or in the negative direction ($m_{rad} < 0$), respectively, can occur only for curvatures higher than the previously attained curvatures in that direction:

   $$\chi_{pl.i}(\phi_i) = (\chi_{peak.i}(\phi_i) - \chi_{peak.i-1}(\phi_i)) + \chi_{pl.i-1}(\phi_i) \tag{5.2}$$

From Eq. (5.2) it comes out that cycles with smaller amplitude than previous cycles do not lead to further increase of the plastic radial curvature $\chi_{pl.i}(\phi_i)$.

Loading and reloading branches

With regard to the loop segments that correspond to loading and reloading, the following rules are applied:

1. Loading and reloading in both directions follow the primary curve until unloading from the post-cracking branch occurs.

2. If unloading is terminated prior to reaching the zero moment axis, reloading in the same quadrant follows a straight line aiming at the previously attained maximum moment in the same direction both for moment at negative peak higher or smaller than m_{cr} (green line in Fig. 5.13). Further loading follows the primary curve.

3. If the considered sector element has not been previously loaded beyond the cracking moment in the considered direction, loading-reloading targets the cracking moment m_{cr}, even if plastic curvatures have been previously developed during loading in the opposite direction (purple and blue line in Fig. 5.13). Further loading follows the primary curve.

4. If the considered sector element has been previously loaded beyond the cracking moment in the considered direction, reloading aims at the previously attained moment in the same direction (red line in Fig. 5.13). Further loading follows the primary curve.

5. If the yield curvature has been previously exceeded in the direction with the lowest radial moment (bottom reinforcement under tension), reloading towards the direction with the highest radial moment (top reinforcement in tension) follows the same stiffness as for reloading in the opposite direction (see Fig. 5.13) up to suppression of plastic curvatures of the reinforcement previously in tension (bottom reinforcement). The plastic curvature locked in the sector element (at angle ϕ_i) with respect to the bending axis) due to sagging radial moment is reduced according to the following formula:

$$\chi_{pl.bot}(\phi_i) = (\chi(\phi_i) - \chi_{y.bot}(\phi_i)) - \chi_{pl.bot.peak}(\phi_i) \leq 0 \qquad (5.3)$$

where $\chi_{y.bot}(\phi_i)$ is the yield curvature for bottom reinforcement in tension and $\chi_{pl.bot.peak}(\phi_i)$ is the plastic curvature at the previous peak that is locked in the sector element due to tensile strains in the bottom reinforcement ($\chi_{y.bot}(\phi_i), \chi_{pl.bot.peak}(\phi_i) > 0$ in Eq. (5.3)).

Further loading aims at the previously attained maximum peak moment in the same direction (red line in Fig. 5.13).

The fifth rule of the above-mentioned procedure is not based on deformation mesurements from tests performed within this research. The established rule is based on the model proposed by [Ozc89] and is included here to predict stiffness increase upon closing of the shear crack developed due to post-yield tensile strains in the bottom reinforcement (pinching effect when loading in the positive direction). Ozcebe and Saatcioglu proposed to consider stiffness increase due to pinching only for loads higher than the cracking load [Ozc89]. According to proposed model, the point of stiffness increase initiation due to pinching (P - see Fig. 5.13) corresponds to $\chi_{pl.bot}(\phi_i) = 0$ using Eq. (5.3), i.e. to the load step for which the plastic radial strain of the bottom reinforcement is suppressed.

For reloading in the negative direction (tension in the top reinforcement reduces), no reduction of the plastic curvature $\chi_{pl.i}(\phi_i)$ is assumed to occur. This assumption is based on crack opening measurements from the tests performed within this research (§5.1.3, Point 4 in §5.1.4).

Influence of gravity loads on the hysteretic response

In the following, the influence of gravity loads on the shape of the hysteresis loops is discussed. The predicted response of slabs PD2 ($\nu = 0.29$) and PD8 ($\nu = 0.14$) is presented in Figures 5.14 and 5.15, respectively, for illustration purposes. Both slabs contained the same amount of reinforcement ($\rho = 0.75\%$). For comparison purposes, the two slabs are analysed for the same loading protocol (Fig. 5.14a and 5.15a) and not for the protocols to which the corresponding tests had been subjected, which differed slightly (Chapter 3). The predicted hysteretic radial moment-curvature relationship for the sector element subjected to alternating maximum and minimum slab rotations ($\phi = \pi/2$ or $3\pi/2$) is shown in Figures 5.14b and 5.15b for slabs PD2 and PD8, respectively. To provide better understanding, the calculated moment-rotation curve of each slab is also shown (Figs. 5.14c and 5.15c, respectively). Circular markers correspond to residual radial curvatures (zero unbalanced moment).
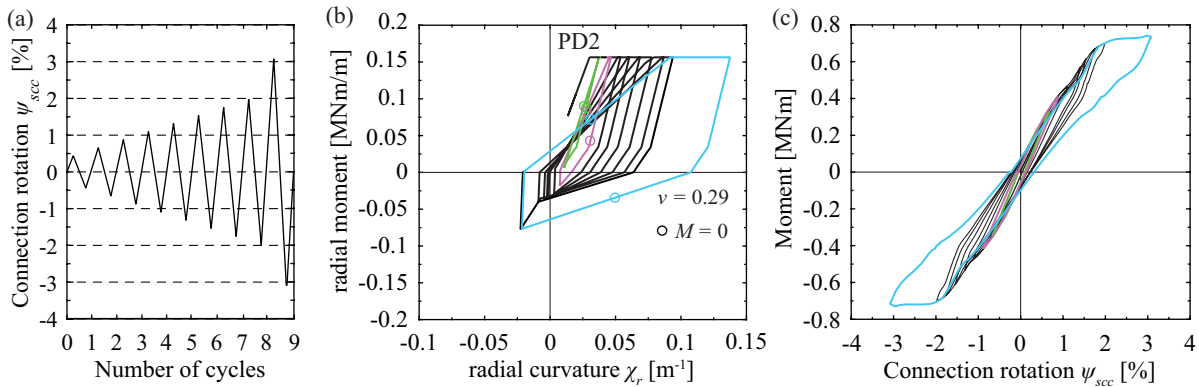
Figure 5.14 – Hysteretic behaviour of slab subjected to large vertical loads ($\nu = 0.29$): (a) adopted loading protocol, (b) $m_{rad} - \chi_{rad}$ relationship of the sector element at angle $\phi = \pi/2$ or $3\pi/2$, and (c) $M - \psi_{scc}$ relationship of the slab-column connection.
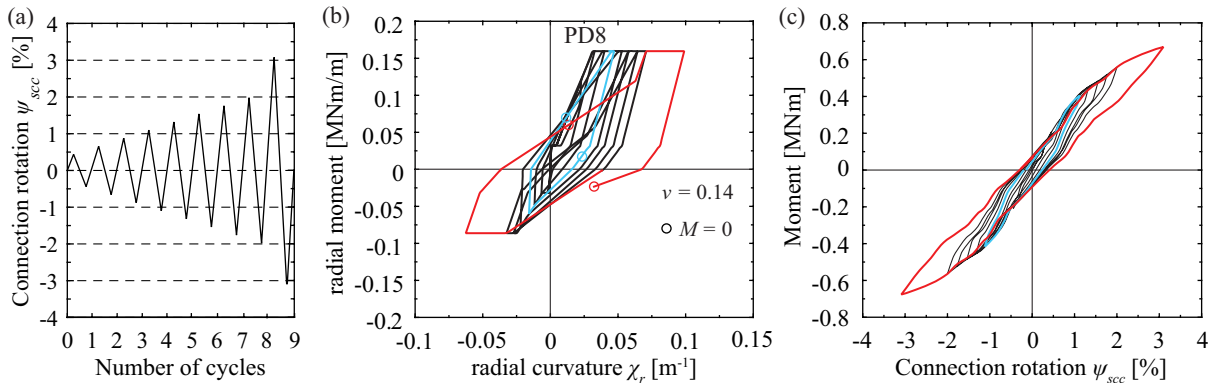
Figure 5.15 – Hysteretic behaviour of slab subjected to small vertical loads ($\nu = 0.14$): (a) adopted loading protocol, (b) $m_{rad} - \chi_{rad}$ relationship of the sector element at angle $\phi = \pi/2$ or $3\pi/2$, and (c) $M - \psi_{scc}$ relationship of the slab-column connection.

As can be seen from Figures 5.14 and 5.15, the adopted approach accounts for higher stiffness degradation with increasing magnitude of inelastic radial curvature at which unloading commences.

For high vertical loads (Fig. 5.14), loading-unloading results in prediction of negative radial curvatures (i.e. upward slab rotations) for the sagging slab half at relatively high connection rotation ($\psi_{scc} > 1\%$). Smaller rotation amplitudes lead to prediction of negative radial moments when loading towards the less reinforced side that may correspond to positive or negative radial curvature at peak (violet or blue loops, respectively - Fig. 5.14b). For close to zero radial curvatures at the sagging slab half,

sector elements subjected to smaller radial curvatures than the sector element at the tip of the sagging slab half (Fig. 5.14b) are characterised by stiffer $m_{rad} - \chi_{rad}$ relationship (Fig. 5.13 - violet/blue loops vs red loop). This leads to a slight final stiffening of the global response (violet and blue loops in Fig. 5.14c). For very small rotation amplitudes, positive radial moments are predicted for both loading and unloading (green loops in Fig. 5.14b), which does not affect significantly the stiffness of the moment-rotation curve (green curve in Fig. 5.14c).

For small vertical loads (Fig. 5.15), stiffening of the response due to close to zero curvatures at the sagging slab half is predicted from very early load stages onwards (e.g. blue loop in Fig. 5.15b). For large rotation magnitude at unloading, suppression of the negative plastic curvature is followed by stiffness increase due to pinching (red loop in Fig. 5.15b).

Influence of reinforcement ratio on the hysteretic response

In the following, the influence of reinforcement ratio on the hysteretic response of slab-column connections is discussed. The predicted response of slabs PD6 ($\rho = 0.75\%$) and PD13 ($\rho = 1.50\%$) is illustrated in Figure 5.16. Both slabs were subjected to a normalised shear force $\nu = 0.19 \sqrt{MPa}$. The adopted loading protocol of the two slabs is the same as the one adopted for slabs PD2 and PD8 above (Fig. 5.14a).
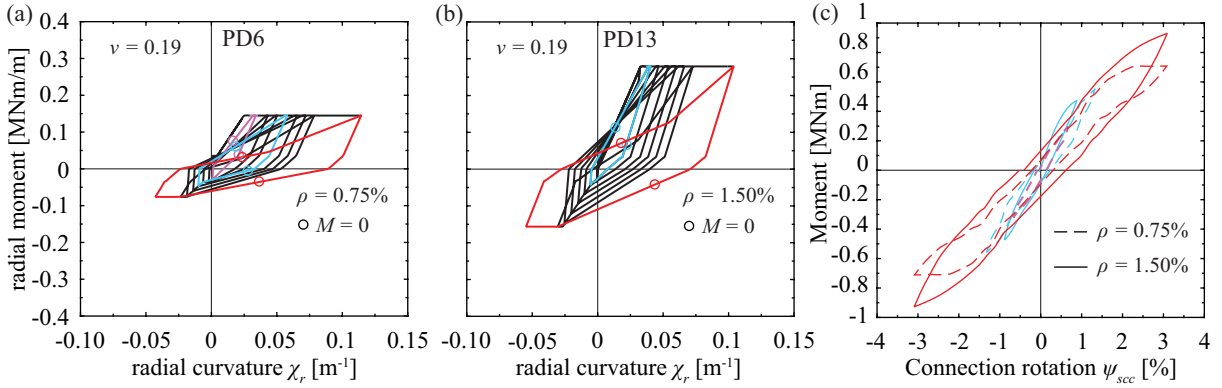
Figure 5.16 – Hysteretic behaviour of slabs with different reinforcement ratio: $m_{rad} - \chi_{rad}$ relationship of the sector element at angle $\phi = \pi/2$ or $3\pi/2$ for: (a) $\rho = 0.75\%$ and (b) $\rho = 1.50\%$ and (c) $M - \psi_{scc}$ relationship of the slab-column connections at selected rotation levels.

As can be seen from Figures 5.16a and b, for the same rotation level, low ρ results in larger positive radial curvatures (downward rotations) and smaller negative radial curvatures (upward rotations) than high ρ. Since high ρ confers higher stiffness to the slab-column connection than low ρ, the hysteretic loops become stiffer for increasing ρ. Moreover, high ρ results in larger residual connection rotation (horizontal distance between circular markers of the same color). Therefore, if no seismic damage is incorporated, high ρ leads to hysteretic loops with higher amount of dissipated energy than small ρ (red loops in Fig. 5.16c).

5.2.3 Seismic damage

Literature review

Once the hysteretic moment-curvature relationship is defined, seismic damage should be incorporated. Various methods have been proposed to account for seismic damage in RC structures, which can be either local (for members or joints) or global (for the entire structure). Detailed state-of-the-art review can be found elsewhere [Wil95,Cao11]. Since this study aims at describing the seismic damage of slab-column connections only local damage indices are treated herein, which can be categorised into two groups:

- Non-cumulative damage indices such as ductility [Ban81, Par86, Pen93] and interstorey drift [Tou83]. Their main advantage is their simplicity and ease of interpretation, while the fact that effects of repeated cyclic loading (number of cycles) cannot be incorporated remains their main shortcoming. Improved non-cumulative damage indices such as the flexural damage ratio [Ban81] and the modified flexural damage ratio [Rou87] have been proposed to consider stffness and strength degradation under repeated cyclic loading which cannot be accounted for by the traditional non-cumulative damage indices.

- Cumulative damage indices, which can be either deformation-based or energy-based. Although mechanisms that contribute to the seismic damage of RC members such as low-cycle fatigue or energy dissipation are considered by these damage indices, their main shortcoming is the need for parameter calibration based on regression analysis of test results. Moreover, they should not be applied to members or connections against which they were not calibrated.

Several researchers have proposed damage indices that combine features of the previous two groups. For example, according to Park and Ang [Par85a, Par85b] seismic structural damage can be expressed as a linear combination of the maximum deformation and hysteretic energy due to cyclic loading expressed in terms of the damage index

$$D = D_\delta + D_c \tag{5.4}$$

The damage index due to maximum deformation D_δ can be calculated as follows:

$$D_\delta = \frac{\delta_{u.cyc}}{\delta_{u.mono}} \tag{5.5}$$

where $\delta_{u.cyc}$ and $\delta_{u.mono}$ is the deformation capacity of the considered member under cyclic and monotonic loading conditions respectively.

The damage index due to cyclic loading D_c can be calculated as follows [Par85a]:

$$D_c = \frac{\beta_c}{F_y\,\delta_{u.mono}} \int dE \tag{5.6}$$

where β_c is the coefficient accounting for cyclic loading effect, dE is the incremental absorbed hysteretic energy and F_y is the yield load of the considered member. For members that do not display an apparent yield point (as is the case for slab-column connections) the yield load F_y can be replaced by the strength of the member F_u.

Adopted seismic damage model

In the framework of this thesis a mechanical model has been developed for monotonically increasing drifts, which combined with the CSCT(mono) failure criterion gives the moment strength and the corresponding deformation capacity of slab-column connections under monotonic loading conditions (Chapter 4). Moreover, the hysteretic moment-curvature relationship described in §5.2.2 allows for calculating the dissipated energy. Therefore, in addition to non-cumulative seismic damage approaches, the mechanical model can also accomodate cumulative approaches for the seismic damage of slab-column connections.

The cyclic tests presented in Chapter 3 have shown that slab-column connections exhibit significant stiffness and strength degradation, in particular for low gravity loads. However, since the database of slab pairs subjected to monotonic and cyclic loading is relatively limited ($N = 5$), it is doubted whether regression analysis on empirical parameters (e.g. β_c in Eq. (5.6)) would produce an empirical total damage index capable of describing accurately enough the seismic damage of slabs against which it was not calibrated (i.e. with different thickness, reinforcement ratio, etc.). Moreover, for the

calculation of the incremental hysteretic energy dE according to Eq. (5.6) the hysteretic moment-rotation relationship should be calculated beforehand, which renders this approach less attractive for engineering practice due to considerable computational effort needs.

As has been shown in §5.1.1, the reduction of the maximum slab rotation ψ_{max} due to cyclic loading gives a good estimate of the moment strength degradation (Point 1 in §5.1.4). Therefore, a non-cumulative seismic damage model was adopted for each sector element of the slab (Fig. 5.17a). The model is based on the Modified Flexural Damage Ratio (MFDR) proposed by Roufaiel and Meyer [Rou87].
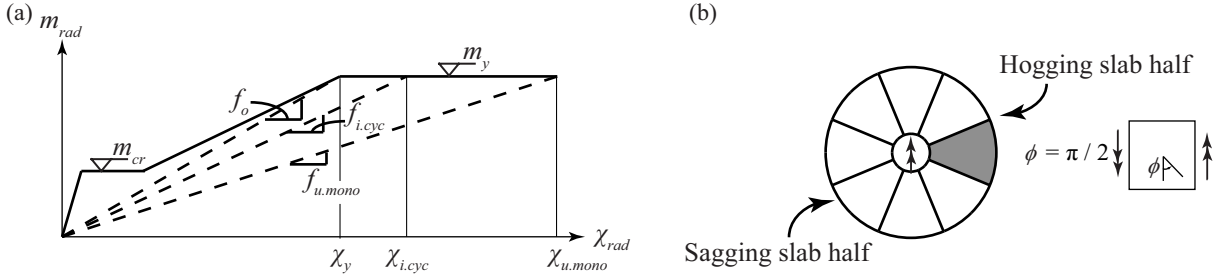
Figure 5.17 – Adopted model for seismic damage for the each sector element of the slab (based on Roufaiel and Meyer [Rou87]).

For the calculation of the seismic damage according to this model only the secant flexibility (inverse of secant stiffness - Fig. 5.17a) at punching failure under monotonic loading conditions should be known beforehand for the sector element that is subjected to the largest slab rotations (grey-shaded element in Figure 5.17b), i.e. the tip of the hogging slab half ($f_{u.mono}(\pi/2) = \chi_{u.mono}(\pi/2) \,/\, m_{rad.u.mono}(\pi/2)$). $f_{u.mono}(\pi/2)$ can be calculated using the analytical model for monotonically increasing drifts (Chapter 4). Afterwards, the damage index $D\left(\phi_i\right)$ can be computed for each sector element as follows

$$D\left(\phi_i\right) = \frac{f_{j.cyc}\left(\phi_i\right) - f_o}{f_{u.mono}(\pi/2) - f_o} \tag{5.7}$$

where f_o is the radial yield flexibility and $f_{j.cyc}\left(\phi_i\right)$ is the secant flexibility at the monotonic (or primary) moment-curvature curve corresponding to the curvature at the peak of cycle j for the sector element at angle ϕ_i from the bending axis. According to [Rou87] the damage index should be computed for the positive and negative loading direction and the maximum of the two values should be used for the considered sector element. Since for slab-column connections subjected to constant vertical load and cyclically increasing moment radial moments are already present after the application of vertical loads, high sagging radial moments could appear only for very low gravity loads and high drift levels. In most realistic cases it is therefore the hogging slab half (positive loading) that determines the seismic damage ratio $D\left(\phi_i\right)$.

It should be noted that the hysteretic moment-curvature relationship described in the previous section allows to calculate the dissipated energy. Therefore, in addition to non-cumulative seismic damage approaches (e.g. [Rou87]), the mechanical model can also accommodate cumulative approaches (e.g. [Gos77]) for the seismic damage of slab-column connections and combined cumulative and non-cumulative approaches (e.g. [Par85a]). However, it should be stated that since the calculation is driven by the global (or connection) rotation and the rotations ψ_{max} and ψ_{min} are calculated to satisfy global equilibrium, the radial curvature of each sector element at peak depends not only on its damage ratio D but also on the damage ratio D of all the other sector elements. Therefore, for the same connection rotation, the cyclic model predicts a decreasing unbalanced moment with increasing number of cycles, even if a non-cumulative damage model is adopted.

Figure 5.18a shows the hysteretic response of slabs PD6 and PD8, which were analysed earlier (§5.2.2),

when cyclic damage is considered. The curves are plotted until ψ_{max} reaches $\psi_{max.u.mono}$, i.e. until $D = 1$. The points corresponding to zero unbalanced moment for the first and the last hysteresis loop before failure are also represented in Figures 5.18b and c (circular markers).
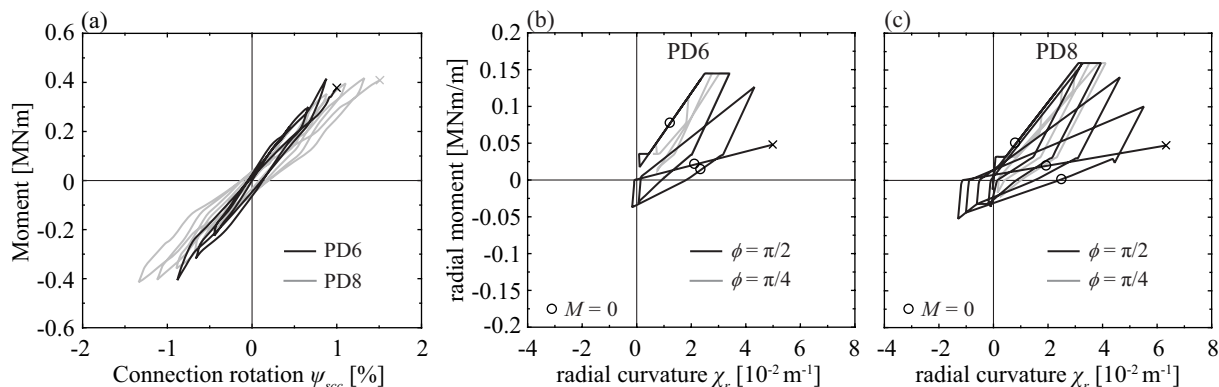
Figure 5.18 – Predicted hysteretic behaviour of slabs PD6 and PD8 when cyclic damage is considered: (a) $M - \psi_{scc}$ curves; (b) and (c) $m_{rad} - \chi_{rad}$ relationships of sector element at $\phi = \pi/4$ and $\phi = \pi/2$.

The adopted approach presents the additional advantage that seismic damage is considered at the sector element level. In this way, sector elements subjected to larger slab rotations (black loops in Figs. 5.18b and c) exhibit higher damage than sector elements with smaller slab rotations (grey loops in Figs. 5.18b and c). This agrees with experimental observations both for the tests performed within this thesis and tests found in the literature [Haw89, Tia07].

Figure 5.18 also shows that the gravity load affects significantly the predicted shape of the hysteresis loops. For the same radial curvature, high gravity load results in earlier exceedance of the yield limit than low gravity load and therefore to higher damage (Fig. 5.18b against c, respectively). Moreover, low gravity load leads to larger residual connection rotation than high gravity load, which in turn leads to prediction of larger amount of dissipated energy for low gravity load than for high gravity load. These trends agree with the observed behaviour of the cyclically tested slabs as shown in Chapter 3.

5.3 Failure criterion

The present chapter assumes that cyclic degradation is accounted for only in the moment-rotation relationship. Therefore, the approach that accounts for shear redistribution between adjacent sector elements of the hogging slab half is used in the present chapter (CSCT(mono) - §4.3.1). Failure is assumed to occur when the shear force acting on the sector elements of the hogging slab half ($0 \leq \phi \leq \pi$) reaches the sum of their shear resistances. The upper limit for the moment strength and the corresponding deformation capacity of slab-column connections subjected to cyclic moment is defined when $D = 1$, i.e. when the secant stiffness at the moment-curvature relationship reaches the secant stiffness at punching failure for monotonic loading conditions.

5.4 Comparison with the performed cyclic tests

This section compares the experimental moment-rotation response of the cyclically tested slabs (Chapter 3) with the predicted moment-rotation response according to the proposed cyclic model (Fig. 5.19). For comparison purposes, the predicted moment-rotation curves according to the monotonic analytical model are also shown in the same figure (dashed black curves). The predicted moment-rotation curves according to the monotonic model should be compared to the experimental curves (grey curves) only up to the intersection with the CSCT(cyc) failure criterion (circular markers).
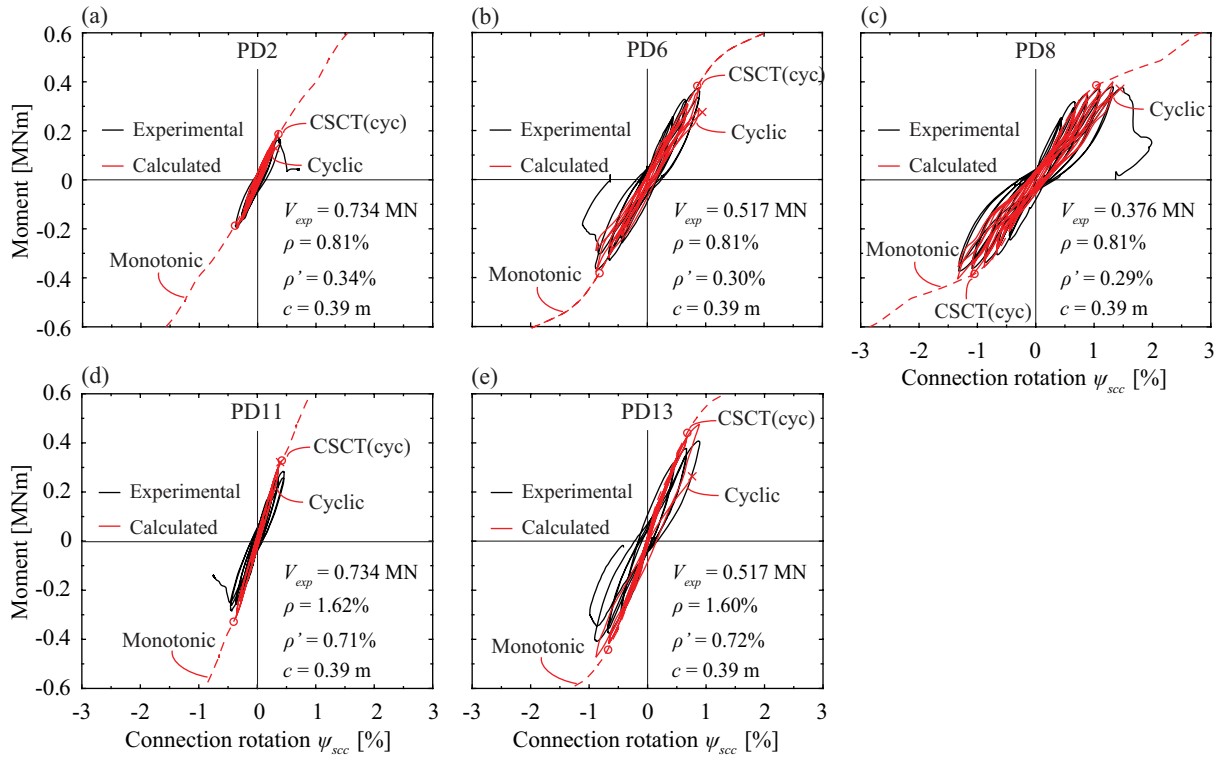
Figure 5.19 – Comparison between experimental and calculated moment-connection rotation curves for the cyclic tests performed within the present research according to the analytical model of Chapter 4 and the model of this chapter: (a) PD2, (b) PD6, (c) PD8, (d) PD11, and (e) PD13.

Figure 5.19 shows that the cyclic model predicts more accurately the final part of the experimental response than the monotonic model. Moreover, the approach of this chapter allows for better prediction of the deformation capacity of the cyclically tested slabs compared to the simplified approach of Chapter 4 since the effect of loading history is explicitly accounted for. The model predicts higher residual connection rotation and higher dissipated energy for low gravity loads than for high gravity loads, which is in accordance with the experimental results. More detailed comparisons of the model predictions with the results of the tests performed within this thesis and tests reported in the literature can be found in the following chapter.

5.5   Loading history effect

This section focuses on the effect of the loading history on the response of slab-column connections according to the analytical model presented in Section 5.2 combined with the CSCT(mono) failure criterion (Section 5.3). First, the influence of seismicity is investigated, followed by the investigation on the influence of reversed against non-reversed cyclic loading on the moment-rotation response. Finally, the effect of the number of cycles is discussed. The investigations of this section are based on the model predictions for the cyclic tests on slabs with $\rho = 0.75\%$ performed within this thesis (PD2, PD6, and PD8).

5.5.1 Seismicity

The effect of seismicity on the hysteretic response of slab-column connections is discussed in the following. For this purpose, the two normalised loading protocols shown in Figure 5.20a are used to distinguish between the demand due to low-moderate seismicity (continuous lines) and due to high seismicity (dashed lines). The value of $\psi_{slab.max}$ is taken equal to the experimental connection rotation at peak moment $\psi_{scc.max}$ (Section 3.7). The loading protocols were determined based on Mergos and Beyer [Mer14] as function of the seismicity, the hysteretic model, the fundamental period T of the structure and the number of cycles per load step. For this study, it was assumed that $T > 0.5$ s (multi-storey building) and $n_c = 2$ (cycles per load step). For the hysteretic model, since RC walls provide lateral strength and stiffness to the building (see Section 3.1), the "thin" Takeda model was adopted [Mer14]. For slab PD2, the seismicity level did not influence significantly the calculated moment-rotation curve. Figures 5.20b and c show the predicted moment-rotation curves of slabs PD6 and PD8, respectively, for both adopted seismicity levels.
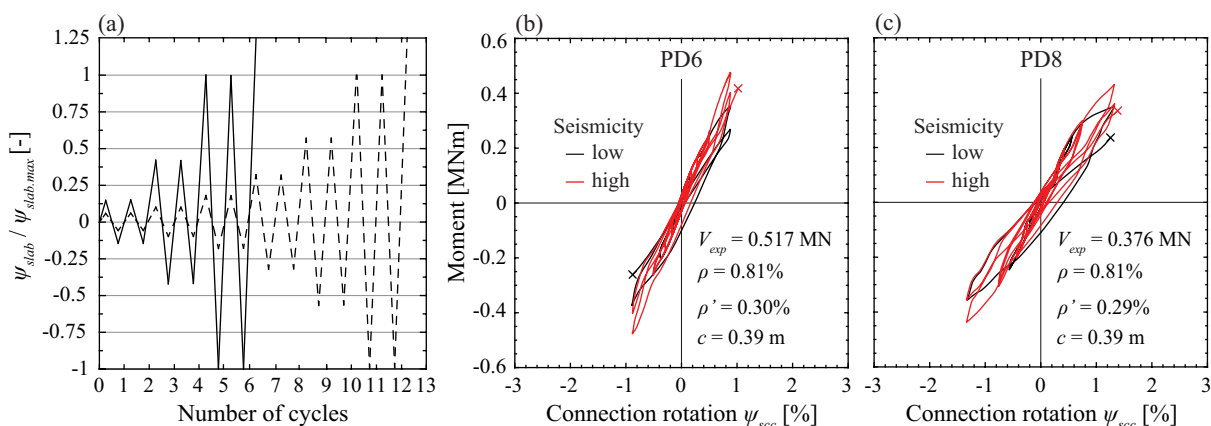
Figure 5.20 – Influence of seismicity on the predicted cyclic response of slabs subjected to low gravity loads tested within this research ($\rho = 0.75\%$): (a) normalised loading protocol for high seismicity and low-moderate seismicity according to [Mer14], and predicted moment-rotation response of slabs (b) PD6 ($\nu = 0.19$), and (c) PD8 ($\nu = 0.14$).

Figure 5.20 shows that for slabs PD6 and PD8, high seismicity leads to larger moment strength than low seismicity. This is because the first inelastic rotation level for low seismicity appears at the last load step ($\psi_{scc} = \psi_{scc.max}$) for both PD6 and PD8. On the other hand, for high seismicity, the first inelastic peak according to the proposed model appears at the 5th load step (i.e. for $\psi_{scc} = 0.57\psi_{scc.max}$). This means that the radius of the critical shear crack is larger for low seismicity ($r_{0.y} = 0.8$ m and 1.17 m for PD6 and PD8, respectively) than for high seismicity ($r_{0.y} = 0.56$ m and 1 m for PD6 and PD8, respectively). Steeper shear crack results in stiffer behaviour of the slab-column connection. Moreover, first inelastic peak at higher rotation level leads to higher value for the damage index D. For this reason, D at peak moment obtains higher values for low seismicity (0.74 and 0.81 for PD6 and PD8, respectively) than for high seismicity (0.63 and 0.69 for PD6 and PD8, respectively). It should be noted that according to the proposed model, high seismicity leads to smaller moment strength than low seismicity only when the rotation at first inelastic peak increases with increasing seismicity level (for instance when $0.42\psi_{scc.max} < \psi_{scc.y} < 0.57\psi_{scc.max}$ - see Fig. 5.20a). The corresponding connection rotation at peak moment does not appear to be influenced by the seismicity level for the case of slabs PD6 and PD8. In Section 5.8 a more systematic study on the influence of the seismicity level on the seismic rotation capacity of slab-column connections will be presented.

5.5.2 Reversed vs Non-reversed cyclic loading

The effect of rotation reversal on the predicted response is examined in the following. Figure 5.21 shows the predicted moment-rotation curves for slabs PD2, PD6 and PD8 for both reversed and non-reversed cyclic loading (red and black curves respectively). The calculation is performed for the same rotation amplitudes as in the experimental campaign (Section 3.6). The curves are plotted in the first quadrant and up to punching failure (predicted according to CSCT(mono)). Table 5.2 summarises the model predictions in terms of moment strength, corresponding connection rotation and connection rotation at punching failure.
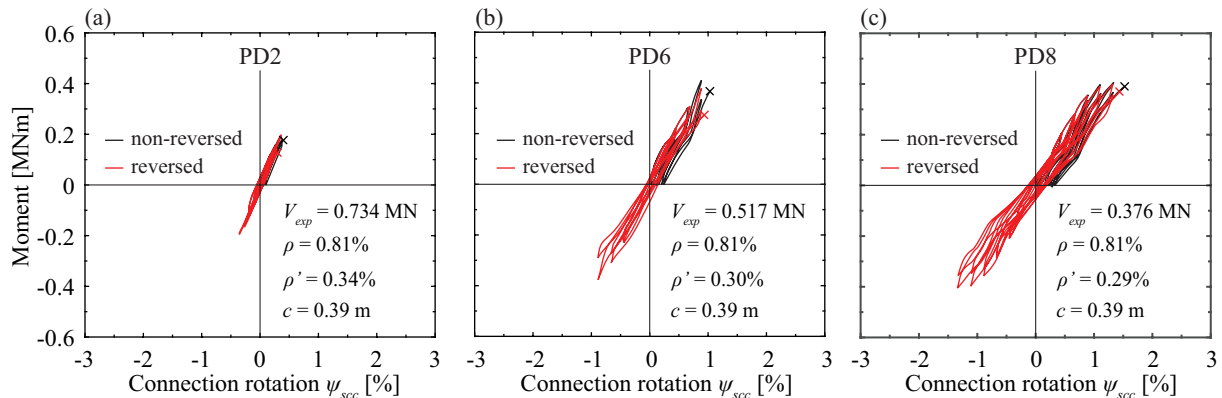
Figure 5.21 – Influence of rotation reversal on the predicted cyclic response of slabs with $\rho = 0.75\%$ tested within this research: (a) PD2, (b) PD6, and (c) PD8.

Table 5.2 – Predictions of moment strength, corresponding connection rotation and connection rotation at punching failure for the tested slabs with $\rho = 0.75\%$ (PD2, PD6, and PD8) for reversed and non-reversed cyclic loading ($n_c = 2$)

Slab	$M_{max.pred}$ [kNm]		$\psi_{scc.max.pred}$ [%]		$\psi_{scc.u.pred}$ [%]	
	reversed	non-reversed	reversed	non-reversed	reversed	non-reversed
PD2	**196**	196	**0.36**	0.36	**0.30**	0.40
PD6	**378**	410	**0.88**	0.88	**0.93**	1.03
PD8	**400**	407	**1.32**	1.32	**1.45**	1.53

values in bold represent the model predictions for the loading pattern adopted in the experimental campaign (reversed loading)

As shown in Figure 5.21, the model predicts smaller moment strength for reversed cyclic loading (red curves) than for non-reversed cyclic loading (black curves). Moreover, non-reversed cycles result in concentration of plastic deformations and consequently in high cyclic damage in the hogging slab half while no cyclic damage occurs in the opposite slab half. Table 5.2 and Figure 5.21 show that the influence of rotation reversal is more pronounced for low gravity loads (Fig. 5.21b and c) than for high gravity loads (Fig. 5.21a). This is expected, since according to the monotonic model, which forms the basis of the model presented in this chapter, the moment-rotation response is less dependent on the loading history for high gravity loads than for low gravity loads. This is in agreement with the experimental findings of Chapter 3. Regarding the deformations, the analytical model predicts that the connection rotation of slabs PD2, PD6 and PD8 at peak moment does not depend on whether the loading pattern is reversed or not. However, the connection rotation at punching failure attains 5-35% higher values for non-reversed loading compared to reversed loading.

5.5.3 Number of cycles

The effect of the number of performed cycles on the seismic behaviour of slab-column connections is examined in the following. The effect of the number of cycles on the moment capacity and the deformation capacity has not been investigated experimentally in the past. For this reason, previous studies have compared the behaviour of similar specimens belonging to different experimental campaigns and subjected to different load histories [Tia07], focusing on the decrease of the deformation capacity due to larger number of cycles. The slabs that were compared contained similar reinforcement ratios and were subjected to similar gravity loads [Gha76, Pan89, Tia08]. However, the slab size and the slab thickness were not similar, therefore not allowing safe conclusions on the influence of the number of cycles on the deformation capacity of slab-column connections to be drawn. The model presented in this chapter allows for a more systematic study of the effect of the number of cycles on the moment strength and the deformation capacity of slab-column connections. Figure 5.22 shows the moment-rotation curves for slabs PD2, PD6 and PD8 that were tested within this research for the same loading protocol as in the experimental campaign (Section 3.6) but with different number of cycles per rotation level (n_c = 1, 2, 3 and 4). The curves are plotted in the first quadrant and up to punching failure (predicted according to CSCT(mono)).
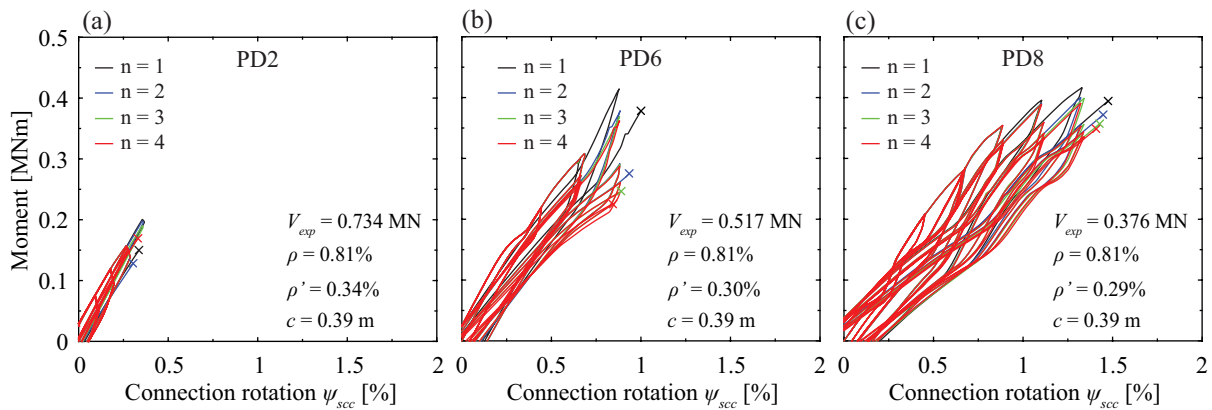
Figure 5.22 – Influence of the number of cycles on the cyclic response of slabs with $\rho = 0.75\%$ tested within this research: (a) PD2, (b) PD6, and (c) PD8.

As can be seen from Figure 5.22, the model predicts that larger number of cycles results in smaller moment strength. The corresponding connection rotation appears to be influenced only to a minor degree by the number of applied cycles. Table 5.3 gives the peak moment and the corresponding connection rotation for the three slabs of Figure 5.22. It is shown that increase of n_c from 1 to 4 leads to decrease of the moment strength by 18%, 13%, and 7% for ν = 0.29, 0.19, and 0.14 $\sqrt{\text{MPa}}$, respectively.

Table 5.3 – Moment strength and deformation capacity predictions for the tested slabs with $\rho = 0.75\%$ (PD2, PD6, and PD8) as function of the applied number of cycles n_c

Slab	$M_{max.pred}$ [kNm]				$\psi_{scc.max.pred}$ [%]			
	$n_c = 1$	$n_c = 2$	$n_c = 3$	$n_c = 4$	$n_c = 1$	$n_c = 2$	$n_c = 3$	$n_c = 4$
PD2	206	**196**	190	169	0.36	**0.36**	0.36	0.33
PD6	414	**378**	369	362	0.88	**0.88**	0.88	0.88
PD8	417	**400**	397	389	1.32	**1.32**	1.11	1.11

values in bold represent the model predictions for the loading protocol adopted in the experimental campaign (Chapter 3)

5.6   Lateral force-resisting mechanisms

This section presents the influence of cyclic loading on the contribution of the different lateral force-resisting mechanisms to the total unbalanced moment. Figure 5.23 shows the influence of the gravity-induced shear and the reinforcement ratio on the predicted γ factors as function of the connection rotation for the same case study of Section 4.4 ($L/d = 35$). The predictions according to the cyclic model (continuous curves) are presented until punching failure and only for positive connection rotation values. Square markers represent the contribution of the different resisting mechanisms at peak unbalanced moment. For comparison purposes, the predictions according to the simplified approach of Chapter 4 are also shown (dashed curves).
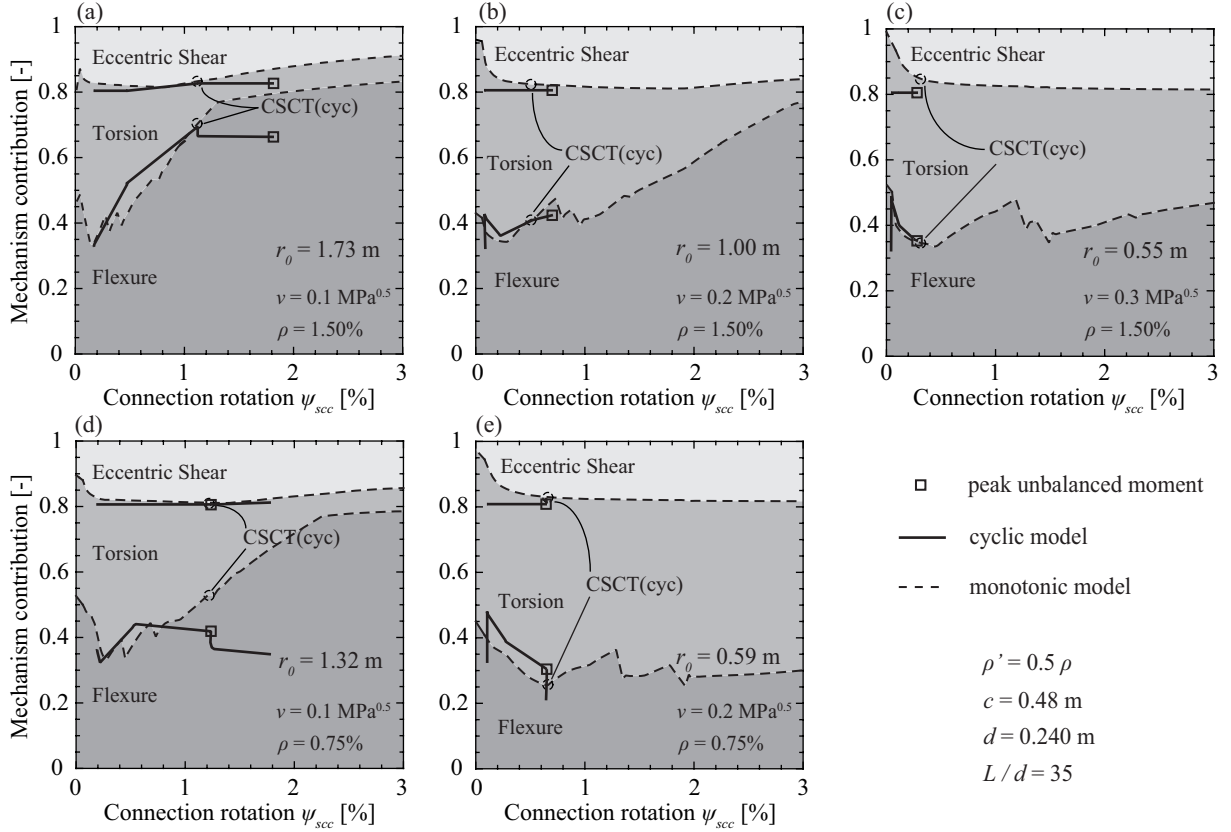
Figure 5.23 – Predicted contribution of flexure, torsion and eccentric shear force according to the proposed model ($c = 2d$; $f_c = 30$ MPa; $L = 35d$; $d_g = 16$ mm and $f_y = 460$ MPa) for $\rho = 1.50\%$: (a) $\nu = 0.1$ $\sqrt{\text{MPa}}$; (b) $\nu = 0.2$ $\sqrt{\text{MPa}}$; (c) $\nu = 0.3$ $\sqrt{\text{MPa}}$; and for $\rho = 0.75\%$: (d) $\nu = 0.1$ $\sqrt{\text{MPa}}$; and (e) $\nu = 0.2$ $\sqrt{\text{MPa}}$.

Figure 5.23 shows that the cyclic analytical model of this chapter predicts higher contribution of flexure at peak unbalanced moment for low gravity loads (Figs. 5.23a, and d) than for high gravity loads (Figs. 5.23b, c, and e). On the other hand, the contribution of eccentric shear force is not significantly affected by the gravity load level. As has been shown is Chapter 4, the flexure contribution to the unbalanced moment equals the sum of the radial moments of all sector elements (Eq. (4.9)). Since cyclic damage is assumed to affect only the radial moment-curvature relationship (§5.2.3), it is anticipated that increasing number of cycles leads to smaller $\gamma_{f.pred}$ values than the simplified approach presented in Chapter 4. This is more marked for small gravity loads than for high gravity loads.

5.7 Slab deformation outside the slab-column connection

In Chapter 4, a method based on the Effective Beam Width approach was proposed in order to calculate the contribution of the slab deformation outside $0.22L$ (ψ_{os}) to the total slab deformation ψ_{slab} (§4.2.5). This section proposes an extension of the same approach for cyclic loading conditions. The only difference between the two cases is the way the rotational stiffness of the slab-column connection (EI_k) is calculated. For monotonic loading, EI_k is taken as the ratio of unbalanced moment M_k and rotation due to slab deformation $\psi_{slab.k}$ (Fig. 5.24a), i.e. equal to the secant stiffness at the considered point k of the moment-rotation curve (Eq. (4.16)). For cyclic conditions, however, EI_k is calculated with respect to the point where the moment-rotation curve intersects the x-axis, i.e. the residual rotation $\psi_{slab.0}$ (Fig. 5.24b). The rest of the formulas for the calculation of the radial bending moment and torsional moment at the perimeter of each sector element ($M_{rad}(\phi_i, r_s)$ and $M_{tor}(\phi_i, r_s)$, respectively) can be found in §4.2.5.

The difference in the moment-rotation response between a continuous slab under monotonic and cyclic loading conditions is illustrated in Figure 5.24c. Comparison of the presented approach with tested continuous flat slabs and simply supported isolated specimens with the verical load applied on the slab surface ($\psi_{os} > 0$) can be found in the following chapter. It should be noted that the presented Effective Beam Width approach does not account for compressive membrane action.
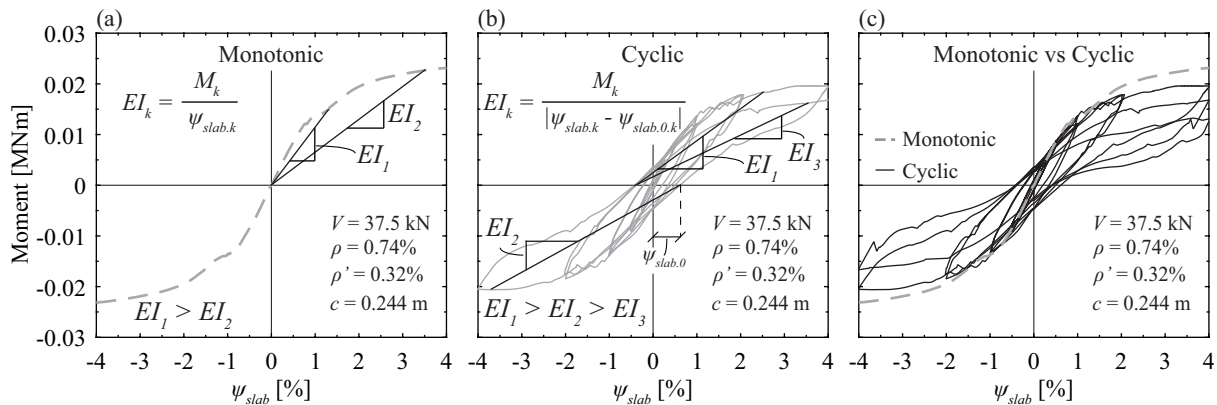
Figure 5.24 – Influence of cyclic loading in the behaviour of continuous flat slabs: (a) rotational stiffness under monotonic loading, (b) rotational stiffness under cyclic loading, and (c) comparison of the moment-rotation response of a continuous flat slab for monotonic and cyclic loading conditions.

5.8 Seismic rotation capacity

In Chapter 4 (Section 4.5) it was shown that the seismic rotation capacity decreases with increasing gravity load acting on the slab-column connection. This section compares the simplified approach presented in Chapter 4 with the approach presented in this chapter. Such comparison will shed light on the influence of the loading history on the rotation capacity of slab-column connections and, whether the simplified approach of Chapter 4 suffices for consideration of the cyclic loading effect. In addition, §5.8.1 discusses the effect of the loading history on the predicted seismic rotation capacity, while §5.8.2 presents the results of a parametric study on the influence of slab depth, slab slenderness and reinforcement content on the predicted rotation capacity.

The adopted normalised loading protocols for the parametric study are the same as in §5.5.1 (Fig. 5.20a) except that for this calculation, the $\psi_{slab.max}$ was estimated using the simplified approach of Chapter 4 (Section 4.5), due to lack of experimental data. For comparison, the allowable drift limit according to ACI-318 [ACI14], the model proposed by Hueste and Wight [Hue99], and the predictions using the monotonic model (Chapter 4) are also shown (grey curves) are also included in the figure.

5.8.1 Influence of loading history

Monotonic vs Reversed cyclic

Figure 5.25a shows the predicted slab rotation ψ_{slab} at peak moment according to the analytical model presented in this chapter as function of the normalised gravity load acting on the slab-column connection (black curves).

Figure 5.25 – Predicted slab rotation at peak moment considering the effect of loading history and allowable drift limit according to ACI-318 [ACI14] and Hueste and Wight [Hue99]: (a) Influence of loading conditions (monotonic vs cyclic) and seismicity level, and (b) moment-rotation curves for slab-column connections in the zone of discontinuity (high seismicity).

Figure 5.25a shows that the deformation capacity according to the cyclic model presented in this chapter can attain 30-50% higher values than the CSCT(cyc) approach. For high gravity loads the influence of loading history on the deformation capacity becomes less important. The simplified approach of Chapter 4 (dashed-dotted grey curve in Fig. 5.25a) provides a reasonable lower-bound estimate of the seismic rotation capacity of slab-column connections if no consideration of the loading history is taken.

Although the shape of the curves according to the monotonic model (drawn in grey) is smooth, the curves according to the cyclic model (drawn in black) display a step at GSR $\approx$ 0.50-0.65. This discontinuity is associated with the cyclic damage of the slab-column connection, as illustrated in Figure 5.25b. When the cyclic damage is not large enough to trigger smaller unbalanced moment at punching failure than at the previous peak, the ψ_{slab} at peak moment coincides with the ψ_{slab} at punching failure (continuous curve in Fig. 5.25b). This case corresponds to the left-hand side of each curve (Fig. 5.25a). On the contrary, when the cyclic damage is large enough to induce punching failure at a smaller unbalanced moment than the maximum previously attained unbalanced moment (dashed-dotted curve in Fig. 5.25b), the ψ_{slab} at peak moment is smaller than the ψ_{slab} at punching failure (right-hand side of each curve in Fig. 5.25a). Figure 5.25a shows that for increasing seismicity the step in the ψ_{slab} - GSR diagram moves to higher GSR values, creating a zone where high seismicity results in larger ψ_{slab} values than low seismicity (0.50 < GSR < 0.65). In this zone, the first inelastic rotation level corresponds to $\psi_{slab.max}$ for low seismicity but only to $0.57\psi_{slab.max}$ for high seismicity. When the first unloading from the post-yield range occurs at the load step that corresponds to $\psi_{slab.max}$ (last load step), the cyclic damage increases significantly and leads to the discontinuity of the ψ_{slab} - GSR curve. High seismicity implies a larger number of applied load steps than low seismicity (in this case 6 instead of 3). Since for high seismicity there is a larger number of load steps before $\psi_{slab.max}$ than for low seismicity, it is expected that the last load step becomes determinant at higher gravity loads for high seismicity that for low seismicity.

The overall influence of the number of cycles before reaching failure in the ψ_{slab} - GSR curves does not appear to be significant (Fig. 5.25a) and therefore confirms the results of §5.5.1. The loading protocol for moderate-low seismicity regions will be used for the parametric studies shown in the following.

Reversed cyclic vs Non-reversed cyclic

In the following, the results of a parametric study on the influence of rotation reversal on the predicted rotation capacity according to the cyclic model are presented. Figures 5.26 and 5.27 show the predicted slab rotation ψ_{slab} as function of the normalised shear force for both reversed and non-reversed cyclic loading for $\rho = 0.75\%$ and 1.50%, respectively. The predicted slab rotation is shown both at peak unbalanced moment (Figs. 5.26a and 5.27a) and at punching failure (Fig. 5.26b and 5.27b).
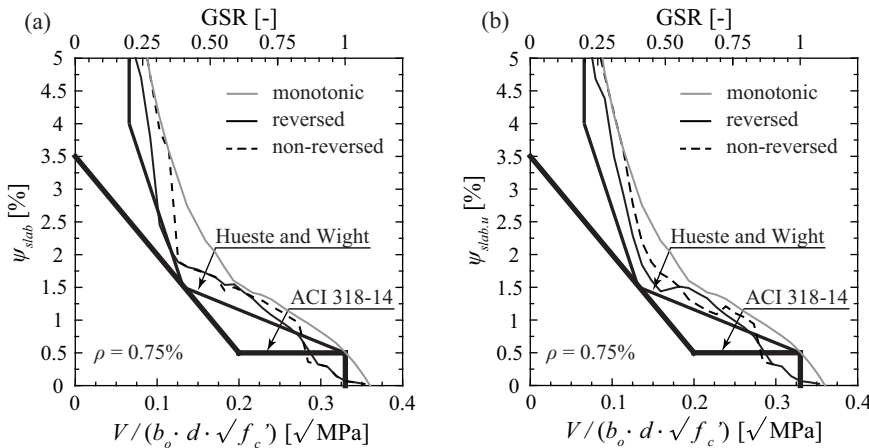
Figure 5.26 – Allowable drift limit according to ACI-318 [ACI14] and Hueste and Wight [Hue99] and predicted slab rotation for reversed and non-reversed loading ($\rho = 0.75\%$, $\rho' = 0.38\%$, $d = 120$ mm, $L = 35d$, $c = 2d$, $f_c = 30$ MPa, $d_g = 16$ mm, and $f_y = 460$ MPa) at: (a) peak unbalanced moment, and (b) punching failure.
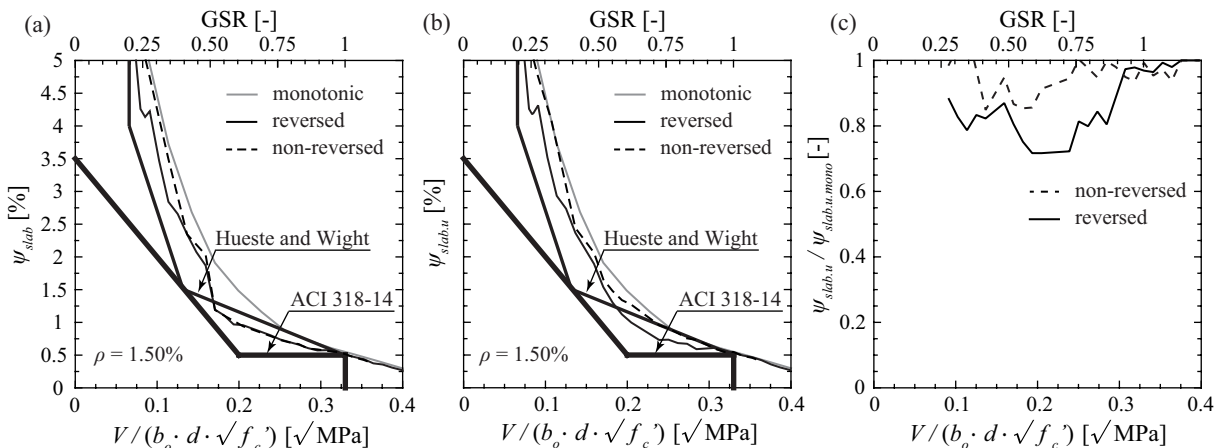
Figure 5.27 – Allowable drift limit according to ACI-318 [ACI14] and Hueste and Wight [Hue99] and predicted slab rotation for reversed and non-reversed loading ($\rho = 1.50\%$, $\rho' = 0.75\%$, $d = 120$ mm, $L = 35d$, $c = 2d$, $f_c = 30$ MPa, $d_g = 16$ mm, and $f_y = 460$ MPa) at: (a) peak unbalanced moment, and (b) punching failure.

In general, rotation reversals lead to smaller slab rotation ψ_{slab}. Figures 5.26a and 5.27a show that this effect is more pronounced for low gravity loads. It can be seen that the effect of rotation reversals is more marked for the slab rotation at punching ($\psi_{slab.u}$ - Figs. 5.26b and 5.27b) than for the slab

rotation at peak unbalanced moment (ψ_{slab} - Figs. 5.26a and 5.27a). As shown in Figure 5.27c (ρ = 1.50%), rotation reversal leads to maximum reduction of the rotation capacity by 30% compared to monotonic loading (for GSR = 0.6). On the other hand, non-reversed cyclic loading results in maximum reduction by only 15% compared to monotonic loading (for GSR = 0.4).

Influence of the number of cycles (reversed cyclic loading)

In the following, the results of a parametric study on the influence of the number of cycles on the rotation capacity of slabs with ρ = 0.75% (Fig. 5.28) and ρ = 1.50% (Fig. 5.29) are presented and discussed. Each figure distinguishes between slab rotation at peak unbalanced moment (Figs. 5.28a and 5.29a) and slab rotation at punching failure (Figs. 5.28b and 5.29b).
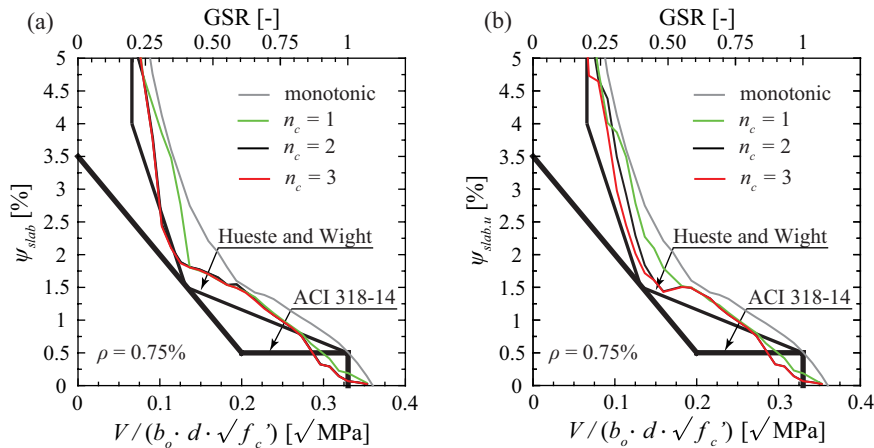
Figure 5.28 – Allowable drift limit according to ACI-318 [ACI14] and Hueste and Wight [Hue99] and predicted slab rotation for n_c = 1, 2, and 3 (ρ = 0.75%, ρ' = 0.38%, d = 120 mm, L = 35d, c = 2d, f_c = 30 MPa, d_g = 16 mm, and f_y = 460 MPa) at: (a) peak unbalanced moment, and (b) punching failure.
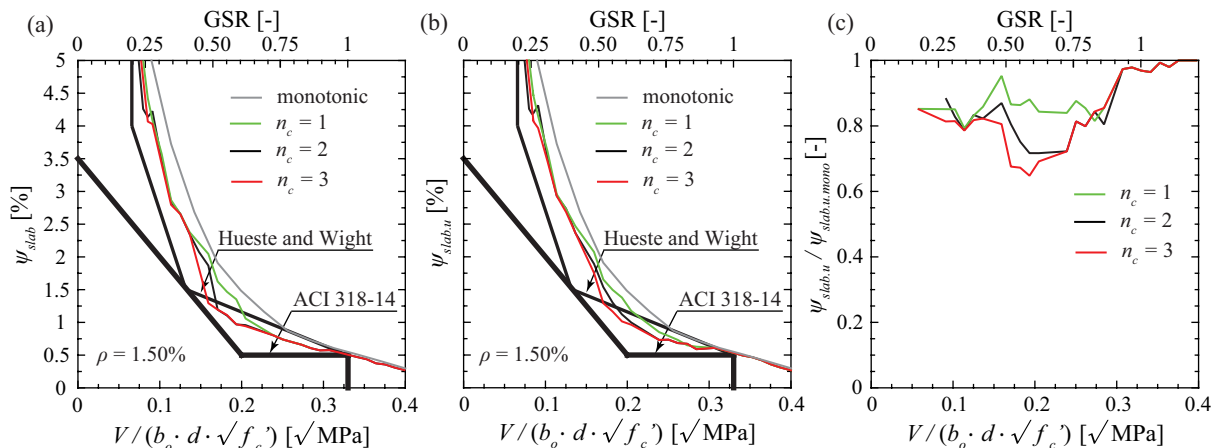
Figure 5.29 – Allowable drift limit according to ACI-318 [ACI14] and Hueste and Wight [Hue99] and predicted slab rotation for n_c = 1, 2, and 3 (ρ = 1.50%, ρ' = 0.75%, d = 120 mm, L = 35d, c = 2d, f_c = 30 MPa, d_g = 16 mm, and f_y = 460 MPa) at: (a) peak unbalanced moment, and (b) punching failure.

Figures 5.28 and 5.29 show that small number of cycles n_c per load step results, in general, in ψ_{slab} predictions closer to the monotonic model. The overall influence of the number of cycles is more marked on the slab rotation at punching failure (Figs. 5.28b and 5.29b) than on the slab rotation at

peak moment (5.28b and 5.29b). As shown in Figure 5.29c ($\rho = 1.50\%$), 1 cycle per drift level leads to maximum reduction of the rotation capacity by 20% compared to monotonic loading (for GSR = 0.85), 2 cycles result in maximum reduction by 30% (for GSR = 0.65), and 3 cycles result in maximum reduction by 35% (for GSR = 0.6).

It should be noted that the main difference between the cyclic model and the monotonic model (grey curves) lies on the assumed shear crack inclination. The monotonic model adopts a rotating shear crack, while the cyclic model adopts a fixed shear crack. The crack angle in the cyclic model corresponds to the angle of load reversal after yielding has been exceeded for the first time. The rotation amplitude at first post-yield unloading $\psi_{slab.y}$ is the parameter that is influencing most the shear crack inclination and consequently the predicted rotation capacity. When $\psi_{slab.y}$ is closer to the slab rotation $\psi_{slab.max}$, the cyclic model gives predictions closer to the simplified approach of Chapter 4.

5.8.2 Influence of geometric properties and reinforcement content

In the following, the influence of the effective depth (Fig. 5.30a), the reinforcement ratio (Fig. 5.30a), and the slab slenderness (Fig. 5.30b) on the predicted seismic rotation capacity is assessed, considering the effect of loading history.
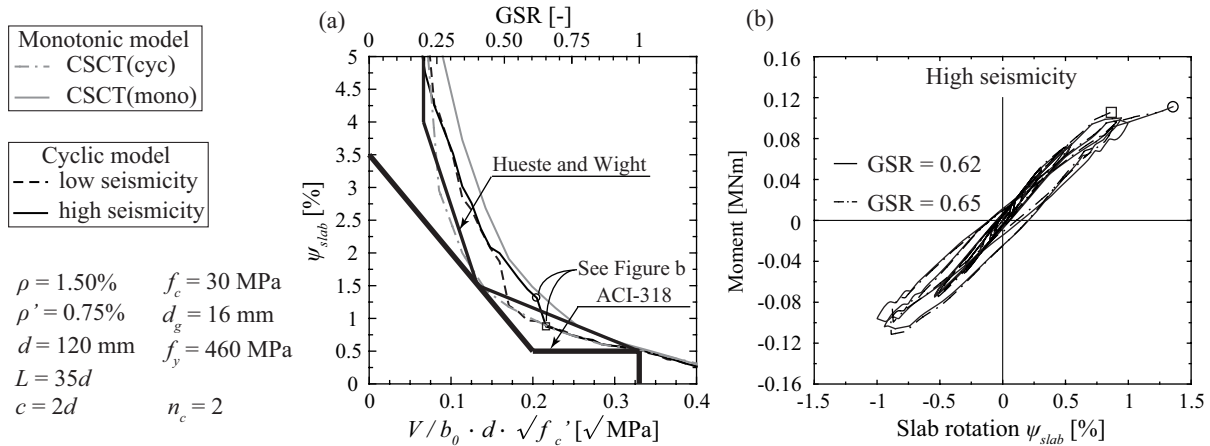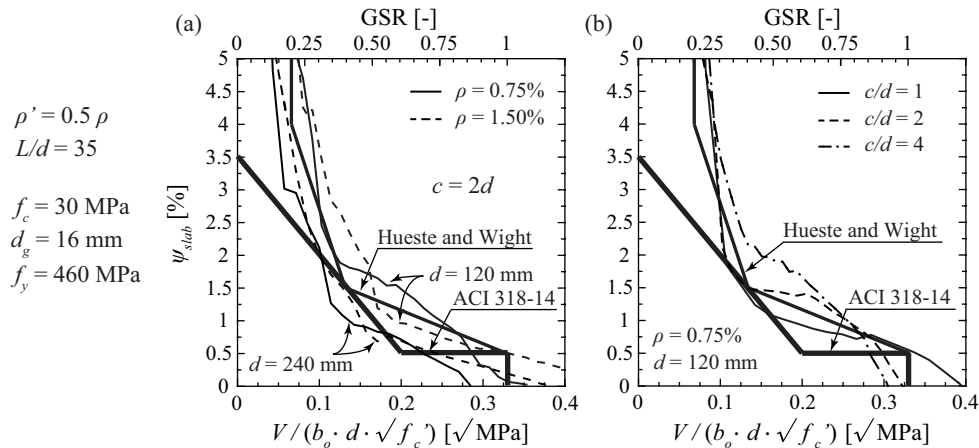

Figure 5.30 – Predicted slab rotation at peak moment considering the effect of loading history and allowable drift limit according to ACI-318 [ACI14] and Hueste and Wight [Hue99]: (a) Influence of slab effective depth and reinforcement ratio on the seismic rotation capacity ($c = 2d$), and (b) Influence of column size on the seismic rotation capacity.

For the shape of the calculated curves of Figure 5.30, similar discontinuities as the one shown in Figure 5.25a can be observed, which correspond to a change in $\psi_{slab.y}$ from $0.15\psi_{slab.max}$ to $0.42\psi_{slab.max}$ and from $0.42\psi_{slab.max}$ to $\psi_{slab.max}$, resulting in a sudden increase of the seismic damage and consequently in a drop of the slab rotation at peak moment. As can be seen from Figure 5.30a, higher slab effective depth confers smaller seismic rotation capacity, as was the case for the simplified approach of Chapter 4 (Section 4.5). Regarding the effect of reinforcement ratio on the rotation capacity predictions, for relatively high gravity loads ($0.5 <$ GSR < 0.85 for $d = 120$ mm and $0.5 <$ GSR < 0.65 for $d = 240$ mm) high ρ results in smaller rotation capacity than small ρ. In these zones $\psi_{slab.y}$ increases with ρ, i.e. first unloading from the post-yield range comes at higher ψ_{slab} for high ρ than for small ρ. On the other hand, for the zones where high ρ leads to higher rotation capacity than small ρ (for instance when GSR < 0.5), $\psi_{slab.y}$ decreases with ρ, i.e. first yielding comes at smaller ψ_{slab} for high ρ than for small ρ. The extent of the different zones depends on the adopted loading protocol. Moreover, Figure 5.30a shows that the effect of reinforcement ratio on the seismic rotation capacity is more pronounced for $d = 120$ mm than for $d = 240$ mm. Figure 5.30b shows that the column size c has also a marked

effect on the seismic rotation capacity. Larger column results in higher rotation capacity, which is in agreement with the results of Section 4.5. It was observed that the slab slenderness has a smaller impact of the seismic rotation capacity.

5.9   Conclusions

This chapter presents an extension of the mechanical model presented in Chapter 4 to account for the hysteretic behaviour and cumulative damage effects on slab-column connections without transverse reinforcement when subjected to cyclic loading. The assumptions of the extended model are based on local deformation measurements from the tests performed within this research (Chapter 3). The main conclusions of this chapter are the following:

1. The extended analytical model allows considering both cyclic loading and maximum deformation when calculating the moment-rotation relationship of slab-column connections subjected to earthquake loading. A fixed shear crack is assumed to govern the post-yield behaviour of the sector elements while a hysteretic moment-curvature relationship is adopted for the radial direction. Seismic damage is incorporated using a model proposed by Roufaiel and Meyer [Rou87].

2. The moment resistance and the rotation capacity are determined by the combination of the moment-rotation relationship with the failure criterion that allows for shear force redistribution between the sector elements of the hogging slab half, as for monotonic loading conditions (CSCT(mono)). The upper-bound limit for punching failure under cyclic loading is determined when the maximum slab rotation ψ_{max} reaches the maximum slab rotation at punching under monotonic loading ($\psi_{max.u.mono}$), i.e. when $D = 1$.

3. The extended model allows for better estimation of the rotation capacity of the slabs tested within this research (Chapter 3) compared to the simplified approach presented in Chapter 4.

4. According to the proposed model, at peak moment, the contribution of flexure (γ_f) to the total unbalanced moment resisted by the slab-column connection decreases with increasing gravity load acting on the slab. For low gravity load, the cyclic model predicts smaller γ_f values at peak moment than the simplified approach of Chapter 4. The influence of the loading history on the predicted γ_v values (contribution of eccentric shear force) is less marked.

5. The model shows that the seismic rotation capacity of flat slabs is considerably influenced by the gravity induced shear and the slab effective depth, but also by the column size. Other parameters such as the seismicity level, the top reinforcement ratio, and the slab slenderness influence the rotation capacity to a smaller extent. The effect of the number of cycles and rotation reversals is more pronounced on the slab rotation at punching than on the slab rotation at peak moment. The simplified approach for cyclic loading presented in Chapter 4 (adoption of CSCT(cyc) instead of CSCT(mono)) represents a reasonable lower-bound solution to be used in engineering practice if no consideration of the loading history is made.

Chapter 6

Validation of the analytical model

The experiments performed within the framework of this thesis as well as experiments found in the literature are used for evaluating the performance of the developed analytical model, presented in Chapters 4 and 5 for monotonic and cyclic loading conditions, respectively.

In Section 6.1, the main assumptions of the analytical model for the moment-rotation relationship are evaluated. The evaluation focuses on the assumptions regarding (a) the inclination of the critical shear crack, and (b) the kinematic law between the slab rotations at varying angles with regard to the direction of excitation.

Section 6.2 presents the evaluation of the performance of the combined model (analytical model for the moment-rotation relationship and failure criterion) to predict the moment-rotation response of isolated slab-column specimens. The comparisons presented in this section comprise tests on square slabs without transverse reinforcement supported on square columns and subjected to monotonic or quasi-static cyclic unbalanced moments. First, the predictions of local slab rotations according to the proposed model are compared to experimentally obtained local slab rotations from the tests performed within this thesis. Afterwards, the model performance in predicting the moment strength and the deformation capacity of slab-column connections is assessed through comparison with results of both the current experimental campaign and previous experimental campaigns. Comparisons with the predictions of the some codes of practice and several other models are also presented. Finally, the contribution of the different lateral force-resisting mechanisms is validated through comparison with NLFEA results. Based on the model predictions for the specimens of the test database, new formulas are proposed for the calculation of γ_v and γ_t within the ACI-318 eccentric shear force model.

Section 6.3 presents the evaluation of the performance of the proposed model in predicting the response of continuous flat slabs. First, the predicted distribution of radial bending moments and torsional moments at $r = 0.22L$ is validated through comparison with NLFEA results. Then, the model predictions for the moment strength and the deformation capacity (combination of the analytical model with the failure criterion) are compared with results of continuous flat slab specimens. Only tests on one-storey flat slabs without transverse reinforcement are treated in this section. The tested specimens were subjected to combined vertical loads and monotonic or quasi-static cyclic lateral loads. The evaluation is focused on interior slab-column connections supported on square columns. Due to the significant implications of tests on continuous flat slabs for the behaviour of actual flat slabs, the evaluation is presented in more detail in comparison with the evaluation for tests on isolated specimens.

6.1 Assumptions

The tests performed within the framework of this thesis were used for evaluating the main assumptions of the proposed model (Chapters 4 and 5):

- The slab rotation follows a sinusoidal law with regard to the bending axis (see Eq. (4.2)).

- For monotonic loading conditions, the radius r_0 of the critical shear crack is equal to the eccentricity e, but no smaller than $r_c + d$ (see Eq. (4.3)).

- For cyclic loading conditions, the radius r_0 of the critical shear crack is equal to the eccentricity e (but no smaller than $r_c + d$) during loading/unloading in the elastic range, while loading/unloading in the post-elastic range is governed by the attained eccentricity at the first post-yield peak.

6.1.1 Kinematic law between slab rotations at varying angles

To validate the adopted sinusoidal law that relates the rotation to the angle with regard to the bending axis, comparisons with experimentally measured slab rotations at different angles are needed. Although the database of existing tests is rather extensive (Appendix A), no data on measured rotations at different angles were collected.

For the tests performed using setup (a), the main aim was to evaluate the punching resistance of slab-column connections in the presence of a constant eccentricity. Therefore, the results represent the punching capacity at a defined level of induced drift rather than the moment capacity of the slab-column connection under increasing earthquake-induced drifts. In addition, since only the central deflection is typically measured, there is a lack of information on the local slab rotations, which influence to a remarkable degree the prediction at both global (specimen) and local (sector element) level (Chapter 4). Therefore, safe conclusions cannot be drawn on the legitimacy of the adopted kinematic law.

For tests carried out using setup (b), only maximum slab rotations are typically reported [Haw89]. Although these tests are useful for assessing the performance of the proposed model in predicting the maximum local slab rotation during moment introduction, they cannot provide information on the local slab rotations at different angles.

For the tests performed using setup (c), which is the most common configuration for experimental investigations under cyclic loading conditions, only the horizontal displacement of the column top is measured. The drift demand on the slab-column connection is expressed as the top displacement of the column divided by the column height. Since the column is designed to remain elastic during the moment introduction, the rotation due to column deformation is zero for this setup configuration and the measured drift corresponds to the rotation due to slab deformation. Nevertheless, such measurement does not provide any information on the distribution of local slab rotations at different angles.

As has been discussed in the introduction (Chapter 1), one of the main objectives of the present research is the development of a relation between local slab rotations and the rotation of the slab-column connection, since the latter one gives an estimation of the contribution of the slab deformation to the interstorey drift. The experimental campaign aimed to provide more insight with respect to this investigation and to verify the sinusoidal kinematic law adopted by the proposed model (Chapter 4) to describe the variation of slab rotation as function of the angle with respect to the axis of excitation. Figures 6.1 and 6.2 show the comparison between experimental slab rotation (grey curves) and calculated slab rotation (black curves) at varying angles and at peak moment for the tests performed within this research (monotonic and cyclic, respectively). Figure 6.2 compares the experimental slab rotation distribution at peak moment with the predicted slab rotation distribution according to both the simplified approach of Chapter 4 (adoption of CSCT(cyc) - continuous black curves) and the cyclic

model proposed in Chapter 5 (adoption of CSCT(mono) - dashed black curves). The measured slab rotations at peak moment are represented by round markers (grey curves).
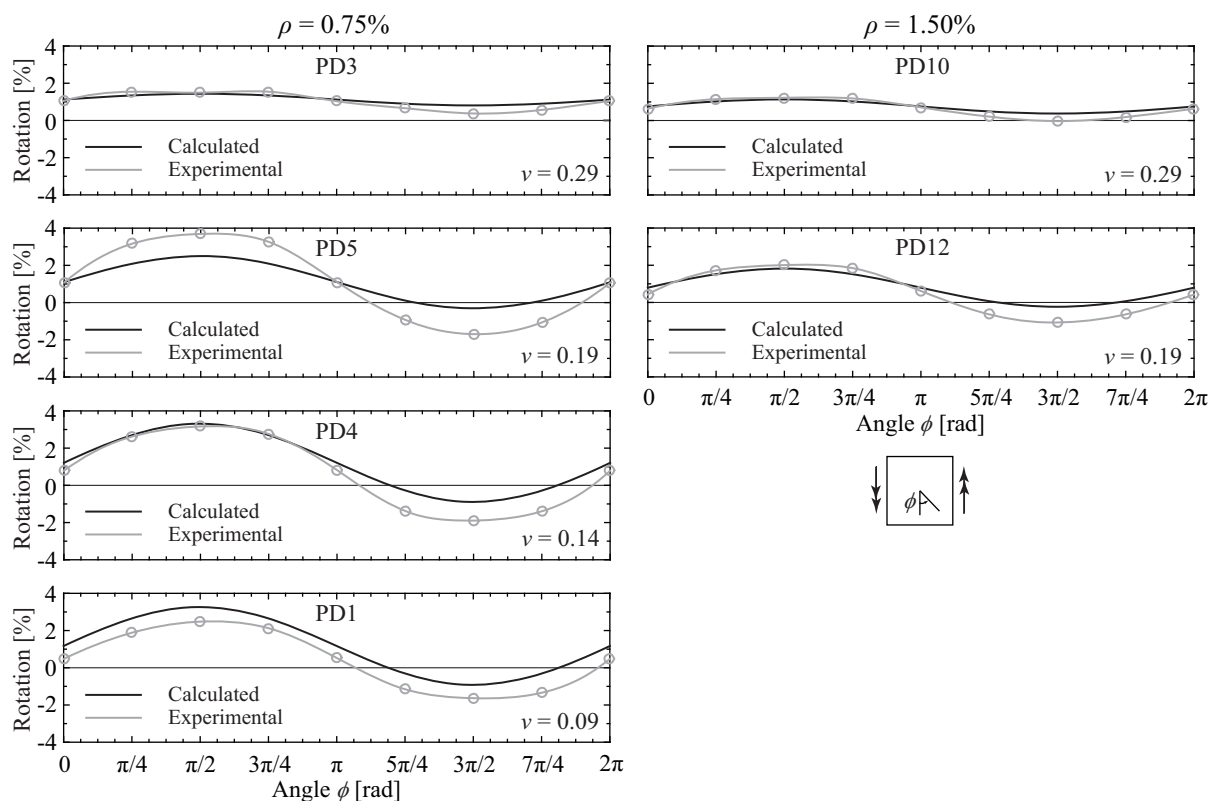
Figure 6.1 – Comparison between peak experimental and calculated slab rotations at varying angles with respect to the bending axis for the monotonic tests performed within this research.
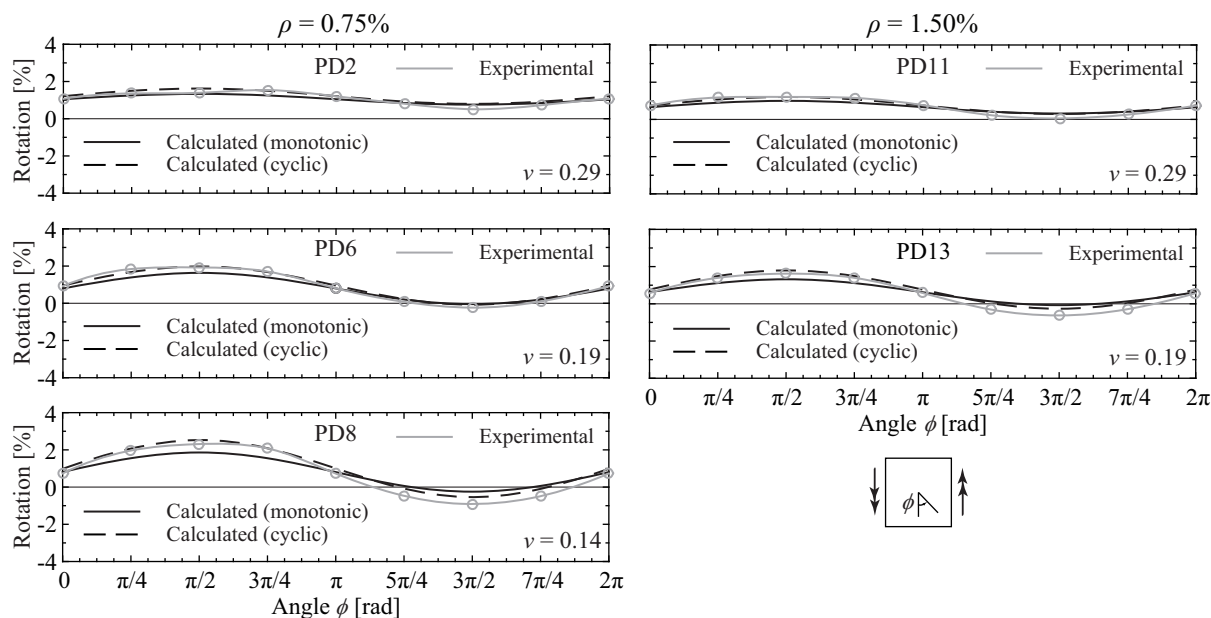
Figure 6.2 – Comparison between peak experimental and calculated slab rotations at varying angles with respect to the bending axis for the cyclic tests performed within this research.

Both Figures 6.1 and 6.2 show that the proposed model follows the experimental trend rather well. In particular, the predictions are more precise for the hogging slab half ($0 \le \phi \le \pi$) than for the sagging slab half ($\pi \le \phi \le 2\pi$). Since the largest slab rotations appear at the hogging slab half and influence considerably the obtained moment-rotation relationship, it is of outmost importance to capture the experimentally measured rotations for this slab half. For the cyclic tests (Fig. 6.2), the simplified approach of Chapter 4 (CSCT(cyc)) predicts consistently stiffer response (black continuous curves) compared to the experimental response as has been noted already (Section 5.4). The cyclic analytical model (dashed black curves), on the contrary, predicts more accurately the measured slab rotations.

Since the torsional moment is proportional to the difference of tangential moments of the two faces of the sector element (Eq. (4.7)) and the tangential moments increase with increased rotation $\psi(\phi)$ (Eq. (4.4)), it comes out that the torsional moment is proportional to the rotation derivative $\psi'(\phi)$. Therefore, the adoption of a sinusoidal law for the slab rotations at varying angles (Eq. (4.2)) maximises $\psi'(\phi)$ (which is proportional to $\cos(\phi)$) at the bending axis ($\phi = 0$ and $\phi = \pi$). Consequently, the torsional moment attains its maximum value at the bending axis. This is in accordance with the elastic plate solution [Mas70] as well as experimental evidence from the presented test campaign (Chapter 3) and previous test campaigns [Haw89, Rha14].

6.1.2   Inclination of the critical shear crack

In the following, the predicted critical shear crack inclination according to the proposed analytical model is compared to the experimentally observed shear crack inclination at failure, on the basis of saw cuts performed after each test (Chapter 3). Since this thesis proposes a different analytical model for monotonically increasing drifts (Chapter 4) and for cyclically increasing drifts (Chapter 5), the comparison distinguishes between monotonic and cyclic tests.

Monotonic tests

Figure 6.3 shows the comparison between saw cuts performed after each monotonic test (drawn in grey) and the assumed radius of the critical shear crack at peak moment, according to the proposed model of Chapter 4 (black lines). As can be seen, assuming that $r_0 = e$ appears rather rational for most performed monotonic tests. It is also verified that r_0 is not smaller than $r_c + d$ (Fig. 6.3a and e).
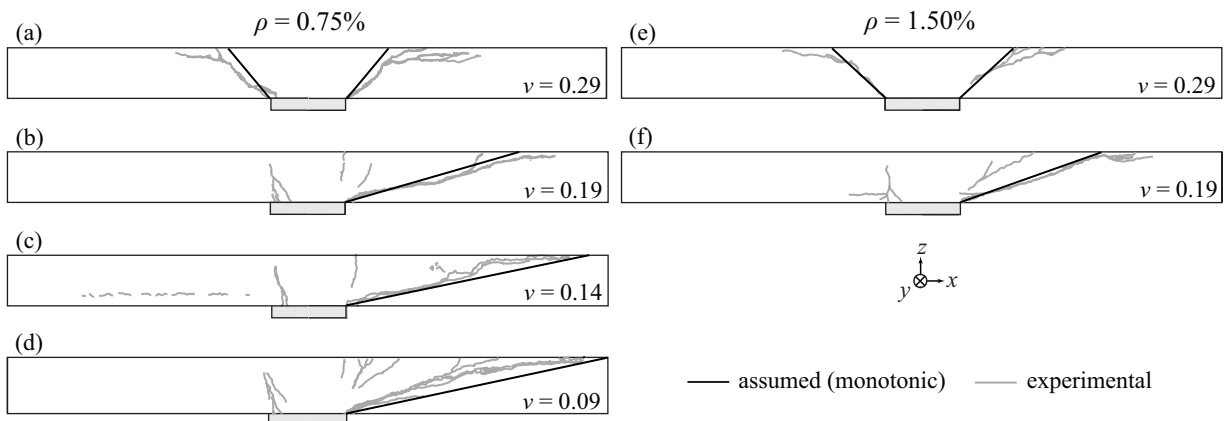
Figure 6.3 – Comparison between experimental shear crack inclination (based on saw cuts) and assumed shear crack inclination at peak moment for the monotonic tests performed within this research.

Cyclic tests

Figure 6.4 shows the comparison between the saw cut of each cyclically tested slab (drawn in grey) and the assumed shear crack inclination at first unloading from the post-elastic range (dashed black lines). To facilitate discussion, the assumed shear crack inclination at peak moment according to the simplified approach of Chapter 4 (monotonic model - CSCT(cyc)) is also shown in the same figure (continuous black lines).
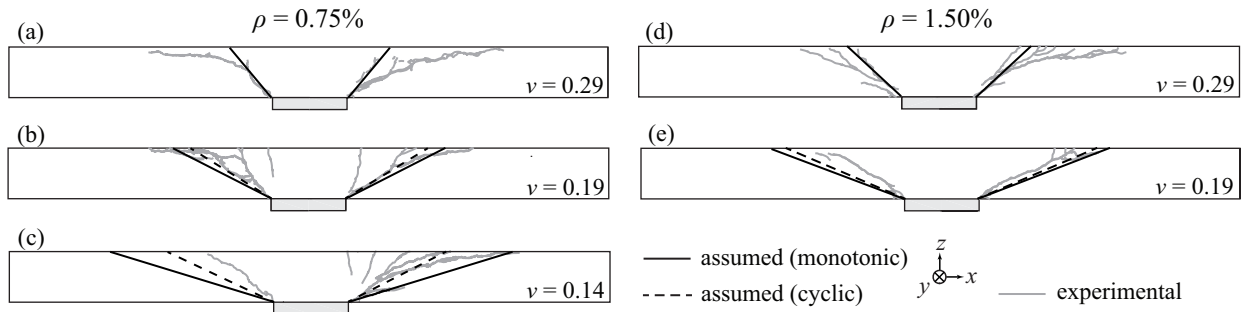
Figure 6.4 – Comparison between experimental shear crack inclination (based on saw cuts) and assumed shear crack inclination for the cyclic tests performed within this research.

For low gravity loads (Fig. 6.4b, c and e), it is shown that by assuming $r_0 = e$ the predicted inclination of the shear crack (continuous black lines) is significantly lower than the experimentally observed one. On the other hand, the assumption that the eccentricity at the first post-elastic peak determines the inclination of the shear crack during subsequent loading/unloading (dashed black lines) leads to prediction of steeper shear cracks, which agrees better with the experimental results. Moreover, the assumption that r_0 cannot be smaller than $r_c + d$ shows good agreement also with the results of the cyclic tests (Fig. 6.4a and d). Moreover, it should be stated that monotonic loading (CSCT(mono)) results in higher peak unbalanced moment, and consequently in flatter shear crack than cyclic loading (CSCT(cyc) - continuous black lines). Therefore, Figure 6.4b, c, and e shows that, for relatively low gravity loads, cyclic loading (dashed black lines) results in prediction of steeper shear crack than monotonic loading (CSCT(mono)). This trend is in accordance with the experimental results, shown in Chapter 3.

6.2 Isolated slab-column specimens

This section aims at assessing the performance of the monotonic and cyclic analytical model presented in Chapters 4 and 5, respectively, with respect to isolated slab-column specimens. First, a rather local prediction assessment is performed, which consists in comparing the predicted and experimentally measured maximum and minimum slab rotations for the slabs tested within this thesis (Chapter 3). Then a global prediction assessment of the analytical model for the moment-rotation relationship combined with the failure criterion of the CSCT is carried out. The predicted moment strength and the deformation capacity are compared with test results of isolated slabs tested by previous researchers and by the author. For discussion purposes, the experimental results are also compared with the predictions of several codes of practice [ACI14,Eur04,Fib11] and other proposed models [Bro09,Hue99]. Finally, the contribution of the lateral force-resisting mechanisms according to the proposed model is compared to numerical calculations using NLFEA. Based on the predictions of the analytical model for the contribution of the different LFRM for tests found in the literature, new formulas are proposed for the calculation of γ_v and γ_t within the framework of ACI-318 [ACI14].

6.2.1 Local slab rotations

As both the failure criterion and the moment-rotation relationship depend on the local slab rotations $\psi(\phi)$, it is important for the analytical model to capture the relationship between local slab rotations and unbalanced moment as well as the local slab rotation at peak unbalanced moment. Although the database of slabs subjected to constant vertical load and unbalanced moment is relatively large, local slab rotations at varying angles were measured only in the test campaign presented in Chapter 3. In the following, the comparison between measured and calculated slab rotations is presented for the maximum slab rotation (ψ_{max}, at $\phi = \pi/2$) and the minimum slab rotation (ψ_{min}, at $\phi = 3\pi/2$) parallel to the x-axis (see Figs. 6.3 and 6.4). Comparison of experimental and calculated slab rotations at different angles ϕ from the bending axis are not included in the following, for illustrative purposes. Table 6.1 compares the experimental and calculated values of ψ_{max} and ψ_{min} at peak unbalanced moment.

Table 6.1 – Experimental and calculated values of ψ_{max} and ψ_{min} at peak unbalanced moment according to CSCT(mono) and CSCT(cyc) [%]

Slab	Loading type	Experimental		CSCT(mono)		CSCT(cyc)	
		ψ_{max}	ψ_{min}	ψ_{max}	ψ_{min}	ψ_{max}	ψ_{min}
PD3	V+M	1.49	0.37	1.43	0.66	-	-
PD5	V+M	3.68	-1.71	2.50	-0.30	-	-
PD4	V+M	3.12	-1.90	3.11	-0.82	-	-
PD1	V+M	2.50*	-1.62*	3.17	-0.88	-	-
PD10	V+M	1.21	-0.03	1.07	0.40	-	-
PD12	V+M	2.02	-1.09	1.63	-0.16	-	-
PD2	V+C	1.34	0.55	1.60	0.79	1.34	0.76
PD6	V+C	1.92	-0.21	1.98	-0.06	1.62	-0.05
PD8	V+C	2.31	-0.85	2.51	-0.57	1.73	-0.22
PD11	V+C	1.22	0.07	1.21	0.32	1.00	0.32
PD13	V+C	1.62	-0.62	1.79	-0.27	1.31	-0.07

*   inconsistent rotation measurement

For monotonic loading, as can be seen from Table 6.1, if slab PD1 is disregarded (due to inconsistent rotation measurement), the predictions of the maximum and minimum slab rotations are slightly conservative but follow the experimental trend rather well for most of the tests. The predictions of the monotonic model are more accurate for the maximum slab rotations rather than the minimum slab rotations. For cyclic loading, the predictions according to the simplified approach of Chapter 4 (columns 7 and 8) are rather conservative estimates of the experimental values (columns 3 and 4). On the other hand, the cyclic model combined with the CSCT(mono) failure criterion gives more accurate predictions of both the ψ_{max} and the ψ_{min} at peak moment (columns 5 and 6).

The experimental and calculated $M-\psi_{max}$ and $M-\psi_{min}$ relationships are compared in Figures 6.5 and 6.6 for monotonic and cyclic tests, respectively. The calculated curves correspond to the monotonic analytical model presented in Chapter 4. The intersection of the analytical model with the CSCT failure criterion (CSCT(mono) in Figure 6.5 - (CSCT(cyc) in Figure 6.6) is also shown.
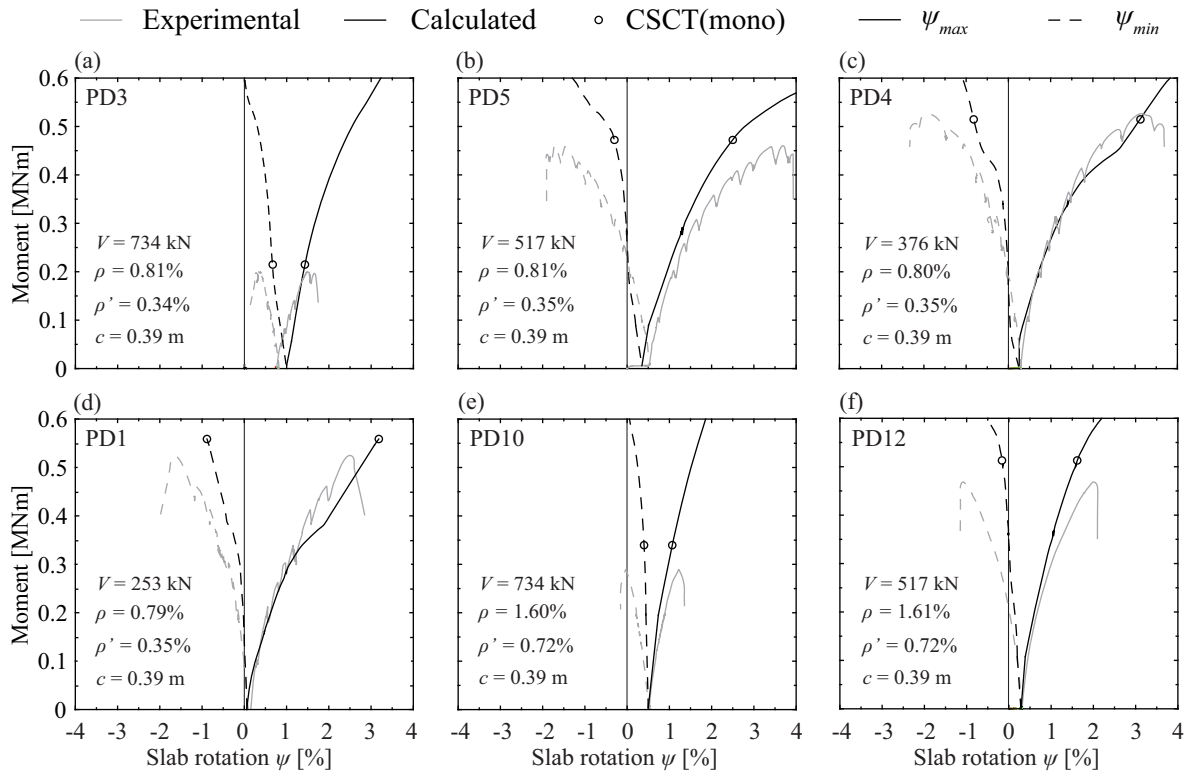
Figure 6.5 – Comparison between experimental and calculated maximum and minimum slab rotations for the monotonic tests performed within this research according to the monotonic analytical model presented in Chapter 4.
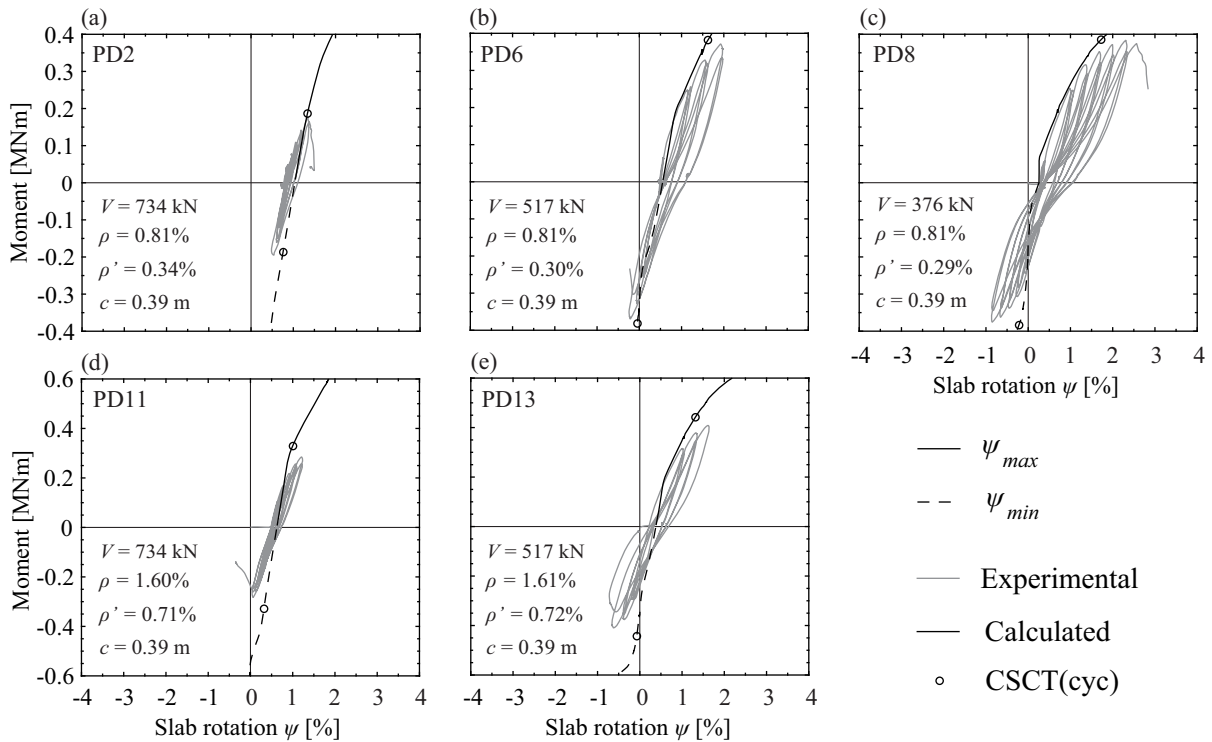
Figure 6.6 – Comparison between experimental and calculated maximum and minimum slab rotations for the cyclic tests performed within this research according to the monotonic analytical model presented in Chapter 4.

As shown in Figures 6.5 and 6.6, the experimentally measured local slab rotations are predicted rather well by the monotonic model. The trend of the relationship between local slab rotations and unbalanced moment is captured both for monotonic tests (Fig. 6.5) and for the envelope of cyclic tests (Fig. 6.6). The good accuracy of the predictions of the local slab rotations with respect to the experimental results proves that the assumption of a sinusoidal law linking the local slab rotations is reasonable also for moments lower than the moment strength (Figs. 6.1 and 6.2).

Figure 6.7 compares the measured and predicted $M - \psi_x$ relationships according to the cyclic analytical model presented in Chapter 5. It should be noted that maximum values of ψ_x correspond to the maximum slab rotation ψ_{max} whereas minimum ψ_x values correspond to the minimum slab rotation ψ_{min}. In the same figure, x markers represent the intersection of the cyclic model with the CSCT(mono) failure criterion or the load step that corresponds to $D = 1$, whichever comes first.
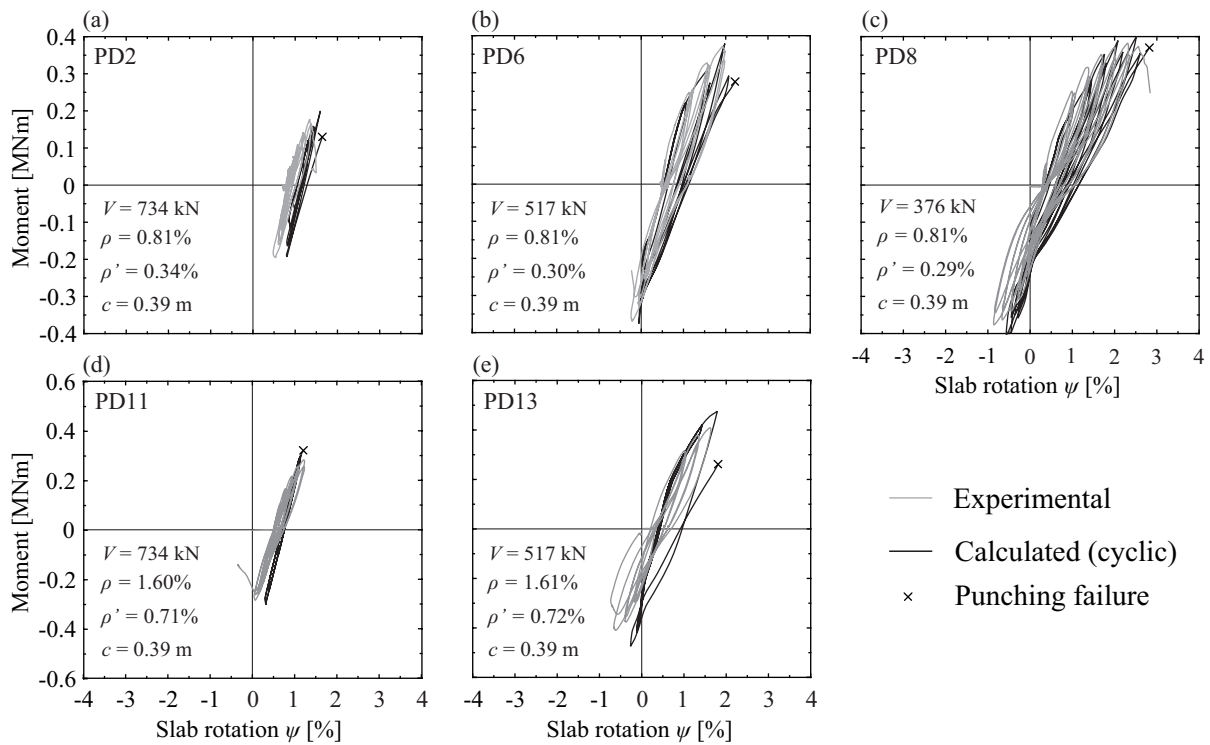
Figure 6.7 – Comparison between experimental and calculated maximum and minimum slab rotations for the cyclic tests performed within this research according to the cyclic analytical model presented in Chapter 5.

Figure 6.7 shows that the cyclic analytical model gives more accurate predictions of the local slab rotation of the cyclically tested slabs than the monotonic analytical model, both at peak and pre-peak loading stage. This is expected since both the hysteretic behaviour of the connections and the cumulative damage due to cyclic loading are taken into account by the cyclic analytical model. In particular, the predictions are more precise for the maximum slab rotations than for the minimum slab rotations. When the minimum slab rotations are close to zero or negative (i.e. sagging), the predicted $M - \psi$ curve is stiffer than the experimental one (Fig. 6.7b, c, and e). This can be explained by the fact that according to the cyclic model loading towards the negative direction is characterised by stiffer $m_{rad} - \chi_{rad}$ relationship for sector elements that have previously developed smaller plastic rotations than the sector element at the tip of the sagging slab half (ψ_{min}) (see Chapter 5). On the other hand, when the minimum slab rotations are positive (i.e. hogging), no response stiffening is predicted (Fig. 6.7a, and d).

6.2.2 Moment strength and deformation capacity

In the following, the proposed model is compared to tests on isolated slabs performed within this research project as well as tests found in the literature. More information on the selected tests is provided in Appendix A. The database comprises 106 isolated slab specimens, among which 53 were tested under constant eccentricity and 53 under constant shear force. While in the first category only monotonic tests are included, the second one comprises slabs subjected to monotonically and cyclically increasing unbalanced moment (18 and 35 tests, respectively). Each test campaign measures the slab-column rotation differently. §4.2.4 outlines for each campaign how the measured quantities are estimated with the analytical model. In Appendix C, the proposed model for the moment-rotation relationship is compared to experimental moment-rotation curves found in literature conducted under either monotonic or cyclic loading conditions. The proposed model for the moment-rotation relationship was found to be in good agreement with the experimental moment-rotation curves. In Appendix D, the predictions of the proposed model (moment-rotation relationship and failure criterion) are compared to the tests of the database (Appendix A) in terms of moment strength and deformation capacity. For monotonic tests, the predictions correspond to the combination of the monotonic moment-rotation relationship (Chapter 4) with the failure criterion CSCT(mono). For cyclic tests, the predictions according to both the approach presented in Chapter 4 (monotonic $M - \psi_{scc}$ relationship combined with the CSCT(cyc) failure criterion) and the model presented in Chapter 5 (cyclic $M - \psi_{scc}$ relationship combined with the CSCT(mono) failure criterion) are provided. In the following, the overall performance of the combined model (analytical model for the moment-rotation relationship and failure criterion) is presented and discussed in terms of moment strength and deformation capacity. In addition, the predictions of several codes of practice [ACI14, Eur04, Fib11] and several proposed models [Bro09, Hue99] are presented and discussed. Their predictions for moment strength and deformation capacity are shown in tabulated form in Appendix D as well.

The evaluation is presented for square isolated slab specimens without transverse reinforcement supported on square columns subjected to either monotonic or quasi-static cyclic unbalanced moment. For all isolated specimens the moment-rotation relationship was calculated using $r_s = 0.22L$. For tests using setup (c) where the vertical load was applied on the slab surface, the radius of the specimen is equal to $0.50L$. For these cases (represented by square markers) the radial and tangential moments acting on the perimeter of the sector elements were not set to zero to account for the influence of the outer region of the slab on the moment-rotation response. For all other cases (represented by round markers) $0.22L$ corresponds to the specimen radius and, therefore, the radial and tangential moments acting on the slab perimeter were set to zero.

The abscissas of all graphs of this subsection represent the normalised shear strength, i.e., the shear force at failure divided by $b_o\, d\, \sqrt{f_c}$, where d is the average effective slab depth, f_c is the concrete compressive strength and b_o is the control perimeter located at $d/2$ from the face of the column, calculated with rounded corners [Fib11]. Note that the normalised shear force $V_{exp}/b_o\, d\, \sqrt{f_c}$ should be multiplied by three when using SI units and divided by four when using imperial units to obtain the Gravity Shear Ratio (GSR) defined according to ACI-318 [ACI14].

Monotonic loading conditions

The tests that are conducted under monotonically increasing unbalanced moment can be classified in two categories depending on the loading parameter that is maintained constant: shear force or eccentricity. In the following, the moment strength predictions and the deformation capacity predictions are presented and discussed separately for each category. All monotonic tests had been performed on slab specimens of the size $0.44L$ x $0.44L$.

Moment strength

Figure 6.8 shows the moment strength predictions according to several codes of practice (Fig. 6.8a, b and c), the model proposed by Broms [Bro09] (Fig. 6.8d) and the model proposed in Chapter 4 (CSCT(mono) - Fig. 6.8e) for slabs subjected to constant vertical load and monotonically increasing unbalanced moment.
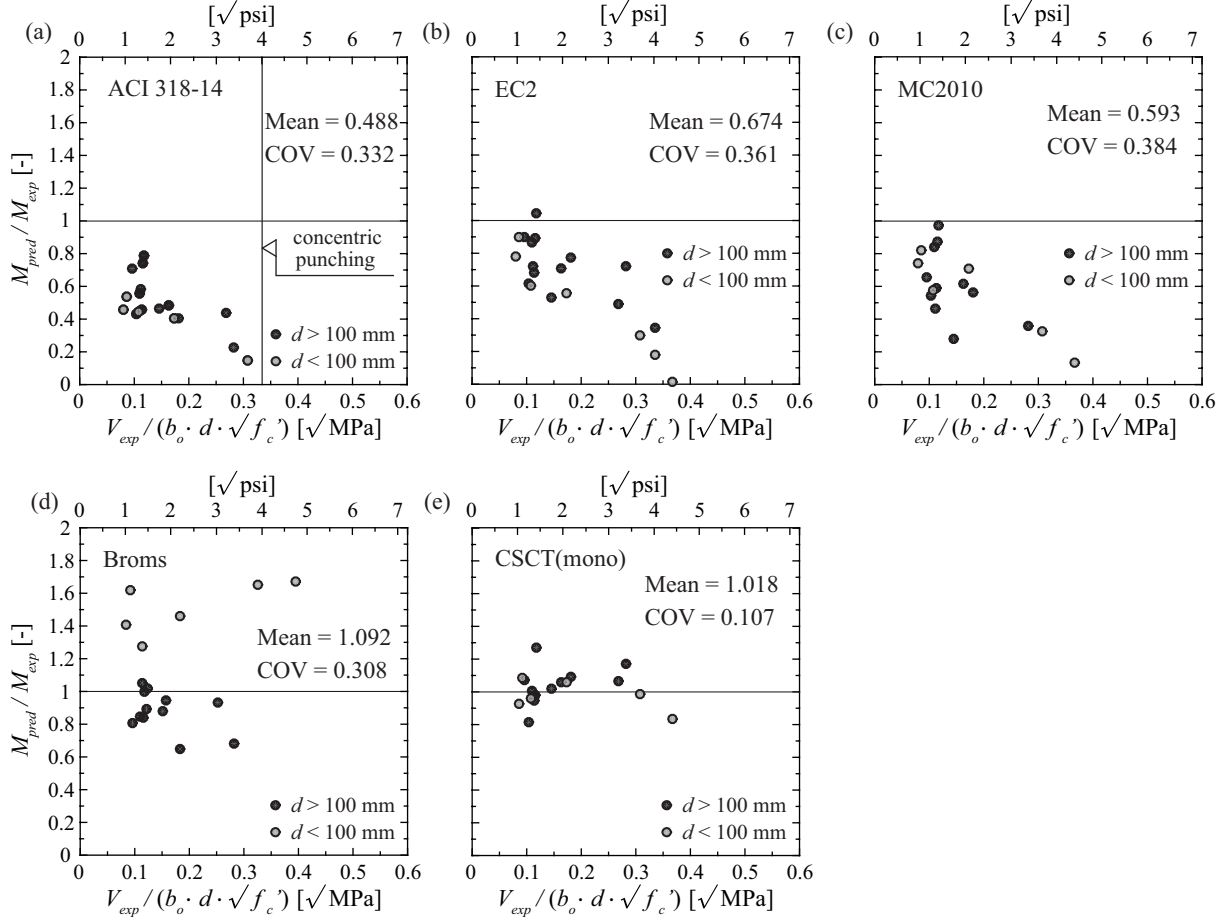
Figure 6.8 – Moment strength predictions for specimens subjected to constant shear force and monotonically increasing unbalanced moment according to: (a) ACI-318 [ACI14], (b) Eurocode 2 [Eur04], (c) Model Code 2010 [Fib11], (d) Broms [Bro09], and (e) the proposed monotonic model (CSCT(mono)).

Figure 6.8a shows that in average the eccentric shear stress model of ACI-318 [ACI14] yields rather conservative estimates of the moment capacity (ratio of predicted to observed values: 0.488 ± 0.332). The conservatism of the moment strength predictions increases with increasing gravity induced shear, as has been reported by others [Bro09, Cho14]. Eurocode 2 [Eur04] and Model Code 2010 [Fib11] (Fig. 6.8b and c, respectively) provide better average predictions of the moment capacity than ACI-318 but with similar scatter (0.674 ± 0.362 and 0.593 ± 0.384, respectively). Broms' model [Bro09] (Fig. 6.8d) shows better performance with respect to the mean value of the ratio M_{pred}/M_{exp} (1.092) but the results are largely scattered (COV = 30.8%). The proposed model combined with the CSCT(mono) (Fig. 6.8e) yields higher prediction accuracy than Broms' model [Bro09] with respect to the average ratio of M_{pred}/M_{exp} (1.018) and significantly reduced scatter (COV = 10.7%).

The moment capacities predicted by ACI-318, Eurocode 2, Model Code 2010, Broms' model, and the proposed model (Chapter 4) are compared to the experimentally obtained moment capacities in Figure 6.9 for slabs subjected to constant eccentricity and monotonically increasing unbalanced moment.
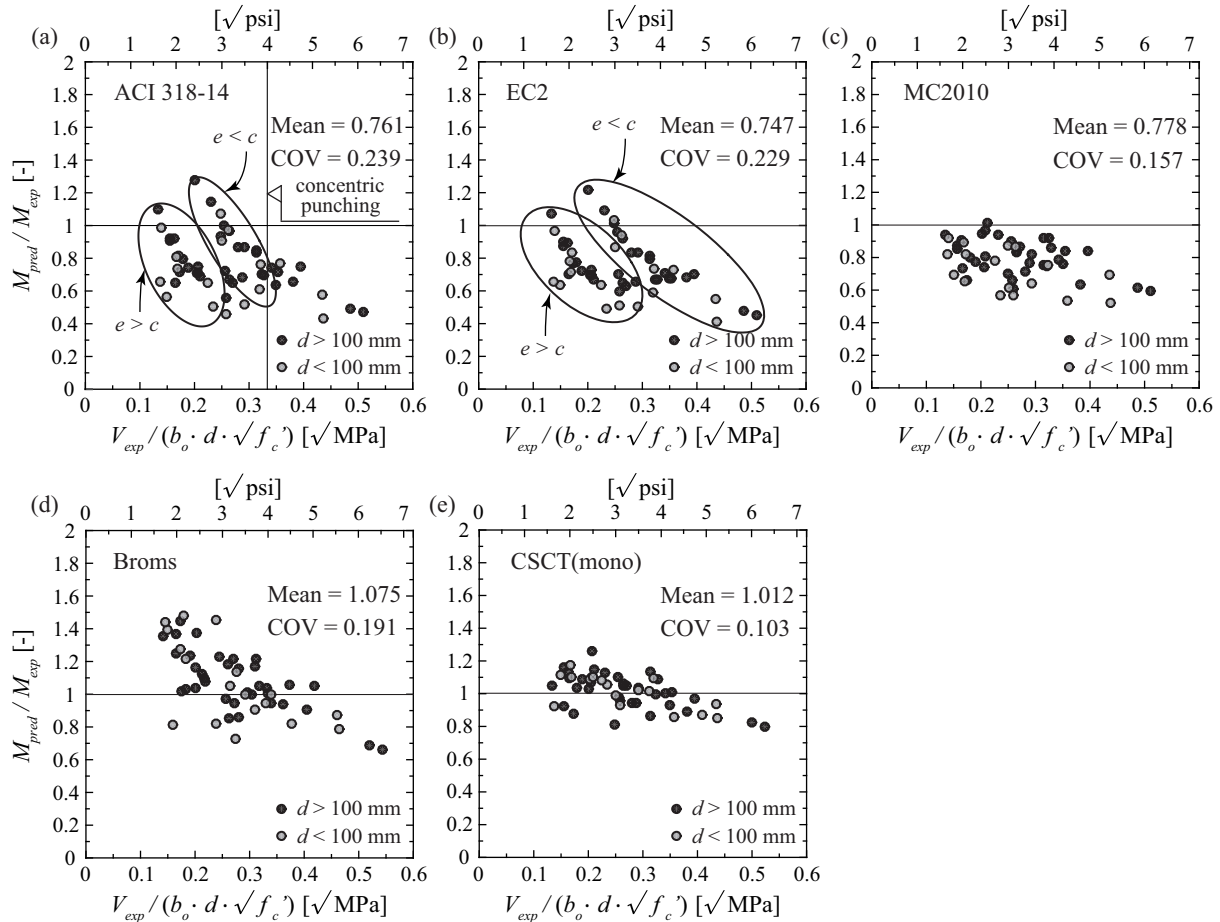
Figure 6.9 – Moment strength predictions for specimens subjected to constant eccentricity and monotonically increasing unbalanced moment (or equally shear force) according to: (a) ACI-318 [ACI14], (b) Eurocode 2 [Eur04], (c) Model Code 2010 [Fib11], (d) Broms [Bro09], and (e) the proposed monotonic model (CSCT(mono)).

As can be seen from Figure 6.9a, in average the predictions of ACI-318 [ACI14] for the moment capacity (or equally the shear strength) of slabs subjected to constant eccentricity are rather conservative (ratio of predicted to observed values: 0.761 ± 0.239). For eccentricities e both higher and lower than the column size c, ACI-318 slightly overestimates the shear strength for tests with low values of gravity load at failure and tends to underestimate the shear strength for tests with intermediate and high values of gravity induced shear at failure. Eurocode 2 [Eur04] shows similar trend with ACI-318 (0.747 ± 0.229 - Fig. 6.9b). Model Code 2010 [Fib11] gives similar average predictions with ACI-318 and Eurocode 2, but with reduced dispersion (0.778 ± 0.157 - Fig. 6.9c). Broms' model [Bro09] shows the same trend with the code predictions (Fig. 6.9a, b, and c) but with significant strength overestimation (1.075 ± 0.191), in particular for low vertical loads at failure (Fig. 6.9d). For the predictions of the proposed model combined with CSCT(mono) (Fig. 6.9e), this trend can still be visible but the mean value of the ratio M_{pred}/M_{exp} falls to 1.012 and the scatter is significantly reduced (COV = 10.3%).

Deformation capacity

For seismic loading, the deformation capacity is as important as the moment capacity. Figure 6.10 presents the predictions of Broms' model [Bro09] and the proposed model (CSCT(mono)) as ratio of calculated to measured rotation of the slab-column connection at peak moment for the tests conducted under constant shear force. The allowable drift limit according to ACI-318 [ACI14] is not compared to monotonic tests.
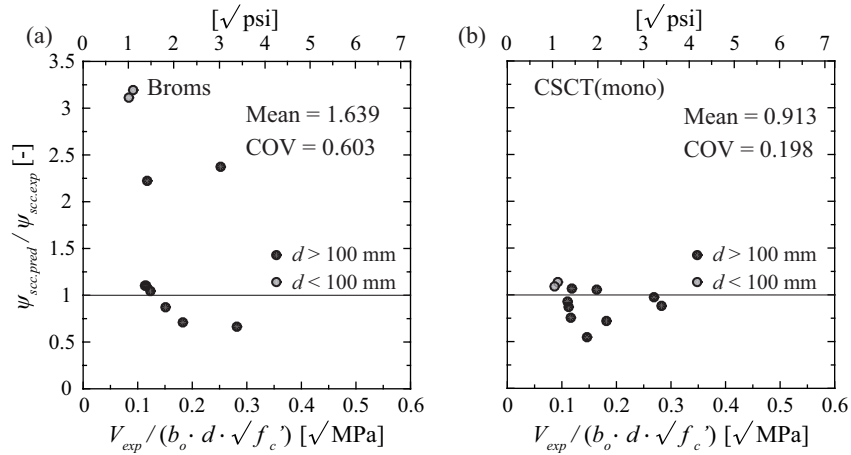
Figure 6.10 – Predictions of connection rotation at peak moment for specimens subjected to constant vertical load and monotonically increasing unbalanced moment according to: (a) Broms [Bro09]; and (b) CSCT(mono).

For monotonic tests, Broms' model [Bro09] (Fig. 6.10a) overestimates in average the rotation capacity and the prediction is also associated to a large scatter (1.639 ± 0.603). The proposed model (CSCT(mono)) (Fig. 6.10b) provides conservative predictions (0.913 ± 0.198) and the scatter is reduced when compared to Broms' model.

Figure 6.11 presents the predictions of the proposed model as ratio of calculated to measured maximum local slab rotation at peak moment for tests conducted under constant eccentricity for which the experimental values are reported. For comparison purposes, the predictions using both the CSCT(mono) and CSCT(cyc) are shown (Fig. 6.11a and b, respectively). Since the reported rotations are local and both ACI-318 [ACI14] and the model developed by Broms [Bro09] provide global ultimate rotations, direct comparison of their performance with regard to the proposed model is not possible. Moreover, ACI-318 [ACI14] provides estimates of the deformation capacity of slab-column connections subjected to cyclic loading. Therefore, no comparison with monotonic test results was performed.
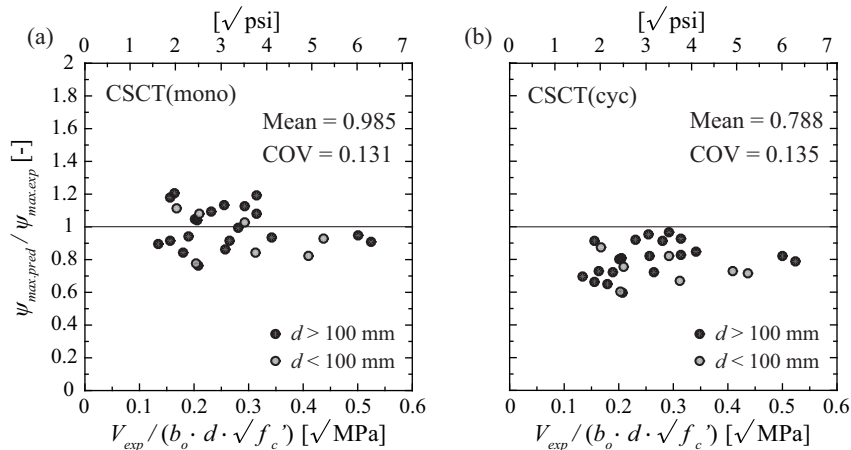
Figure 6.11 – Predictions of maximum local slab rotation at peak moment for specimens subjected to constant eccentricity and monotonically increasing unbalanced moment (or equally shear force) according to the proposed monotonic model combined with: (a) CSCT(mono), and (b) CSCT(cyc).

As can be seen from Figure 6.11, calculating using the failure criterion that accounts for shear redistribution (CSCT(mono) - Fig. 6.11(a)) provides more accurate average predictions of the maximum local slab rotation at peak moment compared to the calculating using the CSCT(cyc) failure criterion (ratio of predicted to observed values: 0.985 ± 0.131 and 0.788 ± 0.135, respectively).

Cyclic loading conditions

Since the experimental campaigns comprising cyclic tests focused on the seismic behaviour of slab-column connections, the shear force, rather than the eccentricity, was maintained constant throughout the test. Most of the cyclic tests had been performed on slab specimens of the size $0.44L$ x $0.44L$. Cyclic tests had, however, partly been conducted on slabs specimens of the size $1.0L$ x $1.0L$. In this case the total slab rotation ψ_{slab} was computed using the Effective Beam Width method described in §4.2.5 and extended in Section 5.7 to account for cyclic loading and cumulative damage effects. Note that Broms' model is not applicable to cyclically loaded slabs [Bro09].

Moment capacity

Figure 6.12 shows the moment strength predictions according to several codes of practice (Fig. 6.12a, b, and c) and the proposed model of Chapters 4 and 5 (Fig. 6.12d and e, respectively).
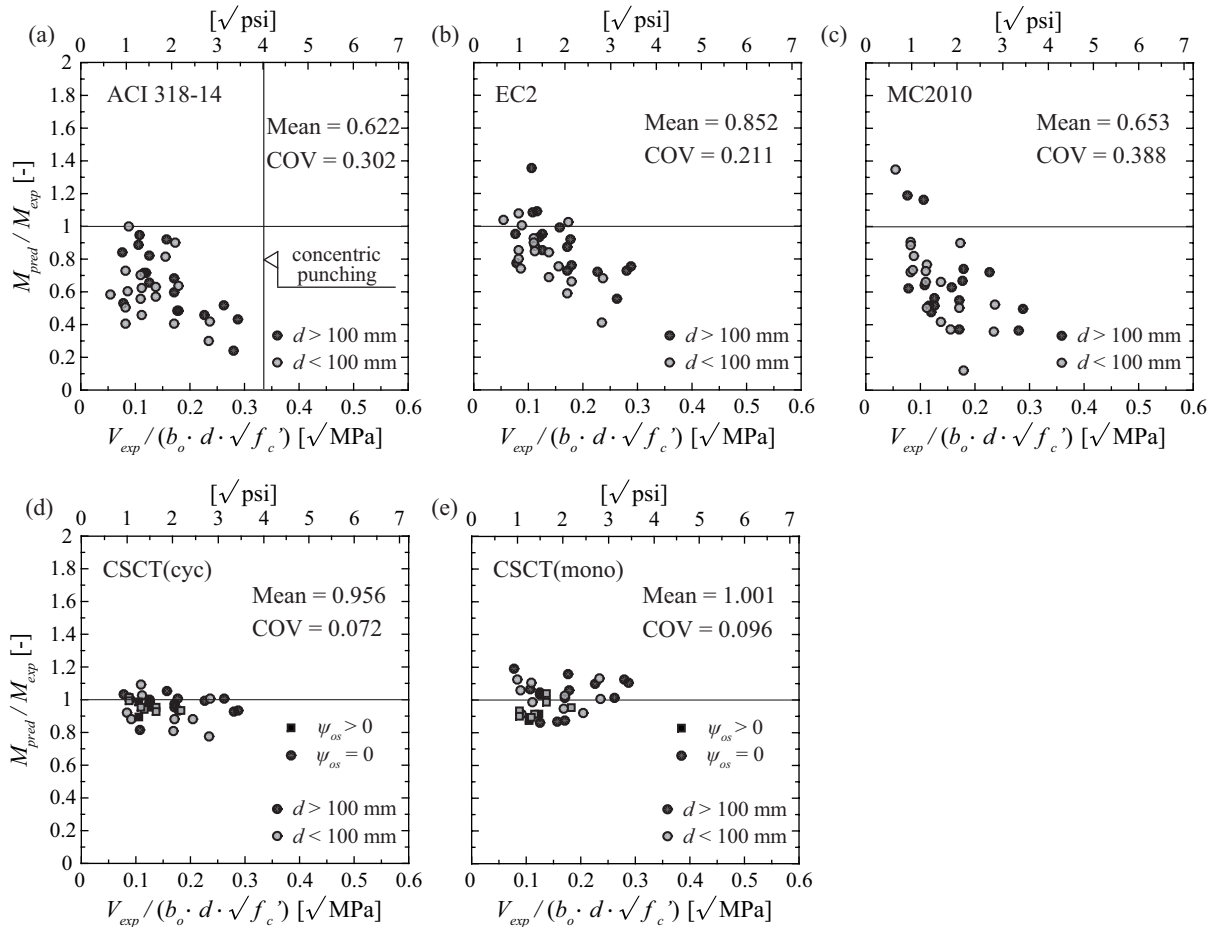
Figure 6.12 – Moment capacity predictions for specimens subjected to constant vertical load and cyclically increasing moment according to: (a) ACI-318 [ACI14], (b) Eurocode 2 [Eur04], (c) Model Code 2010 [Fib11], (d) CSCT(cyc) (Chapter 4), and (e) CSCT(mono) (Chapter 5).

The predictions of ACI-318 [ACI14] and Model Code 2010 [Fib11] for the moment strength of slabs subjected to cyclically increasing moment (Fig. 6.12a and c, respectively) display a similar dependency on the value of gravity induced shear force, as for slabs subjected to monotonically increasing moment (Fig. 6.9a and c, respectively), but with decreased conservatism (0.622 ± 0.302 and 0.653 ± 0.388). The predictions of Eurocode 2 [Eur04] follow the same trend with ACI-318 and Model Code 2010 but the mean value of the ratio M_{pred}/M_{exp} increases to 0.852 while the scatter reduces (COV = 21.1%), as shown in Figure 6.9b. The proposed monotonic model combined with CSCT(cyc) (Fig. 6.12d) offers higher prediction accuracy with respect to both average ratio and scatter of predicted

to observed moment capacities M_{pred}/M_{exp} (0.956 ± 0.072). The proposed cyclic model combined with CSCT(mono) (Fig. 6.12e) offers higher prediction accuracy with respect to the average ratio of predicted to observed moment capacities M_{pred}/M_{exp} but slightly increased scatter (1.001 ± 0.096).

Deformation capacity

Regarding the deformation capacity of cyclically loaded isolated slab specimens, Figure 6.13 presents the predictions of ACI-318 [ACI14], the model proposed by Hueste and Wight [Hue99], the simplified model of Chapter 4 (denoted as CSCT(cyc)) and the cyclic model of Chapter 5 (denoted as CSCT(mono)) as ratio of calculated to measured rotation of the slab-column connection at peak moment.
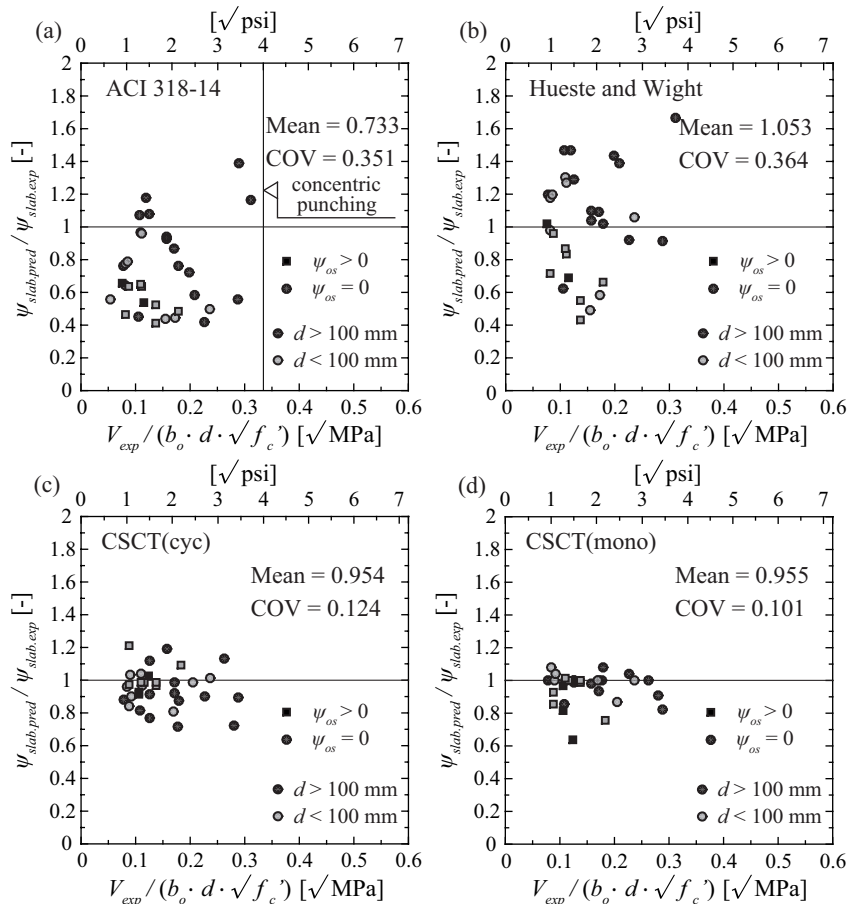
Figure 6.13 – Predictions of slab deformation at peak moment for specimens subjected to constant vertical load and cyclically increasing moment according to: (a) ACI-318 [ACI14]; (b) Hueste and Wight [Hue99]; (c) CSCT(cyc) (Chapter 4) and (d) CSCT(mono) (Chapter 5).

For the slab rotation of slabs subjected to constant shear force and cyclically increasing moment, ACI-318 [ACI14] (Fig. 6.13a) provides in average conservative predictions with rather high scatter (0.733 ± 0.351). The model proposed by Hueste and Wight (Fig. 6.13b) gives more precise average predictions but with similar scatter (1.053 ± 0.364). The CSCT(cyc) provides slightly conservative average predictions (0.954), while the scatter is reduced (COV = 12.4%) when compared to ACI-318 and the model of Hueste and Wight. The cyclic model combined with the CSCT(mono) failure criterion provides similar average predictions with the simplified approach of Chapter 4 (Fig. 6.13c) but further reduced dispersion (0.955 ± 0.101), as shown in Figure 6.13d.

It is recognised that the representation of the predictions of this subsection is penalised by the fact that the ratios of predicted to experimental values is considered for the ordinates and not for the abscissas. However, representing the predictions in the form of interaction diagrams M - V would

seem approximate, since the geometric parameters and material properties of the tests found in the literature present a larger variability compared to the tests of the performed campaign (see Fig. 3.24).

6.2.3 Lateral force-resisting mechanisms

The previous subsection has shown that for slabs subjected to constant eccentricity, the performance of ACI-318, Eurocode 2 and Model Code 2010 with respect to the mean value of the ratio M_{pred}/M_{exp} is similar (Fig. 6.9). On the other hand, for slabs subjected to constant shear force, it was demonstrated that ACI-318 gives the most conservative average moment strength predictions (Figs. 6.8 and 6.12). The conservatism of the strength predictions of ACI-318 (Figs. 6.8a and 6.12a) can be related to the assumed force-resisting mechanism contribution. The American Standard adopts the eccentric shear stress model assuming that the contribution of flexure and eccentric shear force to the total moment, denoted as γ_f and γ_v, depend only on geometric properties; the contribution of torsional moments is neglected (Chapter 2). For interior slab-column connections with square columns, ACI-318 [ACI14] assumes that γ_f and γ_v are equal to 0.6 and 0.4, respectively, for any drift level. Previous studies investigated the pertinence of this assumption, mainly using finite elements [Meg00, Gay08]. As the model presented in Chapter 4 is hitherto the only analytical approach for estimating the contribution of the three lateral force-resisting mechanisms (flexure, torsion, and eccentric shear) to the total resisted moment for flat slabs responding in the post-elastic range, this assumption was further investigated.

Figure 6.14a shows the contribution of the different mechanisms for increasing connection rotation (or increasing moment), which results in decreasing γ_v factors, as has been observed by others [Meg00]. The obtained results were in reasonable agreement with finite element analyses using values for the shear retention factor β equal to 0.83 for small connection rotations [Gru01] and 0.1 for high connection rotations [Ede10] (dashed and dashed-dotted curves, respectively - Fig. 6.14a). The adopted numerical approach is presented in Section 3.3 [CSI14]. The predictions of the proposed model for the contribution of the different actions to the total resisted moment at failure at the critical section (distance equal to $d/2$ from the column face) are shown in Figure 6.14b for slabs subjected to constant shear force and monotonically or cyclically increasing unbalanced moment (Tables A.1 and A.3, Appendix A). For slab-column connections subjected to large gravity loads, the predicted γ_f is close to the value $\gamma_f = 0.33$ obtained from the solution of an elastic homogenous isotropic slab [Mas70]. Moreover, decreased gravity load appeared to confer larger values of γ_f. Figure 6.14b shows also that cyclic loading results in smaller γ_f values than monotonic loading.
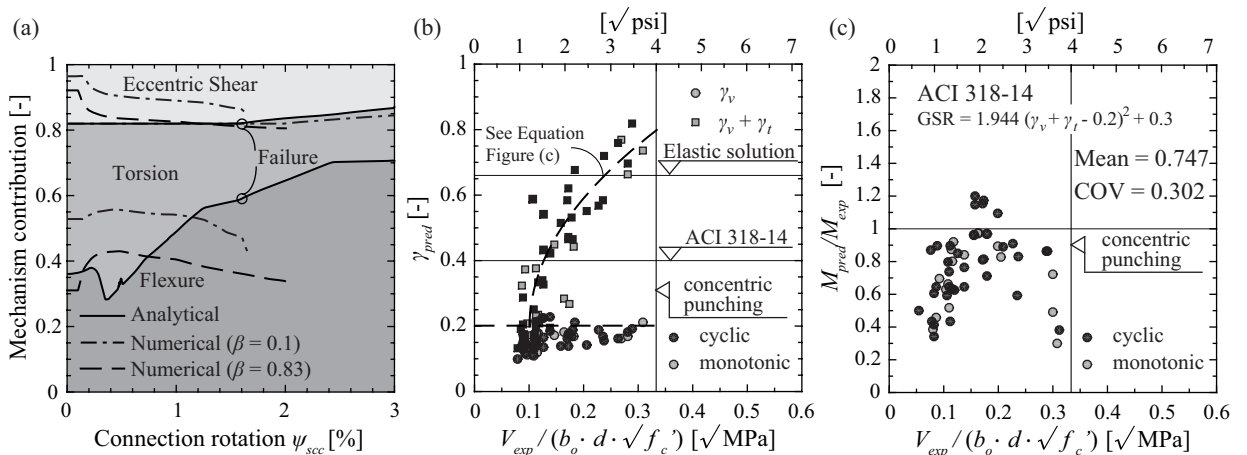
Figure 6.14 – (a) Contribution of moment-resisting mechanisms as function of the connection rotation ψ_{scc} according to numerical analysis and the analytical model ($V = 0.38$ MN; $\rho = 0.81\%$; $\rho' = 0.38\%$; $c = 0.39$ m; $d = 0.198$ m; $B = 3$ m); (b) Prediction of γ factors according to the proposed model for specimens subjected to constant V and increasing M and; (c) ACI-318 [ACI14] moment strength predictions using the γ_v and γ_f values calculated according to equations based on the proposed model.

Based on the predictions of the proposed model γ_t is assumed to follow a parabola (Fig. 6.14b) whereas γ_v is assumed equal to 0.2:

$$\text{GSR} = 1.944 \ (\gamma_v + \gamma_t - 0.2)^2 + 0.3 \tag{6.1}$$

$$\gamma_v = 0.2 \tag{6.2}$$

Application of Eqs. (6.1) and (6.2) to the eccentric shear transfer model of ACI-318 (Fig. 6.14c) leads to more accurate average strength predictions than illustrated in Figures 6.8a and 6.12a, which remain safe and are not overly conservative. Moreover, the predictions become less dependent on the applied gravity load.

6.3 Continuous flat slabs

This study concentrates on isolated slab specimens ($B = 0.44L$). In reality, however, slabs are usually continuous. When the part outside $0.44L$ is neglected, an important component of the total slab deformation is not accounted for. This may result in smaller moment strength and deformation capacity compared to isolated slab specimens. Tests on continuous flat slabs can provide significant information regarding the seismic behaviour of actual flat slabs as well as the influence of the boundary conditions and the membrane action on the response if their results are compared to results of similar isolated slabs. The model presented in Chapter 4 considers both the slab part until $0.44L$ and the part outside $0.44L$ when computing the moment-rotation response. The calculation of the radial bending moment and torsional moment acting to the sector element from the part of the slab outside $r = 0.22L$ is performed using an Effective Beam Width method. The main advantage of this method is the fact that continuity boundary conditions can be modelled. The model has, for example, shown rather good performance in predicting the moment-rotation relationship of isolated specimens with free edges or simply supported edges, as shown in Appendix C. Moreover, the moment strength and the deformation capacity of isolated specimens are also predicted rather well, as shown in Appendix D and discussed in Section 6.2. Nevertheless, the seismic behaviour of isolated slab-column specimens can differ from the behaviour of continuous flat slabs, as has been shown in Chapter 3 and in previous numerical studies on flat slabs subjected either to vertical loads alone [Ein15] or to a combination of vertical and lateral loads [Par06]. In the following, the performance of the proposed model in predicting the seismic response of continuous flat slabs is assessed: first, the predicted distribution of radial and torsional moments at $r = 0.22L$ is compared with NLFEA results; second, the predicted moment-rotation response is compared against results of two tests on continuous flat slabs reported in the literature.

6.3.1 Distribution of radial and torsional moments at $r = 0.22L$

In Chapter 4, a method was proposed to account for the contribution of the slab part outside $0.22L$ to the slab deformations (§4.2.5). This was performed by calculating the radial and torsional moments at $r = 0.22L$ ($M_{rad.022L}$ and $M_{tor.022L}$, respectively) using an Effective Beam Width approach. To validate this approach, the predicted distributions of $M_{rad.022L}$ and $M_{tor.022L}$ according to the model were compared with NLFEA results, since no experimental measurement of $M_{rad.022L}$ and $M_{tor.022L}$ is available. For this validation, the analyses of the continuous flat slab system that were presented in Section 3.3 (§3.3.2) are used to validate the Effective Beam Width model. Figures 6.15 and 6.16 show the torsional moment distribution and the radial bending moment distribution until $r = 0.50L$, respectively, for $\rho = 0.75\%$ and 1.50%. The results are plotted for the moment strength predicted according to ACI-318 [ACI14].
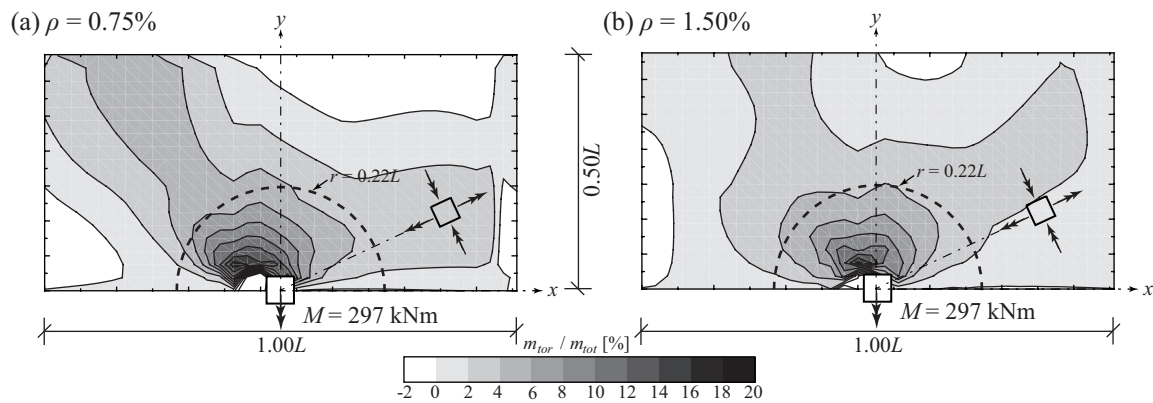
Figure 6.15 – Distribution of torsional moments at the predicted moment strength according to ACI-318 [ACI14] (297 kNm) until $r = 0.50L$ for (a) $\rho = 0.75\%$ and (b) $\rho = 1.50\%$ using [CSI14].
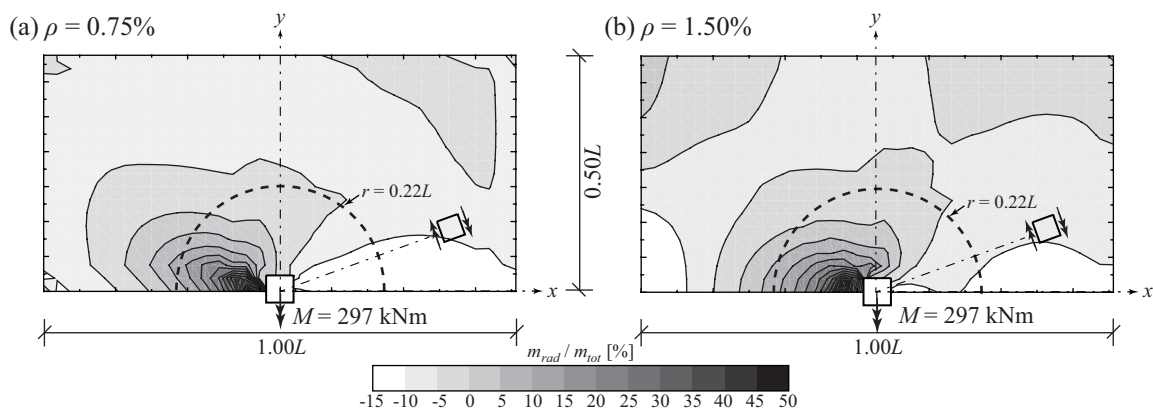
Figure 6.16 – Distribution of radial bending moments at the predicted moment strength according to ACI-318 [ACI14] (297 kNm) until $r = 0.50L$ for (a) $\rho = 0.75\%$ and (b) $\rho = 1.50\%$ using [CSI14].

The highest values of torsional moment and radial bending moment were calculated for $r < 0.22L$ and parallel to the y-axis and x-axis, respectively. For $\rho = 0.75\%$, the average torsional moment per unit width at $r = 0.22L$ was only 5% of the respective value at the column face. For the distribution of radial bending moments (Fig. 6.16b) due to lateral loading, the inflection radius is displaced farther from $0.22L$ at the hogging slab half and closer to the column face at the sagging slab half. For $\rho = 0.75\%$, the average radial bending moment per unit width at $r = 0.22L$ was 17% of the respective value at the column face. For $\rho = 1.50\%$, the obtained values are rather similar.

Figure 6.17 compares the radial and torsional moments at $r = 0.22L$ obtained with the Effective Beam Width model to those obtained from the NLFEA. Grey lines represent the numerical calculation, while the predictions of the proposed model are represented by black lines with circular markers. The predictions of the proposed Effective Beam Width model for the distribution of the radial and torsional moments at $r = 0.22L$ follow the trend of the numerical predictions rather well. The maximum radial bending moment appears at $\phi = \pi/2$ and $\phi = -\pi/2$ (Fig. 6.17a), whereas the maximum torsional moment appears at $\phi = -\pi/4$ (hogging slab half) according to both the analytical and the numerical model (Fig. 6.17b). Moreover, higher reinforcement ratio ρ leads to smaller average torsional moments at $0.22L$, as predicted by both the analytical and the numerical model. The influence of ρ on the average radial moments at $0.22L$ is less significant. The discrepancies between analytical and numerical results could be attributed to the fact that the Effective Beam Width method considers only the slab part between $0.22L$ and $0.50L$ in the direction of excitation, whereas the slab part between $0.22L$ and $0.50L$ in the transverse direction is neglected. For this reason, the analytical model predicts a zero

radial moment at $\phi = 0$ and a small torsional moment at $\phi = 0$ when compared to the finite element calculation.
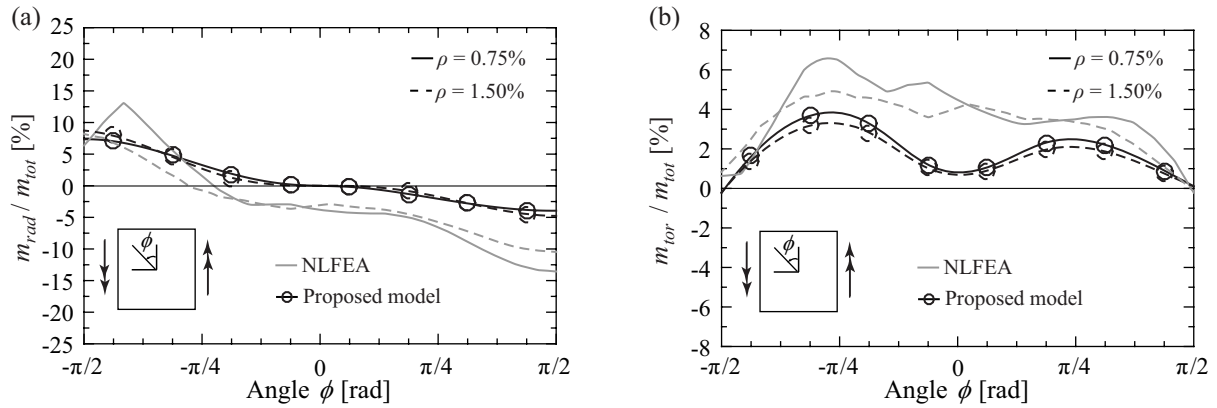
Figure 6.17 – Distribution of (a) radial bending moments and (b) torsional moments at the predicted moment strength according to ACI-318 [ACI14] (297 kNm) at $r = 0.22L$ for $\rho = 0.75\%$ and 1.50% according to NLFEA [CSI14] and the proposed model.

6.3.2 Moment-rotation response

This PhD project focuses on the seismic behaviour of interior slab-column connections. In the following, the moment-rotation response of interior slab-column connections belonging to continuous flat slab systems is analysed. For tests on subassemblies of one interior and two exterior slab-column connections [Dur95] and single-storey continuous flat slabs [Hwa93, Rha14], the unbalanced moment M and the shear force V of each interior slab-column connection were measured during loading using load cells at the top and the base of each column. For multi-storey systems with flat slabs [Moe85, Fic08] however, due to the static indeterminacy only the shear force of each storey and the axial force at the base of each column can be monitored. The internal forces at the internal slab-column connections cannot be measured. For this reason, tests on multi-storey flat slab systems are not treated herein and the proposed model (Chapters 4 and 5) is compared to findings on interior slab-column connections of continuous single-storey flat slabs tested in previous campaigns. In this last category fall only two test campaigns, performed by Hwang and Moehle [Hwa93] and Rha et al. [Rha14], which are analysed in the following. Tests on subassemblies of one interior and two exterior connections are disregarded since the effect of exterior slab-column connections on the behaviour of interior connections is expected to be more pronounced than for tests on continuous flat slab systems.

Hwang and Moehle [Hwa93]

In 1993, Hwang and Moehle tested a flat slab system with 3 bays in each direction under combined vertical and lateral loads [Hwa93]. The plan view and a section cut of the specimen are shown in Figure 6.18a and b. Here the attention is focused on the response of the interior connections supported on square columns (i.e. the connections annotated as b2 and b3 - see Fig. 6.18a). The predictions of the proposed model for the connections b2 and b3 are compared to the experimental results in Figure 6.18c and d, respectively. The experimental moment-rotation curves shown in Figure 6.18c and d (drawn in grey) represent the envelope curves resulting from the tests.
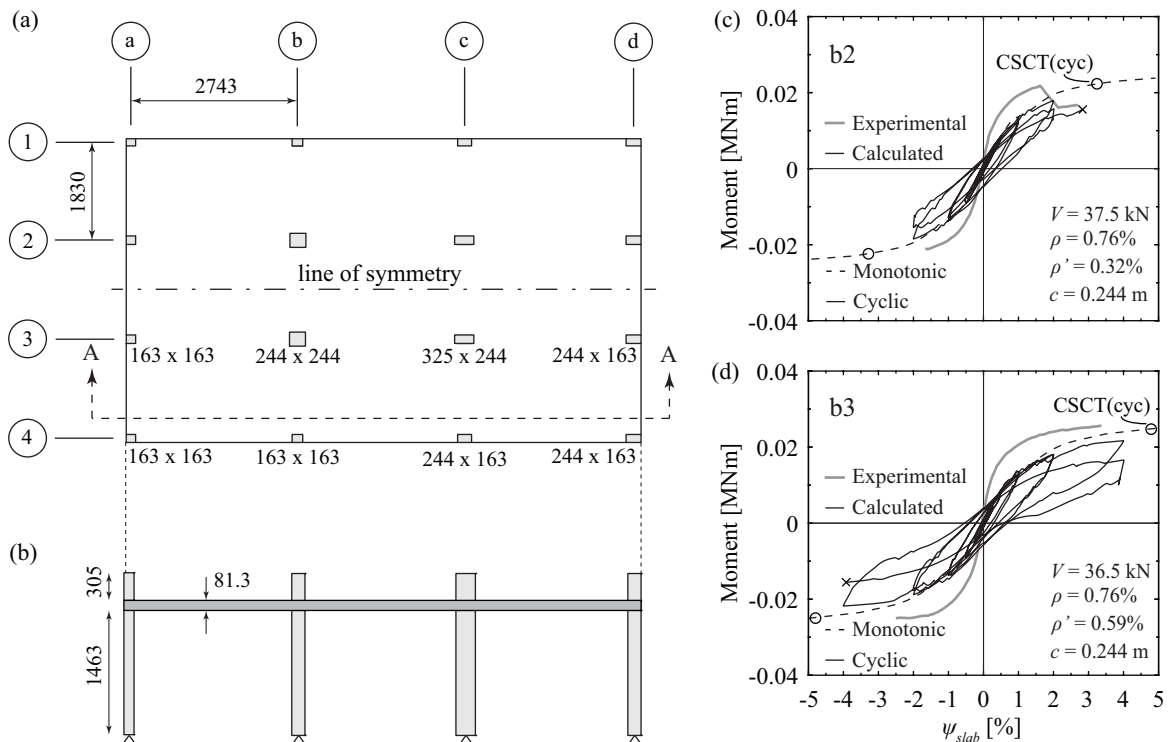
Figure 6.18 – Test campaign on a continuous flat slab by Hwang and Moehle [Hwa93]: (a) Plan view of the specimen, (b) Section A-A (drawn after [Hwa93] - dimensions in mm), and comparison between experimental and calculated moment-rotation relationship for the interior connections (c) b2 and (d) b3.

The experimental slab rotation of the interior connections b2 and b3 at punching is predicted accurately enough by the proposed cyclic model (Chapter 5), as can be seen in Figure 6.18c and d, respectively (continuous black loops). It should be though noted that the calculated initial stiffness (prior to reaching the yielding plateau) is lower than the experimental one. This could be attributed to the compressive membrane action, as has already been demonstrated in Chapter 3 and to the fact that the proposed Effective Beam Width method accounts for the slab part outside $0.22L$ only in the direction of excitation. Use of the simplified approach of Chapter 4 (adoption of the CSCT(cyc) failure criterion) provides more precise predictions for the moment strength but overestimates significantly the deformation capacity (dashed curves).

Rha et al. [Rha14]

In 2014, Rha et al. tested two flat slab systems with 2 x 2 spans under combined vertical and lateral loads [Rha14]. To investigate the influence of cyclic loading on the moment strength and the deformation capacity, the lateral loads were increased either monotonically or cyclically until failure. The plan view of the specimens is shown in Figure 6.19a, while Figure 6.19b shows the adopted loading protocol for the cyclic test. The evaluation is focused on the response of the interior connection C5. The predictions of the proposed model are compared with the experimental results in Figure 6.19c and d (monotonic and cyclic conditions, respectively).
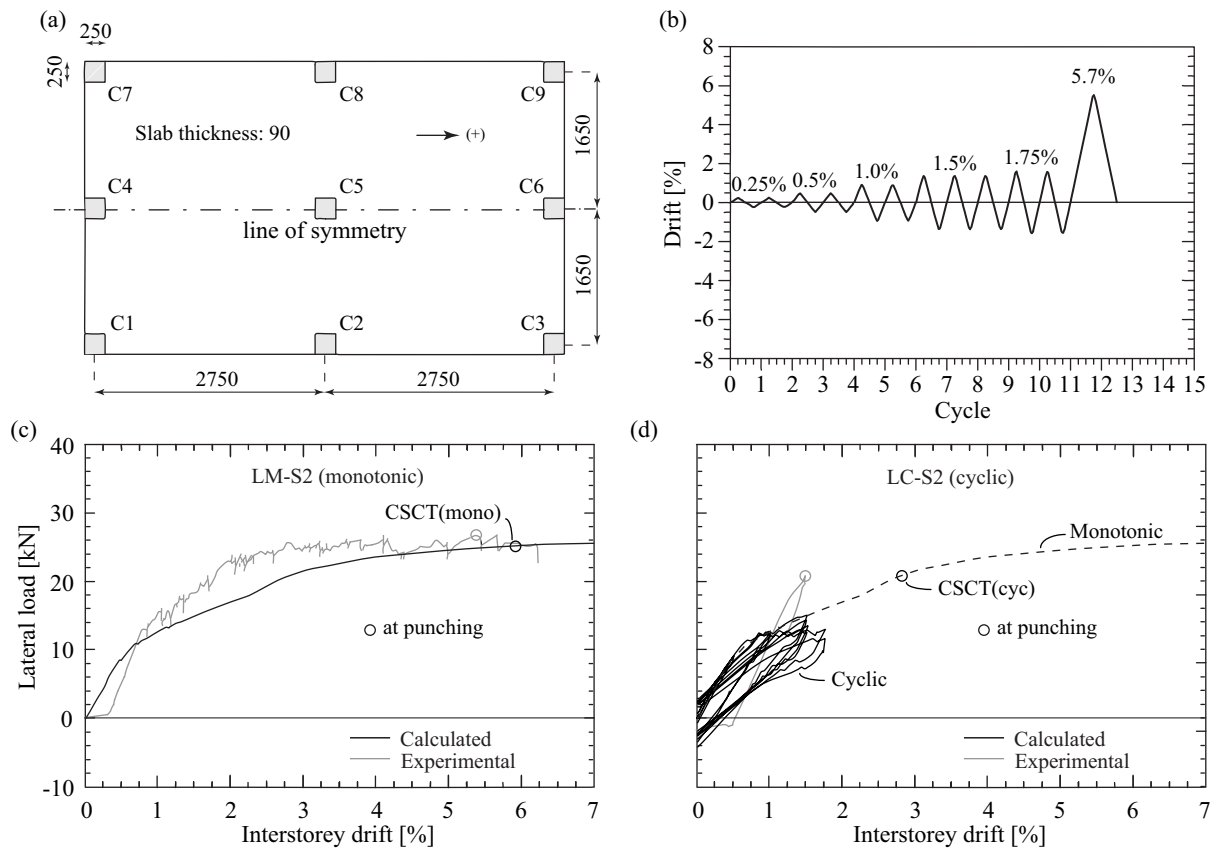
Figure 6.19 – Test campaign on continuous flat slabs by Rha et al. [Rha14]: (a) Plan view of the specimens (drawn after [Rha14] - dimensions in mm), and (b) adopted loading protocol for the cyclic test, and comparison between experimental and calculated lateral load-interstorey drift relationship and punching failure point for the interior connection C5 of (c) the monotonic test, and (d) the cyclic test.

As can be seen in Figure 6.19c and d, the proposed model captures the experimentally measured lateral load-interstorey drift relationship of the interior connection C5 rather well. For the monotonic test LM-S2 (Fig. 6.19c), the lateral load and the corresponding interstorey drift at punching failure are predicted rather well by the monotonic model (Chapter 4). For the cyclic test LC-S2 (Fig. 6.19d), use of the cyclic analytical model (Chapter 5 - continuous curve) leads to more accurate deformation capacity prediction than the simplified approach of Chapter 4 (CSCT(cyc) failure criterion - dashed curve) but to slight underestimation of the experimental moment strength.

Comparison between the experimental and the calculated curves shown in Figures 6.18c, d and 6.19c, d (grey and black curves, respectively) suggest that calculating the moment-rotation relationship of interior slab-column connections of continuous flat slabs assuming a specimen size equal to $0.44L$ combined with the Effective Beam Width method (Sections 4.2 and 5.7 for monotonic and cyclic loading conditions, respectively) gives rather good predictions of the overall global response. It should

be nonetheless noted that the flat slabs tested by [Hwa93] and [Rha14] were relatively thin ($h = 81$ mm and 90 mm, respectively). Tests on flat slab systems with higher slab thickness are needed to check the validity of the presented approach.

The following chapter proposes an Effective Beam Width method for the analysis of buildings with slab-column connections. It proposes to calculate the width reduction coefficient α (see Chapter 2) on the basis of the proposed analytical model. The method aims at calculating the global response of multi-storey flat slab systems using a relatively simple numerical model where slabs are substituted by beams. The model captures the influence of geometric and material properties, vertical and lateral load level, reinforcement ratio, drift, etc. on the global behaviour through the α coefficient.

6.4   Conclusions

This chapter presents the validation of the analytical models for slab-column connections under monotonic loading (Chapter 4) and cyclic loading (Chapter 5). The models are validated against experimental results and results from non-linear finite element simulations. The main findings are:

1. The assumptions of Chapters 4 and 5 regarding the kinematic law between the slab rotations at different angles with respect to the excitation as well as the shear crack inclination were verified by comparison with the results of the slabs tested within this research.

2. The developed monotonic model (Chapter 4) predicts rather well the $M - \psi_{max}$ and $M - \psi_{min}$ relationship of the slabs tested monotonically within the performed test campaign (Chapter 3). For the cyclic tests, the model developed in Chapter 5 allows for more accurate prediction of the local slab rotations than the simplified approach of Chapter 4 (adoption of CSCT(cyc) instead of CSCT(mono)), since both the hysteretic behaviour and the cyclic damage are considered. The improvement of the predictions is more significant for the maximum slab rotations.

3. The proposed monotonic model (Chapter 4) shows good performance in predicting the moment strength of slabs subjected to monotonically increasing unbalanced moment (ratio of predicted to observed values: 1.018 ± 0.107 and 1.012 ± 0.103 for $V = $ cst and $e = $ cst, respectively). The predictions for the corresponding rotation show a larger dispersion and are slightly conservative for constant vertical loads (0.899 ± 0.205 and 0.985 ± 0.131 for $V = $ cst and $e = $ cst, respectively). For cyclic loading, combination of the monotonic model with the CSCT(cyc) failure criterion gives slightly conservative predictions for both the moment strength and the deformation capacity (0.956 ± 0.072 and 0.954 ± 0.124, respectively).

4. The predictions of the proposed cyclic model (Chapter 5) are in very good agreement with experimentally measured peak unabalanced moments for slabs subjected to constant vertical load and cyclically increasing moment. The cyclic model is more accurate than the simplified approach of Chapter 4 (adoption of CSCT(cyc) instead of CSCT(mono)) but the moment strength predictions are associated with slightly larger scatter (1.001 ± 0.096). Regarding the deformation capacity, the cyclic model provides somewhat conservative predictions, as the simplified approach of Chapter 4, but with a slightly reduced scatter (0.955 ± 0.101).

5. Both proposed models provide more accurate moment strength predictions compared to codes of practice [ACI14,Eur04,Fib11] and the model proposed by [Bro09]. Moreover, the proposed models offer more accurate and precise deformation capacity predictions than previously proposed models [Hue99,Bro09] and design limits [ACI14].

6. The performance of the analytical model in predicting the contribution of the different resisting mechanisms is validated through comparison with NLFEA results. Based on the model predictions for the slabs of the database (Appendix A), simplified equations for γ_v and γ_t are proposed. Application of these equations to the eccentric shear model of ACI-318 [ACI14] leads to more

accurate moment strength predictions (ratio of predicted to observed values: 0.747 ± 302) which are less dependent on the applied gravity load.

7. The proposed model combined with the Effective Beam Width approach presented in Chapter 4 predicts rather well the distribution of the radial bending moment and the torsional moment at $r = 0.22L$ for continuous specimens when compared with NLFEA results, both with respect to the location and value of the maxima and minima and the overall trend.

8. The overall moment-rotation response of interior slab-column connections of continuous flat slabs is predicted rather well by the proposed analytical model combined with the Effective Beam Width method. Discrepancies between calculated and experimental results are attributed to the compressive membrane action and the confinement offered by the outer slab in the direction perpendicular to the direction of excitation, which are not accounted for by the proposed model.

Chapter 7

Analysis methods for flat slab buildings

For adequate earthquake-resistant design and seismic assessment of a structure, its dynamic properties (stiffness, mass and damping) should be known in order to accurately estimate the lateral loads that are introduced to each member of the structure. To calculate the seismic moment acting on a slab-column connection and the corresponding interstorey drift, the stiffness of both the slab and the column should be known beforehand, taking into consideration the non-linear behaviour of both members. For the column, the effective stiffness as defined by Priestley et al. [Pri07] has shown good agreement with test results and is usually adopted for seismic analysis. The mechanical model presented in Chapters 4 and 5 can be used to estimate the stiffness of the slab in the proximity of the slab-column connection as well as the rotation due to slab deformation for a given unbalanced moment.

In this chapter, two analysis methods for buildings with slab-column connections are presented based on the proposed analytical model, which was previously found to predict the moment-rotation response of isolated slab specimens (Section 6.2) and continuous slabs (Section 6.3) rather well. Both methods simplify the numerical calculation if a more detailed numerical model for slabs, using for instance shell elements or brick elements, is not opted for. The methods are presented in descending order of computational complexity.

The first method, presented in Section 7.1, belongs to the category of Effective Beam Width methods and proposes the width reduction coefficient to be calculated on the basis of the proposed model, so as to take into account the impact of various parameters (geometric and material properties, gravity and lateral load level, reinforcement ratio, etc.) on the rotational stiffness of the slab-column connection. This method is applicable to slab-column connections either being part of the lateral force-resisting system or not.

The second method, presented in Section 7.2, consists in calculating the contribution of column and slab deformation to the total interstorey drift demand, which is calculated from the numerical analysis of the lateral force-resisting system only. The contribution of slab deformation is computed using the proposed mechanical model, while the contribution of column deformation is estimated through a fixed-fixed beam model. The method can be applied if the slab-column connections are only part of the gravity force-resisting system.

7.1   Effective Beam Width Method

A review of existing Effective Beam Width (EBW) methods can be found in Chapter 2 (§2.2.1). From this review it becomes obvious that a more accurate method for calculating the moment-rotation relationship of a slab-column connection, and consequently the rotational stiffness of the connection is needed. The influence of the connection and panel geometry, vertical and lateral load level, material properties should be captured, as well as the potential appearance of a shear crack in the connection proximity. As shown in Appendix C, the proposed models of Chapter 4 (monotonic loading conditions) and Chapter 5 (cyclic loading conditions) capture rather well not only the moment strength and the deformation capacity, but also the entire moment-rotation relationship prior to failure.

The main difference between the EBW method and the Equivalent Frame (EF) method lies in the simulation of the flexural and torsional stiffness of the slab. In the EBW method, only a portion of transverse midspan-to-midspan distance l_2 is assumed to contribute to flexure while the torsional stiffness contribution is neglected. In the EF method, however, the entire length l_2 contributes to flexure while a transverse torsional member models the torsional stiffness of the slab. The EBW method has proved to be a simpler and more accurate approach for the analysis of flat slab buildings under lateral loads compared to the Equivalent Frame (EF) method and is suitable for three-dimensional analysis using commercial software [Luo95,Rob97,Par09]. Moreover, since the proposed model (Chapters 4 and 5) directly accounts for the contribution of the torsion mechanism to the total unbalanced moment, there is no need for an additional torsional member, as prescribed in the EF method. Therefore, the EBW method is used for the integration of the proposed mechanical model to provide to the structural engineer a relatively simple tool for the analysis of flat slab buildings, as will be shown in the following.

The theoretical principles of the EBW method have already been presented in Chapter 2 but some key assumptions are recalled in the following. This section focuses on the integration of the analytical model presented in Chapters 4 and 5 into the EBW formulation, so as to provide a tool for the numerical analysis of buildings with slab-column connections. At first, the calculation procedure of the proposed EBW method is presented, followed by the validation of the method through comparison with experimental results of flat slab buildings reported in the literature. Finally, based on the model predictions for the slab specimens used for the validation, a short discussion is provided on the influence of the boundary conditions and the slab region outside $0.22L$ on the moment-rotation response.

7.1.1   Calculation procedure

The EBW method assumes that the slab action is represented by an slab-equivalent beam with height equal to the slab thickness and width equal to the transverse midspan-to-midspan distance times a width reduction coefficient α. Regarding the calculation procedure, at first, the formula for the calculation of the width reduction coefficient α according to the theory of elasticity is recalled [Cho01]:

$$\alpha = \frac{M}{\psi_{slab}} \, \frac{l_1}{l_2} \, \frac{1}{E_c \, h^3} \tag{7.1}$$

where M is the unbalanced moment of the slab-column connection, ψ_{slab} is the rotation due to slab deformation, l_1 and l_2 is the distance between supports perpendicular and parallel to the unbalanced moment vector, respectively, h is the slab thickness, and E_c is the modulus of elasticity of concrete. Cracking is typically accounted for through the use of a stiffness reduction coefficient β. Since the proposed analytical formulation already includes the non-linear behaviour in the width reduction coefficient α, there is no need to introduce a cracking factor in an explicit manner.

For continuous flat slabs, both the slab parts inside $0.22L$ (ψ_{scc}) and outside $0.22L$ (ψ_{os}) contribute to the rotation ψ_{slab}. Sections 4.2 (monotonic loading) and 5.7 (cyclic loading) propose an EBW approach to be combined with the analytical model for computing the unbalanced moment M and

the slab rotation ψ_{slab}. Then, Eq. (7.1) is directly used for calculating the width reduction coefficient α.

For the analysis of buildings with slab-column connections using the EBW method which incorporates the proposed analytical model, an iterative procedure should be adopted:

1. Choice of the width reduction coefficient α (for the first iteration, $\alpha = 1.0$ is chosen).

2. Calculation of unbalanced moment M from the numerical analysis of the building (with slab-equivalent beams instead of slabs).

3. Calculation of the corresponding rotation ψ_{slab} according to the analytical model.

4. Calculation of the new width reduction coefficient α using formula (7.1).

5. Repetition of the calculations of steps 2 to 4 using the new α coefficient until convergence between new α and old α values is reached.

It should be mentioned that, alternatively, for the second step of the above-mentioned procedure, the rotation ψ_{slab} can be read from the numerical model instead of the unbalanced moment M. In this case, the corresponding unbalanced moment M should be calculated using the analytical model (step 3). This alternative is adopted for the validation of the method presented in the following. It should be stated that the analytical model calculations are performed externally to the numerical analysis of the (slab-equivalent) beam-column frame, since the option of continuously adapting beam width is not currently available in commercial software packages.

Typically less than ten iterations are required to reach convergence between the values of the coefficient α of two subsequent iterations. The main advantage of this method is that it can be applied not only to slab-column connections that belong only to the gravity force-resisting system (GFRS) but also to slab-column connections that are part of the lateral force-resisting system (LFRS). Its main shortcoming is the fact that one numerical analysis should be performed per iteration. However, the performed analysis is linear elastic and does not require high computational effort.

For monotonic loading conditions, the calculation of the $M - \psi_{slab}$ relationship (Chapter 4) is carried out only once. For cyclic loading conditions, the exact displacement routine should be constructed by the user. To this end, the number of calculations using the proposed model of Chapter 5 should be equal to the number of acceleration (or equally base shear) peaks and each analysis should take into account all previous loading cycles.

7.1.2 Validation

The proposed analysis method is validated against experimental results of flat slab buildings with over-hangs conducted by Fick [Fic08] and Moehle and Diebold [Moe84, Moe85]. For comparison, the method proposed by Hwang and Moehle [Hwa00] and the method by Grossman [Gro97] are also applied (see Chapter 2). Comparison with subassembies of one interior and two exterior slab-column connections [Dur95] was not performed since the behaviour of such specimens is expected to be affected significantly by the response of the exterior slab-column connections. This is outside the scope of the present study (see Chapter 1).

Regarding the validation process that follows, force-controlled analyses were conducted, i.e. the lateral loads corresponding to the experimental base shear were applied to the established numerical models. Since no information on the deformation capacity of individual slab-column connections is reported, comparison between experimental and predicted behaviour is only performed in terms of the global displacement of the top floor (roof) and the storey displacement of each floor of the building.

Column deformation

Tests on isolated slab-column specimens showed rather insignificant column deformation during the unbalanced moment introduction since the column was typically designed to be much stronger than the slab (Chapter 2). In flat slab buildings subjected to earthquake motions significant cracking of the column members is expected to occur, particularly at high drift levels, which results in reduction of the column stiffness. In the case that the columns are proportioned so that flexural plastic hinges form at the column ends prior to shear failure, shear deformations are limited and therefore non-linear force-based beam elements with fibre sections can be used to model the flexural behaviour of the column members [Kab84]. This is the case for both tests analysed in the following. To account for the contribution of column deformation to the interstorey drift values within the proposed EBW method (or equally to calculate the effective column stiffness EI_{eff}), the following procedure is adopted:

1. Modelling of the columns using fibre elements (to account for the non-linear behaviour) and modelling of the slab- equivalent beams as rigid ($I_g \to \infty$). Non-linear analysis of the flat slab building.

2. Calculation of the interstorey drifts corresponding to the desired lateral loads from the non-linear model (due to column deformation alone).

3. Modelling of the columns of the flat slab building using linear elastic beam members with reduced flexural stiffness (to account for the non-linear behaviour) and modelling of the slab-equivalent beams as rigid ($I_g \to \infty$). Linear elastic analysis of the flat slab building applying the desired lateral loads (same as in step 1).

4. Calculation of the interstorey drifts corresponding to the desired lateral loads from the linear elastic model (due to column deformation alone).

5. Comparison between the interstorey drifts calculated in steps 2 and 4. If convergence is not achieved revise the column stiffness reduction factor of the linear elastic model (step 3) until the interstorey drifts calculated in step 4 match the interstorey drifts calculated in step 2.

Table 7.1 gives the main parameters of the inelastic analysis carried out to calculate the effective stiffness of the columns (step 2). Since a fibre-based formulation is chosen for the inelastic analysis of the columns (with the equivalent slab-beams assumed to be rigid), the program SeismoStruct [Sei12] was used. Other methods for calculating the column effective stiffness can also be employed (e.g. [Pri07]). It should be noted that the aforementioned procedure allows to apply different stiffness reduction factors to the columns of each storey. If the same stiffness reduction factor is applied to all columns of the building, its value can be calculated directly from the non-linear analysis and no iterations are required.

Table 7.1 – Inelastic analysis parameters for the calculation of the contribution of the column deformation to the total interstorey drift

Analysis type	Static non-linear
Loading pattern (in height)	Triangular
Vertical load application	Force control
Lateral load application	Displacement control
Column modelling	Fibre-based elements
Slab modelling	Elastic beam elements ($I_g \to \infty$)
Connection modelling	Rigid end zones

The main parameters of the performed elastic analyses for determining the column effective stiffness (step 4) are given in Table 7.2.

Table 7.2 – Elastic analysis parameters for the calculation of the column effective stiffness

Analysis type	Linear elastic
Loading pattern (in height)	Triangular
Vertical load application	Force control
Lateral load application	Force control
Column modelling	Elastic beam elements (EI_{eff})
Slab modelling	Elastic beam elements ($I_g \rightarrow \infty$)
Connection modelling	Rigid end zones

Slab deformation

For determining the contribution of slab deformation to the interstorey drift, the procedure presented in §7.1.1 will be used in the following. The main parameters of the elastic analysis required for each iteration are the same as in Table 7.2 with the only exception that the elastic beam elements that model the slabs are assigned a width $b = \alpha l_2$ instead of a very high stiffness. The width b is updated at each iteration until convergence is achieved.

Fick [Fic08, Puj10]

The geometric properties of the flat slab building tested at full-scale by Fick [Fic08] are shown in Figure 7.1. The building was subjected to combined vertical loading and quasi-static cyclic lateral loading. The rotation levels at which unloading and loading in the opposite direction was performed corresponded to a roof drift (i.e. Δ_{roof}/H_{tot}) of 0.4%, 1.5% and 3.0%. One reversed cycle was performed per rotation level.
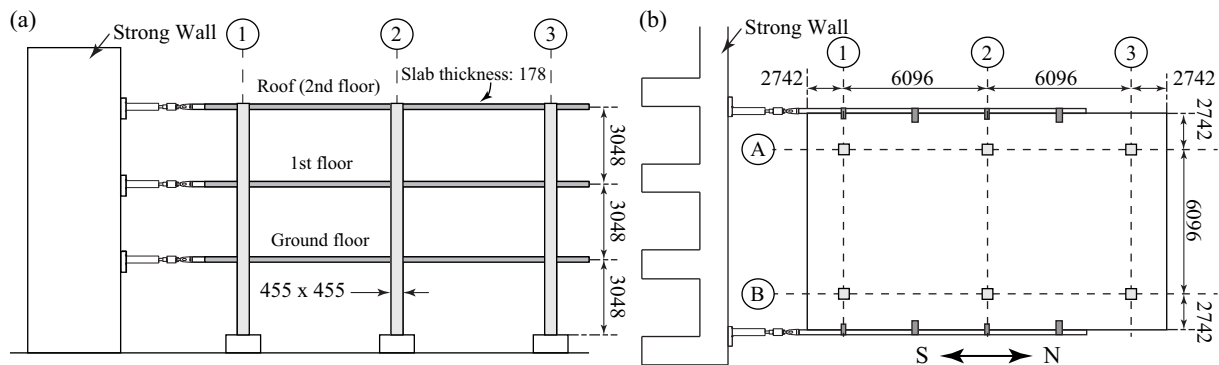
Figure 7.1 – Test of flat slab building by Fick [Fic08]: (a) view of the building parallel to the base motion, and (b) plan view of the building (drawn after [Fic08] - dimensions in mm)

Punching failure was observed at slab-column connection 2-B (1st floor) when loading towards a roof drift of 3.0% in the South direction [Fic08]. After the completion of the full cycle at 3.0% roof drift the test was stopped and all frames were infilled with solid clay bricks and tested again to investigate the influence of masonry infill walls on the global behaviour of the structure. Additional information can be found elsewhere [Fic08, Puj10]. Herein, the focus is drawn on the test of the bare flat slab frame, i.e. until the first punching failure.

Figure 7.2a shows the comparison between the experimental and the calculated base shear-roof displacement ($V_b - \Delta_{roof}$) curve for the flat slab building tested by Fick [Fic08]. The $V_b - \Delta_{roof}$ was computed using three different methods, i.e. the here proposed method, the method by Hwang and Moehle [Hwa00] and the method by Grossman [Gro97]. Figure 7.2b shows the moment-rotation relationship of the slab-column connection 2-B according to the cyclic model (continuous curve). The moment-rotation curve according to the monotonic analytical model is also shown in the same figure (dashed curve), for comparison purposes.
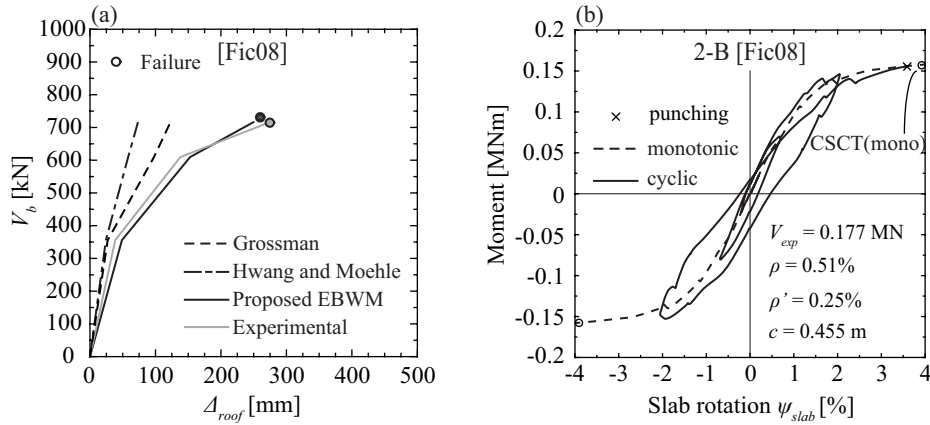
Figure 7.2 – (a) Comparison between experimental and predicted global behaviour ($V_b - \Delta_{roof}$) according to the EBW method proposed in this chapter and the EBW models proposed by Grossman [Gro97] and Hwang and Moehle [Hwa00], and (b) moment-rotation relationship of the slab-column connection 2-B according to the monotonic and cyclic analytical model.

Figure 7.2a shows that both the EBW models by Grossman [Gro97] (dashed line) and by Hwang and Moehle [Hwa00] (dashed dotted line) underestimate the experimental values of roof displacements, in particular for high roof displacements. The model proposed by Grossman [Gro97] provides predictions closer to the experimental roof displacement values than the model by Hwang and Moehle [Hwa00]. This can be attributed to the fact that Grossman's model takes into account the stiffness degradation due to increasing drift values (§2.2.1), which is not the case for the model by Hwang and Moehle. In Grossman's model, the values of factor K_d, which takes into account stiffness degradation due to increasing drift values, were calibrated to match the measured drifts of a flat slab system tested earlier [Hwa93]. This system was, however, subjected to smaller gravity loads than the system tested by Fick [Fic08]. Moreover, for the system tested by [Hwa93] (see §6.3.2) $\rho = 0.76\%$ but for the one tested by Fick [Fic08] $\rho = 0.51\%$. It is therefore anticipated that the model by Grossman predicts stiffer $V_b - \Delta$ curves than the experimental ones.

The proposed EBW method accounts explicitly for the influence of many parameters on the stiffness degradation due to increasing drifts, such as material properties, reinforcement ratio, and gravity loads, which is not the case for the models by [Gro97,Hwa00]. Therefore, the proposed method predicts better the $V_b - \Delta_{roof}$ relationship (Fig. 7.2a) than the other models. The base shear at punching failure is also predicted very accurately (ratio of predicted to measured base shear at punching: 1.020). The corresponding roof displacement is also predicted rather well (ratio of predicted to measured roof displacement at punching: 0.946).

Figure 7.2b compares the predictions of the cyclic model (continuous curve), which was adopted for the validation, with the monotonic model (dashed curve). It can be seen that the cyclic model predicts slightly smaller unbalanced moment at punching (x marker) for the critical slab-column connection (2-B) than the monotonic model (circular marker). Moreover, the cyclic model predicts 9% smaller slab rotation at punching than the monotonic model.

Figure 7.3a and b show two photos of the critical slab-column connection (2-B) [Fic08, Puj10], while Figure 7.3c compares the predicted shear crack inclination according to the cyclic model (dashed line) with a sketch of the failure section for the same connection [Fic08]. The first punching failure (intersection of the cyclic model with the CSCT(mono) failure criterion) is predicted for the slab-column 2-B of the first floor which agrees with the experimental observations (Figs. 7.3a and b). The predicted shear crack inclination (dashed line) is also in good agreement with the experimental shear crack inclination (loading towards the South), as shown in Figure 7.3c.
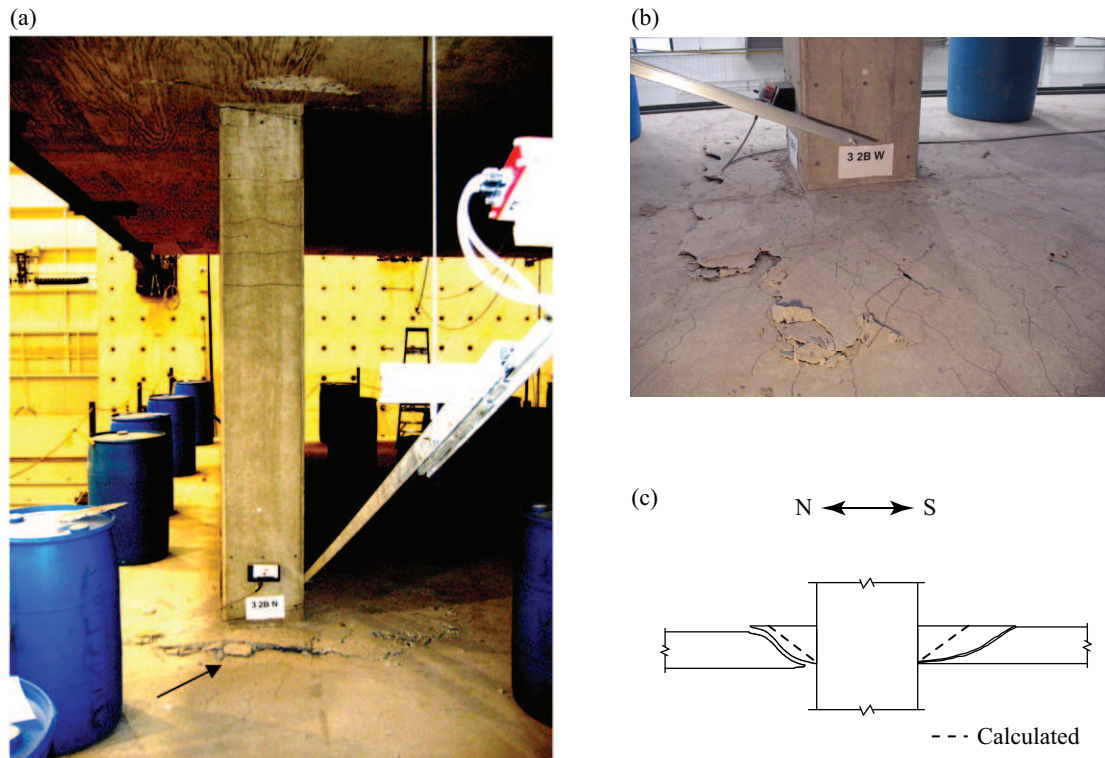
Figure 7.3 – Damage caused by punching shear of the slab-column connection 2-B: (a) photo of the connection at failure (North side) [Puj10], (b) close-up photo of the connection at failure (West side) [Fic08], and (c) comparison between experimental and calculated shear crack inclination at failure according to the cyclic model.

Figure 7.4 shows the comparison between the experimental and the calculated base shear-storey displacement relationship $(V_b - \Delta_{st})$ for each storey of the tested flat slab building according to the proposed method, the model proposed by Grossman [Gro97] and the model proposed by Hwang and Moehle [Hwa00].
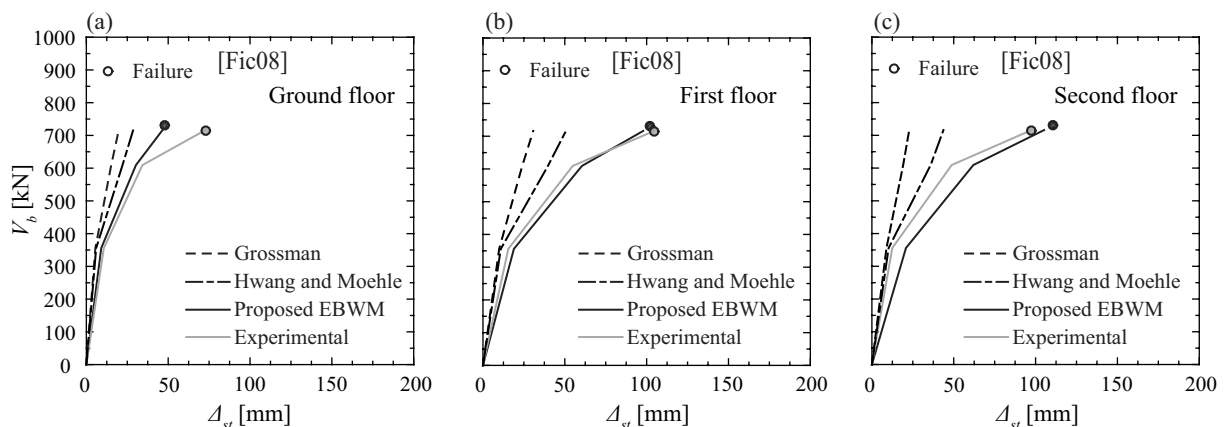
Figure 7.4 – Comparison between experimental and predicted $V_b - \Delta_{st}$ relationships according to the EBW method proposed in this chapter and the EBW models proposed by Grossman [Gro97] and Hwang and Moehle [Hwa00]: (a) ground floor, (b) first floor, and (c) second floor.

As can be seen from Figure 7.4, the proposed EBW method gives rather accurate prediction of the $V_b - \Delta_{st}$ relationships, while the EBW models by Grossman [Gro97] and Hwang and Moehle [Hwa00] provide conservative results, in particular for large storey displacements. The difference between the various models increases with increasing storey displacement.

Table 7.3 gives the calculated stiffness reduction due to non-linear behaviour of both columns and slab-equivalent beams according to the proposed EBW method. The values correspond to the ratio of effective stiffness EI_{eff} to gross (uncracked) stiffness EI_g. For the columns, the ratio EI_{eff}/EI_g is calculated using the method presented earlier [Sei12]. For the slab-equivalent beams, EI_{eff} and EI_g correspond to the uncracked stiffness of a beam with height equal to the slab thickness h and width equal to αl_2 and l_2, respectively. Therefore, for the slabs, the ratio EI_{eff}/EI_g corresponds to the width reduction coefficient α (Eq. (7.1)).

Table 7.3 – Predicted stiffness ratio due to the non-linear behaviour of columns (EI_{eff}/EI_g) and slab-equivalent beams (α) for the flat slab building tested by [Fic08] (proposed EBW method)

Roof drift	Ground floor		First floor		Second floor	
	column	slab	column	slab	column	slab
0.4%	0.650	0.162	0.500	0.137	0.450	0.141
1.5%	0.420	0.111	0.400	0.093	0.300	0.110
3.0%	0.350	0.079	0.300	0.059	0.280	0.067
Failure	0.350	0.077	0.300	0.057	0.280	0.063

Table 7.3 shows that both the ratio EI_{eff}/EI_g of the columns and the α coefficient of the slabs decrease with increasing drift demands. The α coefficient can attain values smaller than 0.1 at high drift levels. For buildings with low reinforcement content in the slabs and relatively high reinforcement content in the columns (like is the case for the building tested by Fick) it is anticipated that slab yielding occurs before column yielding. In this case, the higher the interstorey drift is, the larger is the contribution of the slab deformation to the interstorey drift. For the analysed building, the calculated ratio of roof displacement due to column deformation $\Delta_{roof.col}$ to the total roof displacement Δ_{roof} was 8.6% at $V_b = 609$ kN, but fell to 7.5% at $V_b = 716$ kN and to 7.3% at the predicted punching failure ($V_b = 730$ kN). The same trends were observed for the storey displacement of each floor.

Moehle and Diebold [Moe84, Moe85]

The geometric properties of the flat slab building tested by Moehle and Diebold [Moe84, Moe85] are shown in Figure 7.5. The building was subjected to combined vertical loading and acceleration records that modelled the NS component obtained in El Centro during the 1940 Imperial Valley Earthquake. The structure was tested at reduced scale (3/10) on a shaking table to examine the overall resistance to low, moderate and high intensity ground motions. Although no punching failure occured, this test provided significant information with regard to the response of slab-column connections under dynamic loading. More information can be found elsewhere [Moe84, Moe85].
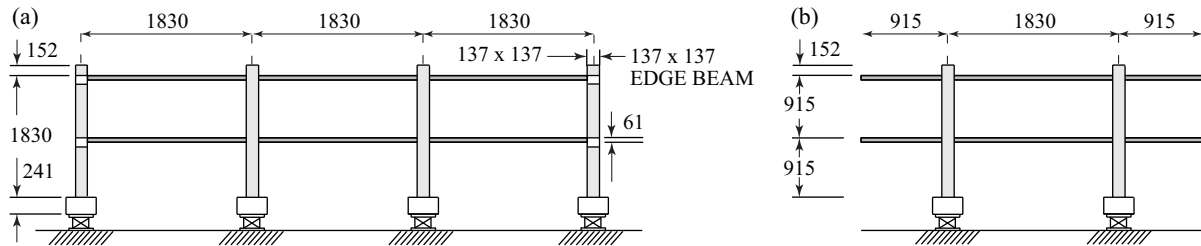
Figure 7.5 – Test of flat slab building by Moehle and Diebold [Moe85]: (a) view of the building parallel to the base motion, and (b) view of the building transverse to the base motion (drawn after [Moe85] - dimensions in mm).

Figure 7.6 compares the experimental and the calculated $V_b - \Delta_{roof}$ curve (Fig. 7.6a) as well as the $V_b - \Delta_{st}$ relationship for both storeys of the tested structure (Figs. 7.6b and c) according to the proposed method, Grossman [Gro97], and Hwang and Moehle [Hwa00]. The experimental curves of Figure 7.6 are drawn based on the maximum measured base shear and the corresponding displacement of each earthquake run. Earthquake runs with applied acceleration histories only in the horizontal direction are considered herein (EQ8 and EQ10). It should be noted that both considered runs correspond to high intensity earthquakes [Moe84]. EQ10 may even be an unrealisticaly intense motion [Moe85] (PGA = 0.606g).

Since various earthquake runs both in the horizontal and in the vertical direction were applied to the flat slab structure prior to the application of EQ8, the loading protocol of each slab-column connection was rather complicated. Hence, for the proposed EBW method, the simplified approach of Chapter 4 is adopted for the calculation of the moment-rotation relationship of the slab-column connections (combination of the monotonic analytical model with the CSCT(cyc) failure criterion).
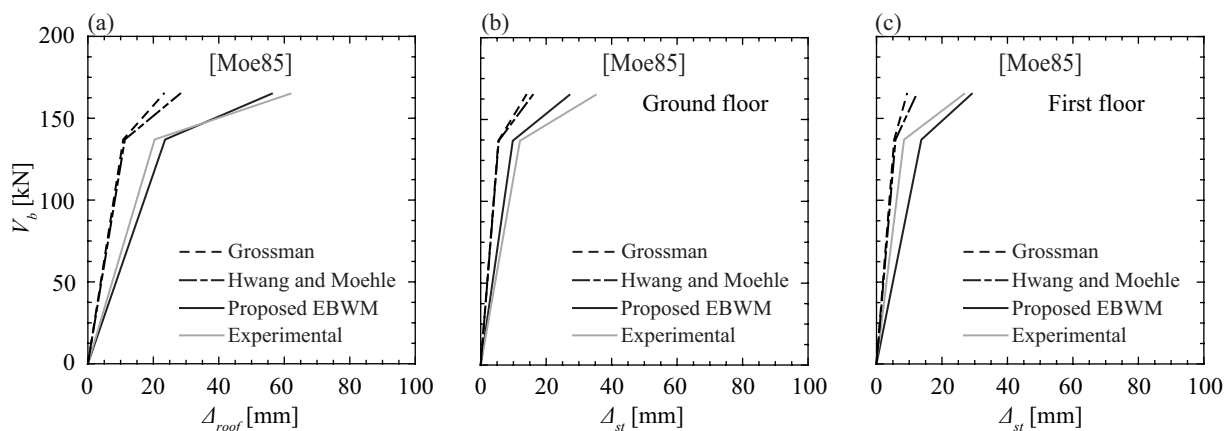
Figure 7.6 – Comparison between experimental and predicted $V_b - \Delta$ relationships according to the EBW method proposed in this chapter and the EBW models proposed by Grossman [Gro97] and Hwang and Moehle [Hwa00]: (a) roof displacement, (b) storey displacement of the ground floor, and (c) storey displacement of the first floor.

As can be seen in Figure 7.6, the proposed method predicts accurately enough the experimental $V_b - \Delta_{roof}$ relationship (Fig. 7.6a) as well as the experimental $V_b - \Delta_{st}$ relationship of both the ground floor (Fig. 7.6b) and the first floor (Fig. 7.6c). The models proposed by Grossman [Gro97] and Hwang and Moehle [Hwa00] provide rather conservative predictions of both the roof displacement and the storey displacement of the two floors. It should be mentioned that, for the considered earthquake runs, the proposed method did not predict punching failure of any slab-column connection. This is in agreement with the experimental data [Moe85]. For the base shear introduced by EQ10, the safety margin according to the proposed method is rather low for the moment resistance (9%) but is relatively large for the deformation capacity (60%). This indicates that for EQ10 a mechanism did not form, which is in agreement with the observed crack pattern (Fig. 7.7).
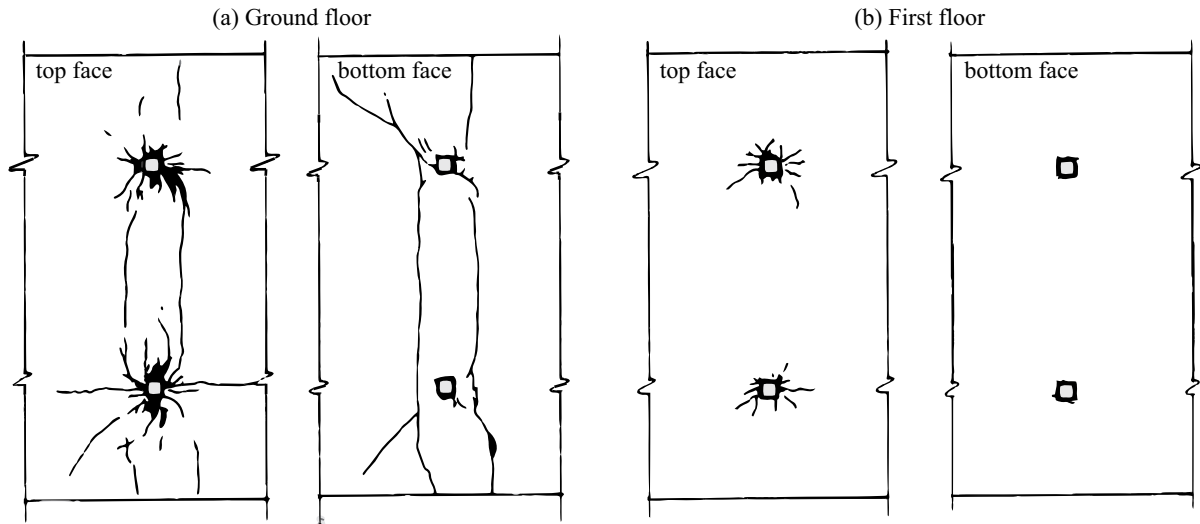
Figure 7.7 – Observed crack patterns (top and bottom slab surface) following EQ10 [Moe85]: (a) ground floor, and (b) first floor.

Table 7.4 gives the calculated stiffness reduction due to non-linear behaviour of both columns and slab-equivalent beams according to the proposed EBW method. It can be seen that the width reduction coefficient α attains very small values, indication of significant non-linear behaviour of the slab-column connections.

Table 7.4 – Predicted stiffness ratio due to non-linear behaviour of columns (EI_{eff}/EI_g) and slab-equivalent beams (α) for the flat slab building tested by [Moe85] (proposed EBW method)

Earthquake run	Ground floor		First floor	
	column	slab	column	slab
EQ8	0.270	0.080	0.280	0.111
EQ10	0.083	0.034	0.118	0.052

Table 7.4 confirms what has been shown earlier that both the ratio EI_{eff}/EI_g of the columns and the α coefficient of the slabs decrease with increasing drift demands. It can be observed that EQ10 results in a very significant decrease in the stiffness of both the columns ($\approx 65\%$) and the slabs ($\approx 50\%$) compared to EQ8. Since the stiffness reduction is more pronounced for the columns than for the slabs, it is expected that the contribution of column deformation to the interstorey drift increases for EQ10 compared to EQ8. Indeed, the calculated ratio $\Delta_{roof.col}/\Delta_{roof}$ was 16% for EQ8 ($V_b = 137$ kN), but increased to 24% for EQ10 ($V_b = 165$ kN).

Figure 7.8 shows the response of the fibre-based numerical models established to compute the contribution of column deformation to the interstorey drift [Sei12] for the flat slab buildings tested by Fick and Moehle and Diebold (Fig. 7.8a and b, respectively). The base shear levels at which the contribution of slab deformation ψ_{slab} was calculated according to the proposed EBW method are also shown in the same figure.
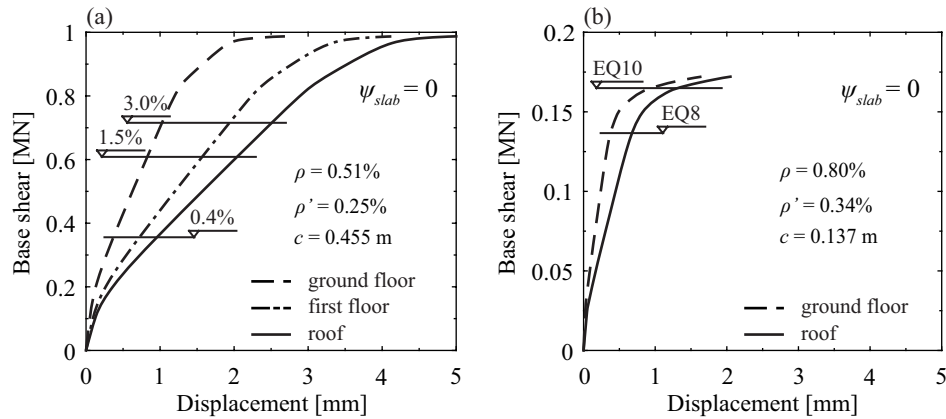
Figure 7.8 – $V_b - \Delta$ relationships according to fibre-based numerical models to calculate the contribution of column deformation to the interstorey drift [Sei12] ($\psi_{slab} = 0$): (a) Fick [Fic08], and (b) Moehle and Diebold [Moe85].

The numerical $V_b - \Delta$ curves of Figure 7.8 show the impact of column deformation in the global response of the modelled flat slab buildings. For the structure tested by Fick, it can be seen that the column stiffness reduction is significant only at very high base shear levels (Fig. 7.8a). On the other hand, for the structure tested by Moehle and Diebold, it can be seen that the response softens significantly when the base shear increases from 137 kN (EQ8) to 165 kN (EQ10), indicating significant yielding of the column rebars (Fig. 7.8b). This is in accordance with strain gauge measurements, indicating first yield of column rebars in the proximity of the slab-column connection of the ground floor and the first floor at $V_b \approx 134$ kN [Moe85].

7.1.3 Influence of slab region outside $0.22L$ on the predicted response

This subsection examines the influence of the slab part outside $0.22L$ and the boundary conditions on the moment-rotation response of the slab-column connections of the flat slab structures that were analysed in §7.1.2. Figure 7.9 shows the calculated moment-rotation curves of the slab-column connections of the buildings tested by Fick [Fic08] and Moehle and Diebold [Moe85] for different boundary conditions (isolated, simply supported at $r = 0.50L$, and continuous at $r = 0.50L$). As can be seen, the predicted response of the isolated specimen (green curves) is stiffer than the predicted response of the continuous flat slab (black curves) because the acting torsional and radial bending moments at $r = 0.22L$ are set to zero. For the specimen that is simply supported at $r = 0.50L$, the model gives intermediate results between the isolated specimen and the continuous slab. Moreover, when the slab rotation outside $0.22L$ (ψ_{os}) is accounted for, the predicted slab rotation ψ_{slab} at punching increases and the moment strength decreases. It is noted that the analytical model neglects the compressive membrane action, which can lead to higher moment strength and smaller deformation capacity. For the considered buildings, however, this effect did not appear to be significant.
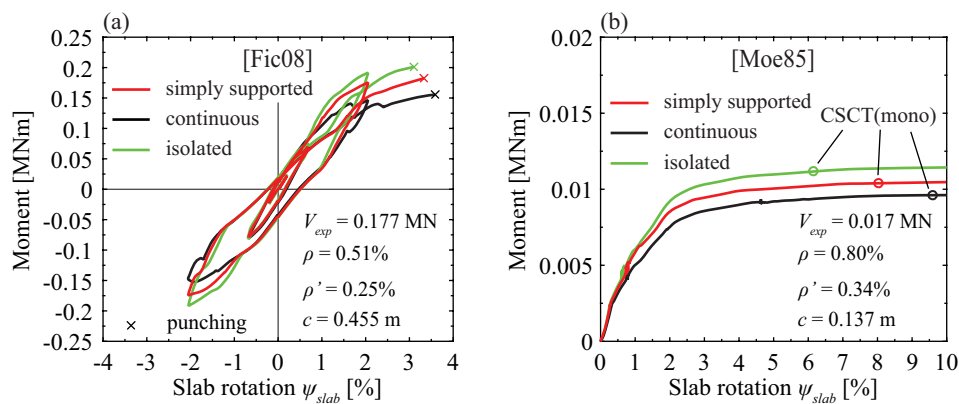
Figure 7.9 – Influence of the slab part outside $0.22L$ and the boundary conditions on the moment-rotation response of the slab-column connections of the buildings tested by: (a) Fick [Fic08], and (b) Moehle and Diebold [Moe85].

It should be mentioned that the geometric properties and the vertical load of the interior slab-column connections of the structure tested by Moehle and Diebold [Moe85] are nominally identical to the ones of an isolated slab specimen tested previously [Zee84]. However, direct comparisons cannot be done since the material properties were significantly different for the isolated component ($f_c = 26.2$ MPa and $f_y = 470$ MPa) and the entire building ($f_c = 36.5$ MPa and $f_y = 434$ MPa). Since both tests were conducted on very thin slabs ($d = 52$ mm), these discrepancies influence significantly the predicted response according to the proposed model. Testing an isolated slab specimen with the same properties of an interior connection of the building tested by Fick [Fic08] ($d = 146$ mm) would be important for understanding the influence of the slab part outside $0.22L$ and the effect of the compressive membrane action on the response. This building offers also the advantage that column deformation is limited (Fig. 7.8a), compared to the one tested by Moehle and Diebold (Fig. 7.8b).

7.2   Direct Drift Demand Method

A further simplified analysis method for buildings with slab-column connections was developed based on the proposed analytical model. The method is suitable only if the slab-column connections are not part of the LFRS of the building and requires iterations for calculating the contributions of column and slab deformation to the interstorey drift from analysis, as described in the following:

1. Numerical analysis of the members that are part of the LFRS (Fig. 7.10b) instead of the full structure (Fig. 7.10a), and calculation of the storey drift demand ψ_{st} at the slab-column connection of interest.

2. Choice of the percentage of the column deformation contributing to the interstorey drift ψ_{st} calculated in step 1.

3. Calculation of the moment M_E at the column ends due to column deformation. This is the unbalanced moment that is introduced to the slab-column connection.

4. Calculation of the rotation due to slab deformation ψ_{slab} that corresponds to the unbalanced moment M_E according to the analytical model.

5. Revision of the rotation due to column deformation ψ_{col} using the following formula:

$$\psi_{col} = \psi_{st} - \psi_{slab} \qquad (7.2)$$

6. Repetition of the calculation of steps 2 through 5 until convergence between new ψ_{col} and old ψ_{col} is reached.
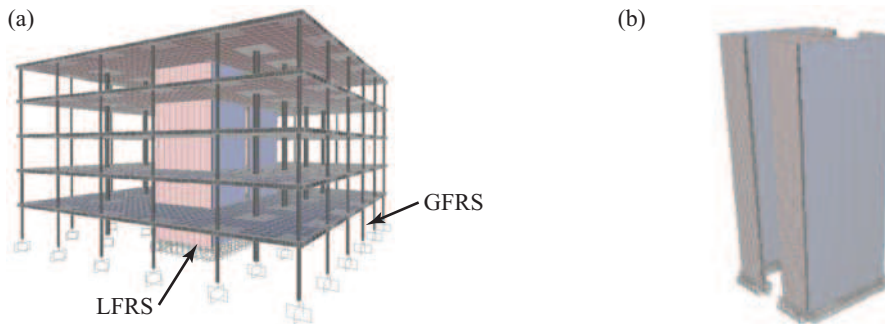
Figure 7.10 – Typical numerical models for seismic analysis of buildings with slab-column connections for (a) full structure, and (b) proposed method (lateral force-resisting system) [Dra15].

The calculation procedure according to the Direct Drift Demand method is illustrated in Figure 7.11. The drift demand of each storey ($\psi_{st.n}$, $\psi_{st.n+1}$, etc.) is computed through numerical analysis of the LFRS and is not iterated. Assuming that gravity columns respond in the elastic range during earthquake motions, the moment $M_{Ec.n}$ that is acting at the column end (fixed-fixed conditions) of the nth floor due to an imposed lateral displacement equal to $\psi_{col.n} H_{st.n}$ is (step 3 of the above-mentioned procedure):

$$M_{Ec.n} = \frac{6\,EI_{eff}}{H_{st.n}^2}\,\psi_{col.n}\,H_{st.n} \qquad (7.3)$$

where $H_{st.n}$ is the storey height of the nth floor and EI_{eff} is the effective stiffness of the column. It can be assumed that $EI_{eff} = 0.5\,EI_g$ if a more elaborated method like the one presented in §7.1.2 or by [Pri07] is not used.

The unbalanced moment introduced to the slab-column connection is equal to the sum of bending moments at the end of the columns framing into the considered slab-column joint (Fig. 7.11a):

$$M_E = M_{Ec.n} + M_{Ec.n+1} \tag{7.4}$$

Once M_E is known, the contribution of slab deformation (ψ_{slab}) to the interstorey drift can be calculated according to the proposed model (Fig. 7.11b). The rotations due to column deformation $\psi_{col.n}$ and $\psi_{col.n+1}$ are then revised and the procedure continues until convergence between two subsequent iterations is achieved.

Figure 7.11 – Illustration of the iterative method for the calculation of the contribution of (a) column deformation, and (b) slab deformation to the interstorey drift.

To reach convergence, a limited number of iterations (typically less than ten) is required. Moreover, since only one numerical analysis is performed, this method is more time-efficient than the EBW method proposed previously (Section 7.1). However, its main shortcoming is that it can be applied only when the columns are not part of the LFRS, i.e. to gravity columns.

For seismic assessment, the maximum value of the rotation due to slab deformation ψ_{slab} from analysis (step 4) should be compared with the rotation due to slab deformation ψ_{slab} at punching failure according to the proposed model (Chapter 4 or 5). Due to lack of experimental data on the response of flat slab buildings with slab-column connections not being part of the LFRS, this method could not be validated experimentally. Nevertheless, several case studies where this method is applied for seismic assessment can be found elsewhere [Sed14, Dra15]. These studies investigated the impact of the seismicity zone (low against moderate) and the structural layout (eccentricity of the LFRS with regard to the centre of mass of the building) on the seismic behaviour of slab-column connections.

It should be stated that the Direct Drift Demand method should be used by the structural engineer if it can be verified that the contribution of the slab-column connections to the structure stiffness can be neglected. This can be done by performing a numerical analysis of the members that are considered to be part of the LFRS and a numerical analysis of all involved structural members (LFRS and GFRS) and comparing the obtained results. Numerical studies by Ghali et al. [Gha12] have demonstrated that neglecting the GFRS gives small discrepancies in the calculated drifts only for cases of low to mid-rise buildings (similar to the prototype building of this study). For high-rise buildings, however, if the GFRS is excluded from the numerical model, the drift and the unbalanced moment introduced to the slab-column connections can be significantly overestimated [Gha12]. Neglecting the slab-column connections in the seismic analysis can lead to overestimation of the natural period T of the structure, which for high periods can result in underestimation of the lateral forces due to seismic excitation and, therefore, in unsafe design. Therefore, for the seismic analysis of high-rise buildings, both the GFRS

and the LFRS should be included in the numerical model [Shi10]. In this case, the method presented in the previous section can be used.

7.3   Conclusions

This chapter proposes two methods for the numerical analysis of buildings with slab-column connections. Both methods are based on the mechanical model proposed in Chapter 4 for monotonic loading conditions and extended in Chapter 5 for cyclic loading conditions. The model has shown good performance in predicting the moment-rotation response of both isolated and continuous slab specimens (Chapter 6, Appendices C and D). The main conclusions of this chapter are as follows:

1. An Effective Beam Width method which incorporates the mechanical model developed in Chapters 4 and 5 is proposed. The novelty of this method is that parameters such as geometric and material properties, gravity loads, and reinforcement ratio are explicitly accounted for when calculating the width reduction coefficient α of the effective beam. An iterative procedure is proposed for the calculation of α, while for each iteration, a linear elastic analysis of the building should be performed.

2. The proposed Effective Beam Width method has shown good performance in predicting the global experimental response of flat slab buildings reported in the literature, both in terms of $V_b - \Delta_{roof}$ and $V_b - \Delta_{st}$ relationship.

3. The predictions of the proposed Effective Beam Width method for the base shear at punching failure and the corresponding displacement are in close agreement with the experimental results. The location of the slab-column connection that fails first is predicted correctly both in plan and in height.

4. Previously proposed Effective Beam Width models predict rather stiff global response when compared with the experimental results and the proposed Effective Beam Width method predictions.

5. A simplified method for the numerical analysis of flat slab buildings with slab-column connections that do not belong to the lateral force-resisting system is proposed. At first, the method consists in analysing only the members of lateral force-resisting system and calculating the drift demand of the slab-column connections of interest. Then, an iterative procedure is employed to calculate the relative contribution of slab deformation and column deformation to the interstorey drift.

Chapter 8

Conclusions and further research

This dissertation consists of four parts: (a) an experimental campaign on isolated slabs subjected to combined gravity loads and unbalanced moment focusing on the influence of loading history (cyclic vs monotonic) for different gravity loads and reinforcement ratios, (b) development of a mechanical model for describing the moment-rotation relationship of slab-column connections subjecting to monotonic loading, (c) extension of the monotonic mechanical model to capture the influence of cyclic loading and cumulative damage effects on the moment-rotation relationship, and (d) development of methods for the numerical analysis of flat slab buildings on the basis of the proposed mechanical models.

Section 8.1 presents a summary of the work and highlights the key contributions of this thesis, while Section 8.2 outlines several related research questions that were outside the scope of this thesis and should be addressed in future studies.

8.1   Contributions and conclusions

8.1.1   Experimental investigation

The experimental campaign investigated the seismic behaviour of interior RC slab-column connections without transverse reinforcement. The main objective of this experimental campaign was to study how cyclic loading affects the force and deformation capacity when compared to monotonic loading-cyclic loading on the moment-rotation response for different gravity loads and reinforcement ratios. For this purpose a test setup that had been used in previous studies documented in the literature was modified. The test setup allowed to apply asymmetric slab rotations as they are induced during earthquakes. These rotations were applied by means of two servo-hydraulic actuators. At the same time, the vertical load on the slab was kept constant through a system of four hydraulic jacks.

The experimental study shows that reversed cyclic loading reduces the moment strength and the deformation capacity of slab-column connections. This effect is more pronounced for smaller gravity loads and smaller reinforcement ratios. In general, the cyclic response envelope followed the monotonic one, with the difference that failure occurred earlier for the cyclic test. For very low gravity loads, however, cyclic loading led to a softer moment-rotation response than for monotonic loading for moments higher than 80% of the peak cyclic moment. Moreover, it is shown that the shear crack at failure is steeper for cyclic tests than for monotonic tests. This is more marked for low gravity loads than for high gravity loads.

This experimental study confirms previous studies showing that increasing gravity load reduces the stiffness and the moment capacity of slab-column connections. For cyclic tests, it is confirmed that the deformation capacity increases with decreasing gravity loads. For monotonic tests, however, a more differentiated trend was identified with regard to the deformation capacity: For GSR > 0.57 (approximately half the punching strength under concentric gravity loads), the deformation capacity increases with decreasing gravity load, as for cyclic tests. For GSR < 0.57, however, the trend did not

continue but smaller gravity loads resulted in a reduced deformation capacity. This was ascribed to the smaller extent of cracking for small gravity loads. It is confirmed that high reinforcement content leads in general to higher moment strength and stiffness and lower deformation capacity than small reinforcement content. This study showed that for low gravity loads, the reinforcement ratio effect on the moment strength was small, while for high gravity loads the reinforcement ratio effect on the deformation capacity was rather insignificant.

The moment strength predictions according to ACI-318 [ACI14], fib-MC2010 [Fib11] are rather conservative estimates of the moment strength of the tested slabs, while EC2 [Eur04] provides higher accuracy and precision. The connection rotation capacity of the cyclic tests is estimated rather accurately by the allowable drift limit of ACI-318 [ACI14]. However, ACI-318 appears to overestimate the rotation capacity for high vertical loads (GSR > 0.6).

8.1.2 Proposed monotonic model

The mechanical model proposed in this thesis to describe the moment-rotation relationship of slab-column connections under monotonically increasing drifts is based on the axisymmetric model proposed by Muttoni for slabs subjected to vertical loads only [Mut08]. The slab is divided into an even number of sector elements and the region inside the shear crack. The experimental campaign and finite element analyses have shown that the local rotations follow approximately a sinusoidal law with respect to the direction of excitation. To calculate the moment-rotation curve the equilibrium is formulated both locally for each sector element and globally for the entire slab until $0.22L$ (L corresponds to the distance from midspan to midspan). The influence of the slab part between $0.22L$ and $0.50L$ on the moment-rotation response is considered using an Effective Beam Width approach. The calculation is iterative with regard to the maximum and the minimum local slab rotations ψ_{max} and ψ_{min}, respectively. The developed model predicts rather well the $M - \psi_{max}$ and $M - \psi_{min}$ relationship of the monotonic tests conducted within this research.

The failure criterion of the Critical Shear Crack Theory (CSCT) [Mut08] is adapted to predict the moment strength and rotation capacity. For monotonic loading, shear force redistribution between sector elements of the hogging slab half is assumed to occur (CSCT(mono)). For cyclic loading, a simplified approach that neglects both shear redistribution and the effect of cyclic loading on the moment-rotation relationship is adopted (CSCT(cyc)). The monotonic model combined with the CSCT(mono) failure criterion predicts accurately enough the moment strength of slabs subjected to monotonically increasing unbalanced moment. The predictions for the corresponding rotation are slightly conservative and are associated with larger scatter. For cyclic loading, combination of the monotonic model with the CSCT(cyc) failure criterion gives slightly conservative predictions for both the moment strength and the deformation capacity.

The model is the first to account explicitly for the contribution of all three different lateral force-resisting mechanisms (eccentric shear, flexure and torsion) to the total unbalanced moment. The model predicts that the contribution of flexure (γ_f) to the total unbalanced moment increases for increasing connection rotation and can attain values higher than the value assumed by ACI-318 [ACI14]. Cyclic loading results in smaller γ_f values at failure than monotonic loading. Increasing reinforcement ratio leads to larger γ_f values, while increasing slab slenderness L/d leads to smaller γ_f and γ_v (contribution of eccentric shear force) values and larger γ_t (contribution of torsion) values.

8.1.3 Proposed cyclic model

This cyclic model proposed in the framework of this thesis is an extension of the monotonic mechanical model in order to consider the hysteretic behaviour and cumulative damage effects when calculating the moment-rotation relationship of internal slab-column connections. The assumptions of the extended model are based on local deformation measurements from the performed cyclic tests. A fixed shear crack is assumed to govern the post-yield behaviour of the sector elements while a hysteretic

moment-curvature relationship is adopted for the radial direction. Seismic damage is incorporated to each sector element separately using a non-cumulative damage model proposed previously. The developed model leads to more accurate prediction of the local slab rotations of the cyclically tested slabs than the simplified approach based on the monotonic model (CSCT(cyc)).

The moment strength and the rotation capacity are deduced from the combination of the moment-rotation relationship with the failure criterion that allows for shear force redistribution between the sector elements of the hogging slab half, as for monotonic loading conditions. Punching failure can occur only for maximum slab rotations ψ_{max} smaller or equal to the maximum slab rotation at punching under monotonic loading ($\psi_{max.u.mono}$). Combination of the failure criterion with the cyclic model leads to improved moment strength predictions for cyclically tested isolated slabs than the simplified approach based on the monotonic model (CSCT(cyc)) but with slightly larger scatter. Concerning the deformation capacity, the cyclic model provides similar average predictions with the simplified approach based on the CSCT(cyc), but with a slightly reduced scatter.

Regarding the contribution of the lateral force-resisting mechanisms to the unbalanced moment, the cyclic model predicts that, at peak moment, γ_f decreases with increasing gravity load acting on the slab. For low gravity load, the cyclic model predicts smaller γ_f values at peak moment than the simplified approach of Chapter 4. The influence of the loading history on the predicted γ_v values is less marked.

The model confirms that cyclic loading leads to smaller slab rotation capacities than monotonic loading. This reduction is larger for smaller gravity loads acting on the slab, which is in agreement with the test results. It is also confirmed that the seismic rotation capacity of flat slabs is mainly influenced by the gravity induced shear and the slab effective depth, but also by the column size. The model captures the effect that increasing gravity load and increasing slab effective depth result in decreasing rotation capacity. Therefore, empirical formulae should not be applied to thicker slabs than those used for the model calibration. The simplified approach for cyclic loading proposed on the basis of the monotonic model (adoption of CSCT(cyc) instead of CSCT(mono)) represents a reasonable lower-bound solution to be used in engineering practice if no consideration of the loading history is made. The model predictions show that other parameters such as the seismicity level, the number of cycles, the top reinforcement ratio, and the slab slenderness influence the rotation capacity to a smaller extent.

8.1.4 Proposed analysis methods

The proposed analytical model combined with the Effective Beam Width approach for considering the contribution of the slab region between $0.22L$ and $0.50L$ to the moment-rotation response predicts rather well the distribution of the radial bending moment and the torsional moment at $r = 0.22L$ for continuous specimens when compared with non-linear finite element analysis results. Moreover, the analytical model predictions show good agreement with the experimental response of interior slab-column connections of continuous flat slab systems.

Based on these results, an Effective Beam Width method is proposed for the numerical analysis of buildings with slab-column connections. The method incorporates both the monotonic and cyclic model and requires an iterative procedure for the calculation of the width reduction coefficient α. For each iteration a linear elastic analysis of the building should be conducted. The proposed method was found to predict rather accurately the global response of multi-storey flat slab buildings tested in past campaigns as well as the base shear and the corresponding lateral displacement at punching failure.

A simplified method is proposed for the numerical analysis of buildings with slab-column connections belonging only to the gravity force-resisting system. The method consists in analysing the lateral force-resisting system of the structure and calculating the drift demand on the connection of interest. An iterative procedure based on the analytical model is then followed to calculate the contribution of column deformation and slab deformation to the numerically calculated interstorey drift.

8.2 Future research

This section discusses the issues that should be addressed by future works as continuation of the present thesis. The proposed further steps are categorised by the adopted method of investigation: experimental investigation and analytical modelling.

8.2.1 Experimental investigation

Regarding the experimental investigation, the following directions may be pursued in future research:

- **Use of transverse reinforcement**: The presented test campaign offers a large number of reference test units for future experimental campaigns. Shear-reinforced slabs are gaining popularity during the last decades in many countries including Switzerland. Previous studies have shown that use of shear reinforcement in the column vicinity can increase the ductility of the slab-column connection considerably [Meg00a, Rob02, Bro07]. However, there are no experimental data on thick shear-reinforced slabs under combined vertical load and unbalanced moment. Therefore, experimental investigation on thick slabs with transverse reinforcement is expected to have high impact on both the engineering practice and further analytical developments.

- **Monotonic vs cyclic tests**: The literature review (Chapter 2) has revealed the lack of experimental data of slab pairs tested under monotonic and cyclic loading conditions. After the completion of the thesis further extension of the test database is needed to provide deeper insight into the cyclic behaviour of slab-column connections of the following cases:

  (a) — Slabs subjected to very low gravity loads or under-reinforced slabs typically fail in flexure when subjected to monotonically increasing unbalanced moment. Cyclic loading may, however, result in premature punching shear failure before reaching the yield plateau. Therefore, cyclic tests for lower gravity loads and reinforcement ratios than the ones adopted in the presented campaign should be conducted to examine whether the loading history has an impact on the failure mode. Moreover, the new tests should allow to verify experimentally the appearance of plastic strains in the bottom reinforcement and to further investigate the shear crack opening/closing process.

  (b) — Slabs without continuous bottom reinforcement over the slab-column connections or with bottom reinforcement with insufficient anchorage length were rather common in flat slab structures designed in North America according to provisions prior to [ACI71]. Several experimental studies have been conducted on slab specimens with curtailed bottom reinforcement [Dur95, Sta05, Rob06, Tia08]. However, testing of slab pairs under monotonic and cyclic loading will provide more insight into the impact of bottom reinforcement continuity on the cyclic behaviour of slab-column connections and on their post-peak response.

  (c) — Slabs with partial debonding of the top reinforcement in the proximity of the slab-column connection have been shown to be an effective solution for increasing the drift capacity of slab-column connections when compared to conventional, fully bonded, slabs [Cho09b]. Testing of slab pairs with debonded top reinforcement in the column proximity under monotonic and cyclic conditions will increase the understanding of the cyclic behaviour of such connection typologies.

  Extension of the test database would allow future developments with respect to analytical modelling of the cyclic behaviour of slab-column connections would benefit of a larger database of slab pairs for validation purposes or to calibrate seismic damage models.

- **Edge and corner slab-column connections**: The test campaign performed in the framework of this thesis focused on the the seismic behaviour of interior slab-column connections. Exterior slab-column connections may influence significantly the stiffness and the strength of flat slab buildings. Past experimental studies investigated the seismic behaviour of exterior connections

with relatively thin slabs. Therefore, further experimental investigation could focus on the seismic behaviour of corner connections and edge connections with bending parallel to the slab edge, particularly for relatively thick slabs.

- **Isolated slabs vs continuous slabs**: This thesis proposed a method to account for the slab region between $0.22L$ and $0.50L$ on the moment-rotation response. Although the method was validated against test results on flat slab systems, no data on slab pairs tested to investigate the influence of the slab region outside $0.22L$ were collected. Future experimental works can provide more in-depth knowledge by testing isolated slab components identical with previously tested flat slab systems (e.g. [Fic08]).

- **Biaxial seismic behaviour of interior slab-column connections**: Although most experimental studies on slab-column connections, including the work presented in this thesis, consider seismic shaking in one principal direction (uniaxial unbalanced moment), in reality shaking occurs simultaneously in both principal directions (biaxial unbalanced moment). Only few experimental campaigns investigated the influence of biaxial unbalanced moments on the seismic behaviour of slab-column connections [Pan89]. Further experimental studies focusing on the biaxial behaviour of interior slab-column connections is needed, in particular for relatively thick slabs.

8.2.2 Analytical modelling

Because of its physical basis and as it satisfies equilibrium, the analytical model is rather versatile and can be adapted to capture a large range of static and kinematic boundary conditions. Several enhancements and extensions can be performed in the future in the following directions:

- **Other non-axisymmetric cases**: The analytical model proposed in this thesis can be applied to inner slab-column connections or edge slab-column connections with bending perpendicular to the slab edge. This study has demonstrated that adopting a kinematic law for the slab rotation at different angles, on the basis of experiments and finite element calculations, can give rather good predictions of both the local behaviour (sector element level) and the global behaviour (specimen level). By developing new relationships to link local slab rotations at different angles as well as relationships between local and global slab rotations, the model can be extended to non-axisymmetric slab and/or column geometries, non-axisymmetric loading conditions, and non-axisymmetric reinforcement layouts:

  (a) — Non-axisymmetric slab/column geometry: The analytical model can be extended to edge slab-column connections with bending parallel to the slab edge as well as corner slab-column connections. Once this last step is achieved, the seismic assessment of entire buildings with exterior and interior slab-column connections would be possible. Moreover, it can be applied to connection typologies of RC bridges that are similar to the one treated in this thesis, e.g. monolithic pier-deck connections. This will allow estimating the effective deck width of RC slab bridges. In addition, it is feasible to extend the analytical so as to capture the behaviour of RC slabs with rectangular columns.

  (b) — Non-axisymmetric loading: The developed model can be extended rather easily to capture the behaviour of slab bridges under non-symmetric gravity loads (e.g. traffic loads in the longitudinal direction alone).

  (c) — Non-axisymmetric reinforcement layout: The model proposed in this thesis accounts for different effective depth of the reinforcing bars per direction. Therefore, it can be easily applied to cases with significantly larger reinforcement content along the strong axis compared to the weak axis, as well as to post-tensioned slabs with tendons running along one principal direction.

- **Influence of compressive membrane action**: The presented analytical model is combined with an Effective Beam Width method in order to account for the contribution of the slab part outside $r = 0.22L$ to the moment-rotation response. This approach, however, neglects the compressive membrane action of actual flat slabs. Future works should aim to incorporate this effect in the moment-rotation relationship.

- **Biaxial seismic behaviour of interior slab-column connections**: Limited number of theoretical studies on slab-column connections investigated the influence of biaxial unbalanced moments. Extension of the presented model to sequential loading protocols [Pan89] is rather straightforward. Additional considerations should be taken to accommodate other loading protocol types (e.g. clover-leaf).

- **Cyclic damage of interior slab-column connections**: The developed cyclic model for the moment-rotation relationship adopted the flexural damage index, which has been proposed by others, to describe the cyclic damage of each sector element. Although this approach predicted rather well the hysteretic response of most tests reported in the literature and conducted within this thesis, other damage models (cumulative or non-cumulative) can be implemented rather easily. This will allow to identify the damage model that best describes the seismic response of slab-column connections and whether there is need for a new damage model for slab-column connections.

Bibliography

[ACI14]   **ACI**, *Building code requirements for structural concrete*, ACI 318-14, American Concrete Institute, ACI Committee 318, 519 p., Farmington Hills, U.S.A., 2014.

[ACI11]   **ACI**, *Recommendations for design of slab-column connections in monolithic reinforced concrete structures*, ACI 352-11, American Concrete Institute, ACI Committee 352, 26 p., Farmington Hills, U.S.A., 2011.

[ACI71]   **ACI**, *Building code requirements for reinforced concrete*, ACI 318-71, American Concrete Institute, ACI Committee 318, 78 p., Detroit, U.S.A., 1971.

[All77]   **Allen F. H., Darvall P. LeP.**, *Lateral load equivalent frame*, ACI Journal, Vol. 74, No. 7, pp. 294-299, Detroit, U.S.A., July, 1977.

[Aki84]   **Akiyama H., Hawkins N. M.**, *Response of flat plate concrete structures to seismic and wind forces*, Structures and Mechanics Report SM84-1, Structural and Geotechnical Engineering and Mechanics, Department of Civil Engineering, University of Washington, pp. 1-145, Seattle, Washington, U.S.A., July, 1984.

[Ani70]   **Anis N. N.**, *Shear strength of reinforced concrete flat slabs without shear reinforcement*, Ph.D. Thesis, Imperial College of Science and Technology, 265 p., London, United Kingdom, 1970.

[Ban81]   **Banon H., Biggs J. M., Irvine H. M.**, *Seismic damage in reinforced concrete frames*, Journal of Structural Engineering, ASCE, Vol. 107, No. 9, pp. 1713-1729, Reston, U.S.A., 1981.

[Ban87]   **Banchik C. A.**, *Effective beam width coefficients for equivalent frame analysis of flat-plate structures*, M.Sc. Thesis, University of California at Berkeley, 56 p., California, U.S.A., 1987.

[Ben12]   **Ben-Sasi O. M.**, *Tests of interior flat slab-column connections transferring shear force and moment*, Proceedings of the 37th Conference on Our World in Concrete & Structures, Singapore, August, 2012.

[Bin05]   **Binici B., Bayrak O.**, *Upgrading of slab-column connections using fiber reinforced polymers*, Engineering Structures, Elsevier, Vol. 27, No. 1, pp. 97-107, January, 2005.

[Bro05]   **Broms C. E.**, *Concrete flat slabs and footings: Design method for punching and detailing for ductility*, Ph.D. Thesis, Royal Institute of Technology, 138 p., Stockholm, Sweden, 2005.

[Bro07]   **Broms C. E.**, *Ductility of flat plates: comparison of shear reinforcement systems*, ACI Structural Journal, Vol. 104, No. 6, pp. 703-711, Farmington Hills, U.S.A., November-December, 2007.

[Bro09]   **Broms C. E.**, *Design method for imposed rotations of interior slab-column connections*, ACI Structural Journal, Vol. 106, No. 5, pp. 636-645, Farmington Hills, U.S.A., September-October, 2009.

[Bu08]   **Bu W.**, *Punching shear retrofit method using shear bolts for reinforced concrete slabs under seismic loading*, Ph.D. Thesis, University of Waterloo, 233 p., Waterloo, Canada, 2008.

[Bu09]   **Bu W., Polak M. A.**, *Seismic retrofit of reinforced concrete slab-column connections using shear bolts*, ACI Structural Journal, Vol. 106, No. 4, pp. 514-522, Farmington Hills, U.S.A., 2009.

[Bu11]   **Bu W., Polak M. A.**, *Effect of openings and shear bolt pattern in seismic retrofit of reinforced concrete slab-column connections*, Engineering Structures, Elsevier, Vol. 33, No. 12, pp. 3329-3340, May, 2011.

[Can88]   **Cano M. T., Klingner R. E.**, *Comparison of analysis procedures for two-way slabs*, ACI Structural Journal, Vol. 85, No. 6, pp. 597-608, Detroit, U.S.A., November-December, 1988.

[Cao93]   **Cao H.**, *Seismic design of slab-column connections*, M.Sc. Thesis, University of Calgary, 201 p., Calgary, Canada, 1993.

[Cao11]   **Cao V. V., Ronagh H., Ashraf M., Baji H.**, *A new damage index for reinforced concrete structures subjected to seismic loads*, Proceedings of the 1st International Postgraduate Conference on engineering, designing and developing the built environment for sustainable wellbeing, pp. 194-199, Queensland, Australia, 2011.

[Cho01]   **Choi J. -W., Kim C. -S., Song J. -G., Lee S. -G.**, *Effective beam width coefficients for lateral stiffness in flat-plate structures*, KCI Concrete Journal, Vol. 13, No. 2, pp. 49-57, Korea, July, 2001.

[Cho07]   **Choi M. -S., Cho I. -J., Han B. -S., Ahn J. -M., Shin S. -W.**, *Experimental study of interior slab-column connections subjected to vertical shear and cyclic moment transfer*, Key Engineering Materials, Vols. 348-349, pp. 641-644, Switzerland, September, 2007.

[Cho09]   **Cho Y. S.**, *Structural performance of RC flat plate slab shear-reinforced interior connections under lateral loading*, Magazine of Concrete Research, Vol. 61, No. 3, pp. 155-164, London, United Kingdom, 2009.

[Cho09b]   **Choi J. -W., Ali M., Alexander S. D. B.**, *Behavior of slab-column connections with partially debonded reinforcement under lateral loading*, Canadian Journal of Civil Engineering, Vol. 36, No. 3, pp. 463-472, Ottawa, Canada, March, 2009.

[Cho14]   **Choi K. -K., Shin D. -W., Park H. -G.**, *Shear-strength model for slab-column connections subjected to unbalanced moment*, ACI Structural Journal, Vol. 111, No. 3, pp. 491-502, Farmington Hills, U.S.A., May-June, 2014.

[Cho15]   **Choi K. -K., Kim J. -C.**, *Nonlinear model simulating load-deformation relationship of flat plate structures*, Engineering Structures, Elsevier, Vol. 85, pp. 26-35, February, 2015.

[Cor70]   **Corley W. G., Jirsa J. O.**, *Equivalent frame analysis for slab design*, ACI Journal, Vol. 67, No. 11, pp. 875-884, Detroit, U.S.A., 1970.

[CSI14]   **Computers and Structures Inc.**, *Structural Analysis Program (SAP2000) v. 17.0 (Trial)*, Berkeley, U.S.A., 2014.

[DiS60]   **Di Stasio J., Van Buren M. P.**, *Transfer of bending moment between flat plate floor and column*, ACI Journal, Vol. 32 (Proceedings Vol. 57), No. 3, pp. 299-314, Detroit, U.S.A., 1960.

[Dov94]   **Dovich L. M., Wight J. K.**, *Lateral response of nonseismically detailed reinforced concrete slab flat slab structures*, Report No. UMCEE 94-30, Department of Civil and Environmental Engineering, University of Michigan, pp. 1-183, Ann Arbor, Michigan, U.S.A., 1994.

[Dov05]   **Dovich L. M., Wight J. K.**, *Effective slab width model for seismic analysis of flat slab frames*, ACI Structural Journal, Vol. 102, No. 6, pp. 868-875, Farmington Hills, U.S.A., November-December, 2005.

[Dra14]   **Drakatos I. S., Muttoni A., Beyer K.**, *Mechanical model for flexural behaviour of slab-column connections under seismically induced deformations*, Proceedings of the 4th International fib Congress, 8p., Mumbai, India, 2014.

[Dra15]   **Drakatos I. S., Muttoni A., Beyer K.**, *Seismic behaviour of flat slabs*, Research Report CemSuisse 201201, EPFL - IBETON - EESD, 48p., Lausanne, Switzerland, 2015.

[Dra16]   **Drakatos I. S., Muttoni A., Beyer K.**, *Internal slab-column connections under monotonic and cyclic imposed rotations*, Engineering Structures, Elsevier, Vol. 123, pp. 501-516, September, 2016.

[Dur95]   **Durrani A. J., Du Y., Luo Y. H.**, *Seismic resistance of nonductile slab-column connections in existing flat-slab buildings*, ACI Structural Journal, Vol. 92, No. 4, pp. 479-487, Detroit, U.S.A., July-August, 1995.

[Ede10]   **Eder M. A., Vollum R. L., Elghazouli A. Y., Abdel-Fattah T.**, *Modelling and experimental assessment of punching shear in flat slabs with shearheads*, Engineering Structures, Elsevier, Vol. 32, No. 12, pp. 3911-3924, December, 2010.

[Ein15]   **Einpaul J., Fernández Ruiz M., Muttoni A.**, *Influence of moment redistribution and compressive membrane action on punching strength of flat slabs*, Engineering Structures, Elsevier, Vol. 86, No. 1, pp. 43-57, March, 2015.

[Elg87]   **Elgabry A. A., Ghali A.**, *Tests on concrete slab-column connections with stud-shear reinforcement subjected to shear-moment transfer*, ACI Journal, Vol. 84, No. 5, pp. 433-442, Detroit, U.S.A., September-October, 1987.

[Els56]   **Elstner R. C., Hognestad E.**, *Shearing strength of reinforced concrete slabs*, ACI Journal, Vol. 53, No. 2, pp. 29-58, Detroit, U.S.A., February, 1956.

[Eur04]   **Eurocode 2**, *Design of concrete structures, part 1-1 : General rules and rules for buildings*, CEN, EN 1992-1-1, 225 p., Brussels, Belgium, April, 2004.

[Far09]   **Fardis M. N.**, *Seismic design, assessment and retrofitting of concrete buildings: based on EN-Eurocode 8*, Springer, Dordrecht, The Netherlands, 2009.

[Far92a]   **Farhey D. N., Yankelevsky D. Z., Adin M. A.**, *Analysis of lateral load transfer by internal slab-column joints*, Engineering Structures, Elsevier, Vol. 14, No. 6, pp. 379-394, January, 1992.

[Far92b]   **Farhey D. N., Adin M. A., Yankelevsky D. Z.**, *RC flat slab-column frame connections: analytical modelling*, Proceedings of the 10th World Conference in Earthquake Engineering, pp. 4001-4006, Rotterdam, Netherlands, 1992.

[Far93]   **Farhey D. N., Adin M. A., Yankelevsky D. Z.**, *RC flat slab-column subassemblages under lateral loading*, Journal of Structural Engineering, ASCE, Vol. 119, No. 8, pp. 1903-1916, Reston, U.S.A., June, 1993.

[Fib11]   **FIB**, fib Model Code for Concrete Structures 2010, fib, 434 p., Ernst & Sohn, Berlin, Germany, 2013.

[Fic08]   **Fick D. R.**, *Experimental investigation of a full-scale flat-plate reinforced concrete structure subjected to cyclic lateral loading in the inelastic range of response*, Ph.D. Thesis, University of Purdue, 188 p., Indiana, U.S.A., 2008.

[Gay08]   **Gayed R. B., Ghali A.**, *Unbalanced moment resistance in slab-column joints: Analytical assessment*, Journal of Structural Engineering, ASCE, Vol. 134, No. 5, pp. 859-864, Reston, U.S.A., May, 2008.

[Gha74]   **Ghali A., Sargious M. A., Huizer A.**, *Vertical prestressing of flat plates around columns*, ACI Publication SP-42, Vol. 2, pp. 905-920, Detroit, U.S.A., 1974.

[Gha76]   **Ghali A., Elmasri M. Z., Dilger W.**, *Punching of flat plates under static and dynamic horizontal forces*, ACI Journal, Vol. 73, No. 10, pp. 566-572, Detroit, U.S.A., October, 1976.

[Gha12]   **Ghali A., Gayed R. B.**, *Lateral stiffness of flat-plate buildings: punching shear consideration*, Canadian Journal of Civil Engineering, Vol. 39, No. 5, pp. 536-545, Ottawa, Canada, April, 2012.

[Gos77]   **Gosain N. K., Brown R. H., Jirsa J. O.**, *Shear requirements for load reversals on RC members*, Journal of Structural Engineering, ASCE, Vol. 103, No. 7, pp. 1461-1476, Reston, U.S.A., July, 1977.

[Gro97]   **Grossman J. S.**, *Verification of proposed design methodies for effective width of slabs in slab-column frames*, ACI Structural Journal, Vol. 94, No. 2, pp. 181-195, Farmington Hills, U.S.A., March-April, 1997.

[Gru01]   **Gruttmann F., Wagner W.**, *Shear correction factors in Timoshenko's beam theory for arbitrary shaped cross-sections*, Computational Mechanics, Springer, Vol. 27, No. 3, pp. 199-207, March, 2001.

[Han68]   **Hanson N. W., Hanson J. M.**, *Shear and moment transfer between concrete slabs and columns*, Journal of the Portland Cement Association, Research and Development Laboratories, Vol. 10, No. 1, pp. 2-16, Skokie, U.S.A., January, 1968.

[Han09]   **Han S. -W., Park Y. -M., Kee S. -H.**, *Stiffness reduction factor for flat slab structures under lateral loads*, Journal of Structural Engineering, ASCE, Vol. 135, No. 6, pp. 743-750, Reston, U.S.A., June, 2009.

[Haw74]   **Hawkins N. M., Mitchell D., Sheu M. S.**, *Cyclic behavior of six reinforced concrete slab-column specimens transferring moment and shear*, Progress Report GI-38717, Division of Structures and Mechanics, Department of Civil Engineering, University of Washington, pp. 1-143, Seattle, Washington, U.S.A., September, 1974.

[Haw89]   **Hawkins N. M., Bao A., Yamazaki J.**, *Moment transfer from concrete slabs to columns*, ACI Structural Journal, Vol. 86, No. 6, pp. 705-716, Detroit, U.S.A., November-December, 1989.

[Hue99]   **Hueste M. B. D., Wight J. K.**, *Nonlinear punching shear failure model for interior slab-colmn connections*, Journal of Structural Engineering, ASCE, Vol. 125, No. 9, pp. 997-1008, Reston, U.S.A., September, 1999.

[Hue07]   **Hueste M. B. D., Browning J., Lepage A., Wallace J. W.**, *Seismic design criteria for slab-column connections*, ACI Structural Journal, Vol. 104, No. 4, pp. 448-458, Farmington Hills, U.S.A., July-August, 2007.

[Hwa93]   **Hwang S. -J., Moehle J. P.**, *An experimental study of flat-plate structures under vertical and lateral loads*, Report UCB/EERC 93/03, Earthquake Engineering Research Center, College of Engineering, University of California, pp. 1-278, Berkeley, California, U.S.A., February, 1993.

[Hwa00]   **Hwang S. -J., Moehle J. P.**, *Models for laterally loaded slab-column frames*, ACI Structural Journal, Vol. 97, No. 2, pp. 345-353, Farmington Hills, U.S.A., March-April, 2000.

[Isl76]   **Islam S., Park R.**, *Tests on slab-column connections with shear and unbalanced flexure*, Journal of the Structural Division, Proceedings of ASCE, Vol. 102, No. ST3, pp. 549-568, U.S.A., March, 1976.

[Kab84]   **Kaba S. A., Mahin S. A.**, *Refined modelling of reinforced concrete columns for seismic analysis*, Report UCB/EERC 84/03, Earthquake Engineering Research Center, College of Engineering, University of California, pp. 1-104, Berkeley, California, U.S.A., 1984.

[Kam90]   **Kamaraldin K.**, *Punching shear and moment trasfer in reinforced concrete flat slabs*, Ph.D. Thesis, The Polytechnic of Central London, 287 p., London, United Kingdom, 1990.

[Kan75]   **Kanoh Y., Yoshizaki S.**, *Experiments on slab-column and slab-wall connections of flat plate structures*, Concrete Journal, Japan Concrete Institute, Vol. 13, pp. 7-19, Tokyo, Japan, June, 1975.

[Kan79]   **Kanoh Y., Yoshizaki S.**, *Strength of slab-column connections transferring shear and moment*, ACI Journal, Vol. 76, No. 2, pp. 461-478, Detroit, U.S.A., March-April, 1979.

[Kan04]   **Kang T. H. -K.**, *Shake table tests and analytical studies of reinforced and post-tensioned concrete flat plate frames*, Ph.D. Thesis, University of California, Los Angeles, U.S.A., 2004.

[Kan08]   **Kang T. H. -K., Wallace J. W.**, *Seismic performance of reinforced concrete slab-column connections with thin plate stirrups*, ACI Structural Journal, Vol. 105, No. 5, pp. 617-625, Farmington Hills, U.S.A., September-October, 2008.

[Kan09]   **Kang T. H. -K., Wallace J. W., Elwood, K. J.**, *Nonlinear modeling of flat-plate systems*, Journal of Structural Engineering, ASCE, Vol. 135, No. 2, pp. 147-158, Reston, U.S.A., February, 2009.

[Ken69]   **Kent D. C.**, *Inelastic behaviour of reinforced concrete members with cyclic loading*, Ph.D. Thesis, University of Canterbury, Christchurch, New Zealand, 1969.

[Kin60]   **Kinnunen S., Nylander H.**, *Punching of concrete slabs without shear reinforcement*, Transactions of the Royal Institute of Technology, No. 158, 112 p., Stockholm, Sweden, 1960.

[Kru99]   **Krüger G.**, *Eccentric punching resistance of flat slabs*, Ph.D. Thesis, No. 2064, EPFL, 191 p., Lausanne, Switzerland, 1999 (in French).

[Luo95]   **Luo Y. H., Durrani A. J.**, *Equivalent beam model for flat-slab buildings - Part I: Interior connections*, ACI Structural Journal, Vol. 92, No. 1, pp. 115-124, Detroit, U.S.A., January-February, 1995.

[Ma76]   **Ma S. -Y. M., Bertero V. V., Popov E. P.**, *Experimental and analytical studies on the hysteretic behavior of reinforced concrete rectangular and T-beams*, Report EERC 76-2, Earthquake Engineering Research Center, College of Engineering, University of California, pp. 1-255, Berkeley, California, U.S.A., May, 1976.

[Man88]   **Mander J. B., Priestley M. J. N., Park R.**, *Theoretical stress-strain model for confined concrete*, Journal of Structural Engineering, ASCE, Vol. 114, No. 8, pp. 1804-1826, Reston, U.S.A., August, 1988.

[Mar96]   **Marzouk H., Emam M., Hilal M. S.**, *Effect of high-strength concrete columns on the behavior of slab-column connections*, ACI Structural Journal, Vol. 93, No. 5, pp. 545-552, Detroit, U.S.A., September-October, 1996.

[Mas70]   **Mast P. E.**, *Stresses in flat plates near columns*, ACI Journal Proceedings, Vol. 67, No. 10, pp. 761-768, Farmington Hills, U.S.A., October, 1970.

[Meg00]   **Megally S., Ghali A.**, *Punching of concrete slabs due to column moment transfer*, Journal of Structural Engineering, ASCE, Vol. 126, No. 2, pp. 180-189, Reston, U.S.A., February, 2000.

[Meg00a]   **Megally S., Ghali A.**, *Punching shear design of earthquake-resistant slab-column connections*, ACI Structural Journal, Vol. 97, No. 5, pp. 720-730, Farmington Hills, U.S.A., September-October, 2000.

[Mer14]   **Mergos P. E., Beyer K.**, *Loading protocols for European regions of low to moderate seismicity*, Bulletin of Earthquake Engineering, Vol. 12, No. 6, pp. 2507-2530, March, 2014.

[Mat15]   **Matzke E. M., Lequesne R. D., Parra-Montesinos G. J., Shield C. K.**, *Behavior of biaxially loaded slab-column connections with shear studs*, ACI Structural Journal, Vol. 112, No. 3, pp. 335-346, Farmington Hills, U.S.A., May-June, 2015.

[Moe61]   **Moe J.**, *Shearing strength of reinforced concrete slabs and footings under concentrated loads*, Bulletin D46, Portland Cement Association, Research and Development Laboratories, 135 p., Skokie, U.S.A., 1961.

[Moe84]   **Moehle J. P., Diebold J. W.**, *Experimental study of the seismic response of a two-story flat-plate structure*, Report UCB/EERC 84/08, Earthquake Engineering Research Center, College of Engineering, University of California, pp. 1-264, Berkeley, California, U.S.A., August, 1984.

[Moe85]   **Moehle J. P., Diebold J. W.**, *Lateral load response of flat-plate frame*, Journal of Structural Engineering, ASCE, Vol. 111, No. 10, pp. 2149-2164, Reston, U.S.A., October, 1985.

[Mor83] **Morrison D. G., Hirasawa I., Sozen M. A.**, *Lateral-load tests of R/C slab-column connections*, Journal of Structural Engineering, ASCE, Vol. 109, No. 11, pp. 2698-2714, Reston, U.S.A., November, 1983.

[Mut08] **Muttoni A.**, *Punching shear strength of reinforced concrete slabs without transverse reinforcement*, ACI Structural Journal, Vol. 105, No. 4, pp. 440-450, Farmington Hills, U.S.A., July-August, 2008.

[Mut13] **Muttoni A., Fernández Ruiz M., Bentz E. C., Foster S. J., Sigrist V.**, *Background to the Model Code 2010 Shear Provisions – Part II Punching Shear*, Structural Concrete, Vol. 14, No. 3, pp. 195-203, Farmington Hills, U.S.A., July-August, 2013.

[Nar71] **Narasimhan N.**, *Shear reinforcement in reinforced concrete column heads*, Ph.D. Thesis, Imperial College of Science and Technology, 268 p., London, United Kingdom, 1971.

[Ozc89] **Ozcebe G., Saatcioglu M.**, *Hysteretic shear model for reinforced concrete members*, Journal of Structural Engineering, ASCE, Vol. 115, No. 1, pp. 132-148, Reston, U.S.A., January, 1989.

[Pan88] **Pan A. D., Moehle J. P.**, *Reinforced concrete flat plates under lateral loading: An experimental study including biaxial effects*, Report UCB/EERC 88/16, Earthquake Engineering Research Center, University of California at Berkeley, pp. 1-285, Berkeley, California, U.S.A., October, 1988.

[Pan89] **Pan A. D., Moehle J. P.**, *Lateral displacement ductility of reinforced concrete flat plates*, ACI Structural Journal, Vol. 86, No. 3, pp. 250-258, Detroit, U.S.A., May-June, 1989.

[Pan92] **Pan A. D., Moehle J. P.**, *An experimental study of slab-column connections*, ACI Structural Journal, Vol. 89, No. 6, pp. 626-638, Detroit, U.S.A., November-December, 1992.

[Par75] **Park R., Paulay T.**, *Reinforced concrete structures*, John Wiley, New York, U.S.A., 1975.

[Par76] **Park R., Islam S.**, *Strength of slab-column connections with shear and unbalanced moment*, Journal of the Structural Division, Proceedings of ASCE, Vol. 102, No. ST9, pp. 1879-1901, U.S.A., September, 1976.

[Par85a] **Park Y. -J., Ang A. H. -S.**, *Mechanistic seismic damage model for reinforced concrete*, Journal of Structural Engineering, ASCE, Vol. 111, No. 4, pp. 722-739, Reston, U.S.A., April, 1985.

[Par85b] **Park Y. -J., Ang A. H. -S., Wen Y. K.**, *Seismic damage analysis of reinforced concrete buildings*, Journal of Structural Engineering, ASCE, Vol. 111, No. 4, pp. 740-757, Reston, U.S.A., April, 1985.

[Par86] **Park R.**, *Ductile design approach for reinforced concrete frames*, Earthquake Spectra, Vol. 2, No. 3, pp. 565-619, Oakland, U.S.A., May, 1986.

[Par06] **Park H., Choi K.**, *Improved strength model for interior flat plate-column connections subject to unbalanced moment*, Journal of Structural Engineering, ASCE, Vol. 132, No. 5, pp. 694-704, Reston, U.S.A., May, 2006.

[Par06b] **Park H., Choi K., Wight J. K.**, *Strain-based shear strength model for slender beams without web reinforcement*, ACI Structural Journal, Vol. 103, No. 6, pp. 783-793, Farmington Hills, U.S.A., November-December, 2006.

[Par07]   **Park Y. -M., Han S. -W., Ryu J. -H.**, *Comparison of seismic behaviors of interior joints on PT and RC flat plate systems*, Key Engineering Materials, Vols. 348-349, pp. 741-745, Switzerland, September, 2007.

[Par09]   **Park Y. -M., Han S. -W., Kee S. -H.**, *A modified equivalent frame method for lateral load analysis*, Magazine of Concrete Research, Vol. 61, No. 5, pp. 359-370, London, United Kingdom, June, 2009.

[Par12]   **Park H. -G., Kim Y. -N., Song J. -G., Kang S. -M.**, *Lattice shear reinforcement for enhancement of slab-column connections*, Journal of Structural Engineering, ASCE, Vol. 138, No. 3, pp. 425-437, Reston, U.S.A., March, 2012.

[Pec75]   **Pecknold D. A.**, *Slab effective width for equivalent frame analysis*, ACI Journal, Vol. 72, No. 4, pp. 135-137, Detroit, U.S.A., 1975.

[Pen93]   **Penzien J.**, *Seismic design criteria for transportation structures*, Structural engineering in natural hazards mitigation: Proceedings of the ASCE Structures Congress 1993, pp. 4-36, Irvine, California, 1993.

[Pri07]   **Priestley M. J. N., Calvi G. M., Kowalsky M. J.**, *Displacement-based seismic design of structures*, IUSS Press, Pavia, Italy, 2007.

[Puj10]   **Pujol S., Fick D. R.**, *The test of a full-scale RC structure with masonry infill walls*, Engineering Structures, Elsevier, Vol. 32, No. 10, pp. 3112-3121, July, 2010.

[Rha14]   **Rha C., Kang T. H. -K., Shin M., Yoon J. B.**, *Gravity and lateral load-carrying capacities of reinforced concrete flat plate systems*, ACI Structural Journal, Vol. 111, No. 4, pp. 753-764, Farmington Hills, U.S.A., July-August, 2014.

[Rob92]   **Robertson I. N., Durrani A. J.**, *Gravity load effect on seismic behaviour of interior slab-column connections*, ACI Structural Journal, Vol. 89, No. 1, pp. 37-45, Detroit, U.S.A., January-February, 1992.

[Rob97]   **Robertson I. N.**, *Analysis of flat slab structures subjected to combined lateral and gravity loads*, ACI Structural Journal, Vol. 94, No. 6, pp. 723-729, Farmington Hills, U.S.A., November-December, 1997.

[Rob02]   **Robertson I. N., Kawai T., Lee J., Enomoto B.**, *Cyclic testing of slab-column connections with shear reinforcement*, ACI Structural Journal, Vol. 99, No. 5, pp. 605-613, Farmington Hills, U.S.A., September-October, 2002.

[Rob06]   **Robertson I. N., Johnson G.**, *Cyclic lateral loading of nonductile slab-column connections*, ACI Structural Journal, Vol. 103, No. 3, pp. 356-364, Farmington Hills, U.S.A., May-June, 2006.

[Rou87]   **Roufaiel M. S. L., Meyer C.**, *Analytical modelling of hysteretic behaviour of R/C frames*, Journal of Structural Engineering, ASCE, Vol. 113, No. 3, pp. 429-444, Reston, U.S.A., March, 1987.

[Sag11]   **Sagaseta J., Muttoni A., Fernández Ruiz M., Tassinari L.**, *Non-axis-symmetrical punching shear around internal columns of RC slabs without transverse reinforcement*, Magazine of Concrete Research, Vol. 63, No. 6, pp. 441-457, London, United Kingdom, September, 2011.

[Sed14]   **Sedili I.**, *Seismic assessment of reinforced concrete buildings with slab-column connections*, M.Sc. Thesis, EPFL, 136 p., Lausanne, Switzerland, 2014 (in French).

[Sei12]   **SeismoSoft - Earthquake engineering software solutions**, *SeismoStruct v. 7.0.2 (Trial) – A computer program for static and dynamic nonlinear analysis of framed structures*, Pavia, Italy, 2012.

[Shi10]   **Shin M., Kang T. H. -K., Grossman J. S.**, *Practical modelling of high-rise dual systems with reinforced concrete slab-column frames*, The Structural Design of Tall and Special Buildings, John Wiley, Vol. 19, No. 7, pp. 728-749, November, 2010.

[Sta74]   **Stamenkovic A., Chapman J. C.**, *Local strength at column heads in flat slabs subjected to a combined vertical and horizontal loading*, Institution of Civil Engineers Proceedings, Vol. 57, No. 2, pp. 205-232, London, United Kingdom, June, 1974.

[Sta05]   **Stark A., Binici B., Bayrak O.**, *Seismic upgrade of reinforced concrete slab-column connections using carbon fiber-reinforced polymers*, ACI Structural Journal, Vol. 102, No. 2, pp. 324-333, Farmington Hills, U.S.A., March-April, 2005.

[Sym76]   **Symonds D. W., Mitchell D., Hawkins N. M.**, *Slab-column connections subjected to high intensity shears and transferring reversed moments*, Report SM 76-2, Division of Structures and Mechanics, Department of Civil Engineering, University of Washington, pp. 1-98, Seattle, Washington, U.S.A., October, 1976.

[Tak70]   **Takeda T., Sozen M. A., Nielsen N. N.**, *Reinforced concrete response to simulated earthquakes*, Journal of the Structural Division, ASCE, Vol. 96, No. ST12, pp. 2557-2573, Reston, U.S.A., 1970.

[Tia07]   **Tian Y.**, *Behavior and modeling of reinforced concrete slab-column connections*, Ph.D. Thesis, University of Texas at Austin, 230 p., Austin, U.S.A., 2007.

[Tia08]   **Tian Y., Jirsa J. O., Bayrak O., Widianto, Argudo J. F.**, *Behaviour of slab-column connections of existing flat-plate structures*, ACI Structural Journal, Vol. 105, No. 5, pp. 561-569, Farmington Hills, U.S.A., September-October, 2008.

[Tia09]   **Tian Y., Jirsa J. O., Bayrak O.**, *Nonlinear modeling of slab-column connections under cyclic loading*, ACI Structural Journal, Vol. 106, No. 1, pp. 30-38, Farmington Hills, U.S.A., January-February, 2009.

[Tou83]   **Toussi S., Yao J. T. P.**, *Hysteresis identification of existing structures*, Journal of Engineering Mechanics, ASCE, Vol. 109, No. 5, pp. 1189-1203, Reston, U.S.A., October, 1983.

[Van83]   **Vanderbilt M. D., Corley W. G.**, *Frame analysis of concrete buildings*, Concrete International, Vol. 5, No. 12, pp. 33-43, December, 1983.

[Vaz07]   **Vaz Rodriguez R.**, *Shear strength of reinforced concrete bridge deck slabs*, Ph.D. Thesis, No. 3739, EPFL, 114 p., Lausanne, Switzerland, 2007.

[Vec86]   **Vecchio F. J., Collins M. P.**, *The modified compression-field theory for reinforced concrete elements subjected to shear*, ACI Journal, Vol. 83, No. 2, pp. 219-231, Detroit, U.S.A., March-April, 1986.

[Vec99]   **Vecchio F. J.**, *Towards cyclic load modeling of reinforced concrete*, ACI Structural Journal, Vol. 96, No. 2, pp. 132-142, Farmington Hills, U.S.A., March-April, 1999.

[Wes21]   **Westergaard H. M., Slater W. A.**, *Moments and stresses in slabs*, ACI Journal, Vol. 17, pp. 415-538, Detroit, U.S.A., 1921.

[Wey92]   **Wey E. H., Durrani A. J.**, *Seismic response of interior slab-column connections with shear capitals*, ACI Structural Journal, Vol. 89, No. 6, pp. 682-691, Detroit, U.S.A., November-December, 1992.

[Wil95]   **Williams M. S., Sexsmith R. G.**, *Seismic damage indices for concrete structures: a state-of-the-art review*, Earthquake Spectra, Vol. 11, No. 2, pp. 319-349, Oakland, U.S.A., May, 1995.

[Zee84]   **Zee H. L., Moehle J. P.**, *Behavior of interior and exterior flat plate connections subjected to inelastic load reversals*, Report UCB/EERC 84/07, Earthquake Engineering Research Center, College of Engineering, University of California, pp. 1-145, Berkeley, California, U.S.A., August, 1984.

Appendices

Appendix A

Test database

This Appendix presents the test database used for validation purposes of the proposed analytical model (Chapters 4 and 5). The slabs tested in the framework of this thesis are also included in the foloowing tables.

Table A.1 – Summary of properties and results of interior slab-column specimens tested under constant vertical load and monotonically increasing unbalanced moment

Source	Mark	c [mm]	h [mm]	d [mm]	B [m]	f_c [MPa]	d_g [mm]	f_y [MPa]	ρ [%]	ρ' [%]	v [$\sqrt{MPa}$]	M_{exp} [kNm]	ψ_{scc} [%]
[Gha74]	B3NP	305	152	114	1.81	23.7	16.0	345	1.39	1.39	0.114	162.0	-
	B5NP	305	152	114	1.81	28.3	16.0	345	1.39	1.39	0.104	196.0	-
[Sta74]	C/I/1	127	76	56	0.87	36.0	9.5	434	1.17	1.17	0.111	7.3	-
	C/I/2	127	76	56	0.87	29.7	9.5	434	1.17	1.17	0.376	10.5	-
	C/I/3	127	76	56	0.87	25.9	9.5	434	1.17	1.17	0.308	13.6	-
	C/I/4	127	76	56	0.87	25.4	9.5	434	1.17	1.17	0.174	16.7	-
[Gha76]	SM0.5	305	152	120	1.83	36.8	16.0	476	0.53	0.18	0.111	100.0	3.60
	SM1.0	305	152	120	1.83	33.4	16.0	476	1.00	0.33	0.116	126.0	2.63
	SM1.5	305	152	120	1.83	39.9	16.0	476	1.35	0.39	0.117	132.0	2.10
[Isl76]	IP1	229	89	70	2.24	27.3	6.0	356	0.83	0.43	0.092	30.5	3.62
	IP2	229	89	70	2.24	31.9	6.0	374	0.83	0.43	0.085	37.7	3.97
[Elg87]	1	250	152	123	1.80	35.0	16.0	452	1.30	0.43	0.149	130.0	1.66†
Test campaign	PD1	390	250	204	3.00	37.9	16.0	559	0.79	0.35	0.091	526.0	1.66*
	PD3	390	250	198	3.00	34.9	16.0	558	0.81	0.34	0.281	200.0	0.45
	PD4	390	250	201	3.00	39.0	16.0	507	0.80	0.35	0.136	527.0	2.01
	PD5	390	250	198	3.00	37.5	16.0	507	0.81	0.35	0.181	461.0	2.19
	PD10	390	250	197	3.00	32.3	16.0	593	1.60	0.72	0.307	290.0	0.49
	PD12	390	250	194	3.00	35.5	16.0	546	1.61	0.72	0.176	469.0	1.21

† ψ_{max} at $0.83 M_{exp}$
* inconsistent rotation measurement

Table A.2 – Summary of properties and results of interior slab-column specimens tested under constant eccentricity and monotonically increasing unbalanced moment

Source	Mark	c [mm]	h [mm]	d [mm]	B [m]	f_c [MPa]	d_g [mm]	f_y [MPa]	ρ [%]	ρ' [%]	e [mm]	V_{peak} [kN]	$\psi_{max.p}$ [%]
[Els56]	A11	356	152	114	1.83	25.9	25.4	326	2.47	1.15	178	529.0	1.39
	A12	356	152	114	1.83	28.4	25.4	326	2.47	2.47	178	529.0	1.39
[Moe61]	M2	305	152	114	1.83	25.7	9.5	481	1.50	-	196	292.2	-
	M2A	305	152	114	1.83	15.5	9.5	481	1.50	-	185	212.6	-
	M3	305	152	114	1.83	22.8	9.5	481	1.50	-	338	207.3	-
	M4A	305	152	114	1.83	17.7	9.5	481	1.50	-	434	143.7	-
	M6	305	152	114	1.83	26.5	9.5	327	1.34	-	168	239.3	-
	M7	305	152	114	1.83	25.0	9.5	327	1.34	-	61	311.0	-
	M8	305	152	114	1.83	24.6	9.5	327	1.34	0.57	437	149.5	-
	M9	305	152	114	1.83	23.2	9.5	327	1.34	-	127	266.9	-
	M10	305	152	114	1.83	21.1	9.5	327	1.34	0.57	308	177.9	-
[Ani70]	B3	203	102	76	1.47	30.4	9.5	431	2.19	-	94	191.3	-
	B4	203	102	76	1.47	29.8	9.5	431	2.19	-	188	139.7	-
	B5	203	102	76	1.47	29.0	9.5	431	2.19	-	313	125.4	-
	B6	203	102	76	1.47	31.3	9.5	431	2.19	-	464	115.7	-
	B7	203	102	76	1.47	33.8	9.5	431	2.19	-	737	69.8	-
[Nar71]	L1	305	178	143	2.28	33.8	9.5	398	1.11	-	305	399.0	-
[Haw89]	6AH	305	152	121	1.83	31.3	19.0	472	0.60	0.28	535	169.0	5.55
	9.6AH	305	152	118	1.83	30.7	19.0	415	0.79	0.50	522	187.0	4.02
	1.4AH	305	152	114	1.83	30.3	19.0	420	1.26	0.63	489	205.0	3.19
	6AL	305	152	121	1.83	22.7	19.0	472	0.60	0.28	135	244.0	3.19
	9.6AL	305	152	118	1.83	28.9	19.0	415	0.79	0.50	135	257.0	2.64
	1.4AL	305	152	114	1.83	27.0	19.0	420	1.26	0.63	136	319.0	2.22
	7.3BH	305	114	82	1.83	22.2	19.0	472	0.64	0.40	488	80.0	4.16
	9.5BH	305	114	83	1.83	19.8	19.0	472	0.79	0.51	483	94.0	4.72
	14.2BH	305	114	79	1.83	29.5	19.0	415	1.22	0.76	500	102.0	3.19
	7.3BL	305	114	83	1.83	18.1	19.0	472	0.64	0.40	98	130.0	3.89
	9.5BL	305	114	83	1.83	20.0	19.0	472	0.79	0.48	117	142.0	4.16
	14.2BL	305	114	76	1.83	20.5	19.0	415	1.22	0.75	129	162.0	3.47
	6CH	305	152	121	1.83	52.4	19.0	472	0.60	0.28	511	186.0	6.24
	9.6CH	305	152	117	1.83	57.2	19.0	415	0.87	0.50	519	218.0	3.14
	1.4CH	305	152	114	1.83	54.7	19.0	420	1.16	0.63	529	252.0	3.05
	6CL	305	152	121	1.83	49.5	19.0	472	0.60	0.28	135	273.0	4.72
	1.4CL	305	152	114	1.83	47.7	19.0	420	1.16	0.63	136	362.0	2.36
	1.4FH	305	152	114	1.83	31.2	19.0	446	0.90	0.22	498	206.0	2.58
	6FLI	305	152	120	1.83	25.9	19.0	472	0.59	0.27	119	227.0	3.15
	10.2FLI	305	152	114	1.83	18.1	19.0	446	1.13	0.49	112	240.0	1.94
	10.2FLO	305	152	114	1.83	26.5	19.0	446	0.77	0.49	121	290.0	2.78
	10.2FHO	305	152	121	1.83	33.8	19.0	446	0.77	0.49	491	183.0	3.05
[Kam90]	SA1	150	80	64	2.00	33.0	10.0	640	0.55	0.55	52	109.0	-
	SA3	150	80	64	2.00	36.0	10.0	640	0.55	0.55	100	85.0	-
	SA4	150	80	64	2.00	32.0	10.0	640	0.55	0.55	336	49.0	-
	SB2	150	80	64	2.00	28.0	10.0	640	1.00	1.00	360	61.0	-
[Mar96]	NHLS0.5	250	150	119	1.87	43.2	19.0	450	0.50	0.28	167	266.2	-
	NHLS1.0	250	150	119	1.87	42.7	19.0	450	1.00	0.38	130	408.2	-
	NNHS1.0	250	150	119	1.87	36.2	19.0	450	1.00	0.38	720	163.6	-
	NHHS0.5	250	150	119	1.87	34.0	19.0	450	0.50	0.28	595	164.3	-
	NHHS1.0	250	150	119	1.87	35.3	19.0	450	1.00	0.38	464	250.3	-
[Kru99]	P16A	300	150	121	3.00	38.6	16.0	460	1.00	-	160	332.0	1.26*
	P32	300	150	121	3.00	30.4	16.0	460	1.00	-	320	270.0	0.93*
[Bin05]	CE	150	75	57	1.02	24.1	9.5	455	1.38	0.70	150	95.6	2.62
[Ben12]	SI-1	180	80	60	1.00	28.1	12.0	335	1.40	1.40	280	65.0	-
	SI-2	180	80	60	1.00	25.0	12.0	335	1.40	1.40	580	37.5	-

*   minimum slab rotation

Table A.3 – Summary of properties and results of interior slab-column specimens tested under constant vertical load and cyclically increasing unbalanced moment

Source	Mark	c [mm]	h [mm]	d [mm]	B [m]	f_c [MPa]	d_g [mm]	f_y [MPa]	ρ [%]	ρ' [%]	v [$\sqrt{MPa}$]	n_c [-]	M_{exp} [kNm]	ψ_{scc} [%]
[Kan75]	H9	200	100	80	1.80	22.8	9.5	361	0.70	0.70	0.111	5	33.0	2.00
	H10	200	100	80	1.80	22.8	9.5	361	1.12	1.12	0.115	5	36.1	2.00
	H11	200	100	80	1.80	23.2	9.5	361	1.12	1.12	0.227	5	25.2	1.00
[Isl76]	IP3C	229	89	70	2.24	29.7	6.0	316	0.83	0.43	0.087		35.8	3.62
[Mor83]	S5	305	76	61	1.83	34.9	9.5	340	1.03	1.03	0.085	5	36.0	4.70
[Zee84]	INT	137	61	52	1.83	26.2	9.5	470	0.80	0.34	0.138	2	10.3	3.79†
[Pan89]	AP1	274	122	100	3.66	33.3	10.0	472	0.76	0.26	0.125	2	61.8	1.60
	AP3	274	122	100	3.66	31.7	10.0	472	0.76	0.26	0.078	2	95.0	3.14
[Cao93]	CD1	250	150	115	1.90	40.4	20.0	395	1.29	0.49	0.287	1	49.9	0.90
	CD5	250	152	115	1.90	31.2	20.0	395	1.29	0.49	0.228	1	70.5	1.20
	CD8	250	155	115	1.90	27.0	20.0	395	1.29	0.49	0.179	1	85.0	1.30
[Rob02]	1C	254	115	95	3.00	35.4	9.5	420	0.75	0.40	0.088	2	58.5	3.52†
[Sta05]	C-02	305	115	82	2.44	30.9	19.0	454	1.42	0.51	0.205	3	43.1	2.30
[Rob06]	ND1C	254	114	89	3.00	29.6	9.5	525	0.52	0.36	0.083	3	39.3	4.99†
	ND4LL	254	114	89	3.00	32.3	9.5	525	0.52	0.36	0.113	3	43.9	3.00†
	ND5XL	254	114	89	3.00	24.1	9.5	525	0.52	0.36	0.178	3	31.9	2.00†
	ND6HR	254	114	89	3.00	26.3	9.5	525	1.03	0.67	0.111	3	55.1	2.97†
	ND7LR	254	114	89	3.00	18.8	9.5	525	0.45	0.36	0.137	3	30.0	2.99†
[Cho07]	S1	300	120	90	2.40	33.5	16.0	458	1.05	0.60	0.090	2	83.1	3.00
	S2	300	120	90	2.40	41.3	16.0	458	1.05	0.60	0.169	2	67.7	2.91
	S3	300	120	90	2.40	37.8	16.0	458	1.59	0.80	0.093	2	118.5	2.89
[Par07]	RI-50	300	132	116	3.40	32.3	19.0	392	0.78	0.27	0.116	3	127.2	3.47†
[Kan08]	C0	254	152	130	2.90	38.6	9.5	452	0.49	0.11	0.109	1	107.6	2.80
[Tia08]	L0.5	406	152	127	3.86	25.6	9.5	469	0.61	0.25	0.126	3	121.0	1.52
[Bu09]	SW1	200	120	90	1.80	35.0	16.0	520	1.25	0.60	0.172	3	64.7	2.71*
	SW5	200	120	90	1.80	46.0	16.0	520	1.25	0.60	0.233	3	65.1	2.75*
[Cho09]	Control	300	150	125	2.80	34.3	25.0	392	0.90	0.25	0.106	3	105.3	4.44†
[Cho09b]	SPB	355	152	121	4.20	34.1	16.0	440	1.27	0.35	0.084	5	137.4	3.68†
[Par12]	RCA	300	135	106	2.70	22.5	9.5	430	1.06	0.79	0.171	3	70.8	1.24
	RCB	300	135	106	2.70	38.7	9.5	430	1.06	0.79	0.157	3	74.0	1.37
Test campaign	PD2	390	250	198	3.00	36.9	16.0	558	0.81	0.34	0.287	2	196.0	0.36
	PD6	390	250	199	3.00	38.3	16.0	507	0.81	0.30	0.192	2	372.0	0.86
	PD8	390	250	198	3.00	32.7	16.0	575	0.81	0.29	0.152	2	384.0	1.30
	PD11	390	250	194	3.00	33.1	16.0	593	1.60	0.71	0.311	2	286.0	0.43
	PD13	390	250	195	3.00	36.5	16.0	546	1.61	0.72	0.190	2	410.0	0.86

†   vertical load partly applied on the slab specimen for which the drift ratio represents the rotation due to slab deformation ψ_{slab}

*   inconsistently high drift measurement (communication with the authors)

Appendix B

Cracking pattern of the top slab surface

This Appendix presents the cracking pattern of the top slab surface for the tests carried within this thesis (Chapter 3). Cracks shown in black were drawn after the application of vertical loads. Cracks shown in red were caused by the introduction of unbalanced moment and were drawn after the completion of each test.
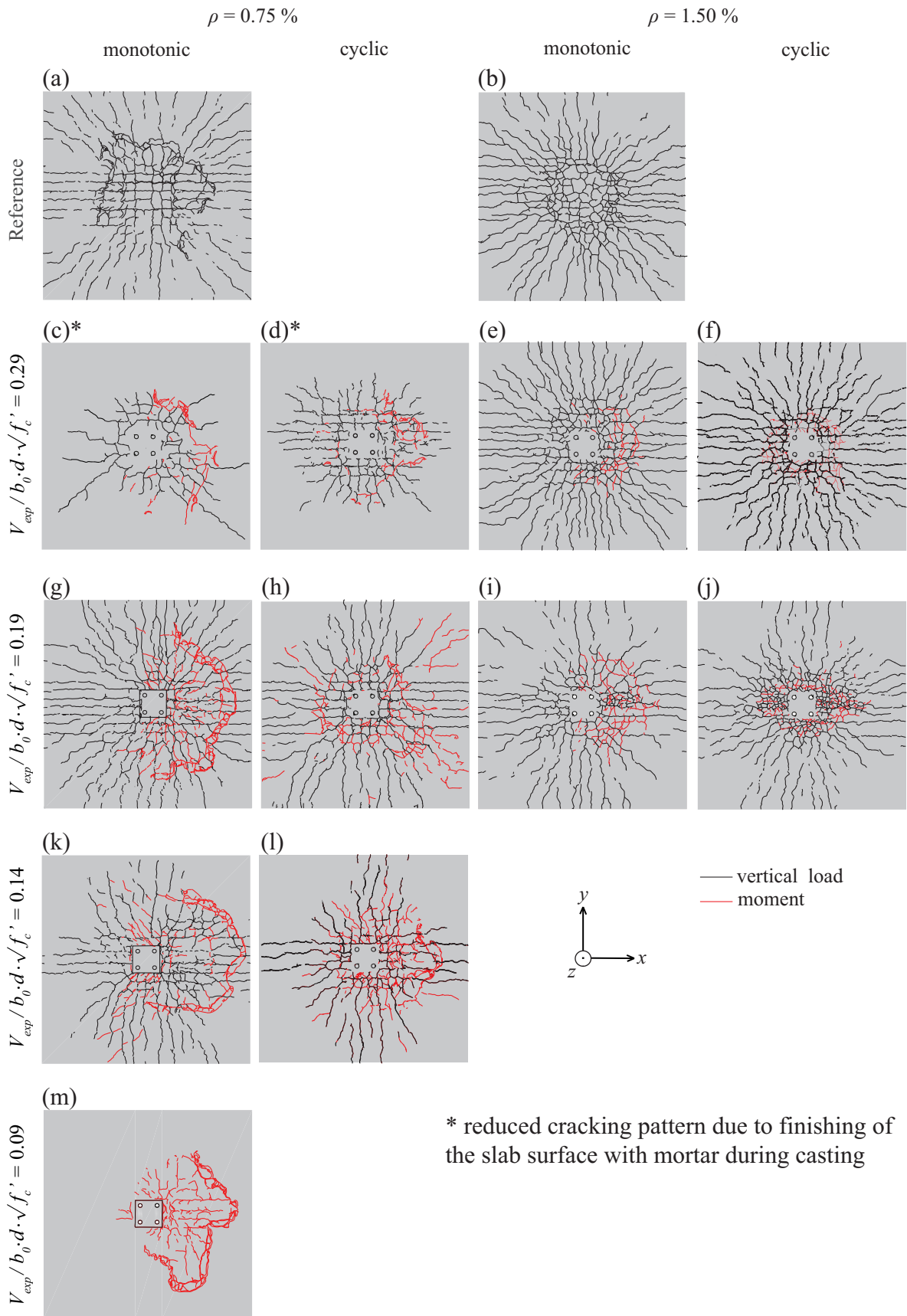
Figure B.1 – Top surface cracking pattern for the tested slabs (Chapter 3) under reducing level of vertical load (vertical axis) and increasing level of flexural reinforcement ratio (horizontal axis).

Appendix C

Moment-rotation relationship evaluation

This Appendix presents the comparison of the analytical model for the moment-rotation relationship (Chapter 4) with experimental moment-rotation curves found in the literature. First, the comparison is presented for quasi-static cyclic tests. Afterwards, the comparison is presented for quasi-static monotonic tests conducted either under constant vertical load or eccentricity.

Circular markers represent the intersection of the monotonic analytical model with the CSCT(mono) failure criterion or the CSCT(cyc) failure criterion, while x markers represent the intersection of the cyclic analytical model with the CSCT(mono) failure criterion or the load step for which $\psi_{max} = \psi_{max.u.mono}$ (i.e. $D(\pi/2) = 1$), whichever comes first.

C.1 Cyclic tests

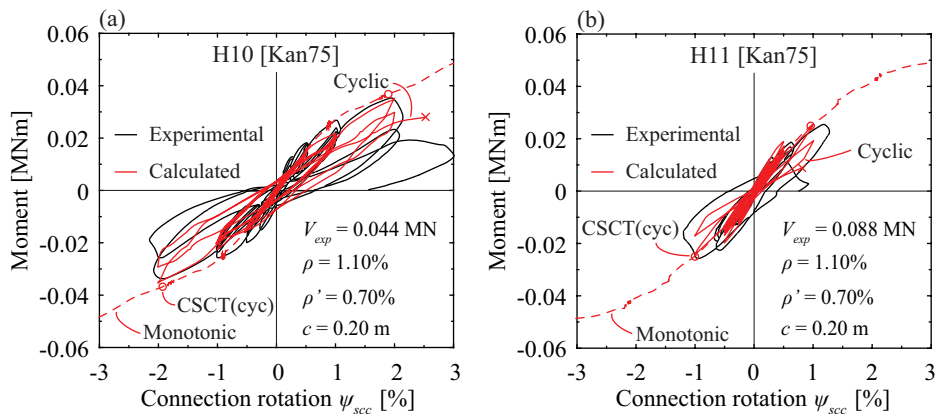**Kanoh and Yoshizaki [Kan75]**

Figure C.1 – Comparison between experimental and calculated moment-connection rotation curves for the isolated specimens tested by Kanoh and Yoshizaki [Kan75]: (a) H10, and (b) H11.
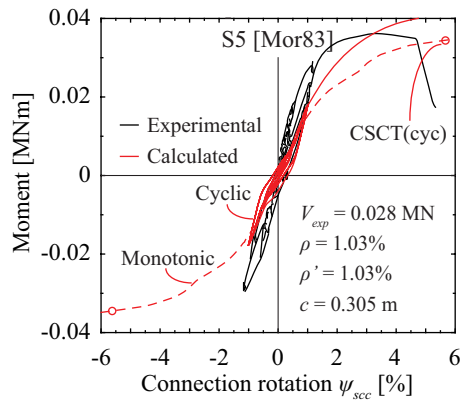
Morrison et al. [Mor83]

Figure C.2 – Comparison between experimental and calculated moment-connection rotation curves for the isolated specimen S5 tested by Morrison et al. [Mor83].
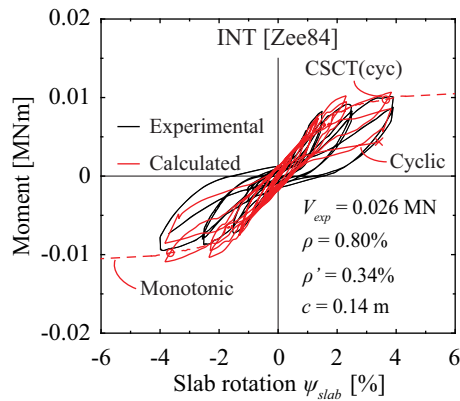
Zee and Moehle [Zee84]

Figure C.3 – Comparison between experimental and calculated moment-connection rotation curves for the isolated specimen INT tested by Zee and Moehle [Zee84].
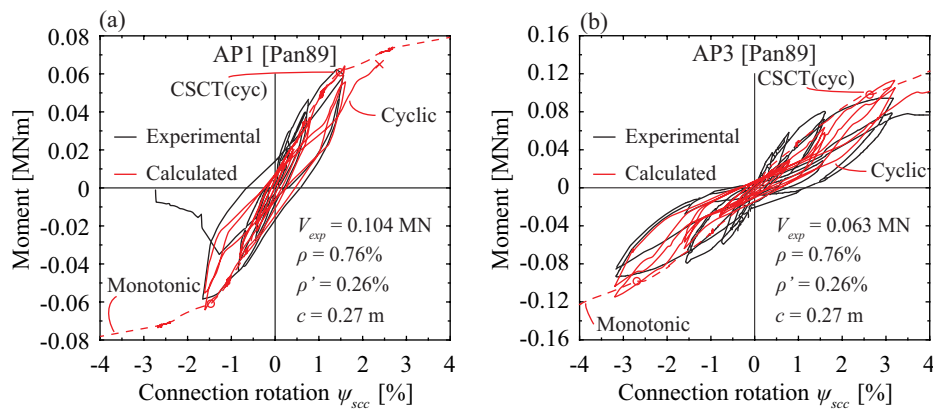
Pan and Moehle [Pan89]

Figure C.4 – Comparison between experimental and calculated moment-connection rotation curves for the isolated specimens tested by Pan and Moehle [Pan89]: (a) AP1, and (b) AP3.

Cao [Cao93]

Figure C.5 – Comparison between experimental and calculated moment-connection rotation curves for the isolated specimens tested by Cao [Cao93]: (a) CD1, (b) CD5, and (b) CD8.

Robertson et al. [Rob02]

Figure C.6 – Comparison between experimental and calculated moment-connection rotation curves for the isolated specimen 1C tested by Robertson et al. [Rob02].

Stark et al. [Sta05]

Figure C.7 – Comparison between experimental and calculated moment-connection rotation curves for the isolated specimen C-02 tested by Stark et al. [Sta05].
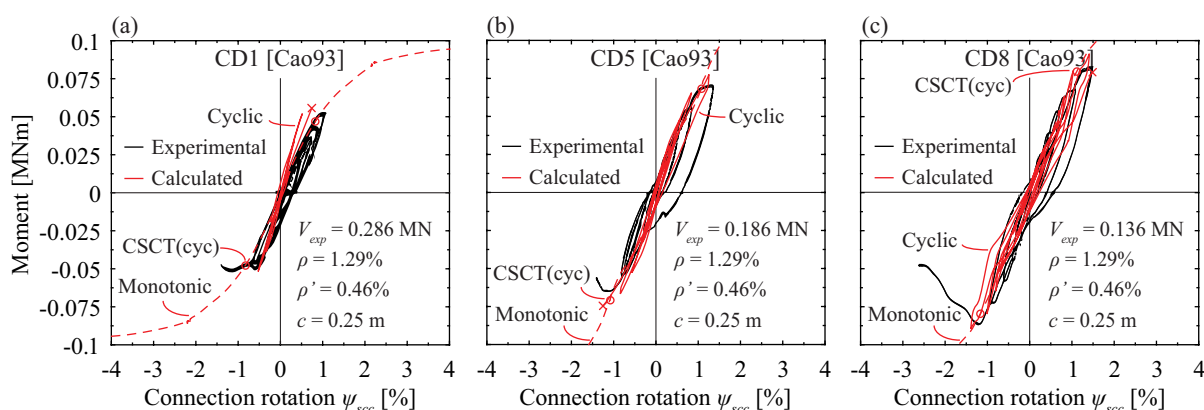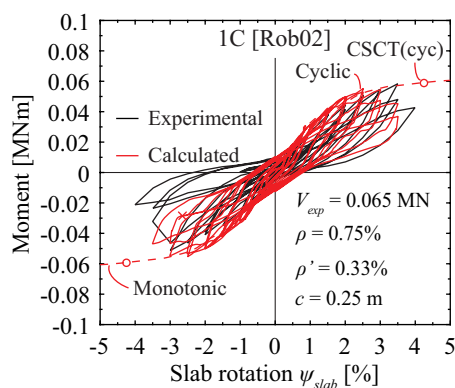
Robertson and Johnson [Rob06]

Figure C.8 – Comparison between experimental and calculated moment-connection rotation curves for the isolated specimens tested by Robertson and Johnson [Rob06]: (a) ND1C, (b) ND4LL, (c) ND5XL, (d) ND6HR, and (e) ND7LR.

Choi et al. [Cho07]

Figure C.9 – Comparison between experimental and calculated moment-connection rotation curves for the isolated specimens tested by Choi et al. [Cho07]: (a) S1, (b) S2, and (c) S3.

Park et al. [Par07]

Figure C.10 – Comparison between experimental and calculated moment-connection rotation curves for the isolated specimen RI-50 tested by Park et al. [Par07].

Kang and Wallace [Kan08]

Figure C.11 – Comparison between experimental and calculated moment-connection rotation curves for the isolated specimen C0 tested by Kang and Wallace [Kan08].
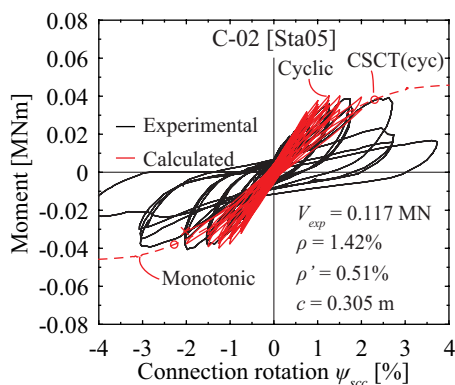
Tian et al. [Tia08]

Figure C.12 – Comparison between experimental and calculated moment-connection rotation curves for the isolated specimen L0.5 tested by Tian et al. [Tia08].
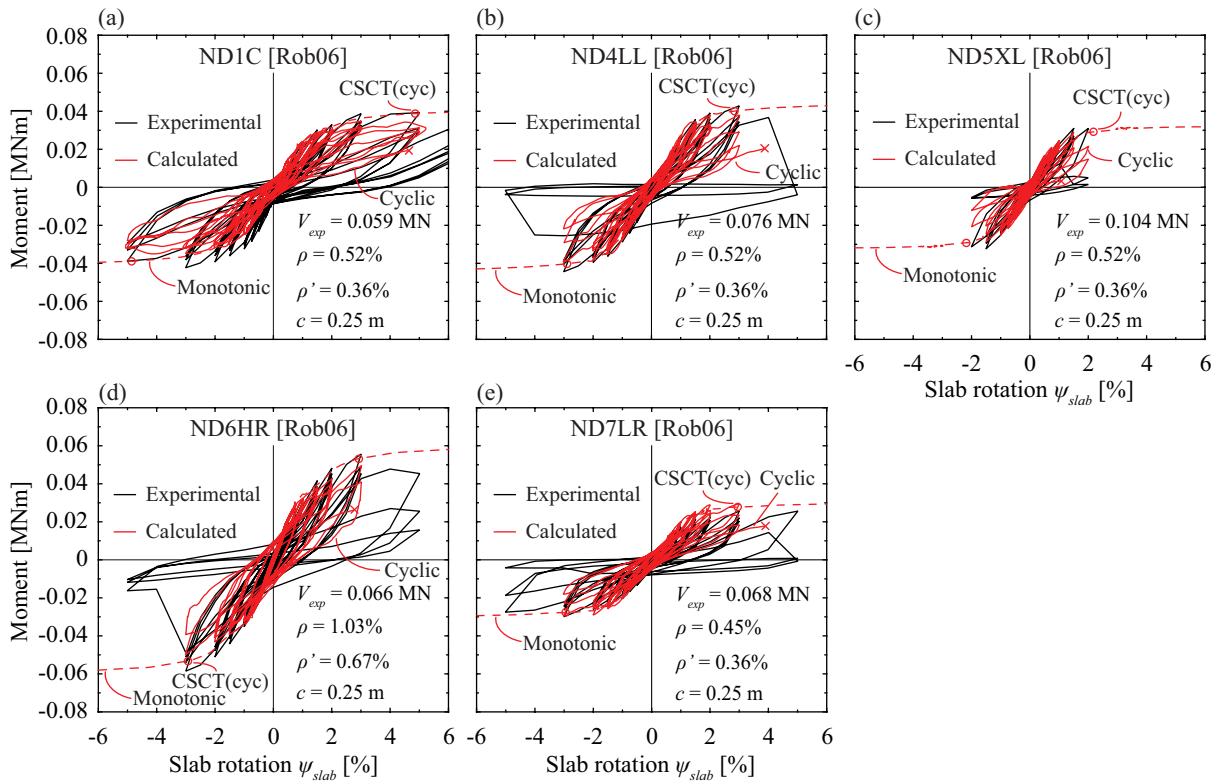
Bu and Polak [Bu09]

Figure C.13 – Comparison between experimental and calculated moment-connection rotation curves for the isolated specimens tested by Bu and Polak [Bu09]: (a) SW1, and (b) SW5.

Cho [Cho09]

Figure C.14 – Comparison between experimental and calculated moment-connection rotation curves for the isolated specimen "Control" tested by Cho [Cho09].
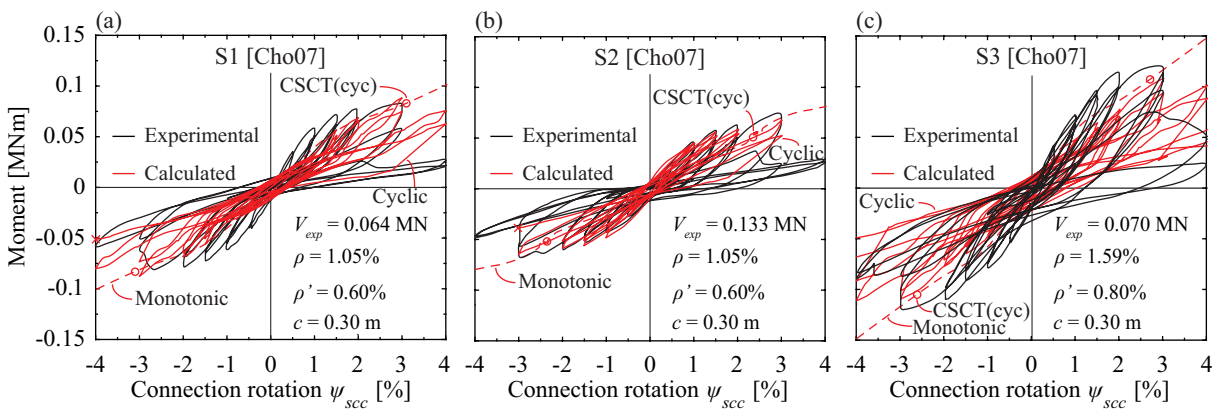
Choi et al. [Cho09b]

Figure C.15 – Comparison between experimental and calculated moment-connection rotation curves for the isolated specimen SPB tested by Choi et al. [Cho09b].
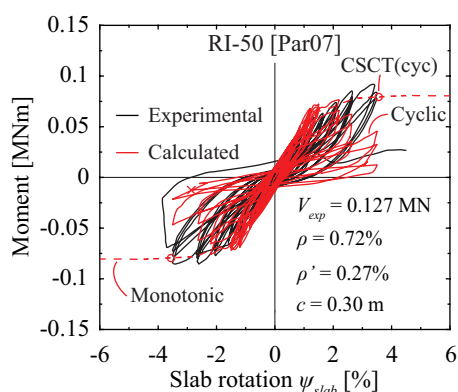
Park et al. [Par12]

Figure C.16 – Comparison between experimental and calculated moment-connection rotation curves for the isolated specimens tested by Park et al. [Par12]: (a) RCA, and (b) RCB.

Test campaign

Figure C.17 – Comparison between experimental and calculated moment-connection rotation curves for the isolated specimens tested within the present research under cyclic conditions: (a) PD2, (b) PD6, (c) PD8, (d) PD11, and (e) PD13.

C.2   Monotonic tests

C.2.1   Constant vertical load

Islam and Park [Isl76]

Figure C.18 – Comparison between experimental and calculated moment-connection rotation curves for the isolated specimen IP2 tested by Islam and Park [Isl76].

Ghali et al. [Gha76]
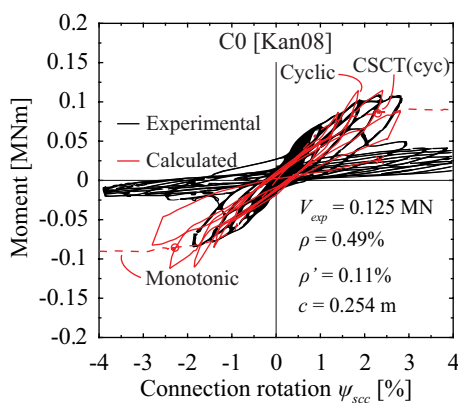

Figure C.19 – Comparison between experimental and calculated moment-connection rotation curves for the isolated specimens tested by Ghali et al. [Gha76]: (a) SM0.5, (b) SM1.0, and (c) SM1.5.

Test campaign

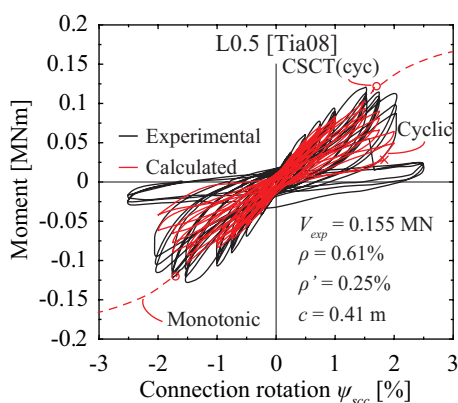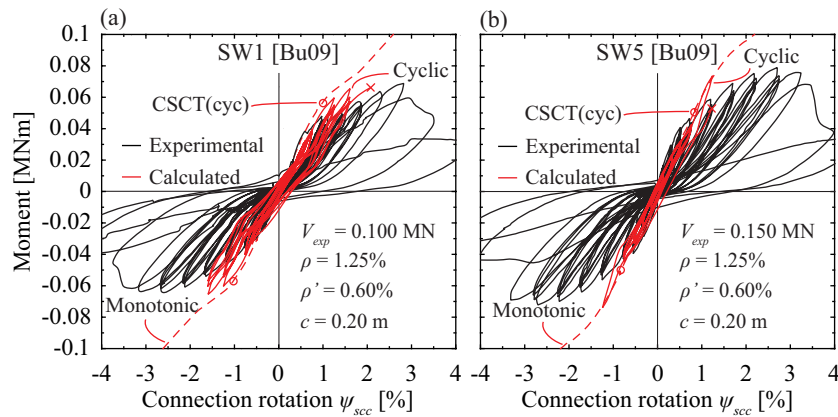Figure C.20 – Comparison between experimental and calculated moment-connection rotation curves for the isolated specimens tested within the present research under monotonic conditions: (a) PD3, (b) PD5, (c) PD4, (d) PD1, (e) PD10, and (f) PD12.

C.2.2 Constant eccentricity

Elstner and Hognestad [Els56]

Figure C.21 – Comparison between experimental and calculated shear force-maximum slab rotation curves for the isolated specimens tested by Elstner and Hognestad [Els56]: (a) A11, and (b) A12.

Hawkins et al. [Haw89]

Figure C.22 – Comparison between experimental and calculated shear force-maximum slab rotation curves for the isolated specimens tested by Hawkins et al. [Haw89]
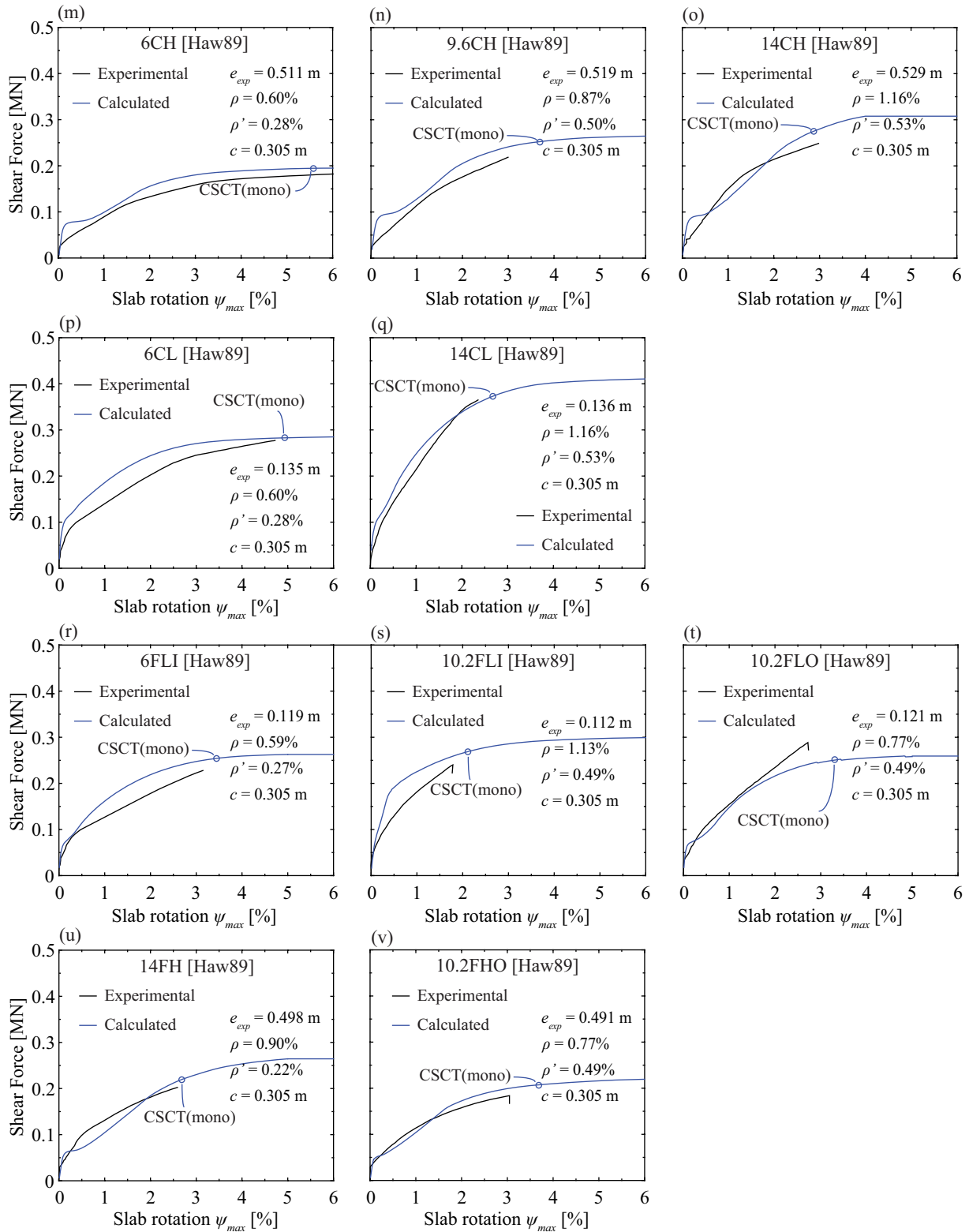
Figure C.23 – Comparison between experimental and calculated shear force-maximum slab rotation curves for the isolated specimens tested by Hawkins et al. [Haw89]

Krüger [Kru99]
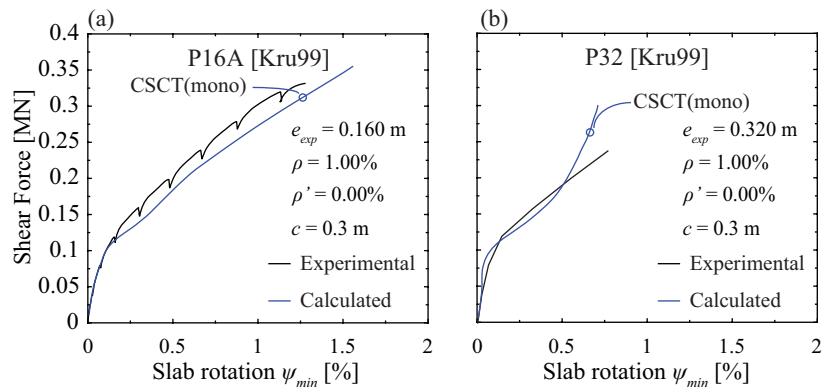
Figure C.24 – Comparison between experimental and calculated shear force-minimum slab rotation curves for the isolated specimens tested by Krüger [Kru99]: (a) P16A, and (b) P30A.
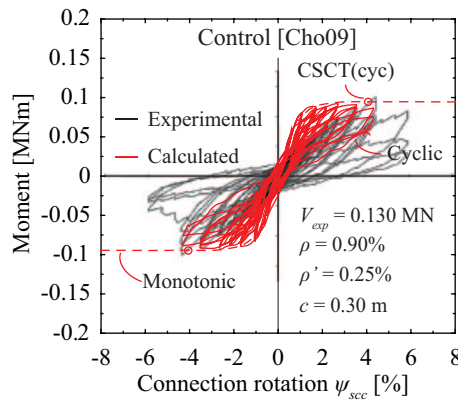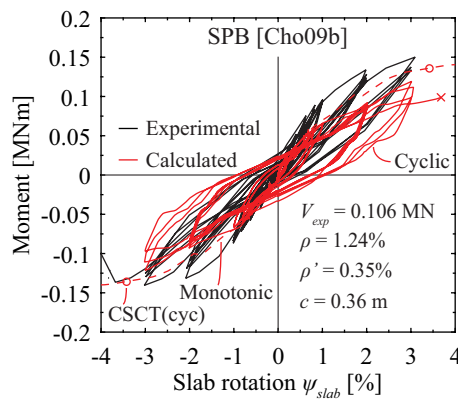
Binici and Bayrak [Bin05]
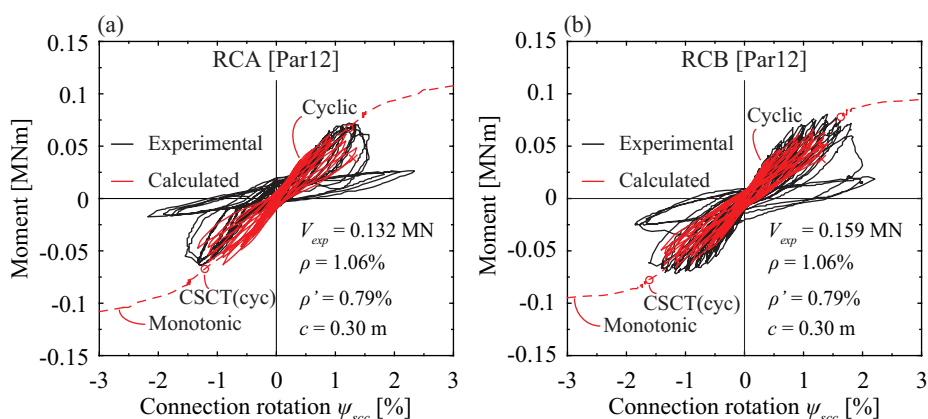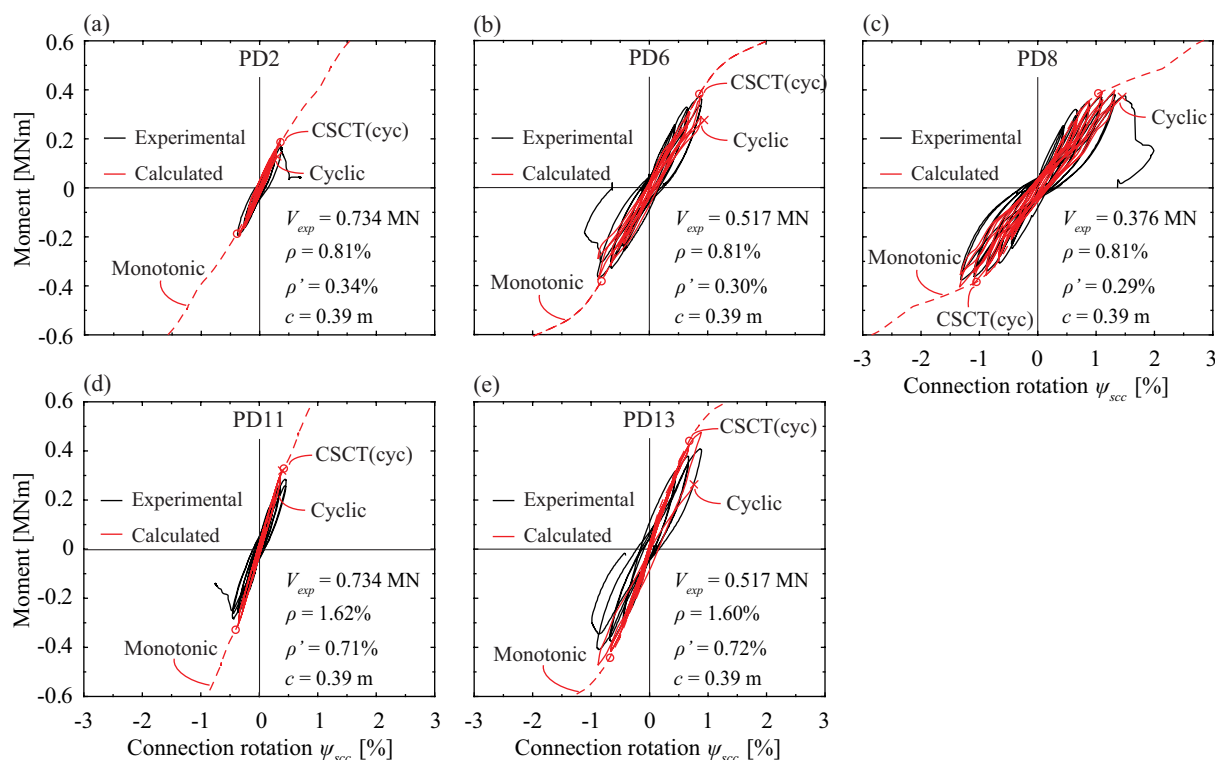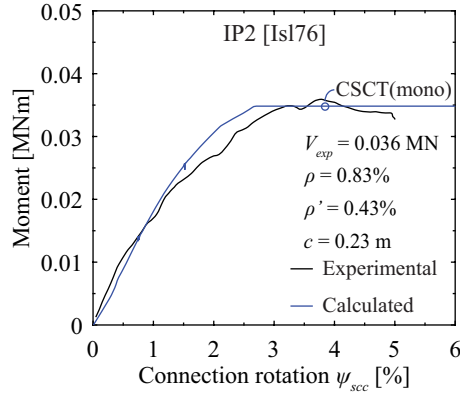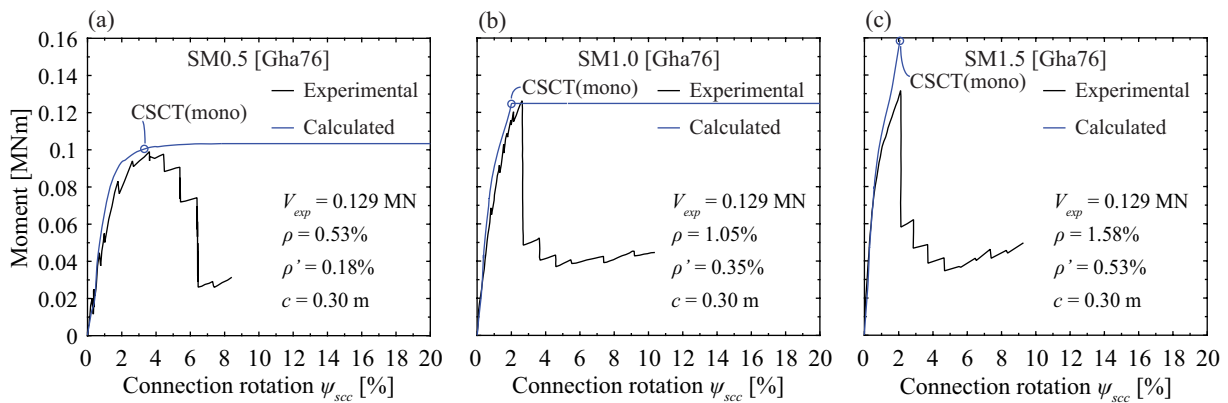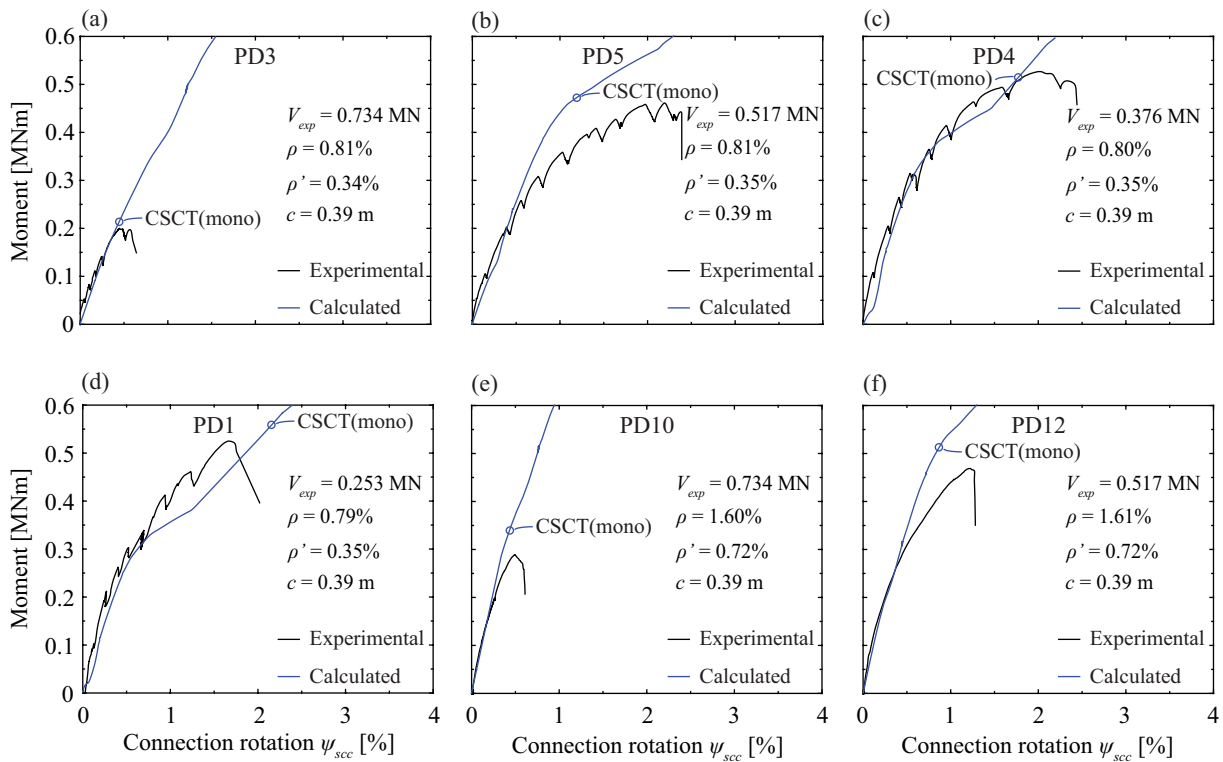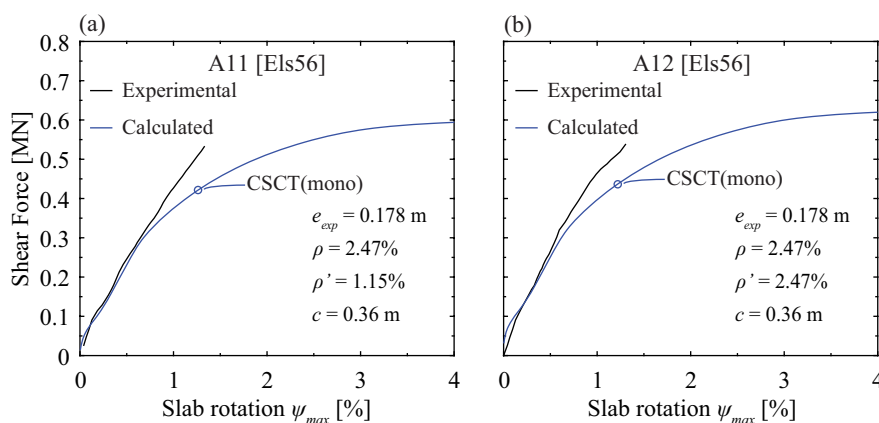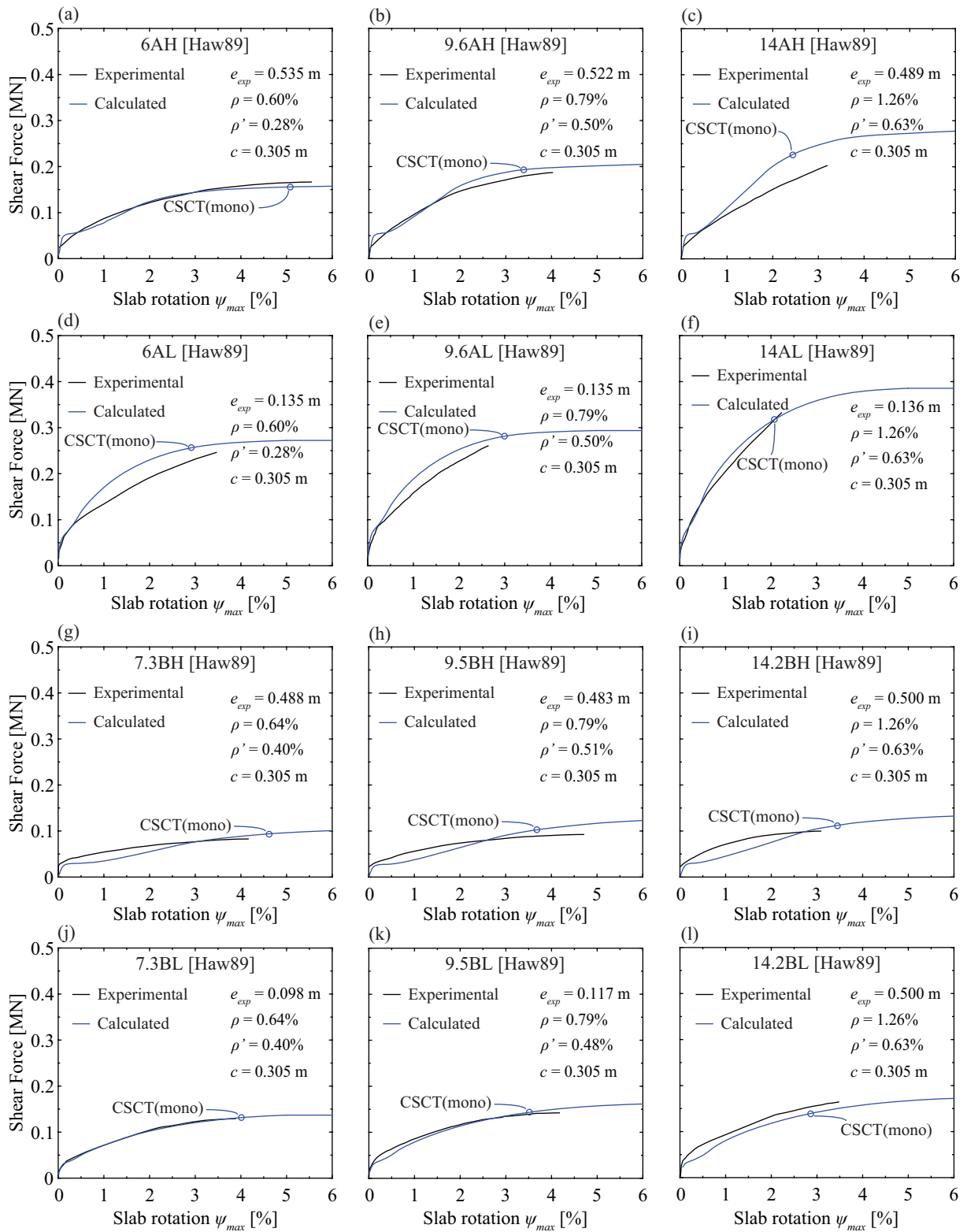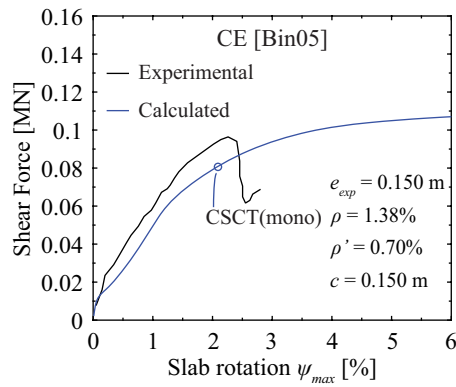

Figure C.25 – Comparison between experimental and calculated moment-connection rotation curves for the isolated specimen CE tested by Binici and Bayrak [Bin05].

Appendix D

Moment and deformation capacity evaluation

Table D.1 – Moment and deformation capacity predictions for interior slab-column specimens tested under constant vertical load and monotonically increasing unbalanced moment

Source	Mark	M_{pred}/M_{exp} [-]						$\psi_{scc.pred}/\psi_{scc.exp}$ [-]		
		CSCT (cyc)	CSCT (mono)	[ACI14]	[Bro09]	[Eur04]	[Fib11]	CSCT (cyc)	CSCT (mono)	[Bro09]
[Gha74]	B3NP	0.696	0.948	0.462	0.896	0.684	0.592	-	-	-
	B5NP	0.674	0.817	0.435	0.851	0.615	0.547	-	-	-
[Sta74]	C/I/1	0.632	0.832	-	1.674	0.014	0.134	-	-	-
	C/I/2	0.779	0.984	0.151	1.656	0.299	0.324	-	-	-
	C/I/3	0.819	1.059	0.409	1.462	0.559	0.707	-	-	-
	C/I/4	0.914	0.962	0.448	1.280	0.607	0.580	-	-	-
[Gha76]	SM0.5	0.955	1.009	0.558	1.000	0.865	0.842	0.637	0.928	2.221
	SM1.0	0.880	0.979	0.744	1.020	0.892	0.873	0.623	0.762	1.049
	SM1.5	0.999	1.268	0.786	1.051	1.047	0.971	0.760	1.063	1.102
[Isl76]	IP1	1.084	1.084	0.536	1.621	0.904	0.822	1.137	1.137	3.194
	IP2	0.926	0.926	0.455	1.412	0.785	0.740	1.094	1.094	3.111
[Elg87]	1	0.822	1.061	0.485	0.945	0.711	0.615	0.825†	1.054†	-
Test campaign	PD1	0.730	1.070	0.710	0.808	0.903	0.655	-*	-*	-*
	PD3	0.945	1.066	0.440	0.933	0.495	-	0.848	0.981	2.369
	PD4	0.771	0.975	0.581	0.840	0.721	0.464	0.522	0.876	1.099
	PD5	0.868	1.021	0.463	0.881	0.530	0.283	0.390	0.545	0.874
	PD10	0.881	1.170	0.231	0.683	0.721	0.362	0.618	0.886	0.661
	PD12	0.864	1.094	0.407	0.651	0.778	0.562	0.503	0.721	0.705
Mean (all tests)		**0.847**	**1.018**	**0.488**	**1.092**	**0.674**	**0.593**	**0.723**	**0.913**	**1.639**
Mean ($d > 0.1$m)		**0.840**	**1.040**	**0.525**	**0.880**	**0.747**	**0.615**	**0.636**	**0.869**	**1.260**
COV (all tests)		**0.140**	**0.107**	**0.332**	**0.308**	**0.361**	**0.384**	**0.328**	**0.198**	**0.603**
COV ($d > 0.1$m)		**0.124**	**0.109**	**0.304**	**0.141**	**0.215**	**0.345**	**0.241**	**0.194**	**0.525**

† ψ_{max} at $0.83 M_{exp}$
*   inconsistent rotation measurement

Table D.2 – Moment and deformation capacity predictions for interior slab-column specimens tested under constant vertical load and cyclically increasing unbalanced moment

Source	Mark	M_{pred}/M_{exp} [-]					$\psi_{scc.pred}/\psi_{scc.exp}$ [-]			
		CSCT (cyc)	CSCT (mono)	[ACI14]	[Eur04]	[Fib11]	CSCT (cyc)	CSCT (mono)	[ACI14]	[Hue99]
[Kan75]	H9	1.094	1.103	0.700	0.928	0.666	1.040	1.000	0.970	1.300
	H10	1.027	0.986	0.626	0.883	0.771	0.970	1.000	0.958	1.270
	H11	1.007	1.008	0.417	0.680	0.522	1.012	1.000	0.500	1.056
[Isl76]	IP3C	1.012	-◇	0.405	0.800	0.724	0.843	-◇	0.641	0.982
[Mor83]	S5	0.924	1.123	0.583	1.042	1.348	0.963	1.077	0.559	-
[Zee84]†	INT	0.954	1.039	0.629	0.689	0.661	0.964	0.987	0.410	0.431
[Pan89]	AP1	0.986	1.032	0.821	0.954	0.520	0.917	1.000	1.079	1.292
	AP3	1.032	1.191	0.534	0.774	0.621	0.882	1.000	0.765	1.195
[Cao93]	CD1	0.931	1.108	0.433	0.756	0.499	0.897	0.823	0.556	0.917
	CD5	0.992	1.101	0.456	0.723	0.721	0.899	1.042	0.417	0.918
	CD8	0.937	1.061	0.486	0.764	0.742	0.875	1.077	0.761	1.023
[Rob02]†	1C	1.011	0.935	0.999	1.009	0.823	1.208	0.855	0.640	0.961
[Sta05]	C-02	0.883	0.921	0.901	1.029	0.902	0.988	0.870	0.444	0.583
[Rob06]†	ND1C	0.992	0.898	0.504	1.076	0.890	0.975	0.930	0.466	0.715
	ND4LL	0.941	0.916	0.462	0.847	0.507	0.988	1.000	0.635	0.837
	ND5XL	0.937	0.955	0.636	0.665	0.119	1.090	0.755	0.485	0.662
	ND6HR	0.957	0.893	0.558	0.899	0.729	0.986	1.010	0.650	0.868
	ND7LR	0.925	0.987	0.571	0.844	0.419	0.987	1.000	0.522	0.552
[Cho07]	S1	0.998	1.057	0.729	0.856	0.907	1.033	1.000	0.772	1.181
	S2	0.810	0.948	0.815	0.758	0.375	0.809	1.003	0.442	0.491
	S3	0.881	0.912	0.604	0.740	0.737	0.902	1.038	0.790	1.196
[Par07]†	RI-50	0.955	0.916	0.719	1.091	0.521	1.025	0.634	0.535	0.690
[Kan08]	C0	0.817	1.068	0.948	1.086	0.646	0.814	0.857	1.074	1.469
[Tia08]	L0.5	1.001	0.859	0.714	0.932	0.478	1.121	0.990	1.180	1.469
[Bu09]	SW1	0.881	1.026	0.409	0.592	0.503	-*	-*	-*	-*
	SW5	0.775	1.132	0.298	0.415	0.362	-*	-*	-*	-*
[Cho09]†	Control	0.897	0.877	0.885	1.354	1.164	0.916	0.968	0.452	0.622
[Cho09b]†	SPB	0.988	0.886	0.841	0.951	1.189	0.930	0.815	0.654	1.023
[Par12]	RCA	0.956	0.873	0.680	0.872	0.553	0.987	0.936	0.865	1.094
	RCB	1.052	0.865	0.919	0.995	0.628	1.190	0.978	0.927	1.039
Test campaign	PD2	1.009	1.010	0.515	0.561	-	1.132	1.000	1.389	2.260
	PD6	0.971	1.016	0.597	0.728	0.372	0.918	1.000	0.829	1.439
	PD8	0.980	1.047	0.659	0.857	0.565	0.766	1.000	0.993	1.100
	PD11	0.928	1.126	0.241	0.731	0.367	0.721	0.907	1.163	1.670
	PD13	1.007	1.159	0.488	0.924	0.668	0.718	1.000	0.680	1.389
Mean (all tests)		**0.956**	**1.001**	**0.622**	**0.852**	**0.653**	**0.954**	**0.955**	**0.733**	**1.053**
Mean ($d > 0.1$m)		**0.967**	**1.011**	**0.643**	**0.885**	**0.641**	**0.924**	**0.943**	**0.842**	**1.212**
COV (all tests)		**0.072**	**0.096**	**0.302**	**0.211**	**0.388**	**0.124**	**0.101**	**0.351**	**0.364**
COV ($d > 0.1$m)		**0.057**	**0.110**	**0.309**	**0.210**	**0.367**	**0.147**	**0.114**	**0.332**	**0.320**

† vertical load partly applied on the slab specimen for which the drift ratio represents the rotation due to slab deformation ψ_{slab}

◇ the loading protocol did not follow a specific pattern

* inconsistently high drift measurement (communication with the authors)

Table D.3 – Moment and deformation capacity predictions for interior slab-column specimens tested under constant eccentricity and monotonically increasing unbalanced moment

| Source | Mark | M_{pred}/M_{exp} [-] | | | | | | $\psi_{max.pred}/\psi_{max.exp}$ [-] | |
		CSCT (mono)	CSCT (cyc)	[ACI14]	[Bro09]	[Eur04]	[Fib11]	CSCT(mono)	CSCT(cyc)
[Els56]	A11	0.796	0.744	0.472	0.664	0.455	0.597	0.906	0.791
	A12	0.825	0.768	0.494	0.690	0.476	0.620	0.950	0.820
[Moe61]	M2	0.927	0.819	0.638	0.945	0.678	0.760	-	-
	M2A	1.088	0.961	0.695	1.054	0.670	0.864	-	-
	M3	1.049	0.832	0.672	0.973	0.653	0.838	-	-
	M4A	1.260	0.966	0.748	1.041	0.729	0.967	-	-
	M6	0.991	0.892	0.703	1.218	0.673	0.921	-	-
	M7	0.965	0.930	0.748	1.055	0.706	0.840	-	-
	M8	1.147	0.937	0.690	1.378	0.671	1.016	-	-
	M9	1.003	0.945	0.714	1.057	0.679	0.843	-	-
	M10	1.048	0.893	0.651	1.185	0.630	0.865	-	-
[Ani70]	B3	0.932	0.880	0.577	0.874	0.553	0.695	-	-
	B4	1.095	1.008	0.609	1.002	0.589	0.746	-	-
	B5	1.017	0.861	0.518	0.905	0.504	0.643	-	-
	B6	0.925	0.759	0.457	0.733	0.510	0.572	-	-
	B7	1.115	0.876	0.567	0.812	0.637	0.698	-	-
[Nar71]	L1	0.940	0.841	0.686	1.000	0.659	0.768	-	-
[Haw89]	6AH	0.918	0.888	0.909	1.252	0.876	0.856	0.915	0.663
	9.6AH	1.032	0.958	0.796	1.236	0.776	0.803	0.841	0.652
	1.4AH	1.101	0.942	0.713	1.082	0.695	0.807	0.762	0.596
	6AL	1.058	0.995	0.968	1.155	0.924	0.837	0.915	0.724
	9.6AL	1.098	1.060	1.002	1.218	0.958	0.904	1.133	0.951
	1.4AL	1.002	0.966	0.743	0.943	0.711	0.792	0.932	0.851
	7.3BH	1.172	1.061	0.988	1.396	0.970	0.920	1.115	0.877
	9.5BH	1.089	0.929	0.812	1.220	0.836	0.822	0.778	0.604
	14.2BH	1.096	0.870	0.809	1.276	0.782	0.897	1.078	0.755
	7.3BL	1.021	0.957	1.070	1.053	1.032	0.874	1.028	0.820
	9.5BL	1.015	0.934	0.971	1.138	0.938	0.869	0.842	0.673
	14.2BL	0.868	0.822	0.762	0.945	0.738	0.756	0.824	0.729
	6CH	1.044	1.024	1.098	1.355	1.070	0.942	0.894	0.697
	9.6CH	1.157	1.090	0.924	1.368	0.900	0.874	1.178	0.916
	1.4CH	1.089	0.949	0.744	1.166	0.726	0.774	0.941	0.725
	6CL	1.028	1.011	1.278	1.127	1.220	0.947	1.044	0.799
	1.4CL	1.036	0.988	0.870	1.169	0.833	0.825	1.127	0.966
	1.4FH	1.063	0.919	0.712	1.098	0.694	0.742	1.039	0.806
	6FLI	1.125	1.091	1.148	1.234	1.095	0.942	1.095	0.924
	10.2FLI	1.129	1.062	0.850	1.006	0.812	0.921	1.082	0.830
	10.2FLO	0.863	0.825	0.835	1.040	0.798	0.753	1.191	0.928
	10.2FHO	1.130	0.987	0.918	1.450	0.893	0.909	1.203	0.731
[Kam90]	SA1	0.852	0.808	0.770	0.819	0.731	0.535	-	-
	SA3	0.987	0.944	0.910	1.003	0.871	0.614	-	-
	SA4	1.096	0.964	0.734	1.484	0.717	0.660	-	-
	SB2	1.051	0.883	0.503	0.820	0.492	0.574	-	-
[Mar96]	NHLS0.5	0.808	0.791	0.936	0.854	1.012	0.704	-	-
	NHLS1.0	0.886	0.813	0.657	0.906	0.683	0.640	-	-
	NNHS1.0	1.093	0.893	0.649	1.023	0.703	0.734	-	-
	NHHS0.5	0.877	0.831	0.713	1.033	0.769	0.662	-	-
	NHHS1.0	0.957	0.788	0.557	0.949	0.596	0.609	-	-
[Kru99]	P16A	0.942	0.898	0.870	1.014	0.832	0.718	0.996	0.917
	P32	0.976	0.911	0.725	0.860	0.701	0.665	0.862	0.820

Source	Mark	M_{pred}/M_{exp} [-]						$\psi_{max.pred}/\psi_{max.exp}$ [-]	
		CSCT (mono)	CSCT (cyc)	[ACI14]	[Bro09]	[Eur04]	[Fib11]	CSCT(mono)	CSCT(cyc)
[Bin05]	CE	0.847	0.746	0.435	0.791	0.414	0.522	0.924	0.716
[Ben12]	SI-1	1.077	0.996	0.651	1.458	0.636	0.785	-	-
	SI-2	0.922	0.835	0.657	1.442	0.660	0.821	-	-
Mean (all tests)		**1.012**	**0.912**	**0.761**	**1.075**	**0.747**	**0.778**	**0.985**	**0.788**
Mean ($d > 0.1$m)		**1.013**	**0.920**	**0.786**	**1.080**	**0.770**	**0.807**	**1.000**	**0.805**
COV (all tests)		**0.103**	**0.098**	**0.239**	**0.191**	**0.229**	**0.157**	**0.131**	**0.135**
COV ($d > 0.1$m)		**0.107**	**0.100**	**0.222**	**0.165**	**0.213**	**0.136**	**0.127**	**0.134**

Curriculum Vitae

1. Personal data

Place and date of birth:	Preveza (GR), February 15, 1989
Academic degrees:	M.Sc. in Civil Engineering at the University of Patras (Greece)
Private address:	Rue de Genève 75, CH-1004 Lausanne, Switzerland
Professional address:	EPFL – ENAC – IBETON, Bât. GC, Station 18, CH-1015, Lausanne, Switzerland
E-mail:	isdr1989@hotmail.gr

2. Academic activity

05/2011- 07/2011   Research assistant at University of Patras

Since 09/2011   PhD student and teaching assistant at Ecole Polytechnique Fédérale de Lausanne

3. Professional experience

07/2009- 09/2009

and   Trainee engineer, Ionios Techniki A.E., Lefkada, Greece

08/2010- 09/2010

4. Awards

- Fellowship from the Greek State Scholarship Foundation (I.K.Y.) for the best grade (University of Patras, Greece, 2007)

- 1st prize for the best article in the 17th Student Conference on Strengthening and Repair of Structures, (University of Patras, Greece, 2011)

5. Peer-reviewed publications

Journal articles

- Drakatos et al.[2016] Drakatos, I. -S., Muttoni, A., Beyer, K., 2016, Internal slab-column connections under monotonic and cyclic imposed rotations, Engineering Structures, Vol. 123, pp. 501-516

- Drakatos and Dritsos[2014] Drakatos, I. -S., Dritsos, S., 2014, Contribution of earthquake-resistant design for reinforced concrete buildings when coping with external explosions, Journal of Earthquake Engineering, Vol. 18, No 4, pp. 502-527

Conference articles

- Drakatos et al.[2017] Drakatos, I. -S., Beyer, K., Muttoni, A., 2017, Analytical model for slab-column connections subjected to cyclically increasing drifts, 16th World Conference on Earthquake Engineering (accepted for publication)

- Drakatos et al.[2014c] Drakatos, I.-S., Beyer, K., Muttoni, A., 2014, Lateral force resisting mechanisms in slab-column connections: An analytical approach, Proceedings of the 2nd European Conference on Earthquake Engineering and Seismology, Istanbul, Turkey, 25-29 August, 11 p.

- Drakatos et al.[2014b] Drakatos, I.-S., Beyer, K., Muttoni, A., 2014, Experimental investigation on seismic behaviour of slab-column connections, Proceedings of the 10th International PhD *fib* Symposium in Civil Engineering, Québec, Canada, 21-23 July, pp. 255-261

- Drakatos et al.[2014a] Drakatos, I.-S., Muttoni, A., Beyer, K., 2014, Mechanical model for flexural behaviour of slab-column connections under seismically induced deformations, 4th International *fib* congress, Mumbai, India, 10-14 February 2014, pp. 639-642

6. Languages

GREEK   mother tongue

ENGLISH   fluent

FRENCH   fluent

ITALIAN   independent